BALLISTIC AND DROP-WEIGHT IMPACT STUDIES OF GLARE 5 FIBER-METAL LAMINATES

by

ALI SEYED YAGHOUBI

A dissertation submitted to the Graduate Faculty in Mechanical Engineering in partial fulfillment of the requirements for the degree of Doctor of Philosophy, The City University of New York

2012

This manuscript has been read and accepted for the
Graduate Faculty in Engineering in satisfaction of the
dissertation requirement for the degree of Doctor of Philosophy.

	Prof. Benjamin Liaw
Date	Chair of Examining Committee
	Prof. Mumtaz K. Kassir
Date	Executive Officer

Prof. Benjamin Liaw, Dept. of Mechanical Engineering, The City College of New York.

Prof. Feridun Delale, Dept. of Mechanical Engineering, The City College of New York.

Prof. Jackie Li, Dept. of Mechanical Engineering, The City College of New York.

Prof. Yiannis Andreopoulos, Dept. of Mechanical Engineering, The City College of New York.

Prof. Nikhil Gupta, Dept. of Mechanical and Aerospace Engineering, Polytechnic Institute of New York University.

Supervision Committee

THE CITY UNIVERSITY OF NEW YORK

ABSTRACT

BALLISTIC AND DROP-WEIGHT IMPACT STUDIES OF GLARE 5 FIBER-METAL LAMINATES

by

Ali Seyed Yaghoubi

Adviser: Professor Benjamin Liaw

The aim of this study is to investigate the low-velocity and ballistic impact responses of the GLARE 5 fiber-metal laminates (FMLs) of various thicknesses, stacking sequences and geometries. The low-velocity impact tests were conducted using an Instron-Dynatup 8250 impact test machine. The impact tests were performed at various energy levels ranging from 10 to 100 joules. The ballistic impact tests were performed using a high-speed gas gun.

Both destructive cross-sectional micrographs and nondestructive ultrasonic techniques were adopted to evaluate the damage created by impact. In addition, a high-speed camera was used to assess damage evolution in the FMLs. Ultrasound C-scans were performed using a Physical Acoustics Corporation (PAC) UltraPAC immersion ultrasonic imaging system. Results showed that only the contour of the entire damage area was obtained using ultrasonic C-scan, whereas more details of the damage were provided through the mechanical cross-sectioning technique.

When subjected to low-velocity impact, thicker GLARE 5 FMLs offered higher impact resistance. It was found that the failure mode changed with varying thickness and

impactor mass. The experimental results showed that the threshold cracking energy changed parabolically with respect to the impact velocity, metal volume fraction (MVF) and the specimen thickness. The impact properties of the FMLs were also affected by laminate stacking sequence. The GLARE 5 FMLs made of unidirectional fibers had the least impact resistance; followed by cross-ply and angle-ply configurations; while the quasi-isotropic lay-up showed the best in resistance to impact. Moreover, the damage patterns and impact behaviors were almost invariant to the change in the specimen geometry.

Three different techniques, namely: laser-beam optoelectronics, chronograph and high-speed photography were used to measure projectile velocities along the ballistic trajectory. The classical Lambert-Jonas' equation was very useful in obtaining the ballistic limit velocities (V_{50}), especially for the cases when obtaining lower incident velocity was difficult experimentally. It was found that by changing the geometry from a plate to a beam, the ballistic limit velocity increased. The results showed that V_{50} varied in a parabolic trend with respect to the MVF and the specimen thickness for both geometries. On the other hand, changing the stacking sequence had a less pronounced effect on V_{50} for both geometries. GLARE 5 beam and plate specimens developed damage similar to both monolithic aluminum alloy and polymer composite laminate. The interfacial debonding as well as the aluminum layers bending and stretching were considered to be the major aspects in dissipating the impact energy in the specimens. However, the permanent global bending deformation of the FML plates was less pronounced compared to the FML beams.

The finite element (FE) code LS-DYNA was used to perform numerical simulations of ballistic impact on the GLARE 5 FMLs of diverse thicknesses, stacking sequences and geometries. The aluminum layers as well as the 0.22 caliber copper bullet were modeled using the simplified Johnson-Cook material model. The Chang-Chang composite model with damage was employed for the prepreg layers. The FE models were validated based on the incident projectile impact velocity versus the residual velocity (V_I~V_R) relation, damage patterns and bullet residual length. Good agreement between FE and experimental results was obtained. The validated FE model was then used to extract some useful information in which experimental results were not available, e.g. the penetration resistance force. The FE results revealed that for the cross-ply beam and plate specimens, the maximum contact force was the highest for the thickest specimen; whereas it was the lowest for the thinnest one. On the other hand, for a given specimen configuration, by increasing the projectile incident velocity up to near its V_{50}, the maximum contact force increased. By further increasing the projectile speed above its ballistic limit velocity, the maximum contact force was almost insensitive with respect to an increase in the projectile incident impact velocity. Similar conclusion was also achieved for beam and plate specimens with different lay-up orientations.

ACKNOWLEDGEMENTS

I wish to acknowledge my mentor, Professor Benjamin Liaw, for his guidance throughout this study. I am also thankful to those who have worked in the Materials Processing and Solid Mechanics Laboratory in the Department of Mechanical Engineering at the City College of New York during the period of my study, with special thanks to Dr. Dave Budhoo and Mr. Frank Chow.

I would like to thank NASA Faculty Award for Research (FAR) for supporting this project under Grant No. NAG3-2259 and PSC-CUNY under Grants 61368-00 39, 62209-00 40, 63168-00 41 and 64543-00 42. Dr. Kenneth J. Bowles and Dr. John P. Gyekenyesi were the Technical Monitors of the NASA grant. Part of the equipment used in this investigation was acquired through Army Research Office Grant No. DAAD19-03-1-0086 and DAAD19-99-1-0366, of which Dr. Bruce LaMattina was the Program Manager. Finally, I would like to express my deepest gratitude and appreciation to my parents for their support and patience, allowing me to spend such a wonderful time to work on my research. Their encouragement and suggestions always help me overcome any difficulty I have encountered.

Ali Seyed Yaghoubi

New York, May 2012

TABLE OF CONTENTS

Abstract	iv
Acknowledgements	vii
List of Tables	xi
List of Figures	xii
Chapter 1. Introduction	**1**
1.1. Objective and distinction of this dissertation	2
1.2. Outline	3
Chapter 2. Literature Review	**5**
2.1. Fiber-metal laminates	5
2.2. Low-velocity impact tests on composite structures	11
2.3. High-velocity impact tests on composite structures	14
2.3.1. Light-gas guns without friction	15
2.3.2. Experimental studies	17
2.3.2.1. Measuring velocity of a projectile	17
2.3.2.2. Impact on composite materials	19
2.3.3. Numerical studies	24
Chapter 3. Materials and Test Setup	**26**
3.1. Specimens	26
3.2. Drop-weight impact tester	28
3.3. Ballistic gas-gun	32
3.4. The ultrasonic damage evaluation system	40
Chapter 4. Drop-Weight Impact Tests on GLARE 5 FMLs	**44**
4.1. Low-velocity impact tests	44
4.2. Effect of specimen thickness	47
4.2.1. GLARE 5 (2/1), (3/2) and (4/3)	48
4.2.2. GLARE 5 (5/4) and (6/5)	50
4.2.3. Strain results	52
4.3. Effect of impactor mass	57
4.4. Threshold cracking energy	60

4.5. Post-impact damage assessment 63
4.6. Effect of stacking sequence 67
4.6.1. GLARE 5 (3/2) square specimens with various lay-up configurations 72
4.6.2. GLARE 5 (3/2) circular vs. square specimens with various lay-up configurations 78
4.7. Conclusions 89
Chapter 5. Measurement of Projectile Velocities in a High-Speed Gas Gun 92
5.1. Effect of target position from the gun muzzle 92
5.2. Intermediate ballistics 97
5.3. Possible errors in measuring the projectile velocity 99
5.4. Determination of the ballistic limit velocity (V_{50}) 104
5.5. Conclusions 105
Chapter 6. Ballistic Impact Tests on GLARE 5 FMLs 107
6.1. Ballistic impact tests on GLARE 5 FML beams 109
6.1.1. Effect of specimen thickness 109
6.1.2. Effect of specimen stacking sequence 122
6.2. Ballistic impact tests on GLARE 5 FML plates 130
6.2.1. Effect of specimen thickness 130
6.2.2. Effect of specimen stacking sequence 140
6.3. Effect of geometry on ballistic impact tests on GLARE 5 FMLs 147
6.4. Conclusions 149
Chapter 7. Finite Element Analysis 152
7.1. Material models 152
7.2. Contact and delamination/debonding model 156
7.3. FE modeling of ballistic impact tests on GLARE 5 FML beams 157
7.3.1. Model validation of GLARE 5 FML beams: thickness effect 159
7.3.1.1. Numerical prediction: thickness effect 166
7.3.2. Model validation of GLARE 5 FML beams: stacking sequence effect 173
7.3.2.1. Numerical prediction: stacking sequence effect 179
7.4. FE modeling of ballistic impact tests on GLARE 5 FML plates 183
7.4.1. Model validation of GLARE 5 FML plates: thickness effect 185

7.4.1.1. Numerical prediction: thickness effect 193
7.4.2. Model validation of GLARE 5 FML plates: stacking sequence effect 195
7.4.2.1. Numerical prediction: stacking sequence effect 200
7.5. Conclusions 202
Chapter 8. Conclusions and Proposed Future Work 204
8.1. Summary 204
8.2. Contributions 207
8.3. Proposed future work 207
References 209
Publications Relevant to the Dissertation 218
Other Publications 220

LIST OF TABLES

Table2.1	Standard GLARE grades.	7
Table3.1	GLARE 5 panels tested in this study with different thicknesses and stacking sequences.	26
Table3.2	Typical values of mechanical properties.	27
Table3.3	Notations used in drop impact equations.	31
Table4.1	Crack lengths and permanent deflections of GLARE 5 with different thicknesses (impactor mass: 12.91 kg).	64
Table4.2	Crack lengths and permanent deflections of GLARE 5 with different thicknesses (impactor mass: 6.14 kg).	65
Table4.3	Crack lengths and permanent deflections of the cross-ply GLARE 5 (3/2) FMLs under different impact energies.	67
Table4.4	Crack lengths and permanent deflections of the GLARE 5 (3/2) FMLs with various stacking sequences under 40J impact energy.	88
Table7.1	Material model parameters used for the 2024-T3 aluminum-alloy layers and 0.22 copper bullet.	155
Table7.2	Material model parameters used for the unidirectional S2-glass/epoxy prepreg layers.	156

LIST OF FIGURES

Fig.2.1	Schematic of fiber-metal laminates.	5
Fig.2.2	Impact performance of various materials.	8
Fig.2.3	Impact strength of GLARE versus thickness.	9
Fig.2.4	Impact strength of GLARE versus surface density.	9
Fig.2.5	Impact properties of various materials.	10
Fig.2.6	Gun parameters.	15
Fig.2.7	Perforation mechanisms.	21
Fig.3.1	A schematic of the cross-ply GLARE 5 FML with the (3/2) configuration.	28
Fig.3.2	(a) Drop Weight impact tester, (b) the specimen fixture.	29
Fig.3.3	Square and circular specimen dimensions for the low-velocity impact test.	30
Fig.3.4	A 16-mm hemispherical steel impactor.	30
Fig.3.5	Different views of the high-speed gas gun setup for ballistic impact tests: (a) front view, (b) angled view.	33
Fig.3.6	Specimen container: (a) setup configuration #1, (b) setup configuration #2.	34
Fig.3.7	Ballistic impact test composite specimens: (a) 152.4 mm × 101.6 mm (6″×4″) plate specimen, (b) 254 mm × 25.4 mm (10″×1″) beam specimen.	35
Fig.3.8	Projectile assembly: (a) unassembled pair of sabots, (b) assembled pair of sabots, (c) 0.22 caliper copper bullet, (d) bullet inserted inside the sabots.	36
Fig.3.9	Velocity measurement using optoelectronic technique during ballistic impact near the gun muzzle: (a) lasers and optical sensors, (b) zoomed-in voltage *vs.* time records.	37

Fig.3.10	(a) The Phantom V710 high-speed camera, (b) typical superposition of two bullet images at times t_1 and t_2 from the high-speed video.	38
Fig.3.11	Schematics of the arrangements of velocity-measuring devices used in: (a) setup configuration #1, (b) setup configuration #2.	39
Fig.3.12	The UltraPAC system.	41
Fig.3.13	Through-transmission technique.	42
Fig.3.14	Comparison of ultrasonic scanning techniques: (a) a specimen containing a delamination, (b) A-scan wave, (c) B-scan view, (d) planar view of the C-scan.	43
Fig.4.1	Schematic of the setup for drop-weight impact tests.	45
Fig.4.2	Schematic of strain gage locations on the square and circular specimens.	46
Fig.4.3	Measurement of the permanent central deflection.	46
Fig.4.4	Impact responses of GLARE 5 (2/1) and (3/2) under 30J impact energy.	49
Fig.4.5	Impact responses of GLARE 5 (3/2), (4/3) and (5/4) under 40J impact energy.	50
Fig.4.6	Impact responses of GLARE 5 (4/3), (5/4) and (6/5) under 60J impact energy.	52
Fig.4.7	Impact responses of GLARE 5 (5/4) and (6/5) under 80J impact energy.	53
Fig.4.8	Impact responses of GLARE 5 (5/4) and (6/5) under 100J impact energy.	54
Fig.4.9	Strain histories for the GLARE 5 specimens with different thickness.	55
Fig.4.10	Back-side (non-impacted) view and corresponding C-scan view of the GLARE 5 FMLs with different thicknesses.	56
Fig.4.11	Cross-sectional view of the GLARE 5 FMLs with different thicknesses.	57
Fig.4.12	Central deflection history (a), contact force history (b), and force-deflection (c), comparisons between the 6.14 kg (LM) and 12.91 kg (HM) impactor mass.	59

Fig.4.13	Comparison of GLARE 5 (3/2) under 30J impact energy using 12.91 kg and 6.14 kg impactor masses. Left/right top: cross-sectional view, left/right bottom: non-impacted side optical and C-scan views.	60
Fig.4.14	Comparison between threshold cracking energy and MVF for 6.14kg and 12.91kg impactor masses. In the formulae x is the MVF and y is the threshold cracking energy.	61
Fig.4.15	Comparison between threshold cracking energy and impact velocity for 6.14 kg (diamond) and 12.91 kg (triangle) impactor masses. In the formulae x is the impact velocity and y is the threshold cracking energy.	62
Fig.4.16	Comparison between threshold cracking energy and thickness of the cross-ply GLARE 5 FMLs. In the formulae x is the impact velocity and y is the threshold cracking energy.	63
Fig.4.17	Permanent central deflection of the GLARE 5 FMLs as functions of (a) impact energy and (b) impact velocity.	66
Fig.4.18	Impact responses of the cross-ply GLARE 5 (3/2) under various impact energies.	68
Fig.4.19	Back-side (non-impacted) view and corresponding C-scan view of the cross-ply GLARE 5 (3/2) FMLs under various impact energies.	69
Fig.4.20	Cross-sectional view of the cross-ply GLARE 5 (3/2) FMLs under various impact energies.	70
Fig.4.21	Impact responses of the GLARE 5 (3/2) square specimens with various stacking sequences under 40J impact energy.	74
Fig.4.22	Back-side (non-impacted) view and corresponding C-scan view of the GLARE 5 (3/2) square specimens with various stacking sequences under 40J impact energy.	75
Fig.4.23	Cross-sectional view of the GLARE 5 (3/2) square specimens with various stacking sequences under 40J impact energy. The symbol ⊙ means that the fiber direction is out of the plane.	76
Fig.4.24	Impact responses of the GLARE 5 (3/2) circular specimens with various stacking sequences under 40J impact energy.	81
Fig.4.25	Comparison of the Impact responses between the square and circular unidirectional GLARE 5 (3/2) specimen under 40J impact energy.	82
Fig.4.26	Comparison of the Impact responses between the square and circular cross-ply GLARE 5 (3/2) specimen under 40J impact energy.	83
Fig.4.27	Comparison of the Impact responses between the square and circular angle-ply GLARE 5 (3/2) specimen under 40J impact energy.	84

Fig.4.28	Comparison of the Impact responses between the square and circular quasi-isotropic GLARE 5 (3/2) specimen under 40J impact energy.	85
Fig.4.29	Back side (non-impacted) view and corresponding C-scan view of the GLARE 5 (3/2) circular specimens with various stacking sequences under 40J impact energy.	86
Fig.4.30	Cross-sectional view of the GLARE 5 (3/2) circular specimens with various stacking sequences under 40J impact energy. The symbol ⊙ means that the fiber direction is out of the plane.	87
Fig.5.1	Comparison of the incident projectile speed measured at the optoelectronic paths near the gun muzzle *vs.* the high-speed camera for: (a) setup configuration #1, (b) setup configuration #2. In the equations, x and y stand for the high-speed camera and laser beams near the gun muzzle velocity, respectively.	93
Fig.5.2	Superposed experimental-results of the incident projectile speed measured at the optoelectronic paths near the gun muzzle *vs.* the high-speed camera for both setup configurations.	94
Fig.5.3	Comparison of the projectile-speed measurements using the chronograph #1 *vs.* the high-speed camera (setup configuration #1). In the equation, x stands for the high-speed camera velocity while y stands for the chronograph #1 velocity.	95
Fig.5.4	Projectile-residual-velocity measurements using the chronograph and high-speed camera (setup configuration #2). In the equation, x stands for the high-speed camera velocity while y stands for the chronograph velocity.	96
Fig.5.5	(a) Shock wave formation before projectile exit, (b) the initial formation of shock waves shortly after projectile exit.	98
Fig.5.6	A typical example of the projectile rebounding off the target in a tumbling motion.	100
Fig.5.7	An example of the bullet exiting a target along a straight line.	101
Fig.5.8	An example of the bullet emerging the target with a smaller yaw-angle of 2.73°.	102
Fig.5.9	An example of the bullet exiting the target with a larger yaw-angle of 15.20°.	103
Fig.5.10	An example of the bullet departing the target in a tumbling motion.	104
Fig.6.1	Classification of impact regimes: a) low-velocity, b) high-velocity and c) ballistic impact.	107

Fig.6.2	A typical composite beam specimen mounted with two strain gages on the ballistic impact side.	109
Fig.6.3	Experimental residual velocity *vs*. incident velocity fitted with Lambert-Jonas' equation using different P values for the GLARE 5 (2/1) beam specimen.	111
Fig.6.4	Experimental residual velocity *vs*. incident velocity fitted with Lambert-Jonas' equation using different P values for the GLARE 5 (3/2) beam specimen.	111
Fig.6.5	Experimental residual velocity *vs*. incident velocity fitted with Lambert-Jonas' equation using different P values for the GLARE 5 (4/3) beam specimen.	112
Fig.6.6	Experimental residual velocity *vs*. incident velocity fitted with Lambert-Jonas' equation using different P values for the GLARE 5 (5/4) beam specimen.	112
Fig.6.7	Experimental residual velocity *vs*. incident velocity fitted with Lambert-Jonas' equation using different P values for the GLARE 5 (6/5) beam specimen.	113
Fig.6.8	Variation of ballistic limit with thickness for the cross-ply GLARE 5 beam specimens. In the equation x stands for thickness and y for V_{50}.	113
Fig.6.9	Variation of ballistic limit with metal volume fraction for the cross-ply GLARE 5 beam specimens with different thicknesses. In the equation x stands for MVF and y for V_{50}.	114
Fig.6.10	Damage induced in the GLARE 5 FML beams with various thicknesses impacted at different incident velocities. Impacted-side (top), non-impacted-side (middle), and side (bottom) views.	116
Fig.6.11	Cross-sectional views of the GLARE 5 FML beams with various thicknesses impacted at different incident velocities.	119
Fig.6.12	High-speed camera footage of the GLARE 5 (2/1) FML beam impacted at 269 m/s.	120
Fig.6.13	High-speed camera footage of the GLARE 5 (6/5) FML beam impacted at 340 m/s.	121
Fig.6.14	Experimental residual velocity *vs*. incident velocity fitted with Lambert-Jonas' equation using different P values for the unidirectional $[0°_4]$ GLARE 5 (3/2) beam specimen.	123
Fig.6.15	Experimental residual velocity *vs*. incident velocity fitted with Lambert-Jonas' equation using different P values for the unidirectional $[90°_4]$ GLARE 5 (3/2) beam specimen.	123
Fig.6.16	Experimental residual velocity *vs*. incident velocity fitted with Lambert-Jonas' equation using different P values for the cross-ply $[0°/90°]_s$ GLARE 5 (3/2) beam specimen.	124

Fig.6.17 Experimental residual velocity *vs*. incident velocity fitted with Lambert-Jonas' equation using different P values for the quasi-isotropic [0°/±45°/90°] GLARE 5 (3/2) beam specimen. 124

Fig.6.18 Variations of ballistic limit velocity as a function of stacking sequence for the GLARE 5 (3/2) FML beams. 125

Fig.6.19 Damage induced in the GLARE 5 (3/2) FML beams with various stacking sequences impacted at different incident velocities. (a) impacted-side view, (b) side view, (c) non-impacted-side view and (d) cross-sectional view. 127

Fig.6.20 High-speed camera footage of the GLARE 5 (3/2)-[$90°_4$] FML beam impacted at 258 m/s. 128

Fig.6.21 High-speed camera footage of the GLARE 5 (3/2)-$[0°/90°]_s$ FML beam impacted at 256 m/s. 129

Fig.6.22 Experimental residual velocity *vs*. incident velocity fitted with Lambert-Jonas' equation using different P values for the GLARE 5 (2/1) plate specimen. 131

Fig.6.23 Experimental residual velocity *vs*. incident velocity fitted with Lambert-Jonas' equation using different P values for the GLARE 5 (3/2) plate specimen. 132

Fig.6.24 Experimental residual velocity *vs*. incident velocity fitted with Lambert-Jonas' equation using different P values for the GLARE 5 (4/3) plate specimen. 132

Fig.6.25 Experimental residual velocity *vs*. incident velocity fitted with Lambert-Jonas' equation using different P values for the GLARE 5 (5/4) plate specimen. 133

Fig.6.26 Experimental residual velocity *vs*. incident velocity fitted with Lambert-Jonas' equation using different P values for the GLARE 5 (6/5) plate specimen. 133

Fig.6.27 Variation of ballistic limit with thickness for the cross-ply GLARE 5 plate specimens. In the equation x stands for thickness and y for V_{50}. 134

Fig.6.28 Variation of ballistic limit with metal volume fraction for the cross-ply GLARE 5 plate specimens with different thicknesses. In the equation x stands for MVF and y for V_{50}. 134

Fig.6.29 Front and back side views of the GLARE 5 FML plates with various thicknesses impacted at different incident velocities. 136

Fig.6.30 Ultrasonic C-scan images of the GLARE 5 FML plates with various thicknesses impacted at different incident velocities. 137

Fig.6.31 Cross-sectional (a,b) and side (c) views of the GLARE 5 FML plates with various thicknesses impacted at different incident velocities. 138

Fig.6.32 Experimental residual velocity *vs*. incident velocity fitted with Lambert-Jonas' equation using different P values for the unidirectional $[0°_4]$ GLARE 5 (3/2) plate specimen. 141

Fig.6.33 Experimental residual velocity *vs*. incident velocity fitted with Lambert-Jonas' equation using different P values for the cross-ply $[0°/90°]_s$ GLARE 5 (3/2) plate specimen. 141

Fig.6.34 Experimental residual velocity *vs*. incident velocity fitted with Lambert-Jonas' equation using different P values for the angle-ply $[\pm45°]_s$ GLARE 5 (3/2) plate specimen. 142

Fig.6.35 Experimental residual velocity *vs*. incident velocity fitted with Lambert-Jonas' equation using different P values for the quasi-isotropic [0°/±45°/90°] GLARE 5 (3/2) plate specimen. 142

Fig.6.36 Variations of ballistic limit velocity *vs*. stacking sequence for the GLARE 5 (3/2) FML plates. 143

Fig.6.37 Front and back side views of the GLARE 5 FML plates with various stacking sequences impacted at different incident velocities. 144

Fig.6.38 Ultrasonic C-scan images of the GLARE 5 FML plates with various stacking sequences impacted at different incident velocities. 144

Fig.6.39 Cross-sectional (a,b) and side (c) views of the GLARE 5 FML plates with various stacking sequences impacted at different incident velocities. 145

Fig.6.40 Comparison of ballistic limit velocity *vs*. thickness between cross-ply GLARE 5 plate and beam specimens. 148

Fig.6.41 Comparison of ballistic limit velocity *vs*. metal volume fraction between cross-ply GLARE 5 plate and beam specimens. 148

Fig.6.42 Comparison of ballistic limit velocity *vs*. stacking sequence between GLARE 5 (3/2) plate and beam specimens. 149

Fig.7.1 Perspective views of the finite element simulation model: (a) far-off view, (b) close-up view. 158

Fig.7.2 Comparison between experimental and FEM residual-incident velocity trend for the GLARE 5 (2/1) beam specimen. 160

Fig.7.3 Comparison between experimental and FEM residual-incident velocity trend for the GLARE 5 (3/2) beam specimen. 160

Fig.7.4 Comparison between experimental and FEM residual-incident velocity trend for the GLARE 5 (4/3) beam specimen. 161

Fig.7.5 Comparison between experimental and FEM residual-incident velocity trend for the GLARE 5 (5/4) beam specimen. 161

Fig.7.6	Comparison between experimental and FEM residual-incident velocity trend for the GLARE 5 (6/5) beam specimen.	162
Fig.7.7	Comparisons between experimental and FE results of ballistic limit velocity (V_{50}) as a function of beam-specimen thickness. In the equations x stands for thickness and y for V_{50}.	162
Fig.7.8	Comparisons of post-impact damage patterns for the GLARE 5 (2/1) beam specimen impacted at 171.5 m/s.	163
Fig.7.9	Comparisons of post-impact damage patterns for the GLARE 5 (3/2) beam specimen impacted at 254 m/s.	163
Fig.7.10	Comparisons of post-impact damage patterns for the GLARE 5 (4/3) beam specimen impacted at: (a) 130 m/s and (b) 234 m/s.	163
Fig.7.11	Comparisons of post-impact damage patterns for the GLARE 5 (5/4) beam specimen impacted at: (a) 168.5 m/s and (b) 321.5 m/s.	164
Fig.7.12	Comparisons of post-impact damage patterns for the GLARE 5 (6/5) beam specimen impacted at 347 m/s.	165
Fig.7.13	Experiment and FE comparisons of bullet residual length of the GLARE 5 beam specimens with various thicknesses at different incident velocities.	166
Fig.7.14	FE predictions of contact history for the cross-ply GLARE 5 FML beams with various thicknesses impacted at: (a) 50 m/s, and (b) 350 m/s.	167
Fig.7.15	FE predictions of contact history for the cross-ply GLARE 5 FML beams with various thicknesses near their ballistic limit velocities.	167
Fig.7.16	FE predictions of contact force as a function of projectile displacement for the cross-ply GLARE 5 FML beams with various thicknesses impacted at 350 m/s: (a) zoomed-out, (b) zoomed-in.	169
Fig.7.17	Comparison of the FE predicted force-history and damage progression for the cross-ply GLARE 5 (6/5) FML beam impacted at 347 m/s.	170
Fig.7.18	Strain contours of the GLARE 5 (6/5) FML beam impacted at 347 m/s.	171
Fig.7.19	Comparisons of transient dynamic strain histories between the experiment and FE prediction for: (a) GLARE 5 (2/1) impacted at 177 m/s, and (b) GLARE 5 (6/5) impacted at 347 m/s.	172
Fig.7.20	Energy history of the GLARE 5 (4/3) FML beam impacted at 150 m/s.	173
Fig.7.21	Comparison between experimental and FEM residual-incident velocity trend for the unidirectional [$0°_4$] GLARE 5 (3/2) beam specimen.	174

Fig.7.22	Comparison between experimental and FEM residual-incident velocity trend for the unidirectional [90°$_4$] GLARE 5 (3/2) beam specimen.	175
Fig.7.23	Comparison between experimental and FEM residual-incident velocity trend for the cross-ply [0°/90°]$_s$ GLARE 5 (3/2) beam specimen.	175
Fig.7.24	Comparison between experimental and FEM residual-incident velocity trend for the quasi-isotropic [0°/±45°/90°] GLARE 5 (3/2) beam specimen.	176
Fig.7.25	Comparisons between experimental and FE results of ballistic limit velocity (V_{50}) as a function of beam-specimen stacking sequence.	176
Fig.7.26	Comparisons of post-impact damage patterns for the unidirectional [0°$_4$] GLARE 5 (3/2) beam specimen impacted at 274.5 m/s.	177
Fig.7.27	Comparisons of post-impact damage patterns for the unidirectional [90°$_4$] GLARE 5 (3/2) beam specimen impacted at 215 m/s.	177
Fig.7.28	Comparisons of post-impact damage patterns for the cross-ply [0°/90°]$_s$ GLARE 5 (3/2) beam specimen impacted at 254 m/s.	178
Fig.7.29	Comparisons of post-impact damage patterns for the quasi-isotropic [0°/±45°/90°] GLARE 5 (3/2) beam specimen impacted at 234 m/s.	178
Fig.7.30	Experiment and FE comparisons of bullet residual length of the GLARE 5 (3/2) beam specimens with various stacking sequences at different incident velocities.	179
Fig.7.31	FE prediction of contact force as a function of time (a), and projectile displacement (b), for the GLARE 5 (3/2) FML beams with various stacking sequences impacted at 100 m/s.	180
Fig.7.32	FE prediction of contact force as a function of time (a), and projectile displacement (b), for the GLARE 5 (3/2) FML beams with various stacking sequences impacted at 250 m/s.	180
Fig.7.33	FE predicted bullet residual length versus specimen stacking sequence impacted at 100 m/s and 250 m/s.	181
Fig.7.34	FE predicted projectile kinetic energy as a function of time for the GLARE 5 (3/2) FML beams with various stacking sequences impacted at 250 m/s.	182
Fig.7.35	Comparisons of the transient dynamic strain histories between the experiment and FE prediction result for the GLARE 5 (3/2)-[0°/90°]$_s$ impacted at 179 m/s: (a) strain gage #1, (b) strain gage #2.	183
Fig.7.36	Perspective views of the finite element simulation model: (a) far-off view, (b) close-up view.	184
Fig.7.37	Comparison between experimental and FEM residual-incident velocity trend for the GLARE 5 (2/1) plate specimen.	186

Fig.7.38	Comparison between experimental and FEM residual-incident velocity trend for the GLARE 5 (3/2) plate specimen.	186
Fig.7.39	Comparison between experimental and FEM residual-incident velocity trend for the GLARE 5 (4/3) plate specimen.	187
Fig.7.40	Comparison between experimental and FEM residual-incident velocity trend for the GLARE 5 (5/4) plate specimen.	187
Fig.7.41	Comparison between experimental and FEM residual-incident velocity trend for the GLARE 5 (6/5) plate specimen.	188
Fig.7.42	Comparisons between experimental and FE results of ballistic limit velocity (V_{50}) as a function of plate-specimen thickness. In the equations x stands for thickness and y for V_{50}.	188
Fig.7.43	Comparisons of post-impact damage patterns for the GLARE 5 (2/1) plate specimen impacted at 153 m/s.	189
Fig.7.44	Comparisons of post-impact damage patterns for the GLARE 5 (3/2) plate specimen impacted at 201.5 m/s.	189
Fig.7.45	Comparisons of post-impact damage patterns for the GLARE 5 (4/3) plate specimen impacted at: (a) 153 m/s and (b) 327 m/s.	190
Fig.7.46	Comparisons of post-impact damage patterns for the GLARE 5 (5/4) plate specimen impacted at: (a) 141 m/s and (b) 368 m/s.	191
Fig.7.47	Comparisons of post-impact damage patterns for the GLARE 5 (6/5) plate specimen impacted at: (a) 194 m/s and (b) 366.5 m/s.	192
Fig.7.48	Experiment and FE comparisons of bullet residual length of the GLARE 5 plate specimens with various thicknesses at different incident velocities.	193
Fig.7.49	FE predictions of contact history for the cross-ply GLARE 5 FML plates with various thicknesses impacted at: (a) 50 m/s, and (b) 350 m/s.	194
Fig.7.50	FE predictions of contact history for the cross-ply GLARE 5 FML plates with various thicknesses near their ballistic limit velocities.	194
Fig.7.51	Comparison between experimental and FEM residual-incident velocity trend for the unidirectional $[0°_4]$ GLARE 5 (3/2) plate specimen.	196
Fig.7.52	Comparison between experimental and FEM residual-incident velocity trend for the cross-ply $[0°/90°]_s$ GLARE 5 (3/2) plate specimen.	196
Fig.7.53	Comparison between experimental and FEM residual-incident velocity trend for the angle-ply $[\pm 45°]_s$ GLARE 5 (3/2) plate specimen.	197

Fig.7.54	Comparison between experimental and FEM residual-incident velocity trend for the quasi-isotropic [0°/±45°/90°] GLARE 5 (3/2) plate specimen.	197
Fig.7.55	Comparisons between experimental and FE results of ballistic limit velocity (V_{50}) as a function of plate-specimen stacking sequence.	198
Fig.7.56	Comparisons of post-impact damage patterns for the unidirectional [$0°_4$] GLARE 5 (3/2) plate specimen impacted at 290.5 m/s.	198
Fig.7.57	Comparisons of post-impact damage patterns for the cross-ply [0°/90°]$_s$ GLARE 5 (3/2) plate specimen impacted at 201.5 m/s.	199
Fig.7.58	Comparisons of post-impact damage patterns for the angle-ply [±45°]$_s$ GLARE 5 (3/2) plate specimen impacted at 227 m/s.	199
Fig.7.59	Comparisons of post-impact damage patterns for the quasi-isotropic [0°/±45°/90°] GLARE 5 (3/2) plate specimen impacted at 178 m/s.	200
Fig.7.60	Experiment and FE comparisons of bullet residual length of the GLARE 5 (3/2) plate specimens with various stacking sequences at different incident velocities.	200
Fig.7.61	FE prediction of contact force as a function of time for the GLARE 5 (3/2) FML plates with various stacking sequences impacted at: (a) 50 m/s, (b) 350 m/s.	201
Fig.7.62	FE predictions of contact history for the GLARE 5 (3/2) FML plates with various stacking sequences near their ballistic limit velocities.	202

CHAPTER 1: INTRODUCTION

A structural composite is a material system consisting of two or more phases on a macroscopic scale, whose mechanical performance and properties are designed to be superior to those of the constituent materials acting independently. One of the phases, called reinforcement, is usually discontinuous, stiffer, and stronger, whereas the less stiffer and weaker phase, called the matrix, is continuous. Sometimes, because of chemical interactions or other processing effects, an additional phase called an interphase exists between the reinforcement and the matrix. The properties of a composite material depend on the properties of the constituents, their geometry, and the distribution of the phases [1]. Since 1970s, composite structures have been widely used for engineering applications. Compared to metals, composite materials offer a number of distinct advantages, which include, but not limited to, higher strength-to-weight and stiffness-to-weight ratios, superior corrosion resistance, as well as improved fatigue properties [2-5]. In spite of these advantages, laminated composite structures are more susceptible to impact damage than a similar metallic structure. It has been well known that impacts by foreign objects can occur during manufacturing, service, and maintenance operations. An example of in-service impact occurs during aircraft takeoffs and landings, when stones and other small debris from the runway are propelled at high velocities by the tires [2].

Due to the combining beneficial properties of monolithic metals and fiber-reinforced composites, fiber-metal laminates (FMLs) provide drastically improved mechanical properties compared to conventional polymer matrix composites or aluminum alloys [6-8]. GLARE 5 is a member of the family of FMLs made of interlacing layers of 2024-T3 aluminum alloy sheets and high strength S2-glass/epoxy laminates (formed by 4 layers of

unidirectional laminae in the $[0°/90°]_s$ lay-up configuration). The symmetry of the prepreg layers with stacking sequence $[0°/90°]_s$ as well as the unidirectionality of the S2-glass fibers, make GLARE 5 beneficial for impact applications. Because of the interest in impact prone areas of aircraft, e.g. cockpit, research was carried out to optimize a GLARE configuration specifically for impact performance. The result showed that the FMLs produced using 2024-T3 aluminum alloy and unidirectional S2-glass fibers, i.e. GLARE 5, provided maximum impact performance when compared to laminates made with either S2-glass or E-glass weaves [8].

1.1. Objective and distinction of this dissertation

The aim of this study is to investigate low-velocity and ballistic impact responses of GLARE 5 FMLs at room temperature. On the contrary to the non-FML based composite materials, there was limited literature available on impact behavior of FML based composite materials. However, literature review showed that there was meager information on impact performance of GLARE 5 FMLs subjected to low- and high-velocity impact. It is thus critical to acquire more information on impact-damage resistance of this class of hybrid composites, which will indeed lead to better design and application in industries, such as aerospace. Various GLARE 5 panels with different stacking sequences, thicknesses and geometries were chosen for this study.

The low-velocity impact tests were conducted using an Instron-Dynatup 8250 impact test machine. The impact tests were performed at various energy levels ranging from 10 joules through 100 joules. The ballistic impact tests were conducted using an in-house-designed high-speed gas gun equipped with a high-speed camera. Both destructive cross-sectional micrographs and nondestructive ultrasonic techniques were used to evaluate the

damage created by low-velocity and ballistic impact. Ultrasound C-scans were performed using a Physical Acoustics Corporation UltraPAC immersion ultrasonic imaging system. Finally, numerical studies were conducted using a commercially available finite element (FE) package, LS-DYNA. The numerical simulations were only performed on GLARE 5 FMLs subjected to ballistic impact. The research topics considered in this study are as follows:

- Study the effects of thickness, impactor mass, stacking sequence and geometry on low-velocity impact response of GLARE 5 FMLs. In addition, the threshold level of cracking energy was estimated.
- Study the projectile speed along its ballistic trajectory using different techniques, namely: laser-beam optoelectronics, chronograph and high-speed photography.
- Study the effects of target position from the gun muzzle and propellants.
- Study the effects of stacking sequence, thickness and geometry on ballistic impact response of GLARE 5 FMLs.
- Develop an FE model to predict the behavior of GLARE 5 FMLs under ballistic impact.
- Validate the developed FE model based on experimentally obtained results.

1.2. Outline

The research presented in the current dissertation consists of both experimental and numerical work. Chapter 2 presents literature review on both low- and high-velocity impact. Chapter 3 contains materials and test setup used in this study. In Chapter 4, the effects of thickness, impactor mass, stacking sequence and geometry under various impact energies were studied to evaluate the low-velocity impact behavior of the

GLARE 5 FMLs through drop weight tests. Chapter 5 provides different techniques that were used to assess the projectile velocities in a high-speed gas gun. Possible errors in velocity measurements using the chronograph technique have also been considered. Furthermore, the target position from the gun muzzle as well as different propellant gases was discussed.

The topic of ballistic impact on GLARE 5 FMLs is dealt with in Chapter 6. The goal of this chapter is to assess GLARE 5 panels with various thicknesses, stacking sequences and geometries under ballistic impact. Chapter 7 describes finite element analysis on GLARE 5 panels under ballistic impact. The scope of this chapter is first to validate the model with the experimental results obtained in Chapter 6 and then extract some useful information in which experimental results were not available. Finally, future work is described in Chapter 8. All references are listed at the end of the study. Publications from this study are listed at the end of this dissertation.

CHAPTER 2: LITERATURE REVIEW

2.1. Fiber-metal laminates

Fiber-metal laminates (FMLs) were developed in the Netherlands around 1980 [9,10]. FMLs are lightweight materials, consisting of alternating layers of thin metallic sheets (usually aluminum alloys) and fiber reinforced adhesives for aircraft structural applications (Fig. 2.1). The aim of engineering design for these materials is to combine the best properties of metals and fiber-reinforced composites [10].

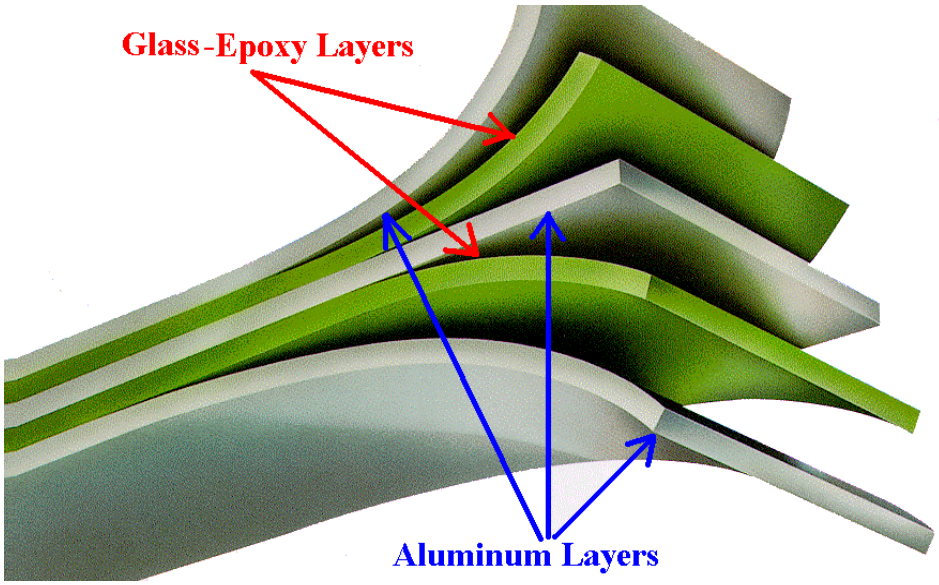

Fig.2.1. Schematic of fiber-metal laminates.

There are two major types of commercially available FMLs: the glass-fiber reinforced FMLs (GLARE (GLAss REinforced) [11]), which are made of alternating glass-epoxy and aluminum layers, and the aramid-fiber reinforced FMLs (ARALL), which are formed by alternating aramid-epoxy and aluminum layers. These hybrid laminates combine the beneficial properties of monolithic metals and fiber-reinforced composites, providing superior mechanical properties compared with conventional polymer matrix composites

or aluminum alloys [6-8,10,12]. A patent of GLARE was first filed on the 14th of October 1987 by AKZO with Roebroeks and Vogelesang named as the inventors [8]. GLARE was originally developed for application in primary aircraft structures, such as the fuselage skin and lower wing skins [8]. GLARE was considered for aircraft fuselage skins at a moment in time that the first member of the FMLs family (ARALL) appeared not to be able to cover any aircraft application. GLARE 5 belongs to the family of GLARE FMLs and is made of alternating layers of 2024-T3 aluminum alloy sheets and unidirectional $[0°/90°]_s$ cross-ply S2-glass/epoxy laminates. The GLARE 5 patent was based on the optimization of a GLARE configuration for impact performance [8].

FMLs have gained wide attention in the aerospace and space industries [9] for many advantages such as low density, high strength, higher damage tolerance to fatigue crack growth and impact damage caused by foreign objects or blast loading, corrosion prevention, fire retardation, etc. [9,13-20]. One major concern with polymer-based composite materials is their response to impact events. Typically, internal damage was formed in composite laminates extending well beyond the impacted area [8,21], which significantly reduced the strength and stiffness of the composite. This internal delamination damage was not usually apparent on the surface of the specimen. It is thus critical that the response of the composite laminates be well understood, so that the size of damage can be estimated from a given impact [8,21]. On the other hand, FMLs did not show such an undesirable response. Under impact loading, they developed damage similar to both a monolithic alloy and a polymer-based composite laminate [8,21]. The internal impact damage in GLARE was mostly confined to a relatively small area surrounding the point of impact. Its size was always smaller than the size of the visible

plastically deformed dent exposed at the outer aluminum layers for GLARE laminates [8,21].

GLARE has six different standard grades [8]. They are all based on unidirectional S-glass fibers embedded with FM 94 adhesive resulting in a 0.127 mm thick prepreg with a nominal fiber volume fraction of 59%. This prepreg is laid-up in different orientations in between the aluminum alloy sheet, resulting in the different standard GLARE grades [8]. Table 2.1 shows these grades, including the most important material advantages. For example GLARE 4B-4/3-0.4 defined as a GLARE laminate with fiber orientation according to the GLARE 4B definition in Table 2.1. It consists of 4 layers of aluminum and 3 fiber layers; each aluminum layer is 0.4 mm thick [8].

Table2.1. Standard GLARE grades [8].

Glare grade	sub	Metal sheet thickness [mm] & alloy	Prepreg orientation in each fibre layer	Main beneficial characteristics
Glare1	-	0.3-0.4 7475-T761	0/0	fatigue, strength, yield stress
Glare 2	Glare 2A	0.2–0.5 2024-T3	0/0	fatigue, strength
	Glare 2B	0.2-0.5 2024-T3	90/90	fatigue, strength
Glare 3	-	0.2-0.5 2024-T3	0/90	fatigue, impact
Glare 4	Glare 4A	0.2-0.5 2024-T3	0/90/0	fatigue, strength in 0° direction
	Glare 4B	0.2-0.5 2024-T3	90/0/90	fatigue, strength in 90° direction
Glare 5	-	0.2-0.5 2024-T3	0/90/90/0	impact
Glare 6	Glare 6A	0.2-0.5 2024-T3	+45/-45	shear, off-axis properties
	Glare 6B	0.2-0.5 2024-T3	-45/+45	shear, off-axis properties

Research had been carried out to optimize a GLARE configuration specifically for impact performance. Effects of aluminum alloy, glass fiber type, thickness of the fiber layers and unidirectionality versus weaves were investigated and the results are shown in Fig. 2.2. It

is evident that FMLs produced using unidirectional S2-glass fibers provided maximum impact performance when compare to laminates made with either S2-glass or E-glass weaves. This work supported the patent for GLARE 5 [8]. Since impact strength of a component is also dependent on thickness of the component, it is more illustrative to compare impact strength on an equal thickness basis. Figure 2.3 compares different grades of GLARE to 2024-T3 aluminum sheets as a function of thickness. The impact strengths of FMLs made from weaves are also shown. The lower impact strength compared to the patented GLARE, i.e. GLARE 5, is significant [8].

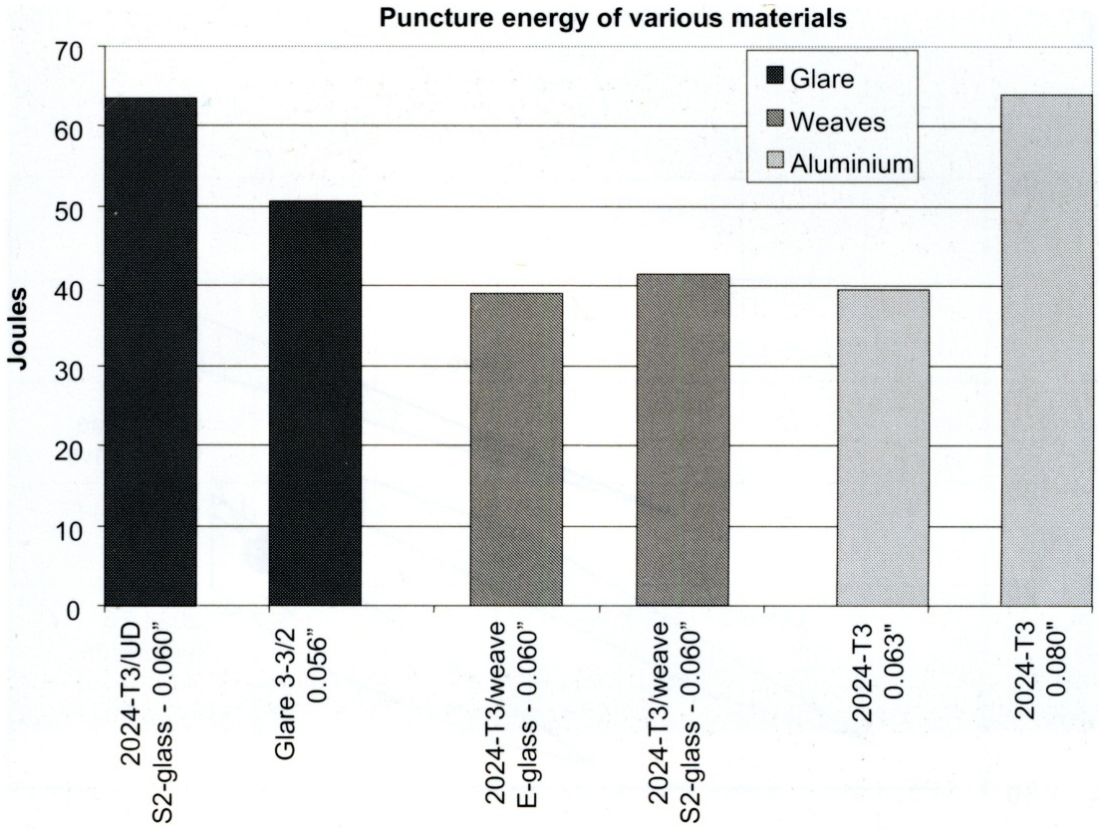

Fig.2.2. Impact performance of various materials [8].

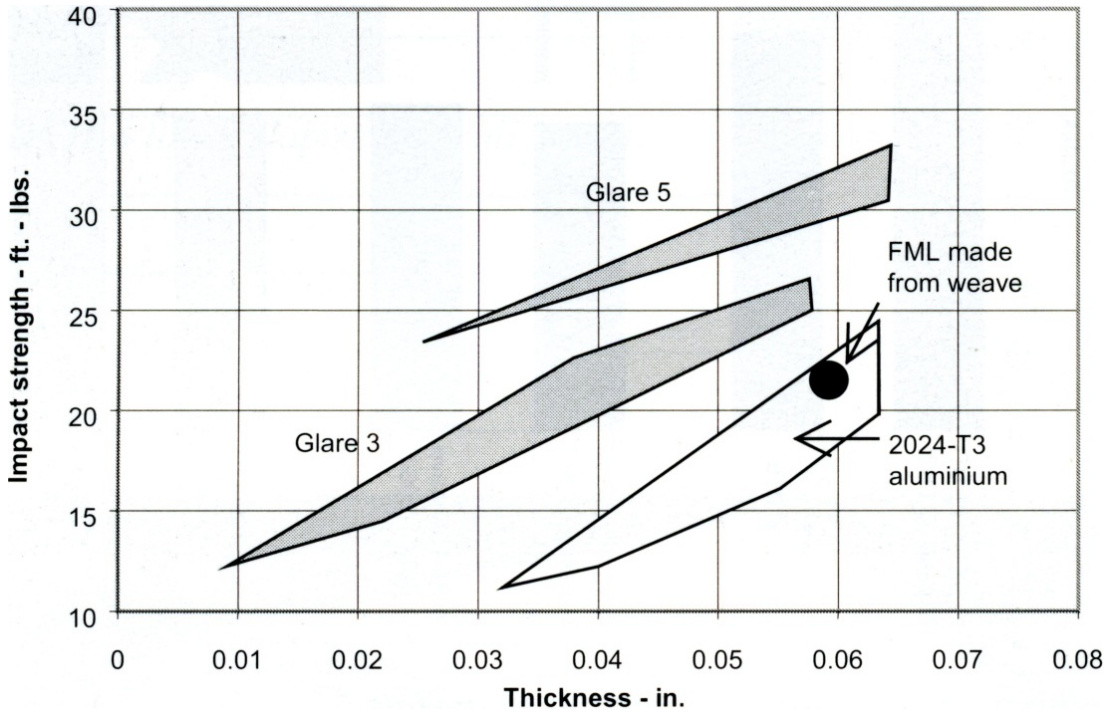

Fig.2.3. Impact strength of GLARE versus thickness [8].

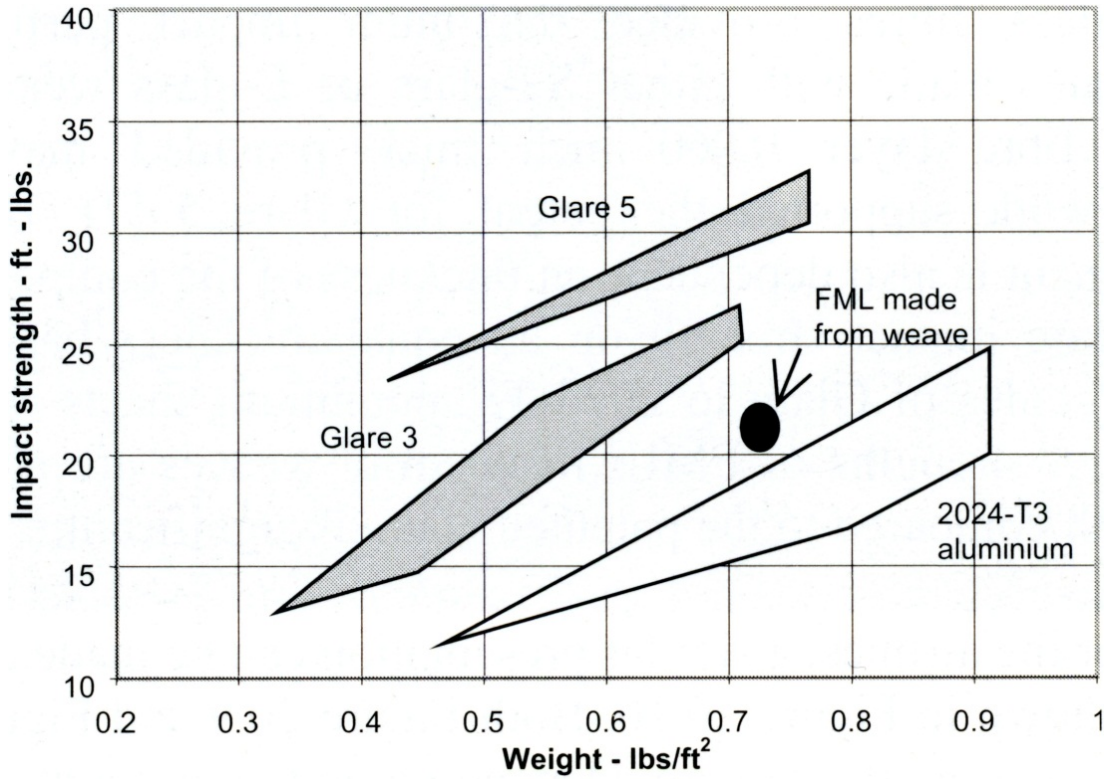

Fig.2.4. Impact strength of GLARE versus surface density [8].

More importantly for the airlines, a similar presentation could be made as a function of surface density, as shown in Fig. 2.4. Both Figs. 2.3 and 2.4 show the outstanding impact strength of GLARE [8]. Furthermore, Fig. 2.5 shows the comparison of impact properties for different materials given by Structural Laminates Company [22]. As is apparent from this figure, GLARE offers higher outer layer cracking energy when subjected to both low- and high-velocity impact. The density of FMLs is lower than that of monolithic aluminum but greater than fiber reinforced composites. With the saving in density, plus the added strength of FMLs over monolithic metals, a structure made of FMLs can save up to 30 percent of its self-weight [10].

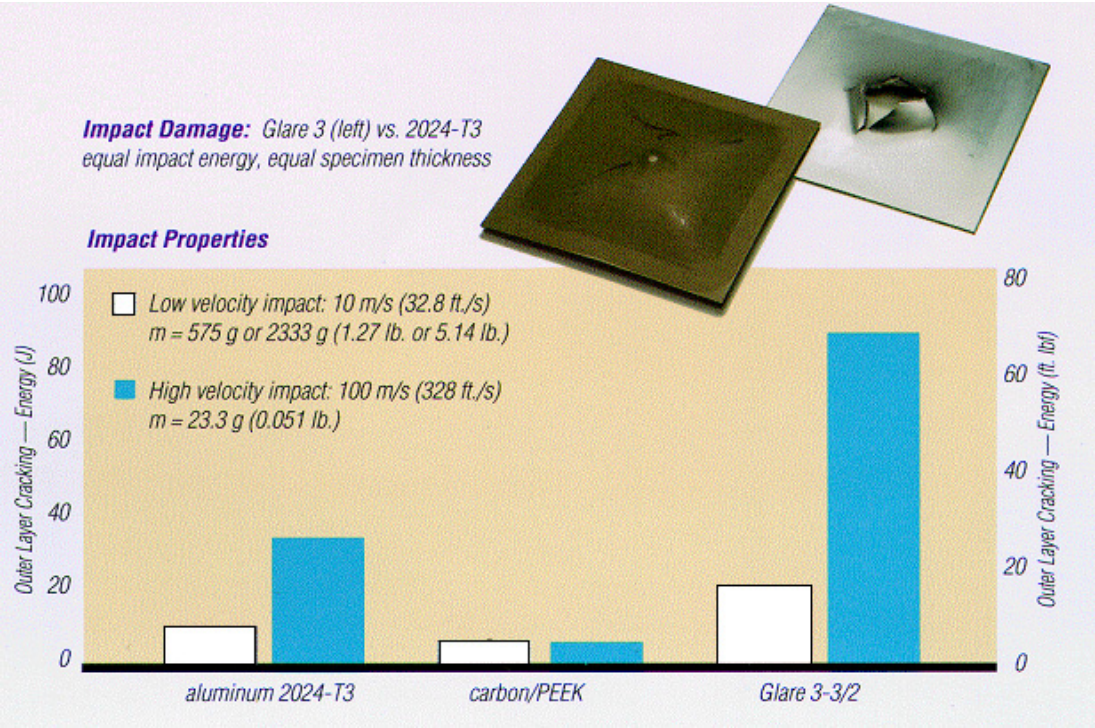

Fig.2.5. Impact properties of various materials [22].

Vlot [23] reported that at low velocities GLARE is as good as aluminum and superior to carbon fiber composites, while at higher speeds the glass fiber in the laminate becomes relatively much stronger and the impact properties much better than that of aluminum. He

stated that GLARE was more resistant to impact than other materials. Furthermore, it was shown that the damage, permanent deformation and the denting of the aluminum layers in the laminate could be found easily with naked eye due to plastic deformation [23]. Composites did not deform plastically; hardly any dent was created and therefore damage was much more difficult to detect in this type of materials [23]. The mechanical properties of GLARE after impact damage was created also appeared to be better [23]. In 1990 the excellent impact properties of GLARE were implemented in the cargo floor in the Boeing 777. This was the first commercial application of a GLARE product [23].

2.2. Low-velocity impact tests on composite structures

The impact responses of composite structures are dominated by the constituent materials, fiber orientations and lay-up configurations, impact energies, geometry of structures, types of impactors, etc. Liu et al. [24, 24a] investigated low-velocity impact damage on ARALL 3 and various GLARE grades, i.e. GLARE 1, 2 and 3. They found that GLARE 1 with glass-epoxy prepregs possessed higher impact tolerance than ARALL 3 with aramid-epoxy prepregs. They also concluded that GLARE 3 with [0°/90°] cross-ply glass-epoxy prepregs offered better impact resistance than GLARE 2, which is made of $[0^{\circ}_2]$ unidirectional glass-epoxy prepregs. Reyes Villanueva et al. [25] studied the mechanical properties of thermoplastic-based FMLs. Park et al. [26] used fiber-vinylester composite materials to examine the effect of laminate thickness on the impact behavior of aramid. They reported that the absorption mechanism of impact energy changed at a thickness between three layer composites and four layer composites. Chen et al. [27] studied the thickness effect on the contact behavior of a composite laminate. They found that their model could predict the force-deflection relationships of several thin laminates.

Tai et al. [28] considered the effects of thickness on the fatigue behavior of quasi-isotropic carbon-epoxy composites before and after low energy impacts. They concluded that low energy impact had a more significant influence on tensile strength for thinner than for thicker laminates. They also found that the energy required to penetrate the laminates was proportional to the thickness of the composites. Furthermore, a drastic decrease in fatigue life was detected for thick laminates when the low energy impact was applied. The low-velocity impact response of FMLs based on a woven glass fiber prepreg and 2024-O aluminum alloy sheets was studied by Fan et al. [29]. They reported that increasing the target size, the plate thickness, and the indenter diameter resulted in an increase in the energy required to perforate the target. In addition, their finite element model prediction for load-displacement traces was in good agreement with the experimental results. Some other researchers also reported that thickness had significant effects on the performance of composite materials under low-velocity impact, e.g. [30-32]. Seo et al. [33] simulated glass-fiber-reinforced aluminum laminates with diverse impact damage. Their results showed good agreement with experimental measurements.

Hitchen et al. [34] considered the effect of stacking sequence on impact damage in a carbon fiber-epoxy composite. They concluded that altering the layer stacking sequence influenced a range of properties, including the peak force during impact, the delamination area, and the pre- and post-impact compression strength in 16-ply carbon fiber toughened epoxy laminates. They also reported that the total delamination area was a function of stacking sequence. Atas et al. [35] studied the effect of the weaving angle on the low impact response of woven composites. No significant effect was reported. Tsartsaris et al. [36] examined low-velocity impact behavior of FML made of 7475-T761 aluminum alloy

and unidirectional S2 glass/epoxy. The test results showed that the panel were capable of absorbing energy through localized plastic deformation and through interfacial failure between the layers. Choi et al. [37] concluded that ply orientation and stacking sequence could significantly affect impact damage. The test results showed that stacking sequence significantly affected the impact energy required to initiate the impact damage. They reported that re-ordering the stacking sequence varied the magnitudes and distributions of the interlaminar shear and transverse tensile stresses. Due to the important roles that these stresses played in initiating impact damage in laminated composites, the effect of these two stresses on the location of the initial failure could be changed significantly. They also found that impact damage was more sensitive to the change of stacking sequence than of thickness. The influence of lay-up configuration on graphite-epoxy composite material was studied by Guynn et al. [38]. They concluded that the difference in compression failure strain due to stacking sequence were small. Mili et al. [39] took into account the effect of stacking sequence on the impact-induced damage in cross-ply E-glass epoxy composite plates. They found that the contact force and displacement histories depended only on the incidental velocity of the projectile. They also concluded that the shape of the contact areas changed according to the number of plies oriented at 0° and 90°. Cantwell et al. [40] investigated geometrical effects in the low-velocity impact response of CFRP. They found that in short thick beams damage initiated at the edge of the point of impact as a result of the locally high impact stresses, whereas in long thin beams fracture occurred as a result of splitting between the lower surface fibers. Moreover, they stated that circular plates under certain conditions were capable of absorbing less energy than small simple beam-like specimens. Cantwell [41] also studied geometrical effects in the

low-velocity impact response of GFRP. He drew a conclusion based on tests of a range of circular and square plates that the degree of damage within the structure was related to the force generated during the impact event. Strait et al. [42] indicated that the quasi-isotropic lay-ups possessed better overall impact resistance than cross-ply or [0/±45] lay-ups

Chun et al. [43] assumed that the contact area between the striker and plate was very small, and used the Hertzian contact law to evaluate the contact force. Choi et al. [44] performed a parametric study on contact law by changing the value of the contact coefficient and exponent in the law. It was shown that accurate analytical results could be achieved using the linearized contact law. A line-nose impactor was adopted by Choi et al. [37,45,46] to study the impact damage mechanisms of composites, which could be substantially simplified from a three-dimensional to a two-dimensional event. They also found that the impact responses of composites was affected by the mass of impactor. Kim et al. [47] showed that a higher impact force and longer impact duration were obtained when the shape of impactor was blunter through a dynamic contact analysis.

2.3. High-velocity impact tests on composite structures

Impact dynamics has two features which distinguish it from the more conventional disciplines of the classical mechanics of rigid or deformable bodies under quasi-static conditions. The first is the importance of inertia effects which must be considered in all of the governing equations based on the fundamental conservation laws of mechanics and physics. The second is the role of stress wave propagation in the analysis of problems and the recognition that most impact events are transient phenomena where steady-state conditions do not exist [48].

2.3.1. Light-gas guns without friction

Applying Newton's law of motion to the problem of projectile motion in a barrel (Fig. 2.6) yields [48]:

$$m\frac{dv}{dt} = m\frac{dv}{dx}v = pA \tag{2.1}$$

with m the projectile mass, v the instantaneous velocity after the distance x, p the base pressure, and A the cross-sectional area of the barrel.

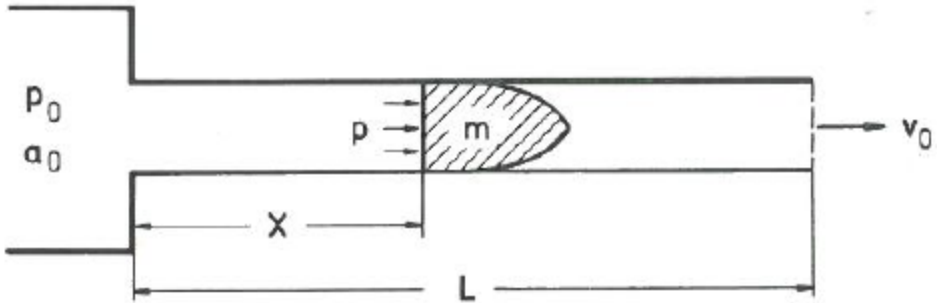

Fig.2.6. Gun parameters [48].

Integration over the total length L of the barrel gives:

$$\frac{mv_0^2}{2} = A\int_0^L pdx \tag{2.2}$$

where v_0 is the muzzle velocity at the end of the barrel. For the simplest case of a constant base pressure $\bar{p}$ over the length of traveling, the muzzle velocity is:

$$v_0 = \sqrt{2\bar{p}\frac{AL}{m}} \tag{2.3}$$

This equation gives the main factors from which the projectile velocity for a frictionless motion depends. For a given cross-sectional area A, the mass m of the projectile must be small, the length L of the barrel large, and the pressure $\bar{p}$ as high as the strength of the gun and the projectile can withstand this pressure. Due to the enlargement of the volume

behind the projectile in all guns, the base pressure $\bar{p}$ behind the projectile is not constant. It depends on driver gas and the reservoir pressure p_0. The following equations show the fundamental requirements for a driver gas to achieve high muzzle velocities.

If an ideal gas with a pressure p_0 and sound velocity a_0 expands from a large reservoir into a barrel, then the pressure p in the expansion stream is a function of the following parameters:

$$p = p_0 \left(1 - \frac{v}{\left(\frac{2}{\gamma} - 1\right) a_0} \right)^{\frac{2\gamma}{(\gamma-1)}} \tag{2.4}$$

where v is the velocity of the expanding gas and γ is the ratio of the specific heats.

By applying this equation to the gas flow behind a projectile, it is evident that the pressure ratio p/p_0 depends on the relation:

$$\frac{v(\gamma - 1)}{2a_0}$$

As the gas expands from the high pressure reservoir, it must consume a portion of the stored energy in it to accelerate its own mass. A maximum flow velocity is reached when the gas must spend all of its energy accelerating itself. This means that the base pressure p drops to zero, or:

$$v_{esc} = \frac{2}{(\gamma - 1)} a_0 \tag{2.5}$$

The maximum velocity v is termed the escape velocity v_{esc}:

$$v_{esc} = \frac{2}{(\gamma - 1)} a_0 = \frac{2}{\gamma - 1} \sqrt{\frac{\gamma R T_0}{M}} \tag{2.6}$$

With T_0 the temperature in the reservoir, M the molecular weight of the gas, and R the gas constant. This relation gives the answer to which type of gas produces the highest escape velocity. It must be a gas with a low molecular weight M and a high temperature T_0 in the reservoir. A gun in which such a driver gas is used is called a light-gas gun [48]. In high velocity guns it is necessary to carry the projectile in the lunch tube with sabots. Sabot is a French word which means wooden shoe. A set of sabots is used to launch various projectile shapes and subcaliber projectiles. The sabots align, support, and protect the projectile during acceleration. They prevent projectile contact with the launch tube wall and separate the projectile from the hot driver gas. Outside the lunch tube, the sabots must separate from the projectile with a minimum of disturbance and interface. The sabots should move away from the projectile trajectory [48].

2.3.2. Experimental studies

2.3.2.1. Measuring velocity of a projectile

Time interval measurement and event time determination are the most important data in all ballistic and impact tests. The velocity measurement is a specific application of time measurement. Velocity measurement systems are necessary to control the muzzle velocity, measure aerodynamic drag of projectiles and fragments, control the impact velocity, measure residual velocities of projectiles and fragments for all kinds of terminal ballistic tests, measure shock wave velocities, particles, and free surface velocities, etc. [48]. Børvik et al. [49] used a compressed gas gun to lunch the sabot mounted projectile at impact velocities well above and just below the ballistic limit of the target plates. They measured initial projectile velocity using a photocell system that had two identical light-barriers with LED-light sources on the upper side of the projectile path and detector on

the lower side was used. When the projectile passed between the sources and detectors in the barrier, light was interrupted and signals were given to a digital oscilloscope and a nanosecond counter. They developed a similar system to measure residual velocities if perforation occurred. In addition, a digital high-speed camera system was used to record the projectile both before and after perforation. The digital images made it possible to measure the impact angles and projectile velocity during perforation. Several tests were carried out at different velocities without placing a target plate inside the impact chamber and they found that the difference in measured velocity between the initial and residual velocity station was less than 1%. It was also reported that the accuracy in the camera measurements was high and deviation was normally within 3-4% of the velocity measured by the other optical measurement systems. In another study by Børvik et al. [50], they installed two extra chronographs to increase the accuracy and to get replicate measurements of the velocities. The velocity measurements were validated by firing bullets through all four velocity stations without a target, and the spread in results between the different measuring systems was in general found to be within 1-2%. Sarva et al. [51] performed their ballistic tests using a single-stage gas gun. The initial velocity of the projectile was measured by using two velocity sensors at the muzzle. The residual velocity of the projectile, which was slightly magnetic due to the iron content in its composition, was measured by means of two magnetic coil residual velocity sensors. In addition, high-speed photography and flash radiography were used to verify that the yaw did not exceed 5° and impact was normal. Zhao et al. [52] used laser velocity measurement device to measure the initial striking and residual velocities of bullet. Nesterenko et al. [53] measured the initial velocity of the projectile by the interruption of

two parallel laser beams located 152.4 mm apart. The laser beams were directed onto photodiodes connected to a time interval meter which recorded the transit of the bullet passage. The terminal velocity of the striker was determined from signals generated by successive closure of two circuits composed of two sets of parallel aluminum foils separated by a distance of 158 mm. Some researchers, e.g. [54-56], utilized chronographs to record the impact and residual velocities. Starratt et al. [57] studied an efficient method for continuous measurement of projectile motion in ballistic impact experiments. Their measurements were based on progressively blocking and unblocking of a laser-light sheet by the projectile. The corresponding change in total intensity was measured and converted to a displacement-time curve. The system could be used to determine the time histories of projectile velocity, acceleration, impact force and projectile energy loss during an impact event. Their data analysis was based on the assumption that the target absorbed all of the available energy. However, if projectile deformation occurred it also had to be taken into account. They also recommended that the enhanced laser velocity system should not be used for brittle materials such as concrete where obvious problems would arise due to spalling, flying debris, and the like.

2.3.2.2. Impact on composite materials

Plate failure is due to the interaction of a variety of mechanisms with one predominating, depending on material properties, geometric characteristics and impact velocity. The most frequent types are shown in Fig. 2.7, consist of fracture, radial fracture, spalling, scabbing, plugging, front or rear petalling, or fragmentation and ductile hole enlargement [58]. These types of failure can be explained with reference to Fig. 2.7 as follows.

- Fracture: failure involving fracture results in the perforation of thin or intermediate targets. Fracture due to initial stress waves, which are stronger than the ultimate compressive strength of the target, could typically occur in weak, low density materials. Radial fracture would be limited to brittle targets such as ceramics.

- Spall failure (scabbing): scabbing is a material failure due to the reflection of the initial compressive wave from the far side of the plate and is a commonplace phenomenon under explosive loading.

- Plugging: plugging develops when a nearly cylindrical slug of approximately the same diameter as the penetrator is set in motion by the projectile. Failure occurs due to shearing produced around the moving slug. Plugs are most likely to be found in very hard plates of moderate thickness. Its presence most frequently occurs when blunt penetrators are used and it is sensitive to velocity angle of attack.

- Petalling: petalling is most frequently observed in thin plates struck by ogival or conical penetrators at relatively low impact velocities or by blunt projectiles near the ballistic limit. As the material in the bulge on the back of the plate is further deformed by the projectile, the elastic properties of the armor are eventually exceeded and a star-shaped crack develops around the tip of the penetrator. The sectors subsequently formed are then pushed back by the motion of the projectile, forming petals.

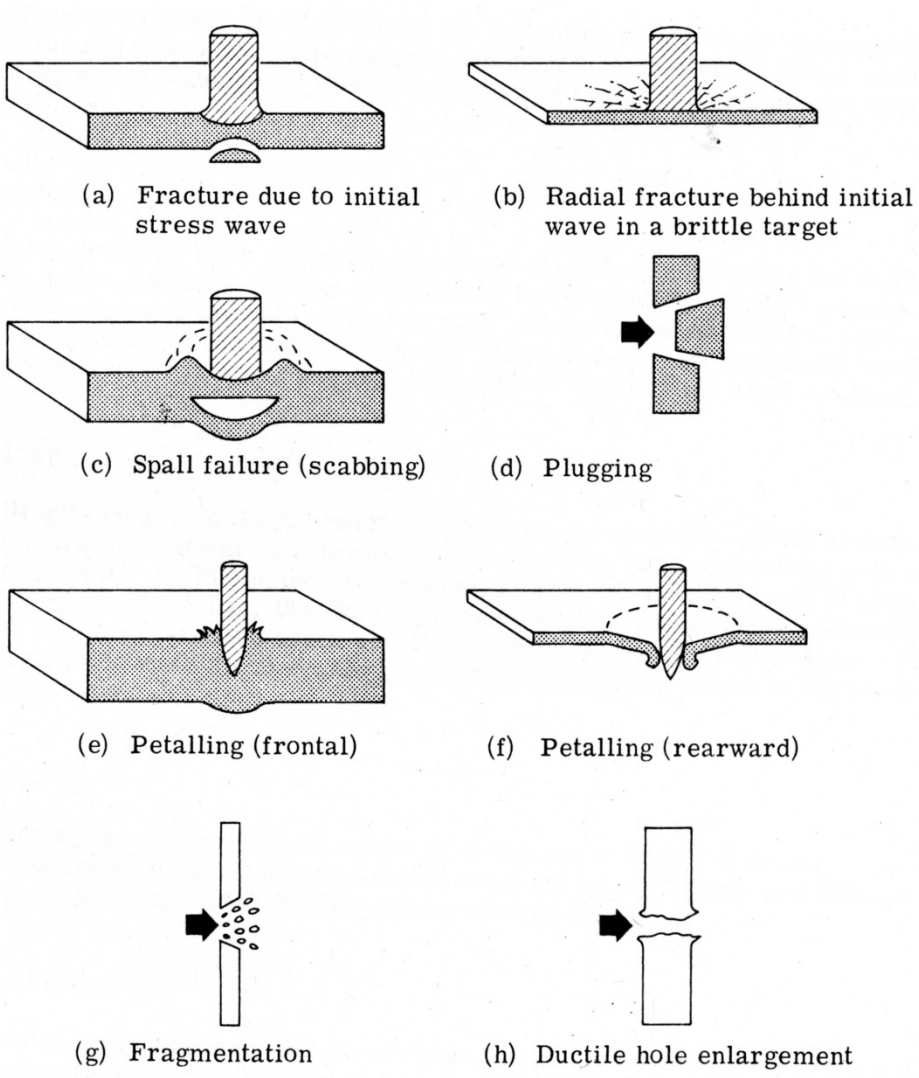

Fig.2.7. Perforation mechanisms [58].

- Fragmentation: fragmentation occurs when the target is composed of brittle material. The fragments generated by a failed target themselves act as projectiles and must be considered as penetrators when meeting any subsequent target.

- Ductile failure: the ductile type of failure is the kind most commonly observed in thick plates. The perforation is accomplished by radial expansion of the plate material as the projectile pushes through.

Ballistic impact response of S2-glass fiber/toughened epoxy and S2-glass/IM7 graphite fibers/toughened SC-79 resin composite beams were examined by Sevkat et al. [59,60, 60a]. Their approach was based on both experimental and numerical techniques to assess damage in the composite beams. They estimated the ballistic limit velocity, V_{50}, with sufficient accuracy by combining results obtained from ballistic tests and finite element predictions. Budhoo [60b] evaluated the temperature effect of the same composite materials as in Ref. [60a] under impact. Czarnecki [61] developed a semi-empirical method to estimate the ballistic limit of composite laminates. Gellert et al. [62] studied the effect of target thickness on the ballistic perforation of glass fiber reinforced plastic composites. They concluded that thicker targets are more ballistically efficient, especially against blunt projectiles. Cortes et al. [63] investigated the impact properties of high-temperature FMLs. They concluded that under high velocity impact conditions, glass fiber-reinforced poly-ether-imide laminates offered the highest specific perforation energy among the laminates they had considered. They also reported that interlaminar and interfacial delaminations appeared to be the primary mechanisms for absorbing and dissipating energy during the impact event in those laminates**.** The ballistic response of fabric-reinforced composites had also been studied, e.g. [64-67]. Naik et al. [68-70] had a number of publications especially on the analytical modeling of woven composites. Their models were based on the various energy absorbing mechanisms, namely: cone formation on the back face of the target, tensile failure of primary yarns, deformation of secondary yarns, delamination, matrix cracking, shear plugging and friction during penetration. Morye et al. [71] developed a simple model for calculating the energy absorption of polymer composites upon ballistic impact. A good correlation was found between the

radius of the deformed region measured using high speed photography and a prediction based on the speed of propagation of the transverse wave. Hoo Fatt et al. [72] studied the ballistic impact on GLARE FMLs. They derived analytical solutions based on test results to predict the ballistic limit and energy absorption of fully clamped GLARE panels subjected to ballistic impact by a blunt titanium cylinder. It was illustrated that ballistic limit varied linearly with panel thickness. Their result showed the deformation energy due to bending and membrane accounted for 84-92% of the total energy absorbed. However, the energy dissipated in delamination represented 2-9% of the total absorbed energy and the remaining absorbed energy, about 7%, was attributed to tensile fracture energy of both glass/epoxy and aluminum. Furthermore, based on their study, thinner panels absorbed a higher percentage of deformation energy than thicker panels since it was easier for them to bend and stretch before fracture. Meanwhile, the thinner panels absorbed lower percentage of delamination energy than the thicker panels since they had fewer plies to delaminate.

Abdullah et al. [16] examined the impact resistance of polypropylene-based FMLs. They showed that multi-layer FMLs based on the stronger 2024-T3 alloy offered a superior perforation resistance to those based on a 2024-O alloy. Goldsmith et al. [73] considered quasi-static and ballistic perforation of carbon fiber laminates. They reported that the ballistic limit increased approximately linearly over the range of thicknesses investigated: 1.3 to 6.6 mm. Zhao et al. [52] experimentally studied the impact resistance properties of T300/epoxy composite laminates. They concluded that at the same initial striking velocity for the same stacking sequence, the thick plate could absorb more energy than the thin plate because the thick laminate had a higher strain rate than the thin one. They

also reported that for the same initial striking velocity and laminate thickness, the energy absorbed by specimens could be influenced by different stacking sequences. Vaidya et al. [74] did research on ballistic performance of graphite/epoxy and S2-glass/epoxy composites with polycarbonate facing. They concluded that woven S2-glass/epoxy were more damage resistant as compared to the prepreg graphite/epoxy laminates. They also reported that the ballistic limit and absorbed energy increased with increase in thickness of the laminate for a given polycarbonate thickness. Naik et al. [70] considered ballistic impact behavior of typical woven fabric E-glass/epoxy thick composites. They observed that for the same mass and diameter of the projectile, as the thickness of the target increased, ballistic limit velocity increased.

Behavior of FMLs subjected to blast loading had been studied by some researchers, e.g. [75-78]. Langdon et al. [75] investigated the behavior of FMLs subject to localized blast loading. Their experiments were based on samples of varying thickness and material distribution. The influence of stacking configuration was also considered. They concluded that the size and shape of the front and back face damage regions depended on the thickness of the panels.

2.3.3. Numerical studies

Li et al. [79,80] developed a numerical model, based on the Mindlin [81] plate element for directly and completely simulating the low-velocity impact-induced damages in laminated plates which could describe the various damages and their mutual effects. A continuum damage mechanics (CDM) model for unidirectional composite layers based on plane-stress state was reported by Matzenmiller et al. [82]. Studies reported in Refs.

[83,84] showed that CDM-type post failure-initiation models can significantly improve the prediction of impact progressive damage/failure in composite structures.

Sevkat et al. [59,60] used LS-DYNA to estimate ballistic limit velocity with sufficient accuracy by combining results obtained from ballistic tests and finite element predictions for S2-glass fiber/toughened epoxy and S2-glass-IM7 graphite fibers/toughened SC-79 resin composite beams. Gama et al. [85] investigated impact, damage evolution and penetration of thick-section composites using explicit finite element analyses. They validated their model with ballistic experiments over an impact velocity range of 50-1000m/s. It was shown that the impact and penetration process was divided into short and long time phases. They reported that 75% of the kinetic energy of the projectile was transferred to the composite laminate in the first 25-30 μs of time. At around V_{50}, about 80% of the impact energy was converted into the strain energy or internal energy of the composite laminate and the rest of the energy was converted into sliding energy and kinetic energy of the projectile-composite system. It had also been shown that 45% of the total internal energy was dissipated in the rear quarter of the composite plate. Buyuk [86] used LS-DYNA to simulate the ballistic impact tests on 2024-T3/T351 aluminum material. They showed that mesh refinement did not necessarily provide better results for ballistic limit simulations without considering and calibrating the interrelated factors, such as material model parameters.

CHAPTER 3: MATERIALS AND TEST SETUP

3.1. Specimens

Materials investigated in this study were GLARE 5 FML panels provided by Aviation Equipment Structure Inc. All GLARE 5 panels considered in this study were made of 2024-T3 aluminum alloy with a thickness of 0.305mm (0.012″) per sheet and unidirectional S2-glass/epoxy laminated layers, each with a thickness of 0.508 mm (0.020″). Each S2-glass/epoxy layer had a lay-up orientation according to Table 3.1. The configuration of GLARE 5 panels with different thicknesses, stacking sequences and typical mechanical properties of constituents are described in Tables 3.1 and 3.2, respectively. The typical mechanical properties of the constituents in Table 3.2 were obtained from the suppliers and open literature [87-89].

Table3.1. GLARE 5 panels tested in this study with different thicknesses and stacking sequences.

Lay-up Configuration (m/n)	Prepreg Plies & Orientation	Total Thickness	MVF
2/1	$[0°/90°]_s$ cross-ply	1.117mm (0.044")	0.546
3/2	$[0°_4]$ unidirectional	1.930mm (0.076")	0.474
3/2	$[90°_4]$ unidirectional	1.930mm (0.076")	0.474
3/2	$[0°/90°]_s$ cross-ply	1.930mm (0.076")	0.474
3/2	$[\pm45°]_s$ angle-ply	1.930mm (0.076")	0.474
3/2	[0°/±45°/90°] quasi-isotropic	1.930mm (0.076")	0.474
4/3	$[0°/90°]_s$ cross-ply	2.743mm (0.108")	0.445
5/4	$[0°/90°]_s$ cross-ply	3.556mm (0.140")	0.429
6/5	$[0°/90°]_s$ cross-ply	4.368mm (0.172")	0.419

Table3.2. Typical values of mechanical properties [87-89].

Mechanical Property		Aluminum 2024-T3	UD S2 Glass/FM 94 Epoxy Prepreg
Tensile ultimate strength [MPa]	L	455	1900
	T	448	57
Tensile yield strength [MPa]	L	359	–
	T	324	–
Tensile modulus [GPa]	L	72	54
	T	–	9.4
Ultimate strain (%)	L	19	3.5
	T	–	0.6
Compressive yield strength [MPa]	L	303	–
	T	345	–
Compressive modulus [GPa]	L	74	54.4
	T	–	11
Density [g/cm^3]		2.79	2.00

The symbols, L and T, stand for longitudinal (the rolling direction for the aluminum) and transverse directions, respectively.

The configuration notation (m/n) used in Table 3.1 means the panel is composed of m aluminum-alloy sheets interleaved with n fiber-reinforced epoxy layers. For example, a cross-ply GLARE 5 specimen with the 3/2 configuration consists of three layers of aluminum 2024-T3 alloy and two sets of S2-glass/epoxy composite laminae, where each set of lamine consists of four layers of unidirectional S2-glass/epoxy in a lay-up configuration of [0°/90°/90°/0°] sandwiched between adjacent aluminum 2024-T3 alloy sheets. A schematic of this FML is shown in Fig. 3.1. The term MVF in Table 3.1 represents metal volume fraction and is defined as the ratio of the sum of the thicknesses of all aluminum layers over the total thickness of the FML [8]:

$$\mathrm{MVF} = \frac{\sum t_{\text{aluminum}}}{t_{\text{FML}}} \tag{3.1}$$

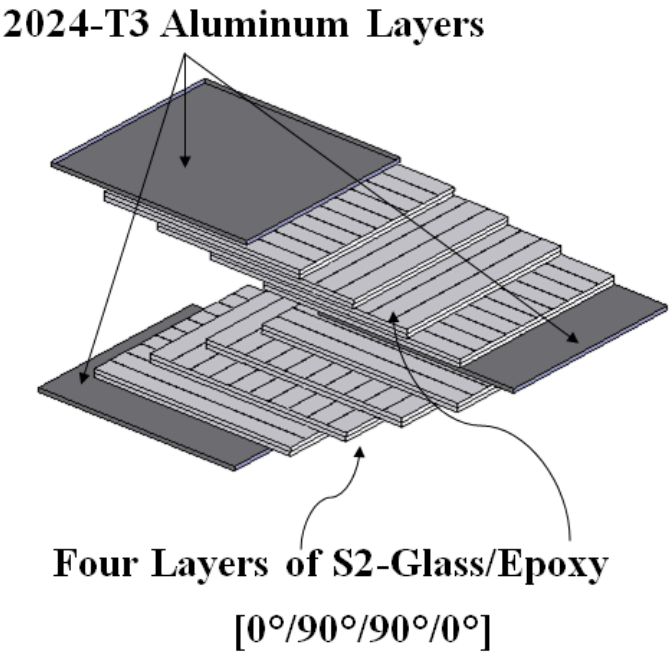

Fig.3.1. A schematic of the cross-ply GLARE 5 FML with the (3/2) configuration.

3.2. Drop-weight impact tester

In this study, all impact tests were performed using an Instron Dynatup 8250 pneumatic assisted instrumened drop-weight impact tester equipped with an environmental chamber, as shown in Fig. 3.2. In addition, the tester also contains a pair of pneumatic breaks to ensure no multiple strikes during impact test (Fig. 3.2(b)). By changing the drop height or using the attached pneumatic assist system, the impact velocity can be varied in the range of 0.61 m/sec up to 13.41 m/sec. Also, the impact energy ranges from 0.67 joules up to 442 joules [90].

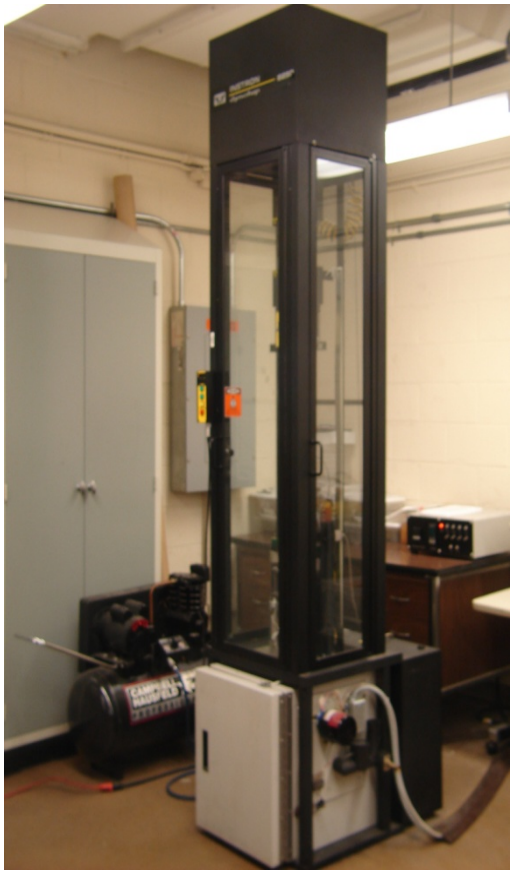

(a)

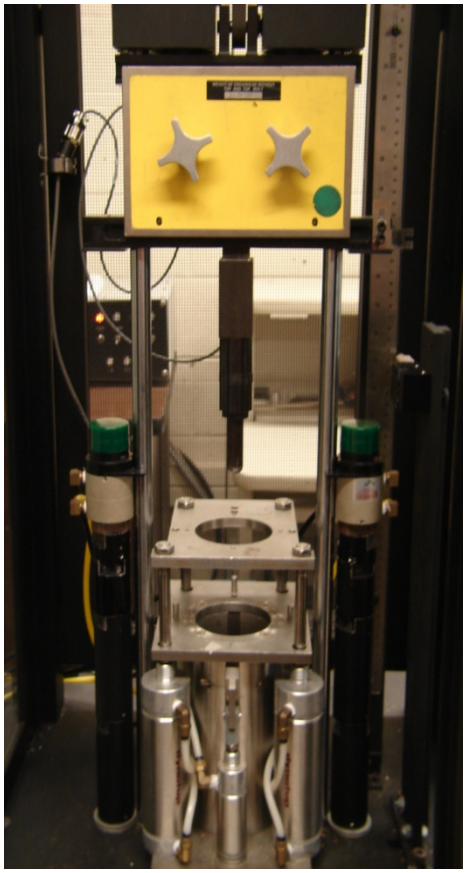

(b)

Fig.3.2. (a) Drop Weight impact tester, (b) the specimen fixture.

All drop-impact tests were conducted on two different geometrical shapes: square and circular, with dimensions of 101.6 mm x 101.6 mm (4″ x 4″) for the square specimens and 101.6 mm (4″) in diameter for the circular specimens (Fig. 3.3). The specimens were clamped circumferentially along a diameter of 76.2 mm (3″) in the specimen fixture and impacted by a hemispherical steel impactor of diameter 16 mm (Fig. 3.4) with two different masses of 6.14 and 12.91 kg.

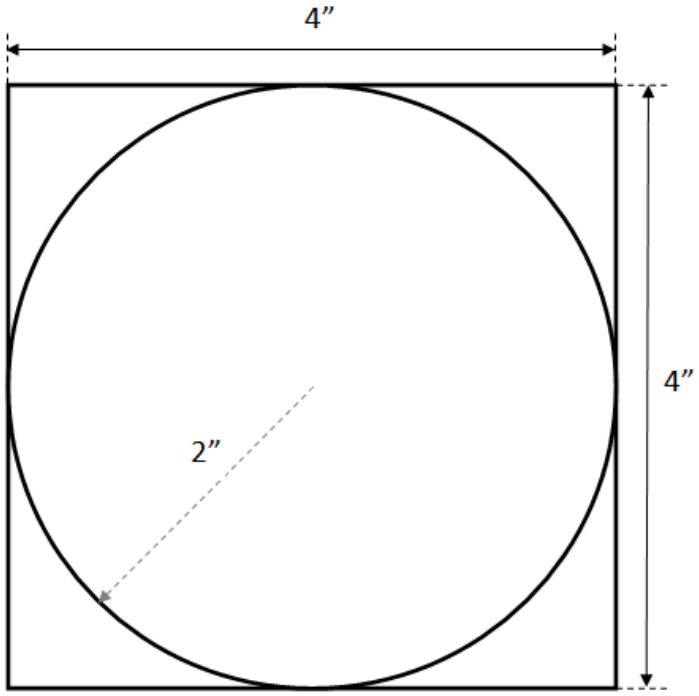

Fig.3.3. Square and circular specimen dimensions for the low-velocity impact test.

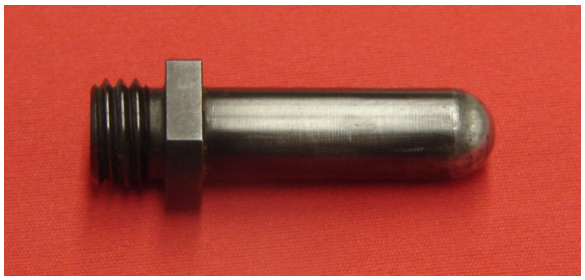

Fig.3.4. A 16-mm hemispherical steel impactor.

Using Dynatup 930-I data acquisition system, the time histories of impact loads were measured and recorded using a load cell located just above the impactor nose and the impact velocity was also measured by one pair of photoelectric-diode system attached to the base of the test machine. With Dynatup 930-I data acquisition system, only load (the resistive force of the specimen) vs. time and initial impact velocity (just prior to impact) can be measured directly. Using the equations of motion and conservation of energy

principle, energy absorbed by the specimen, velocity of impactor and deflection at the impact center can be derived and recorded into a file. The equations used are as follows (assuming data collection starts at t = 0) [91]:

Table3.3. Notations used in drop impact equations.

Notation	
v_i	Impact velocity measured by photodiodes
$p(t)$	Resistive force of specimen at time t
m	Total mass of impactor
g	Acceleration of gravity
$f(t)$	Resultant force acting on the impactor at time t
$a(t)$	Resultant acceleration of the impctor at time t
$v(t)$	Velocity of the impactor at time t
$x(t)$	Deflection (position) of the impactor at time t
$K(t)$	Kinetic energy of the impactor at time t
$V(t)$	Potential energy of the impactor at time t
$E_a(t)$	Energy absorbed by the specimen at time t
$E(t)$	Total energy of the impactor and specimen system at time t

$$f(t) = mg - p(t) \tag{3.2}$$

$$a(t) = \frac{f(t)}{m} = g - \frac{p(t)}{m} \tag{3.3}$$

$$v(t) = v_i + \int a(t)dt = v_i + gt - \frac{1}{m}\int p(t)dt \tag{3.4}$$

$$x(t) = \int v(t)dt = v_i t + \frac{1}{2}gt^2 - \frac{1}{m}\int (\int p(t)dt)dt \tag{3.5}$$

Since the load p(t) provided to the tup from the specimen is not a genuine mathematical function, direct integration cannot be used in equations (3.4) and (3.5). Therefore, the software uses the trapezoidal numerical approximation for calculating the integral of the load curves and the subsequent velocity and deflection values. From the conservation of energy principle applied to the drop weight-specimen system, the total energy is computed as follows:

$$E(t) = K(t) + V(t) + E_a(t) = \text{Constant} \tag{3.6}$$

If t=0 be the time of impact (x=0) and knowing that V(0) = 0 and $E_a(0) = 0$, then it can be shown that E(0) = K(0) = Constant. Thus:

$$E(t) = K(t) + V(t) + E_a(t) = K(0) \tag{3.7}$$

where

$$K(0) = \frac{1}{2} m v_i^2 \tag{3.8}$$

By rearranging equation (3.7):

$$E_a(t) = K(0) - K(t) - V(t) = \frac{1}{2} m\left[v_i^2 - v^2(t)\right] - mgx(t) \tag{3.9}$$

If the displacement is really small, the potential energy can be neglected. Then, the energy absorbed by specimen can be computed as follows:

$$E_a(t) = K(0) - K(t) = \frac{1}{2} m\left[v_i^2 - v^2(t)\right] \tag{3.10}$$

3.3. Ballistic gas-gun

The ballistic impact tests were performed at room temperature using an in-house-designed gas-gun. The gun consists of a pressurized tank, a gas storage vessel, a solenoid valve and a stainless-steel barrel. The picture of the gas gun is shown in Fig. 3.5 from two different angles.

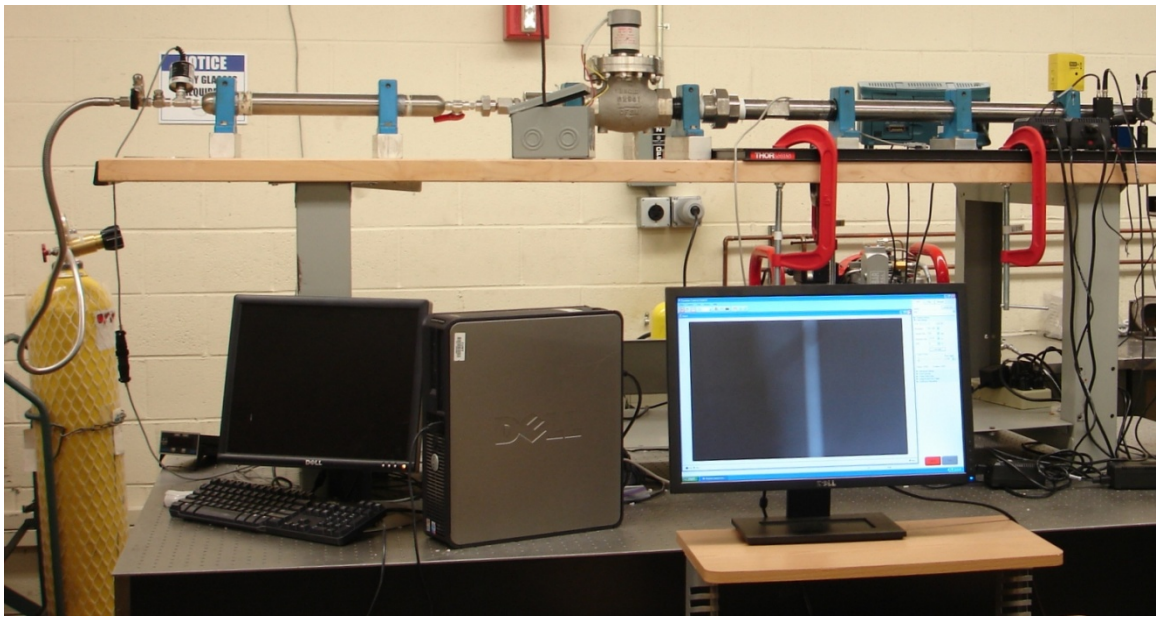

(a)

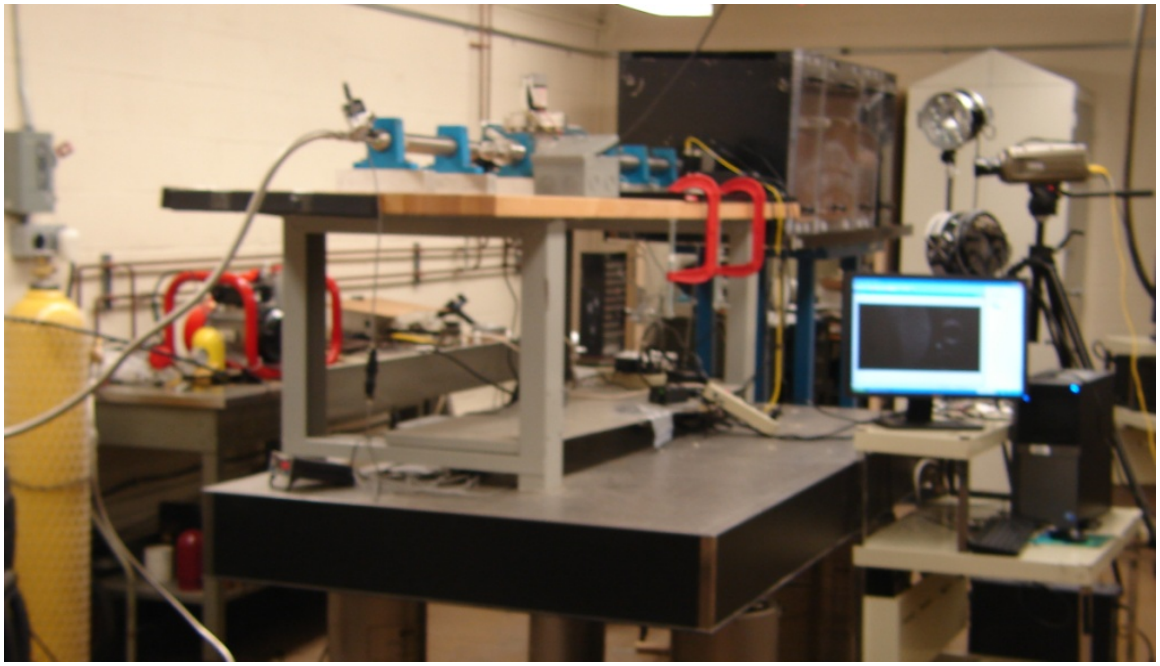

(b)

Fig.3.5. Different views of the high-speed gas gun setup for ballistic impact tests: (a) front view, (b) angled view.

Helium and compressed air were used as the propellants. Target inside the specimen container was placed at two different positions away from the gun muzzle. Figure 3.6 shows two setup configurations, i.e. #1 and #2, that were used in this study. For the setup

configuration #1, target was located 93.98 cm (37″) away from the gun muzzle; while for the second configuration, i.e. #2, a distance of 50.8 cm (20″) was chosen for the target.

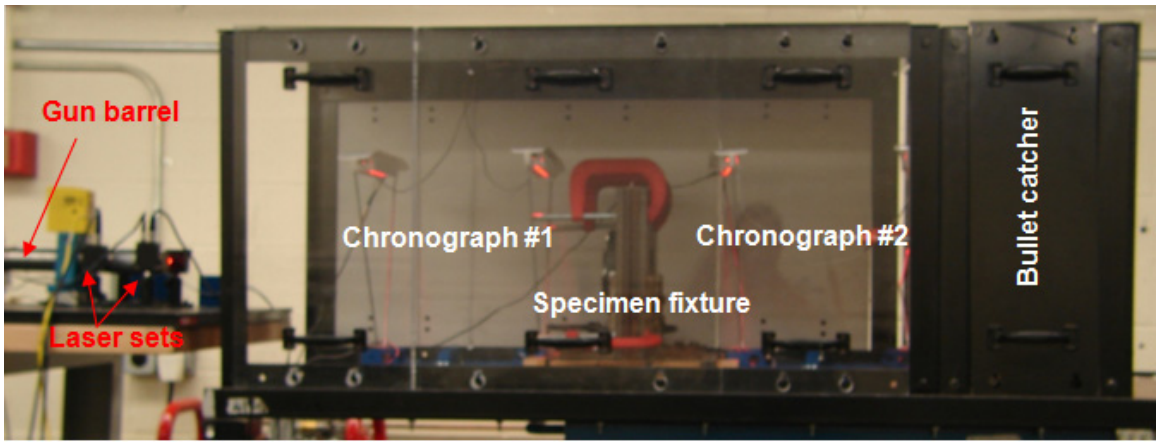

(a)

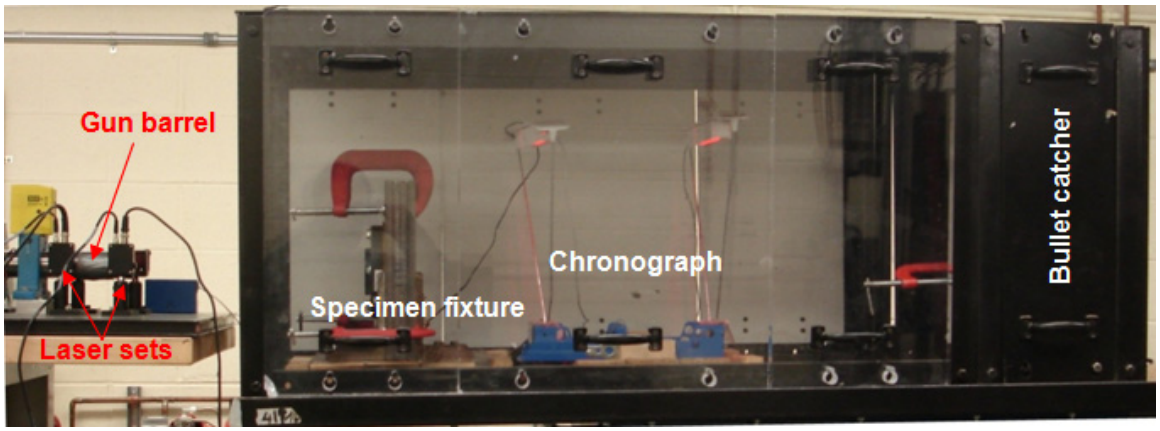

(b)

Fig.3.6. Specimen container: (a) setup configuration #1, (b) setup configuration #2.

Specimens with two different geometries were clamped from both ends: the plate specimen was secured by clamping 25.4 mm (1″) of each end, Fig 3.7(a), while the beam specimen was clamped over a length of 50.8 mm (2″) from each side, Fig. 3.7(b). The specimen fixture was extra supported by four C-clamps inside the specimen container (Fig.3.6). This would provide a fixed-fixed boundary condition at both ends of the clamped specimen.

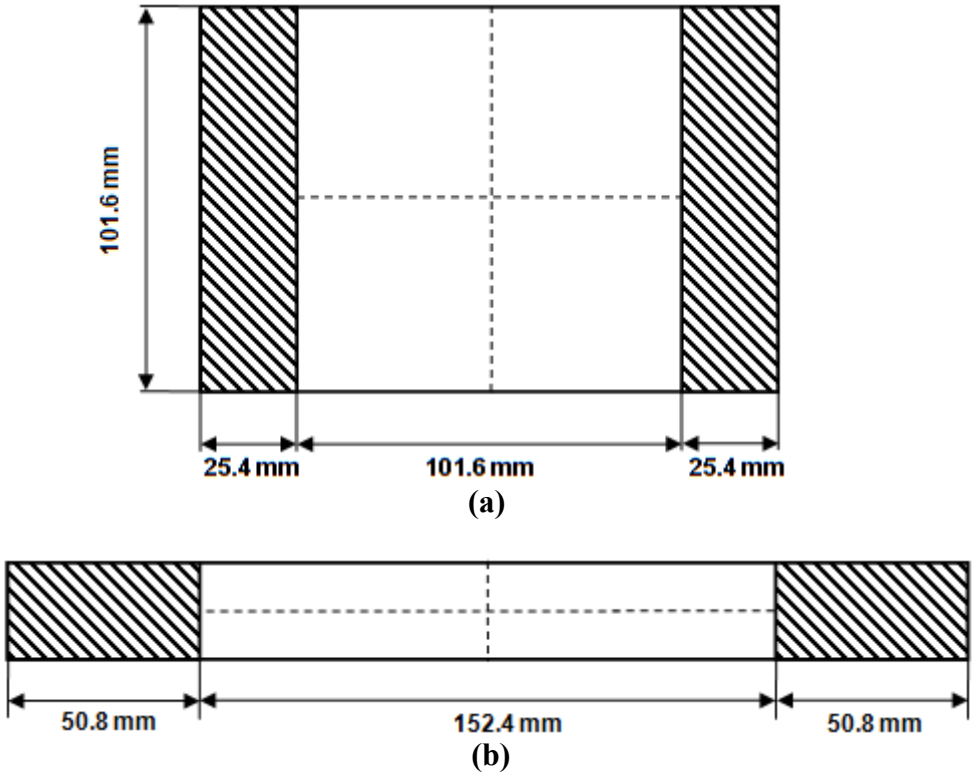

Fig.3.7. Ballistic impact test composite specimens: (a) 152.4 mm × 101.6 mm (6″×4″) plate specimen, (b) 254 mm × 25.4 mm (10″×1″) beam specimen.

A 0.22 caliber copper bullet was used as a projectile. The bullet was mounted inside a pair of plastic sabots and then inserted into the gun barrel. Figure 3.8 illustrates how the 0.22 caliber copper bullet was mounted inside the sabots. For the same type of sabots, the projectile initial velocity can be controlled by changing its position inside the barrel and/or varying the input pressure of the gun. Once high-pressure gas was released by a fast acting solenoid valve, a 0.22 caliber copper bullet accelerated through the 1.016 m (40″) gun barrel to the desired speed.

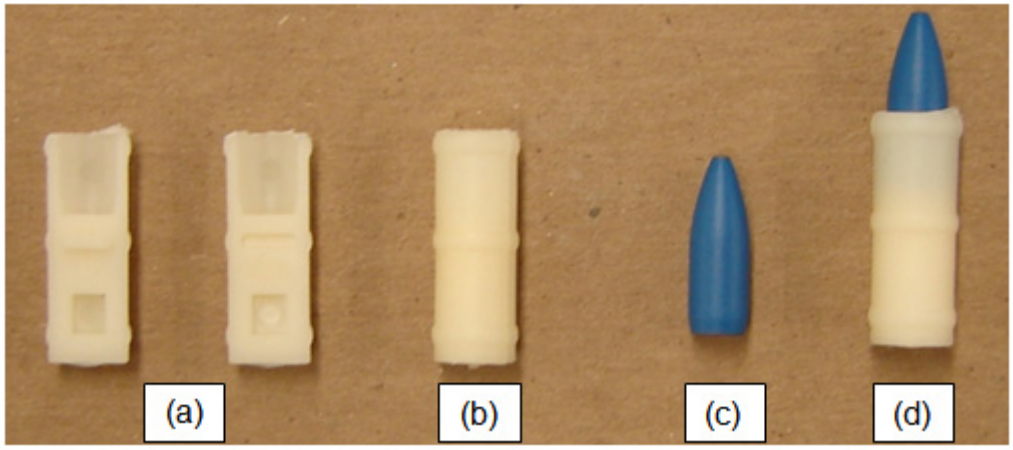

Fig.3.8. Projectile assembly: (a) unassembled pair of sabots, (b) assembled pair of sabots, (c) 0.22 caliper copper bullet, (d) bullet inserted inside the sabots.

In both setup configurations, the projectile velocity was measured in three distinct ways. First, two pairs of diode-lasers/amplified-photodiodes, separated by 101.6 mm (4″), were located near the exit of the gun barrel, forming two optoelectronic gates to measure the speed of the projectile at the gun muzzle. When the projectile passes through these optoelectronic gates, it blocks the lasers causing oscilloscope to trigger and capture the voltage changes. The speed of the projectile is then calculated by dividing the known distance between the optoelectronic gates by the elapsed time for the projectile to pass through the two optoelectronic gates. Figure 3.9 shows the two diode-laser/amplified-photodiode pairs and typical voltage-time records captured with a digital storage oscilloscope.

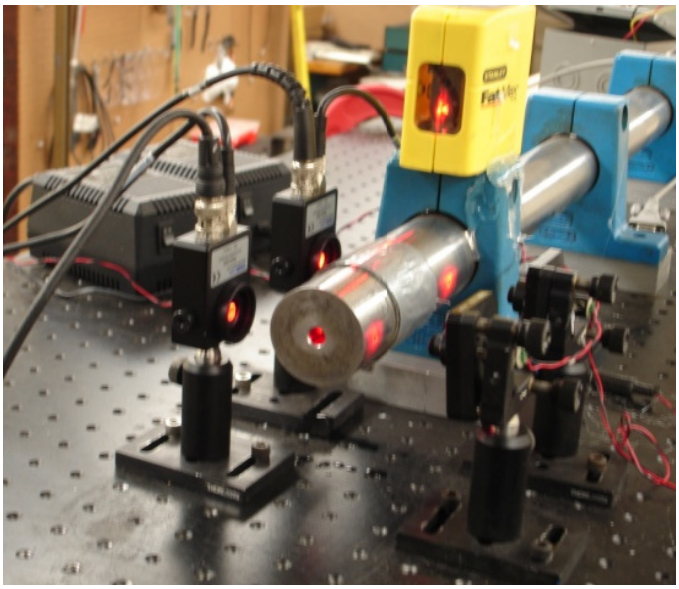

(a)

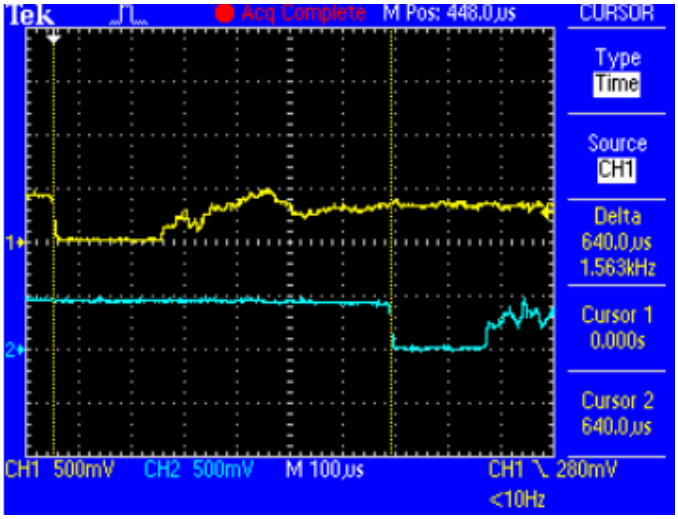

(b)

Fig.3.9. Velocity measurement using optoelectronic technique during ballistic impact near the gun muzzle: (a) lasers and optical sensors, (b) zoomed-in voltage *vs.* time records.

For the second measurement technique, two pairs of chronographs were used for the setup configuration #1 to measure the projectile speeds before and after impact. One pair was located in front of the target, while the second was located behind the target (Fig. 3.6(a)). As illustrated in Fig. 3.6(b), a pair of chronographs was used in the setup

configuration #2, to measure the projectile velocity after perforating the target. Since the target position was close to the gun muzzle, there was not enough space to locate another pair of chronographs to measure the velocity before the projectile hitting the target. The chronographs were triggered by traversing an object, e.g. bullet, through their infrared optical screens. For this technique, the bullet speed was calculated based on the similar mathematics as described above.

Last, for the third technique, a Phantom V710 high-speed camera (Fig. 3.10(a)) was used to videotape the bullet motion during the test. The bullet velocities were then determined by using the captured high-speed video. In this study, the high-speed camera was set perpendicular to the projectile ballistic trajectory. Figure 3.10(b) shows a typical superposition of two bullet images, i.e. at times t_1 and t_2, from the high-speed video for measuring the bullet velocity. The arrangements of all measuring devises for each setup configuration are schematically shown in Fig. 3.11.

(a)

Fig.3.10. (a) The Phantom V710 high-speed camera, (b) typical superposition of two bullet images at times t_1 and t_2 from the high-speed video.

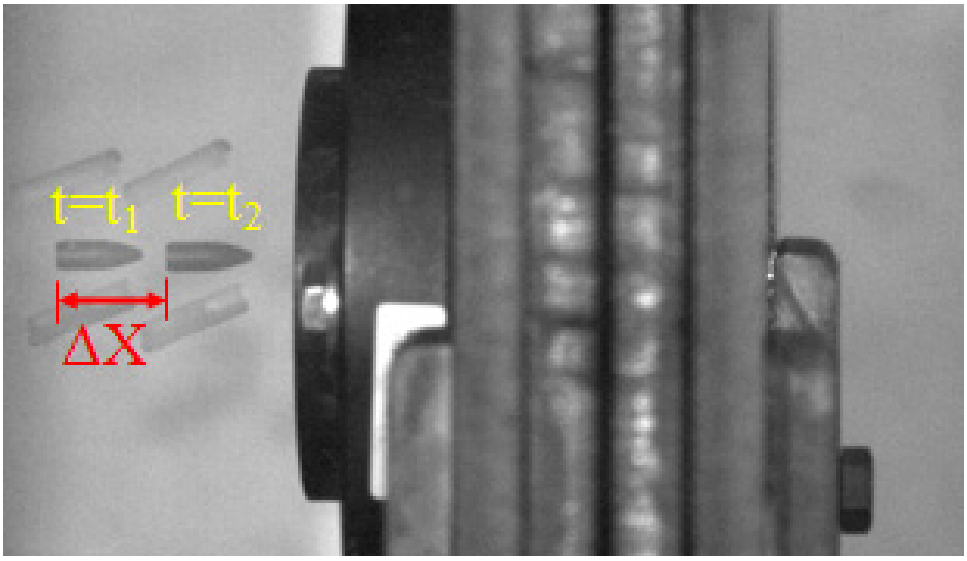

(b)

Fig.3.10. (Continued)

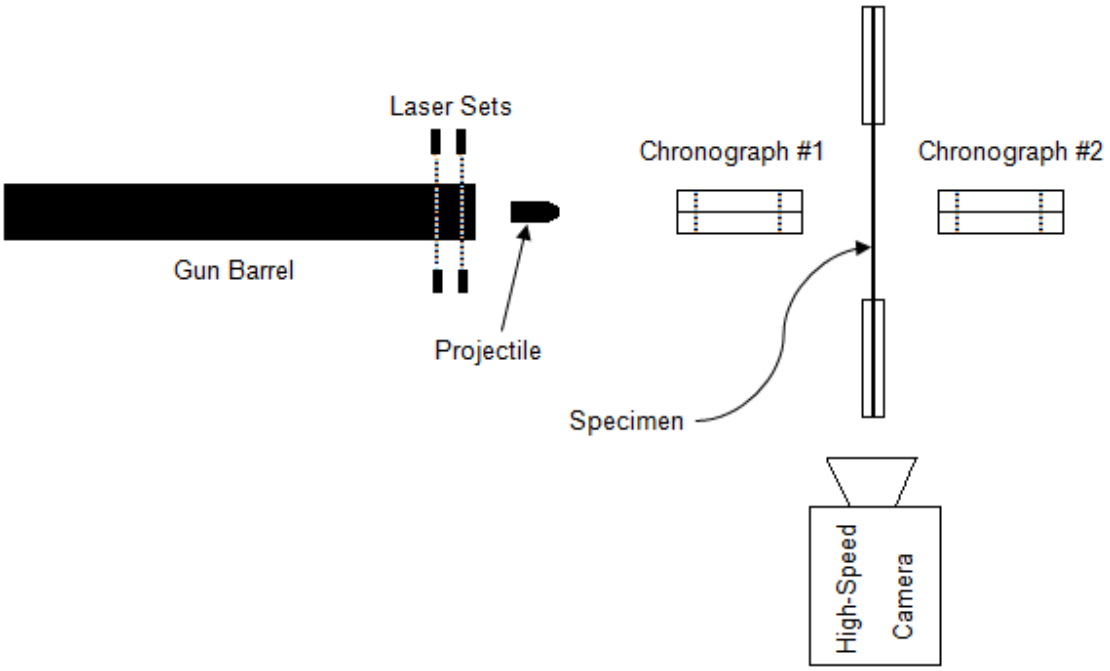

(a)

Fig.3.11. Schematics of the arrangements of velocity-measuring devices used in: (a) setup configuration #1, (b) setup configuration #2.

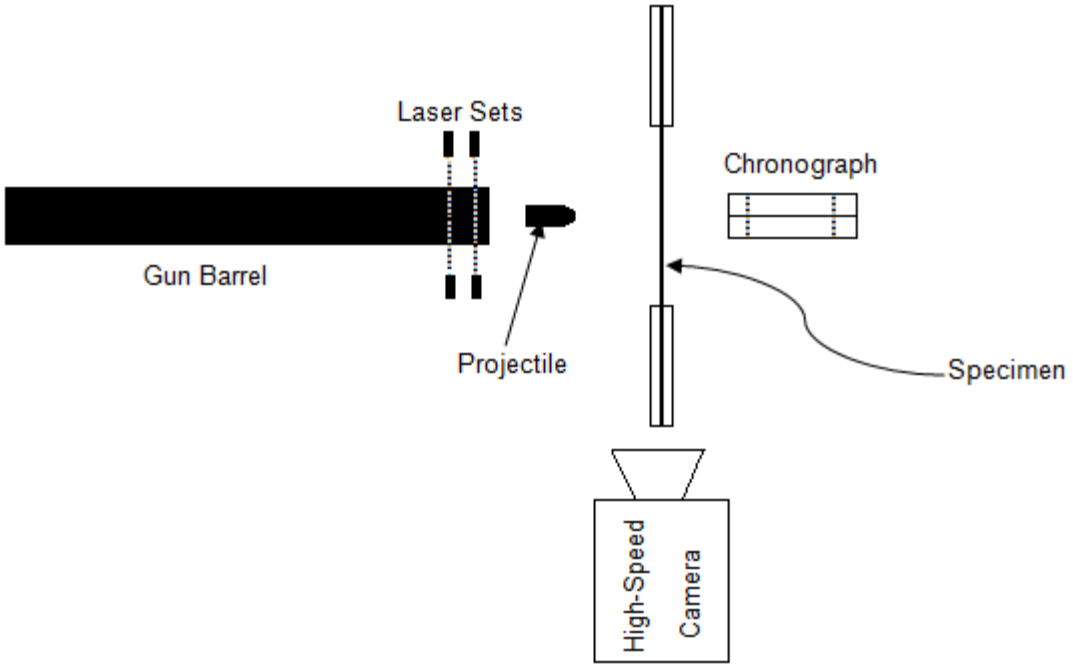

(b)

Fig.3.11. (Continued)

3.4. The ultrasonic damage evaluation system

Ultrasonic measurements are most commonly used to detect damage in composite structures. The basic principle of all these techniques is that ultrasonic pulses, usually in the frequency range from 0.5 to 25 MHz, are generated which: (i) are transmitted through the material to a transducer (through-transmission mode); or (ii) are reflected back to the input transducer by defects or material inhomogeneities (reflection or pulse-echo mode) [92]. In this study, UltraPAC, an advanced, modular and expandable ultrasonic system offered by Physical Acoustics Corporation (Fig. 3.12), was used to conduct the damage evaluation of the impacted specimens.

Fig.3.12. The UltraPAC system.

In general, a frequency of 10 MHz or higher is used for thin laminates while the frequency can be as low as 2 MHz for thick laminates. As the sound waves propagate through the material, some of them are interrupted by the presence of defects or materials inhomogenities, and the energy levels are attenuated. Some of these attenuated waves propagate through the specimen, while other waves are reflected back to the surface. The amplitude, frequency dependence and arrival times of detected pulses are used for defect analysis. Careful examination of the dependence of ultrasonic attenuation on frequency allows materials properties to be assessed or damage to be monitored [92].

In the through-transmission mode where two transducers are used, the axes of the sending and receiving transducers must be perfectly aligned across the thickness of specimen for maximum efficiency. A coupling medium with high acoustic impedance, e.g. de-ionised water, grease or gel, is needed between the transducer and the specimen to maximize the energy transfer [92]. A standard through-transmission technique employs two flat

transducers, which usually generates relatively blur ultrasonic images. To tackle this issue, a modified through-transmission technique, which incorporates a flat and a focused transducer, was used. In this study, a pair of 5 MHz ultrasonic transducers (one focused and another flat) in through-transmission mode, as shown in Fig. 3.13, was adopted to access the damage in the impacted specimens. It should be mentioned that all the ultrasonic results presented in this study were based on amplitude measurements.

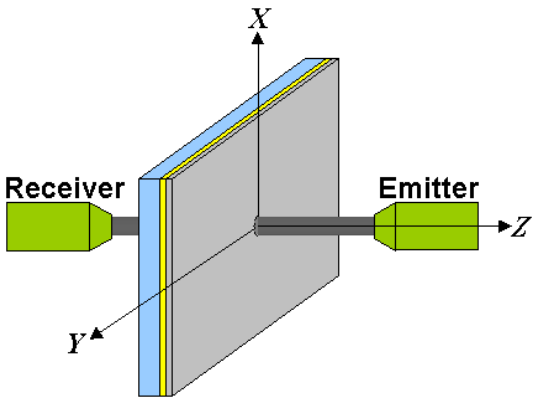

Fig.3.13. Through-transmission technique.

Once the composite part is scanned at regular intervals across it surface, the ultrasonic map of defects can be presented in three different modes, namely A-scan, B-scan and C-scan. They are described in the following with reference to Fig.3.14 [92].

i. A-scan. In the A-scan mode, the attenuated signals are displayed as a series of peaks against the time scale on an oscilloscope. The position of the signal echo along the time axis allows the location of the defect in the thickness direction to be determined, while the amplitude of the echo can give some indication of the size and nature of the defect.

ii. B-scan. In the B-scan analysis mode, cross-sectional measurement can be made along any vertical plane, eliminating the need for destructive cross-sectioning of

specimen. B-scan is basically a series of very close-spaced A-scans through the thickness of specimen.

iii. C-scan. The well-established ultrasonic technique for advanced composite materials is the C-scan mode where the extent of damage or internal inhomogeniety can be examined and the depth profile of damage can be obtained by varying the time gate for C-scan data acquisition. In the conventional C-scan analysis, the transducer is moved in a plane parallel to the specimen surface in a rectilinear raster pattern to provide a planar view of the defect in a 'one-shot' image. This image eliminates the need to produce multiple scans.

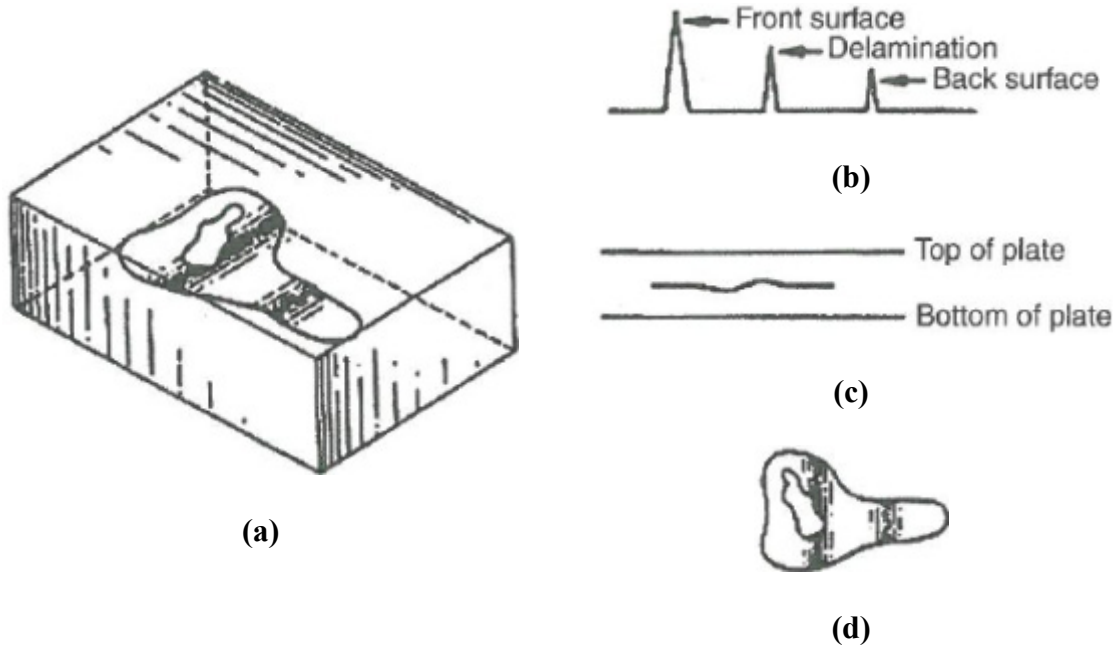

Fig.3.14. Comparison of ultrasonic scanning techniques: (a) a specimen containing a delamination, (b) A-scan wave, (c) B-scan view, (d) planar view of the C-scan [92].

CHAPTER 4: DROP-WEIGHT IMPACT TESTS ON GLARE 5 FMLS

4.1. Low-velocity impact tests

The impact properties of FMLs vary with their constituents (i.e. fibers, resin and alloy types), fiber orientation, stacking sequence, thickness, operating temperature, geometry and material type of the impactor, and surface preparation technique, etc. In this chapter, the effects of thickness, impactor mass, stacking sequence and geometry will be discussed. In addition, threshold cracking energy was also studied.

All impact tests were conducted using an Instron Dynatup 8250 pneumatic-assisted, instrumented drop-weight impact tester. The specimens were clamped circumferentially along a diameter of 76.2 mm (3″) in the specimen fixture and impacted by a hemispherical steel impactor of diameter 16 mm. Unless specified, otherwise all impact experiments were performed using an impactor mass of 12.91 kg. Figure 4.1 shows the schematic drawings of the experimental setup for the low-velocity impact tests.

Panels were cut into two different geometrical shapes: square and circular, with dimensions of 101.6 mm x 101.6 mm (4″ x 4″) for the square specimens and 101.6 mm (4″) in diameter for the circular specimens. In order to measure the strain outputs, two sets of strain gages were chosen to mount on the specimens with a distance 25.4 mm (1″) away from the impact center. The locations of these two sets of strain gages are shown in Fig. 4.2 for both geometrical shapes. The first set consists of a pair of strain gages located at 0° and 90° with respect to the 0° fiber direction in order to measure the radial and hoop strains along the 0° fiber and its transverse directions, respectively. The second set of the strain gages was placed at angles of ±45° with respect to the 0° fiber direction for measuring the hoop and radial strains at ±45°.

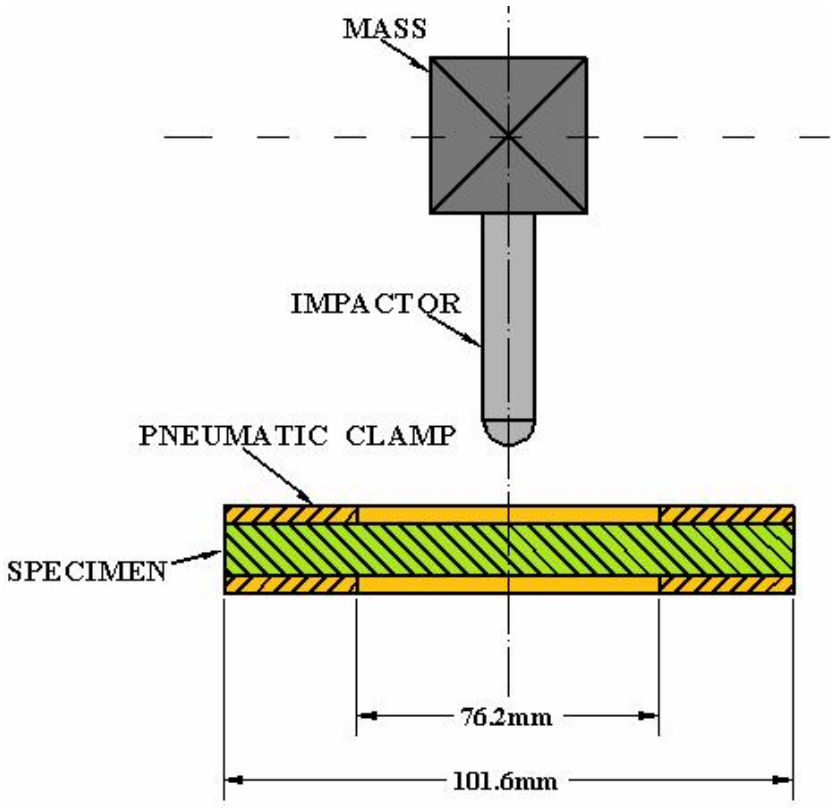

Fig.4.1. Schematic of the setup for drop-weight impact tests.

After each test, the specimen was carefully removed from the fixture for post-impact damage assessments. Figure 4.3 illustrates how the post-impact permanent central deflection was measured. Both nondestructive and destructive evaluation techniques were used to assess the impact damage inside the impacted panels. The impacted specimens were first scanned through an UltraPAC immersion ultrasound system for nondestructive damage evaluation, and then carefully sectioned into two halves using a diamond blade through the impact center. Finally, cross-sectional optical pictures were taken to reveal the more detailed damage inside the specimens.

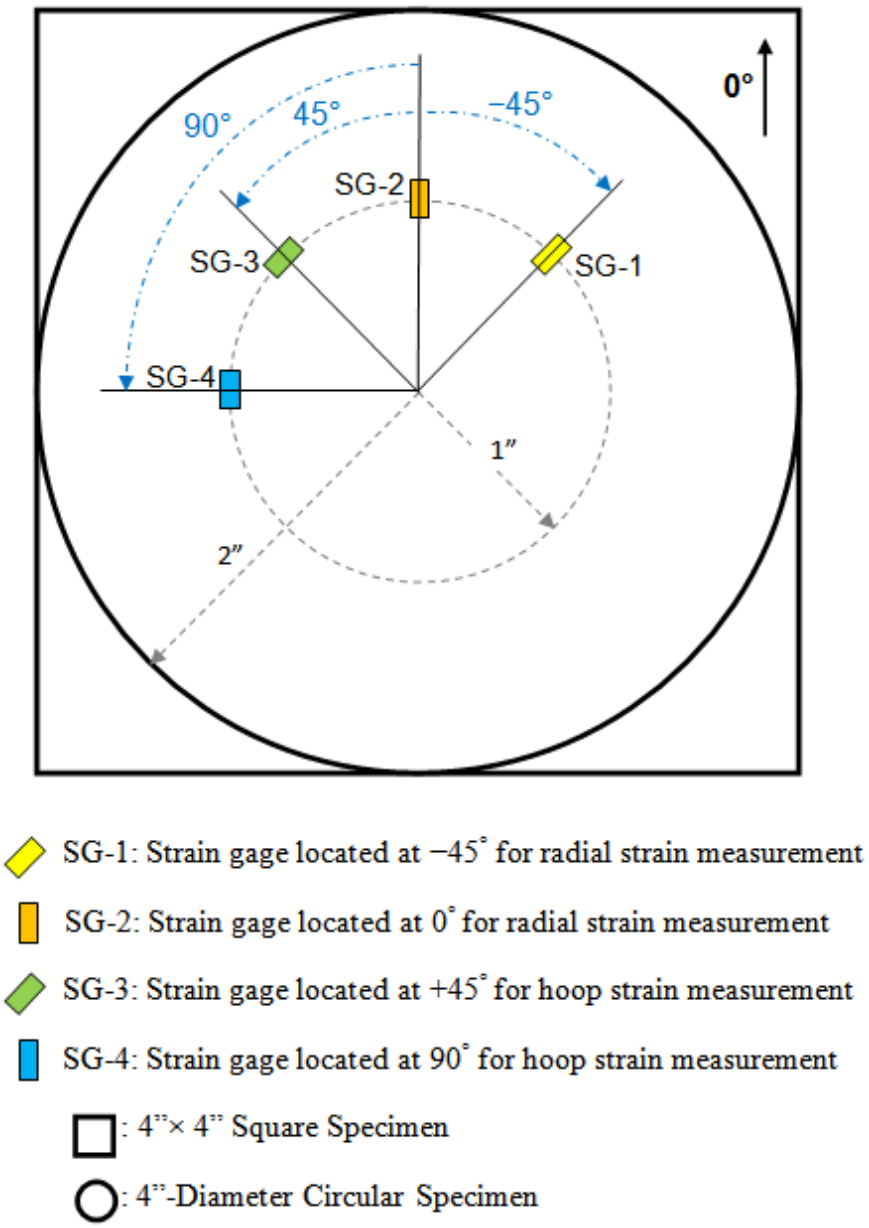

Fig.4.2. Schematic of strain gage locations on the square and circular specimens.

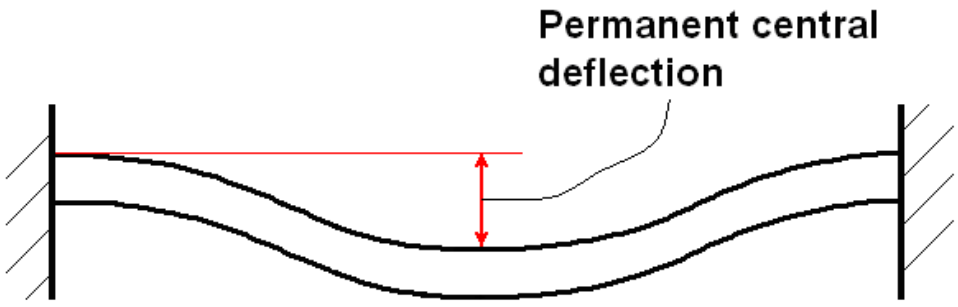

Fig.4.3. Measurement of the permanent central deflection.

4.2. Effect of specimen thickness

In this study, the GLARE 5 panels with different thicknesses were chosen to assess the thickness effect. The range of thickness is from 1.117 mm (0.044″) of GLARE 5 (2/1) up to 4.368 mm (0.172″) of GLARE 5 (6/5). Figures 4.4 through 4.8 show histories of the absorbed energy, central displacement, contact force and force-deflection for the GLARE 5 specimens with (2/1), (3/2), (4/3), (5/4) and (6/5) configurations, respectively. The noticeable damage type in the specimens is the local and global permanent deformations. The global permanent deformation has an important role in dissipating energy, especially in thinner specimens. By increasing the panel thickness, the capability of absorbing impact energy increased, while the maximum central deflection decreased. In addition, the peak contact force as well as the force rate increased, while the duration of contact decreased. This is due to the increase of the panel stiffness. Decreasing of contact time means that damage cannot be fully developed in the specimen. It can be observed from part (d) in Figs. 4.4 through 4.8 that under the same impact energy, as the panels became thicker, the initial slope of the force-deflection increased. In other words, resistance of the panels in the impact direction increased with increasing thicknesses. Thus, thicker panels offered more resistance to the transverse impact.

Figure 4.9 shows the strain histories for the GLARE 5 specimens with different thicknesses under various impact energies. Figure 4.10 compares the C-scan results as well as the back-side (non-impacted) view of the GLARE 5 specimens with various thicknesses under different impact energies using the 12.91 kg impactor mass. As is obvious from this figure, the area of the entire damage contour increased with increasing impact energies. In general, under the same impact energy, as the specimen became

thicker the area of the entire damage contour increased. Figure 4.11 shows the cross sectional view of the GLARE 5 FMLs with different thicknesses. In the sequel, detail of these tests will be exemplified.

4.2.1. GLARE 5 (2/1), (3/2) and (4/3)

The flat horizontal curve in Fig. 4.4(a) indicates that the GLARE 5 (2/1) panel had reached its saturated level of absorbing energy. That is, an increase in the impact energy to above 30J would cause impactor perforation through the specimen. There was no rebounding energy for this case. The force-time curve showed a smooth incremental increase to the maximum force at time 5.07 ms. There was then a sharp initial drop in the force, followed by an oscillatory decrement in the force (Fig. 4.4(c)). This corresponded to the initial failure of the bottom aluminum layer, followed by breakage and splitting of the fiber, and eventually top aluminum layer failure (Fig. 4.11). In the GLARE 5 (3/2) data, there was a minor drop at time 4.81 ms, followed by a major oscillatory drop at time 5 ms. The minor drop corresponded to matrix cracking, which was the initiation of damage, while the major drop corresponded to fiber breakage and splitting. This was followed by the initiation of a crack in the bottom layer of aluminum that propagated along the aluminum transverse direction. As is apparent from Fig. 4.11, there was very large debonding between the bottom aluminum layer and its adjacent prepreg layer. The reason for this is that there was no constraint to the bottom aluminum layer. The failure pattern exhibited by the GLARE 5 (3/2) specimen can be seen in the GLARE 5 (4/3) data as well, but at elevated impact energies.

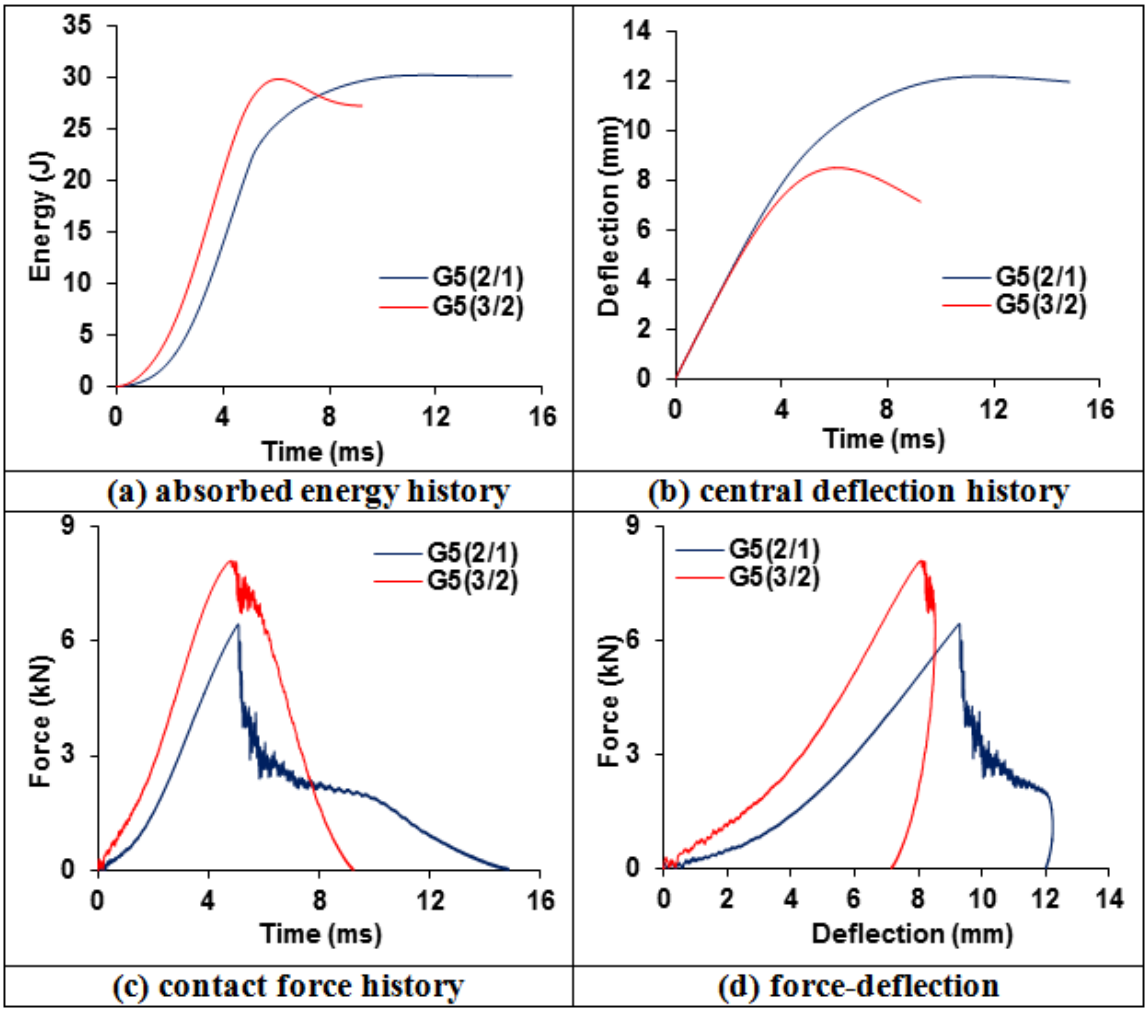

Fig.4.4. Impact responses of GLARE 5 (2/1) and (3/2) under 30J impact energy.

It can be summarized that by increasing the impact energy, for GLARE 5 (2/1), (3/2) and (4/3) the first major failure type was debonding between the bottom aluminum layer and its adjacent prepreg layer. This was caused by shear of the interface, which had reached its saturated level by means of specimen bending. In the thinner GLARE 5 (2/1) specimen, the bottom aluminum layer was next to fail, while the thicker GLARE 5 (3/2) and (4/3) specimens exhibited fiber breakage and splitting prior to failure of the bottom aluminum layer (Fig. 4.11). The damage in GLARE 5 (3/2) and (4/3) further progressed through failure of the aluminum and prepreg layers from bottom to top as the impact

energy increased, e.g. 40J for the (3/2) and 50J-60J for the (4/3) configuration, as shown in Figs. 4, 5 and 10. The induced cracks in the back side of the specimens were caused by bending stresses.

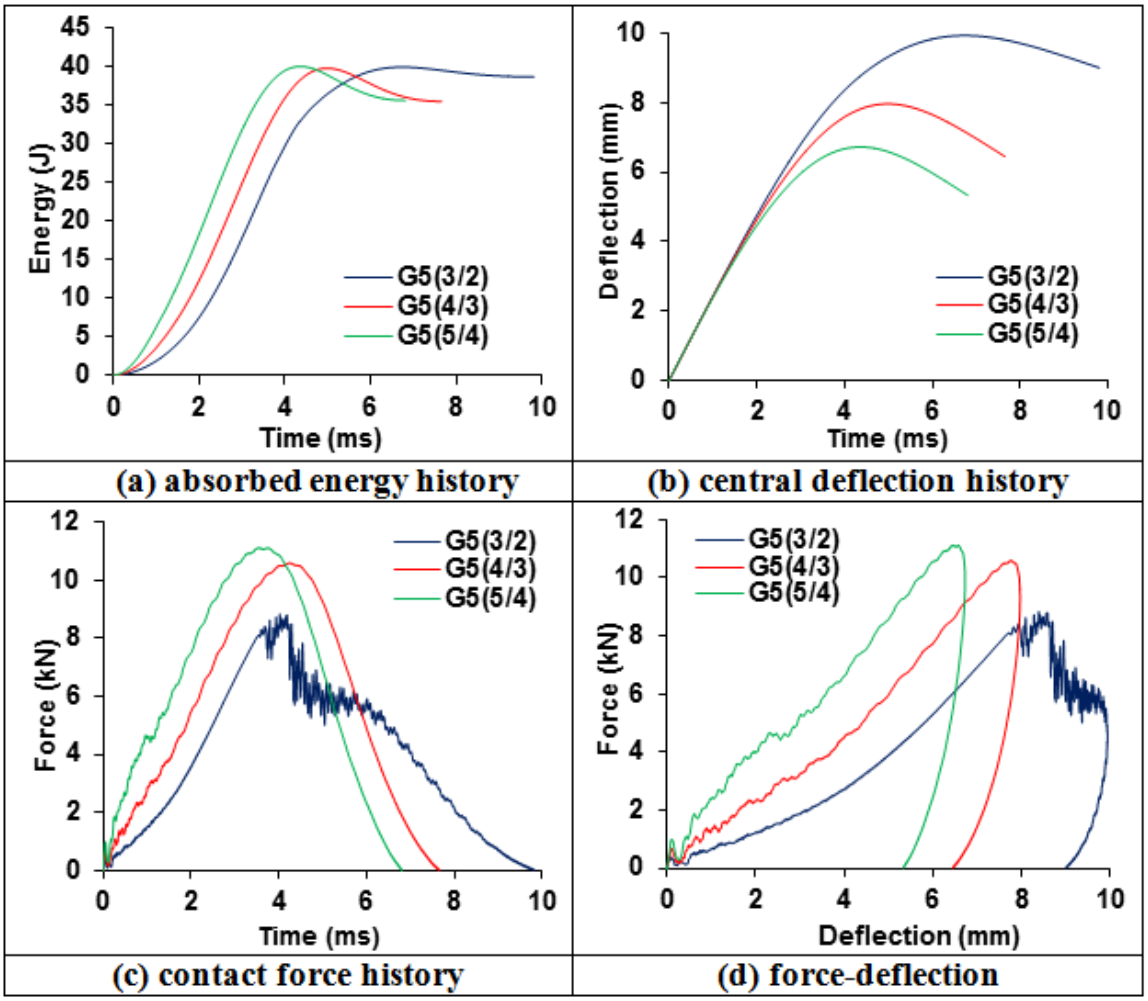

Fig.4.5. Impact responses of GLARE 5 (3/2), (4/3) and (5/4) under 40J impact energy.

4.2.2. GLARE 5 (5/4) and (6/5)

For both GLARE 5 (5/4) and (6/5) under 40J and 60J impact energies, respectively, fairly smooth force history curves are exhibited, except between 0.96 and 1.15 ms for the GLARE 5 (5/4) and between 0.53 and 0.83 ms for the GLARE 5 (6/5). During these time intervals the force-time curve became flat with very negligible oscillation. It is believed

that the delamination between the 0° and 90° prepreg layers took place during those time intervals (Fig. 4.11). At higher impact energies, a change in the slope of force history occurred several times. These repetitions can be explained by the intensity and propagation of damage in the prepreg layers in different time intervals. The initiation and propagation of delaminations resulted in a loss in local rigidity, which manifested itself as an obvious change of slope. In summary, as the panel became even thicker, i.e. GLARE 5 (5/4) and (6/5), the first major failure type was delamination. These delaminations took place in layers closer to the impacted face (Fig. 4.11). This is due to the high, localized contact stresses. As the impact energy increases, e.g. from 60J-100J for the (5/4) and 80J-100J for the (6/5) configuration, as depicted in Figs. 4.6-4.8 and 4.11, various types of damage, such as debonding between the bottom aluminum layer and the adjacent prepreg layer, fiber breakage and splitting, aluminum failure, etc., took place. Due to the panel thickness, stress concentrations on the impacted side initiated cracks from the top and damage progressed from the top down. However, cracks in the very bottom layers were caused by bending stresses (Fig. 4.11).

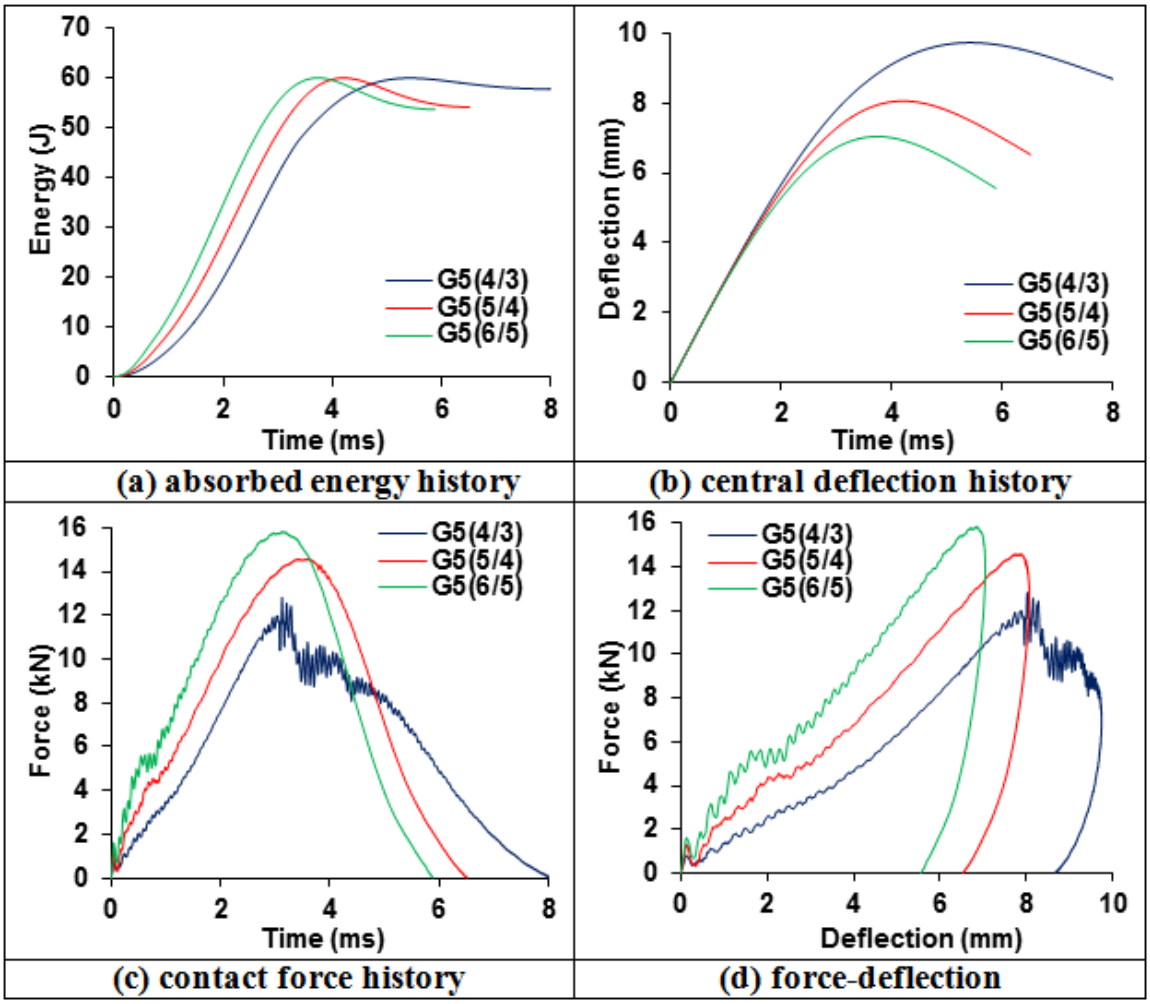

Fig.4.6. Impact responses of GLARE 5 (4/3), (5/4) and (6/5) under 60J impact energy.

4.2.3. Strain results

Figure 4.9 shows the strain history for the GLARE 5 specimens with different thicknesses. In this figure, dashed lines in some of the curves indicate that the signal was cropped electronically. Convex-up curves represent strain results in the radial directions, whereas concave-down curves represent strain results in the hoop directions. The bolder curves correspond to strain results from strain gages located at 0° and 90°, whereas the thinner curves correspond to strain results from strain gages located at ±45°.

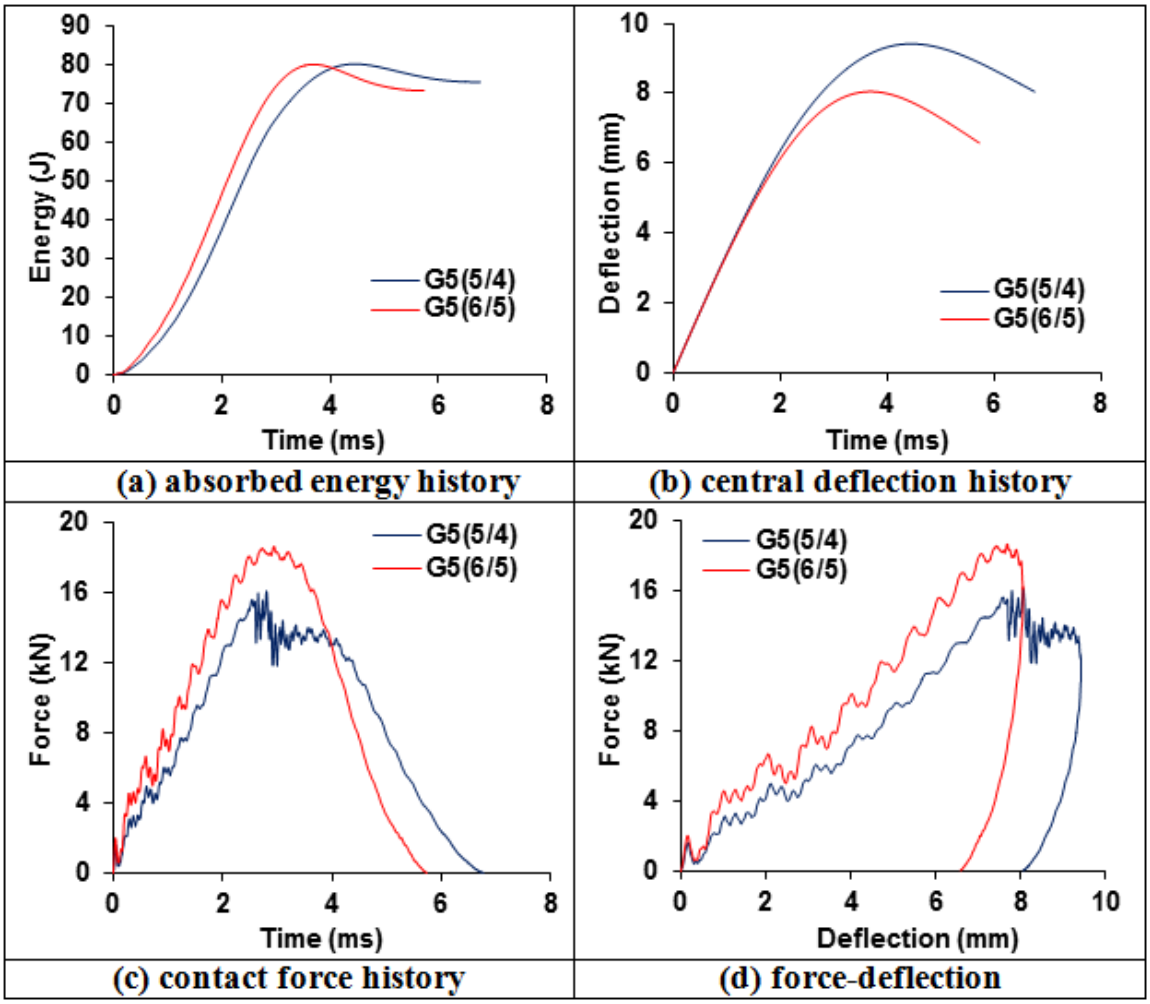

Fig.4.7. Impact responses of GLARE 5 (5/4) and (6/5) under 80J impact energy.

Based on Fig. 4.9, strain results in the ±45° directions are higher than 0°/90° directions. This is believed to be due to the influence of the fiber direction with respect to the strain gage locations. That is, since the top aluminum layer, where the strain gages were mounted, was very thin and had a very good bonding with the adjacent prepreg layer, therefore the strains were influenced by the fiber direction. Thus, the strain gages measuring the strains along the fiber direction yielded lower strains compared to those measuring the strains at an angle to the fiber direction. Since the fibers resist stretching along their direction more than stretching along other directions. In addition, Fig. 4.9

reveals that under the same impact energy, both radial and hoop strains decreased when the panel thickness increased. This is because the central deflection of the panel under the impact decreased with increasing panel thickness and, hence, the strain readings from the strain gages reduced accordingly.

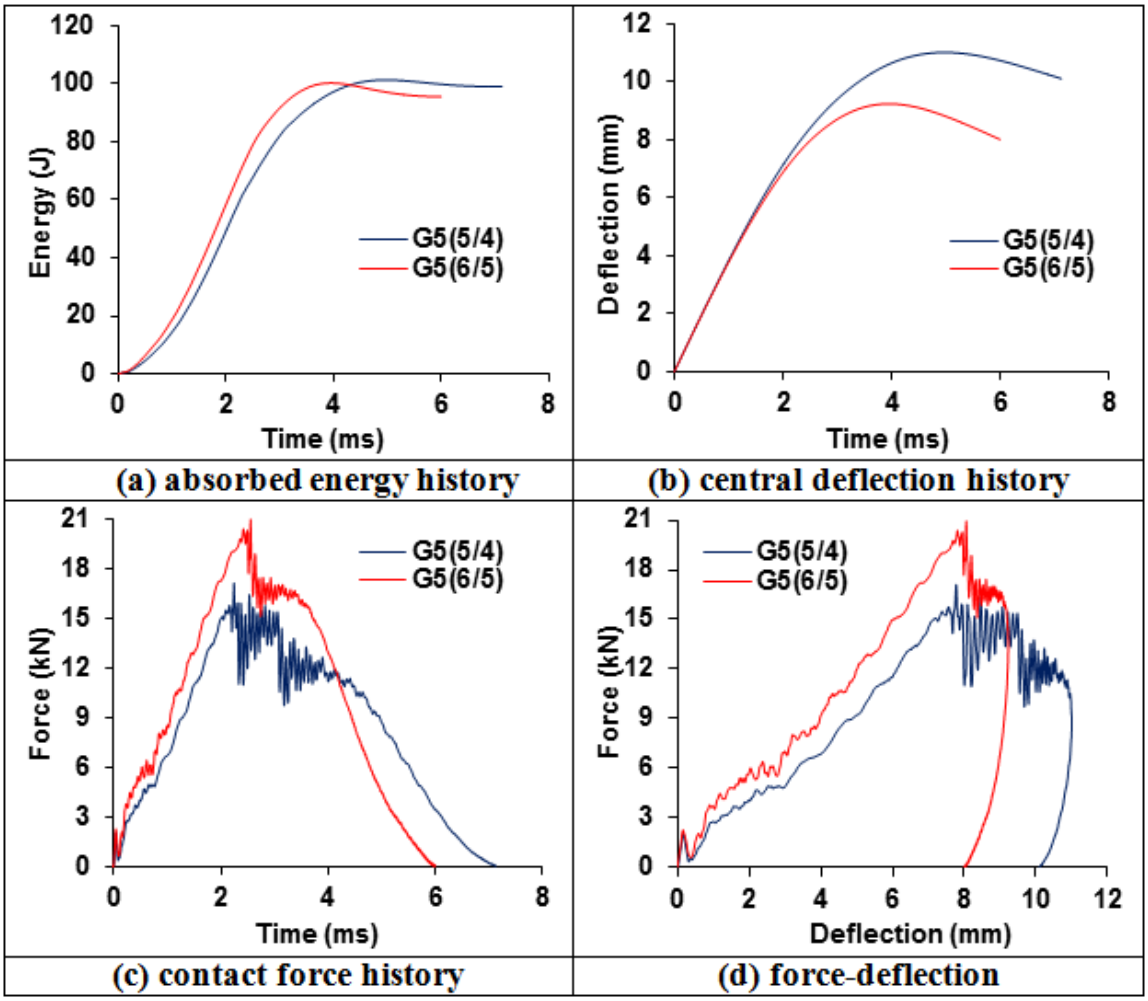

Fig.4.8. Impact responses of GLARE 5 (5/4) and (6/5) under 100J impact energy.

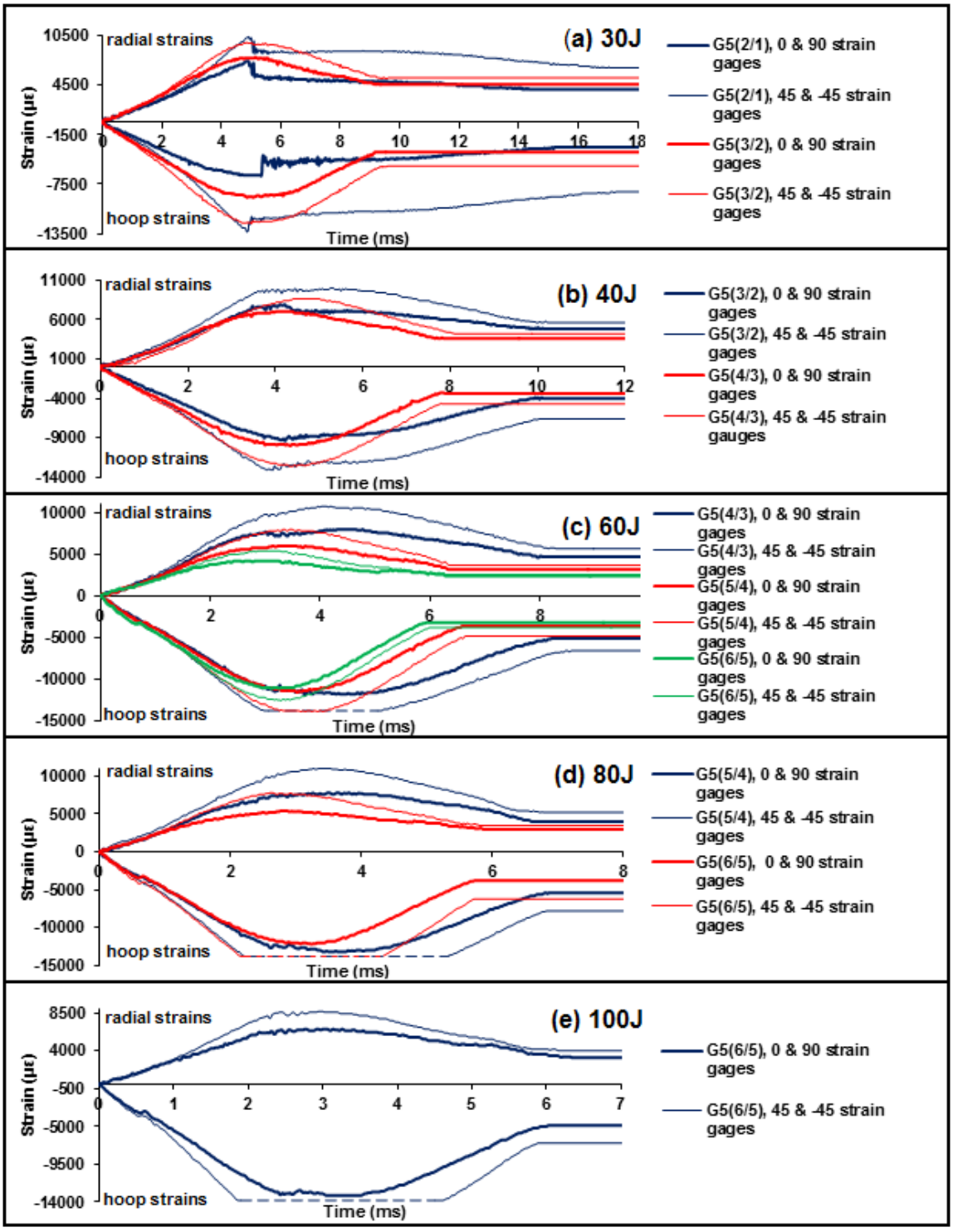

Fig.4.9. Strain histories for the GLARE 5 specimens with different thickness.

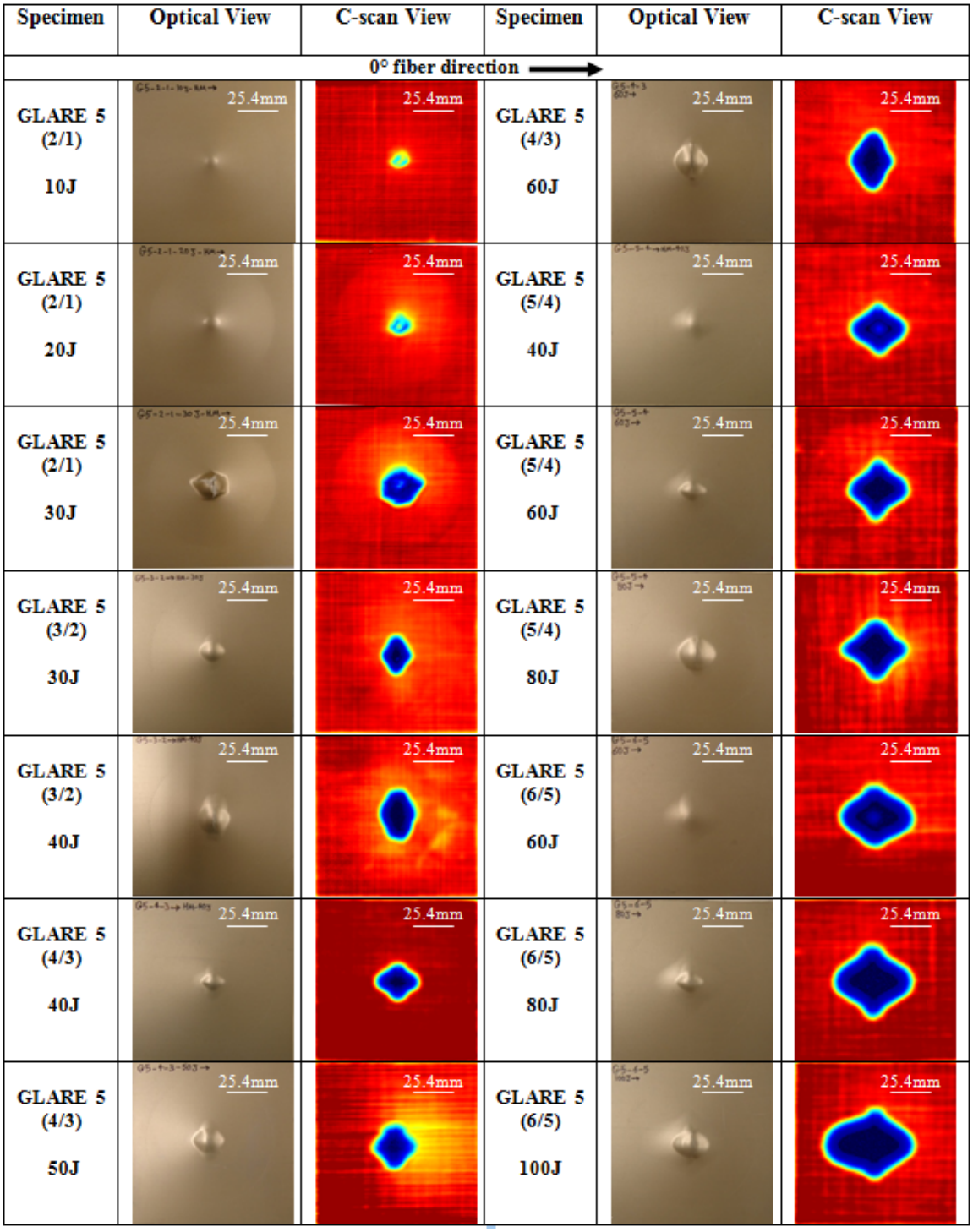

Fig.4.10. Back-side (non-impacted) view and corresponding C-scan view of the GLARE 5 FMLs with different thicknesses.

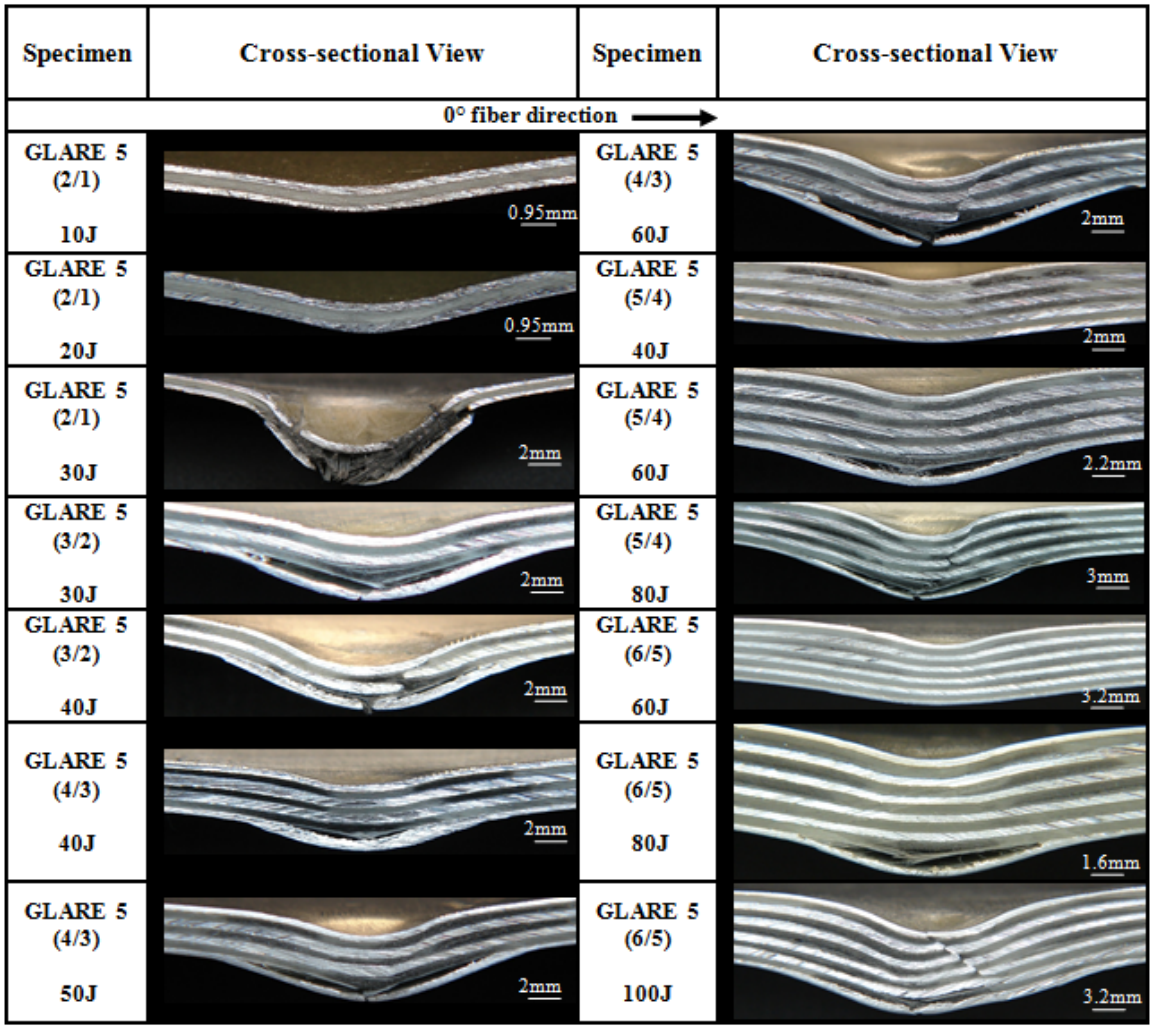

Fig.4.11. Cross-sectional view of the GLARE 5 FMLs with different thicknesses.

4.3. Effect of impactor mass

In order to study the impactor mass effect, an impactor mass of 6.14 kg was chosen in addition to the previous impactor mass of 12.91 kg. Since repeating all the above tests will make this dissertation very lengthy, thus only a few of them were reported here.

Figure 4.12 compares the histories of the central deflection, contact force and force-deflection under 6.14 kg and 12.91 kg impactor masses. Under the same impact energy, the contact force increased with a decrease in the impactor mass. The contact time also decreased with decreasing impactor mass. However, Fig. 4.12 shows that this was not the

case for GLARE 5 (4/3) and (5/4). Therefore, contact time was not a reliable parameter to characterize impact behavior.

By decreasing the impactor mass, the initial slope of the force-deflection curve tended to become stiffer under the same impact energy. This also means that under the same impact energy, the damage pattern would be different for the same panel with the same thickness but with different impactor mass. This difference is demonstrated in Fig. 4.13 for the GLARE 5 (3/2) specimen. It is apparent from Fig. 4.13 that the bottom aluminum layer failed under 30J impact energy, using 12.91 kg impactor mass. No crack appeared in the bottom layer of aluminum under the same condition while using the 6.14 kg impactor mass. Moreover, by looking at the cross-sectional and C-scan view of the specimens, different damage patterns can also be observed. By maintaining the same impact energy, the overall damage area increased with increasing impactor mass (Fig. 4.13). It can also be concluded from Fig. 4.12 that the maximum deflection of the impactor was independent of the impactor mass. However, the same conclusion cannot be made regarding permanent central deflection (Tables 4.1 & 4.2).

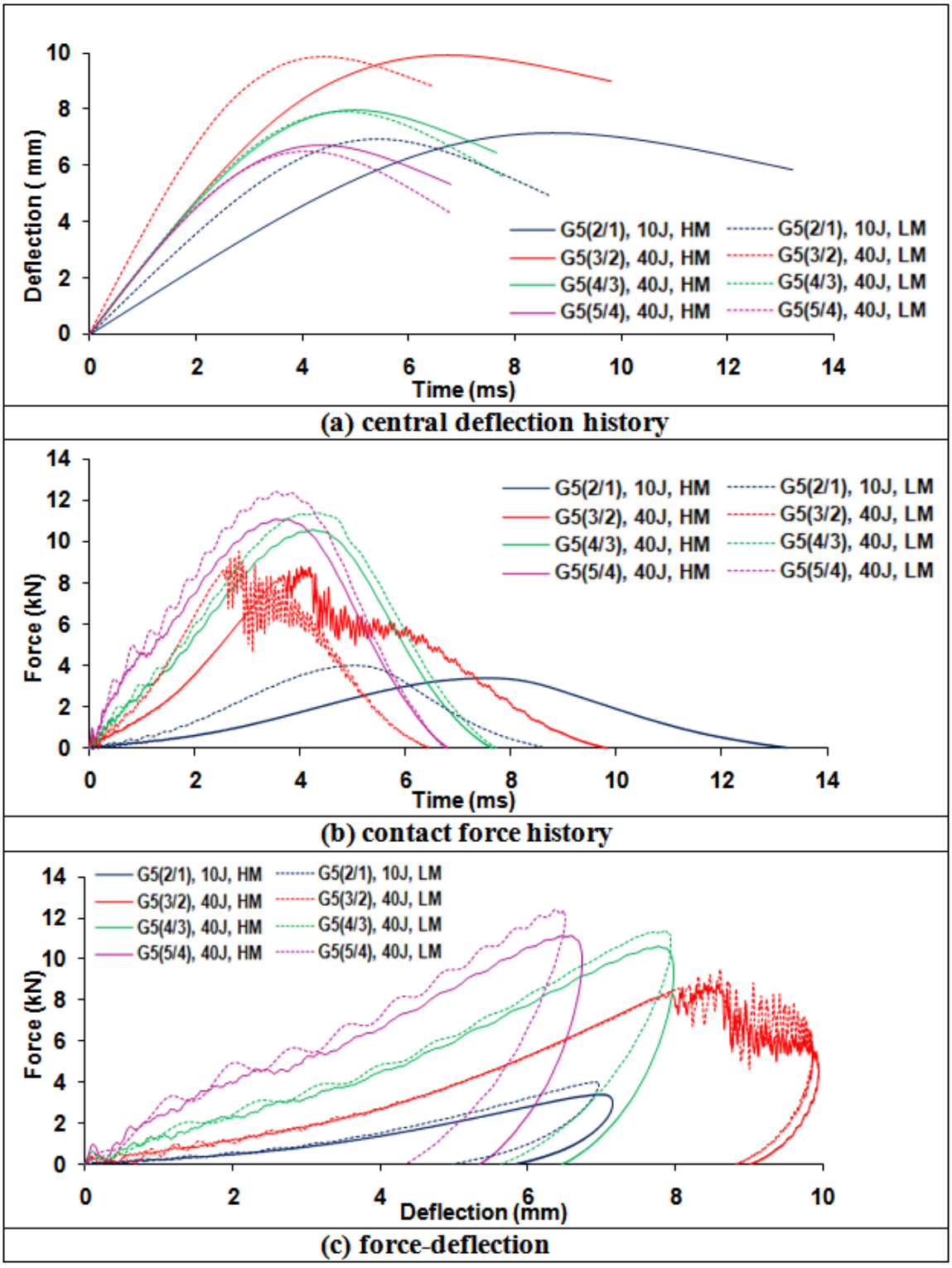

Fig.4.12. Central deflection history (a), contact force history (b), and force-deflection (c), comparisons between the 6.14 kg (LM) and 12.91 kg (HM) impactor mass.

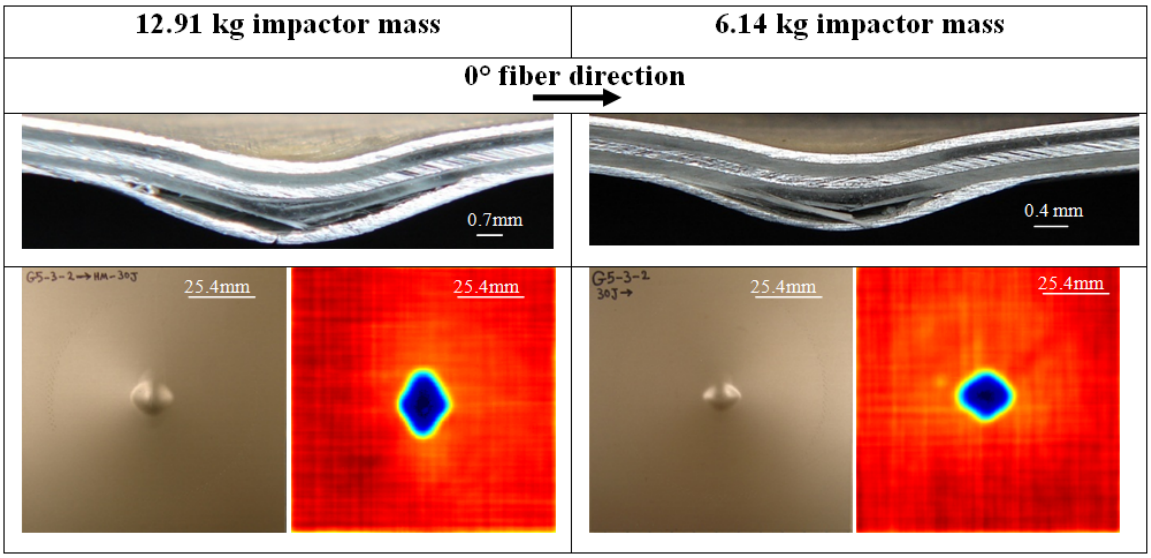

Fig.4.13. Comparison of GLARE 5 (3/2) under 30J impact energy using 12.91 kg and 6.14 kg impactor masses. Left/right top: cross-sectional view, left/right bottom: non-impacted side optical and C-scan views.

The test results indicated that impact damage was much more sensitive to the impactor velocity than to its mass. However, C-scan results showed that the contour of overall damage tended to increase as the impactor mass increased. Depending upon the impactor mass and shape, an impactor may or may not cause damage under a given impact energy. Therefore, it would be inadequate to select impact energy alone as the parameter to characterize impact damage. Thus for characterizing the impact damage under the same impactor shape, the impactor mass or velocity in addition to the impact energy must also be taken into consideration.

4.4. Threshold cracking energy

Threshold cracking energy was studied on the cross-ply GLARE 5 specimens with various configurations using 6.14 kg and 12.91 kg impactor masses. In this study, threshold cracking energy is defined as the minimum impact energy required to create a crack in the bottom aluminum layer.

Figure 4.14 compares the threshold energy with respect to the metal volume fraction for 6.14 kg and 12.91 kg impactor masses. The variation of threshold cracking energy with respect to the impact velocity is illustrated in Fig. 4.15 for both impactor masses. The relationships between MVF and impact velocity with respect to the threshold cracking energy could be fitted with a parabolic plot using a least square method, as shown in the figures.

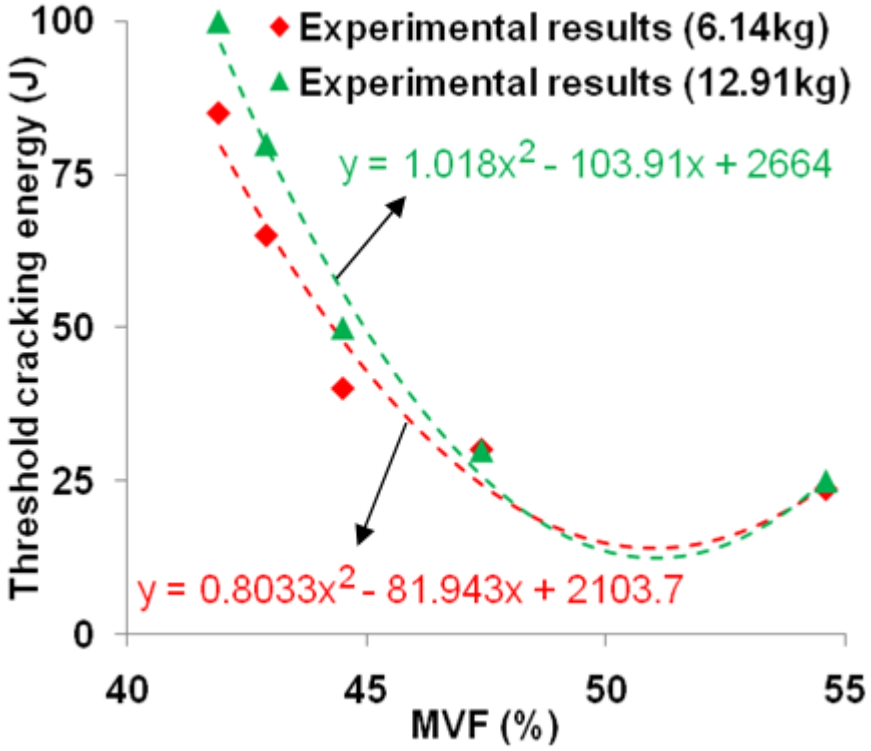

Fig.4.14. Comparison between threshold cracking energy and MVF for 6.14kg and 12.91kg impactor masses. In the formulae x is the MVF and y is the threshold cracking energy.

As is obvious from Figs 4.14, by increasing the metal volume fraction of the panels, the threshold cracking energy decreases parabolically. Moreover, for the same MVF value, the cracking energy increased as the impactor mass increased. However this was relatively negligible for the thinner panels, i.e. (2/1) and (3/2). By increasing the panel configuration, as shown in Fig. 4.15, the velocity required to meet the threshold cracking

energy condition increased parabolically for both impactor masses. The figure also suggests that under the same impact velocity, the threshold cracking energy increased by increasing the impactor mass.

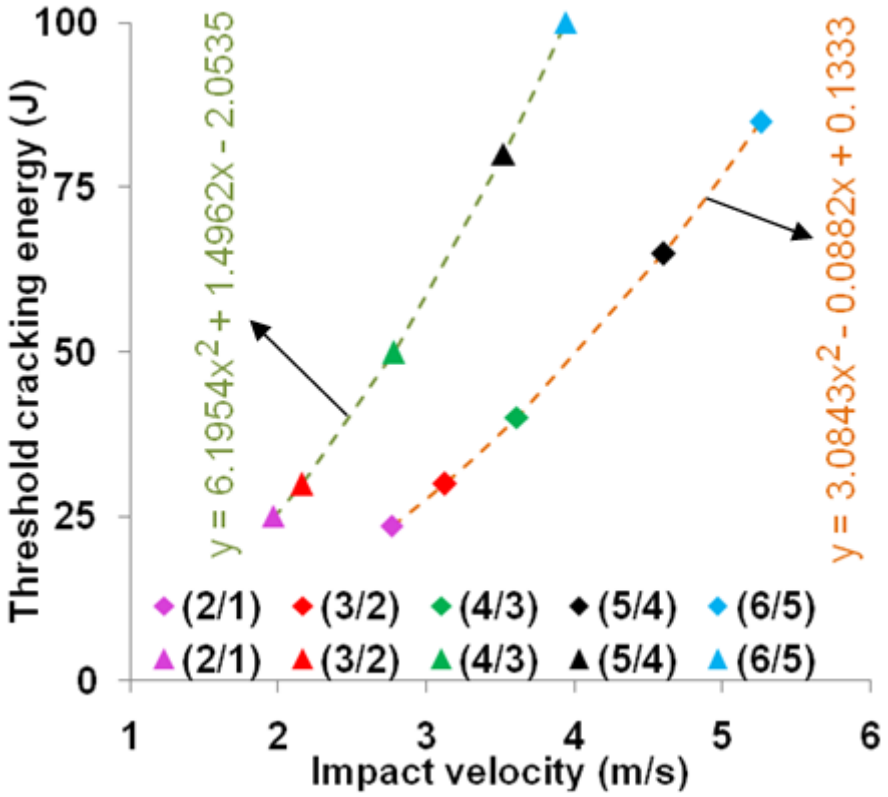

Fig.4.15. Comparison between threshold cracking energy and impact velocity for 6.14 kg (diamond) and 12.91 kg (triangle) impactor masses. In the formulae x is the impact velocity and y is the threshold cracking energy.

Figure 4.16 depicts the comparison between the threshold cracking energy and the specimen thickness for both impactor masses. As is apparent, the threshold cracking energy increased parabolically as the thickness of the specimens increased. Furthermore, for a given panel thickness, the energy required to induce a crack in the bottom aluminum layer increased by increasing the impactor mass. This was relatively pronounced for the panels with thicknesses above 2 mm.

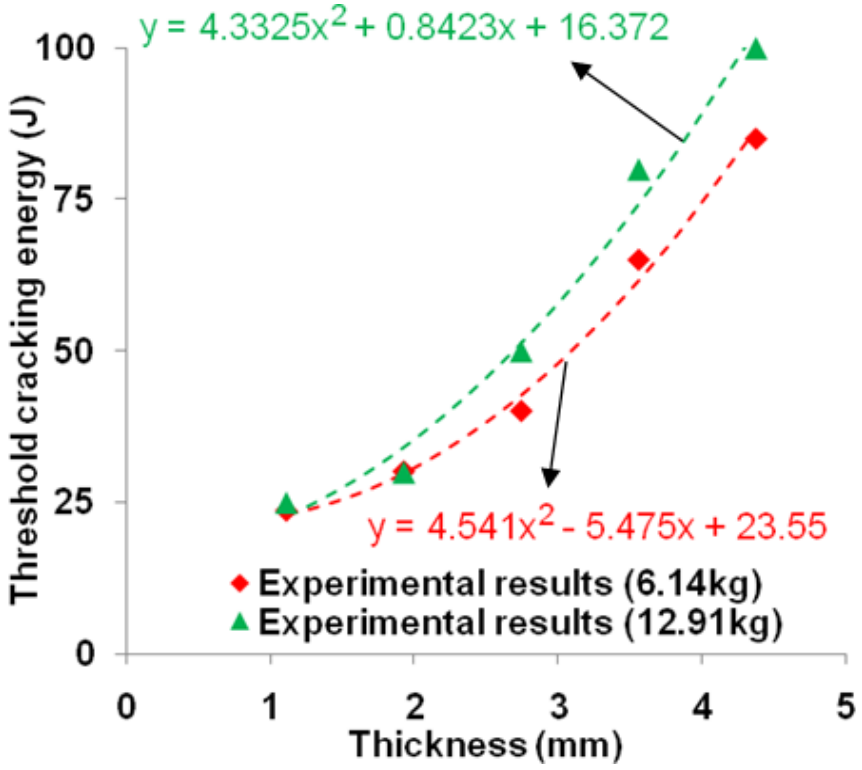

Fig.4.16. Comparison between threshold cracking energy and thickness of the cross-ply GLARE 5 FMLs. In the formulae x is the impact velocity and y is the threshold cracking energy.

4.5. Post-impact damage assessment

Tables 4.1 and 4.2 summarize experimental results of the impact-induced crack lengths measured on the impacted side (the top aluminum sheet) and the non-impacted side (the bottom aluminum sheet), respectively, along with the impact velocity and the post-impact permanent central deflection in the GLARE 5 composite materials with different thicknesses under two impactor masses and various impact energies. Figure 4.17 illustrates the permanent central deflection of the GLARE 5 panels as functions of impact energy and impact velocity under two different impactor masses, i.e. 12.91 kg in solid lines and 6.14 kg in dotted lines. From this figure it is obvious that by reducing the mass of the impactor while maintaining the same impact energy, the permanent central deflection increased. This is because the impactor velocity for the lighter mass was higher

when compared to the heavier one under a given impact energy. In addition, the amount of pressure applied to the specimen is also functions of impactor velocity and mass.

Table4.1. Crack lengths and permanent deflections of GLARE 5 with different thicknesses (impactor mass: 12.91 kg).

GLARE 5	Thickness (mm)	Impact Energy (J)	Crack Length in Outer Layer (mm)		Permanent Deflection (mm)	Impact Velocity (m/s)
			Impacted Side	Non-impacted Side		
(2/1)	1.12	10	0	0	3.28	1.24
		20	0	0	5.18	1.76
		30	11	19★	8.69	2.16
(3/2)	1.93	30	0	9	4.82	2.16
		40	8	17	6.42	2.49
(4/3)	2.75	40	0	0	3.83	2.49
		50	0	13.5	4.45	2.78
		60	7	22	5.26	3.05
(5/4)	3.56	40	0	0	2.5	2.49
		60	0	0	3.67	3.05
		80	5	19	5.17	3.52
		100	9	27.5	6.62	3.94
(6/5)	4.37	60	0	0	3.2	3.05
		80	0	0	3.98	3.52
		100	9	15	4.85	3.94

★: Bi-directional crack. The major crack length was selected.

Furthermore, for the lighter mass, the slope of the permanent central deflection versus impact energy was higher as compared to the heavier mass. This means that the panel under the test with lighter impactor mass reached the perforation limit faster than the heavier one. For example, for the GLARE 5 (2/1) specimen, the impactor with the lighter weight penetrated fully through the specimen even with an impact energy less than 30J,

whereas under the same impact energy but with the heavier impactor, the specimen still supported the impact load without any penetration of the impactor through the specimen (Tables 4.1 and 4.2).

Table4.2. Crack lengths and permanent deflections of GLARE 5 with different thicknesses (impactor mass: 6.14 kg).

GLARE 5	Thickness (mm)	Impact Energy (J)	Crack Length in Outer Layer (mm)		Permanent Deflection (mm)	Impact Velocity (m/s)
			Impacted Side	Non-impacted Side		
(2/1)	1.12	10	0	0	3.5	1.8
		20	0	0	5.7	2.55
		22	0	0	6.6	2.68
		23.5	8	10	7.2	2.77
		25	Through curved crack		8.3	2.85
		30	Penetration			3.13
(3/2)	1.93	10	0	0	2.2	1.8
		20	0	0	3.65	2.55
		30	0	0	5	3.13
		40	9	18	6.75	3.61
(4/3)	2.75	30	0	0	3.5	3.13
		40	0	7	4.1	3.61
		50	0	18	5	4.04
(5/4)	3.56	40	0	0	2.7	3.61
		50	0	0	3.3	4.04
		60	0	0	4.1	4.42
		65	0	12	4.5	4.60
		70	5	20	5	4.78
(6/5)	4.37	70	0	0	3.7	4.78
		85	0	10	4.5	5.26
		100	6	20	5.5	5.71

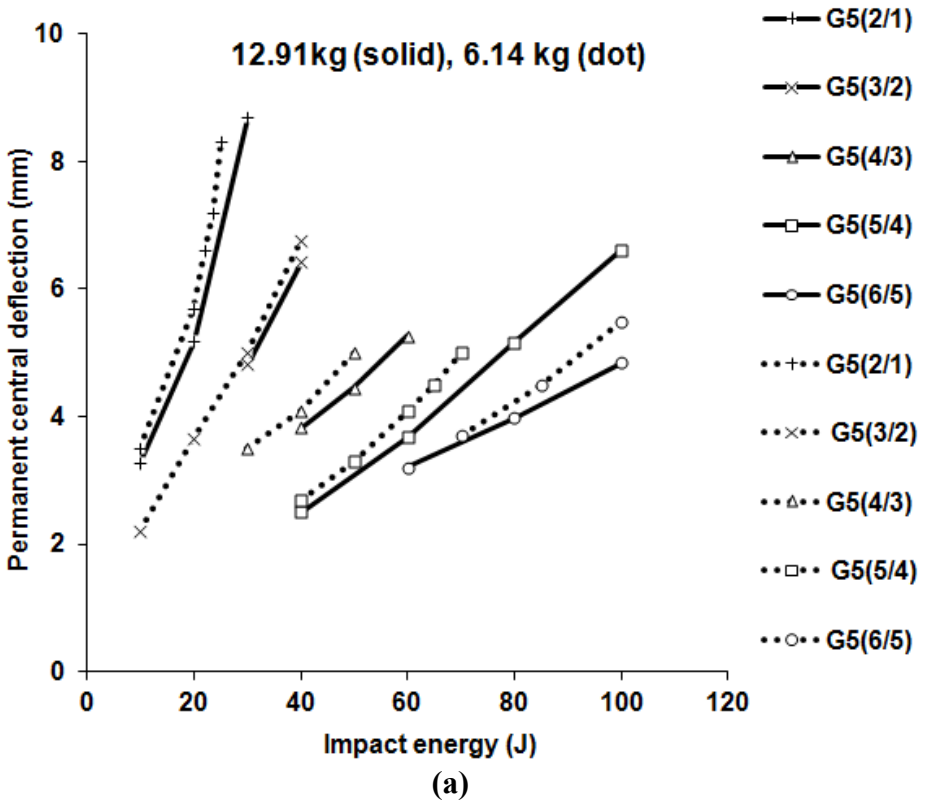

(a)

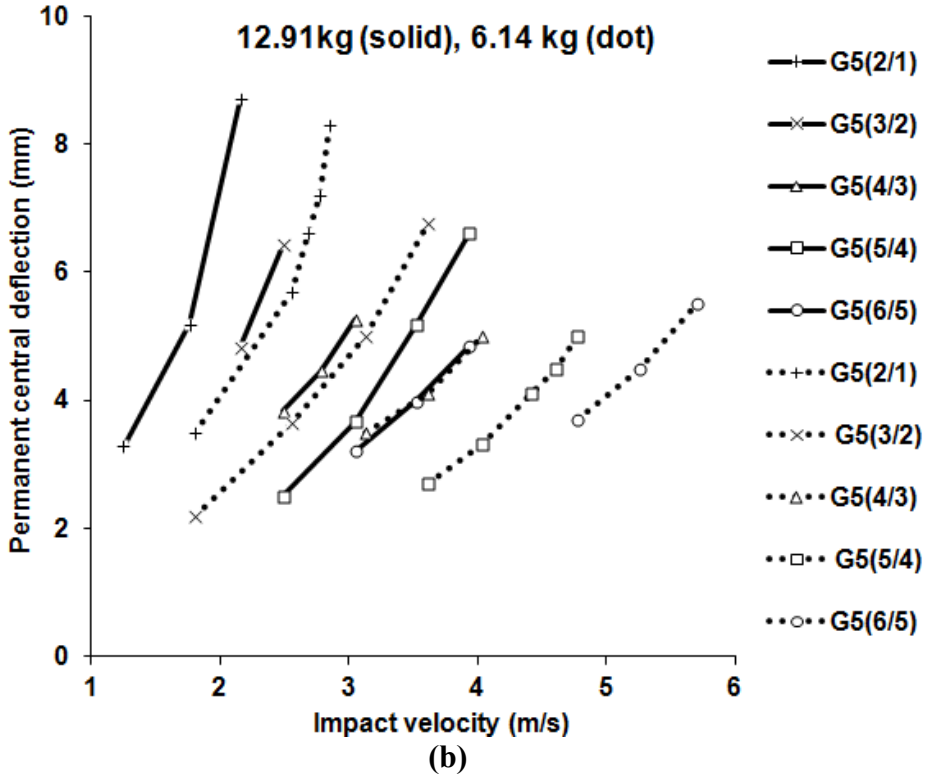

(b)

Fig.4.17. Permanent central deflection of the GLARE 5 FMLs as functions of (a) impact energy and (b) impact velocity.

4.6. Effect of stacking sequence

An impactor mass of 6.14 kg was considered to study the effect of stacking sequence. As a benchmark, twenty drop-weight tests were conducted on the square GLARE 5 (3/2) specimens with the cross-ply lay-up configuration to determine a proper impact energy for studying and comparing the impact responses and damage patterns of GLARE 5 (3/2) of various stacking sequences later. Table 4.3 summarizes the crack lengths on the impacted and non-impacted sides as well as the permanent deflection of the square cross-ply GLARE 5 (3/2) panels subject to 10, 20, 30 and 40J impact energies, respectively.

Table4.3. Crack lengths and permanent deflections of the cross-ply GLARE 5 (3/2) FMLs under different impact energies.

Impact Energy (J)	Crack Length in Outer Layer (mm)		Permanent Deflection (mm)
	Impacted Side	Non-impacted Side	
10	0	0	2.2
20	0	0	3.65
30	0	0	5
40	9	18	6.75

Figure 4.18 shows typical histories of the absorbed energy, central displacement, contact force, contact stiffness and strains. The coherence in contact stiffness during the loading phase, as shown in Fig. 4.18(d), implies that the force-deflection relation depends mainly on impact energy, as reported in [39]. Figures 4.19 and 4.20 depict the C-scan results and the back-side (non-impacted) views as well as the cross-sectional views of the impacted FMLs.

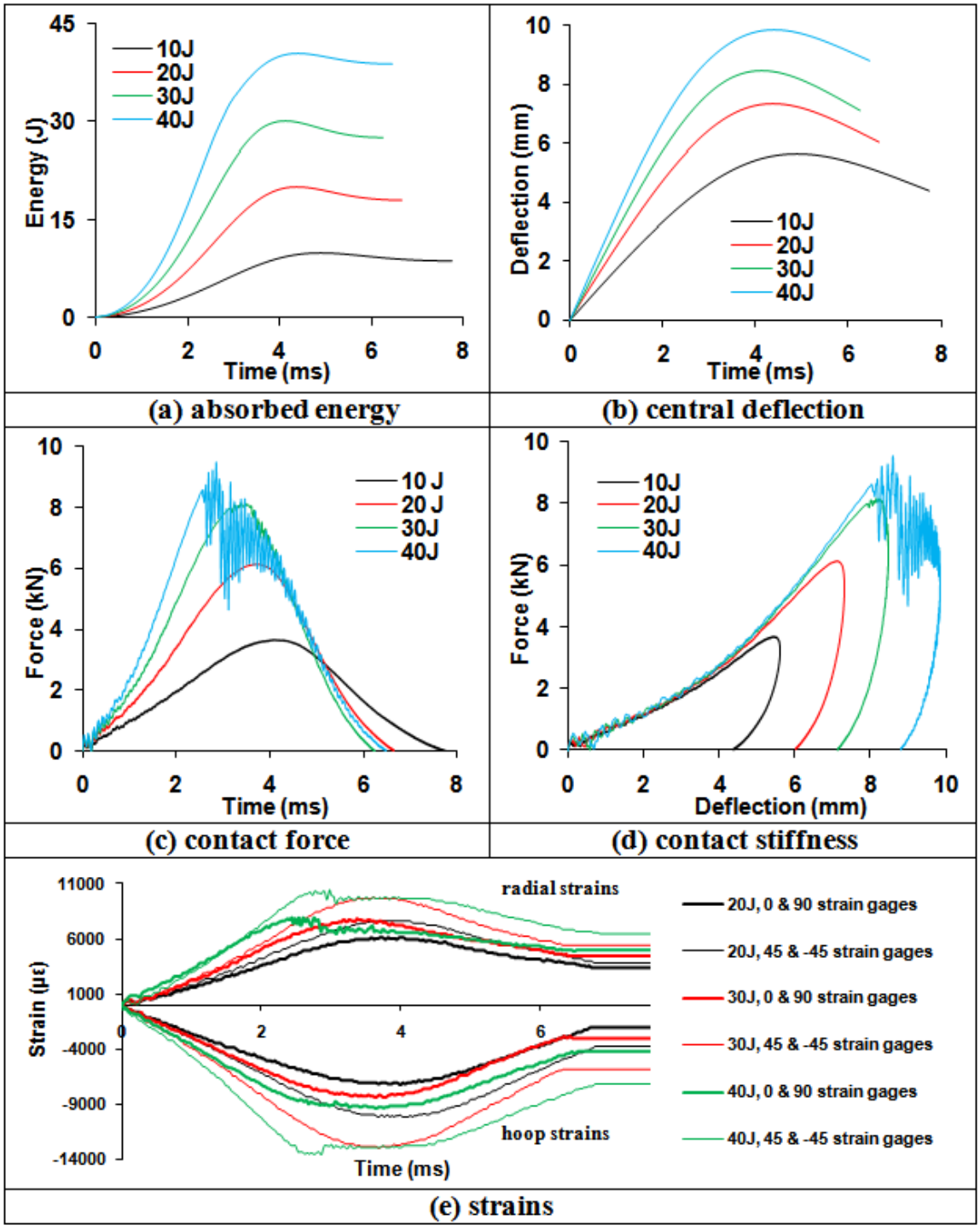

Fig.4.18. Impact responses of the cross-ply GLARE 5 (3/2) under various impact energies.

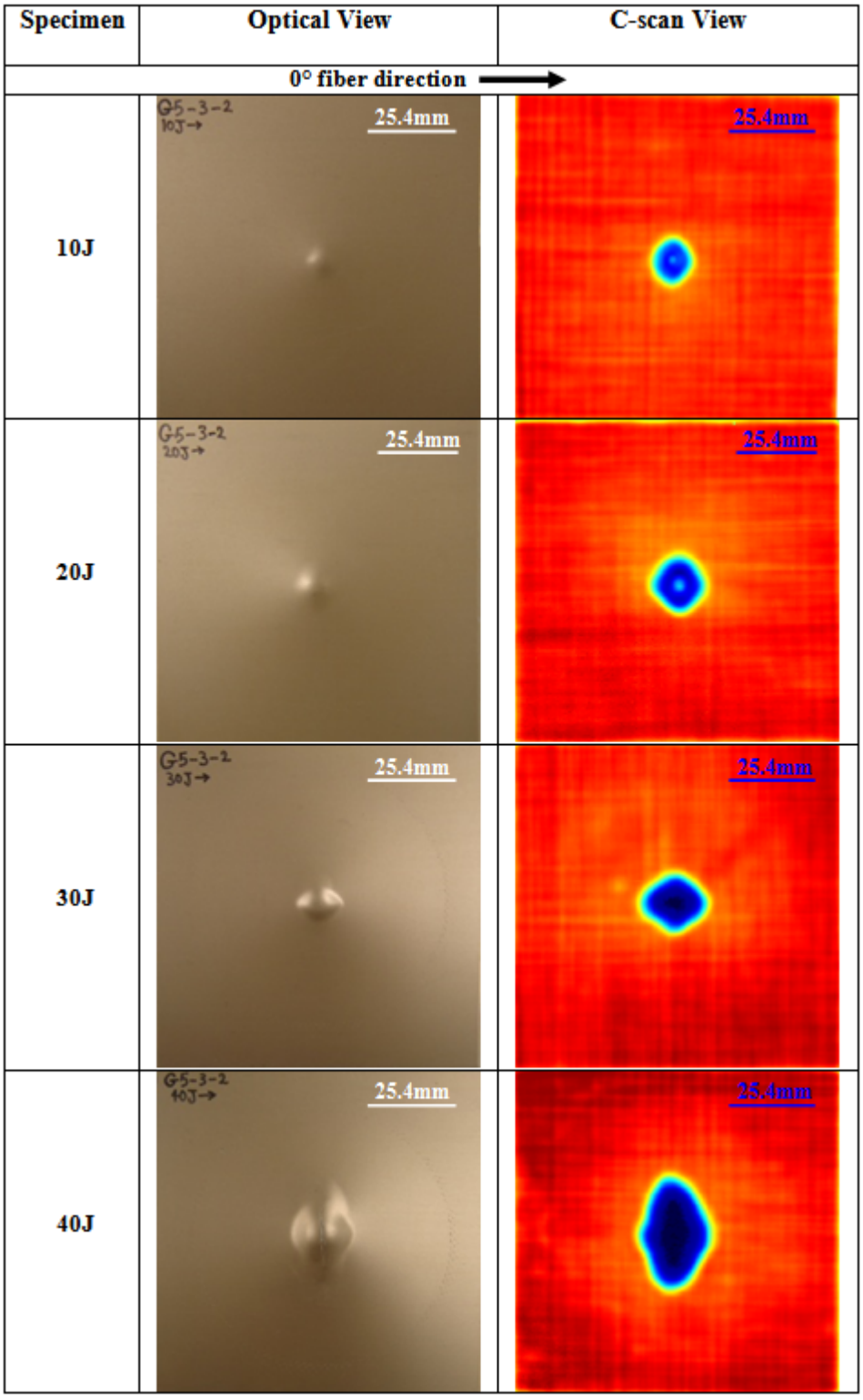

Fig.4.19. Back-side (non-impacted) view and corresponding C-scan view of the cross-ply GLARE 5 (3/2) FMLs under various impact energies.

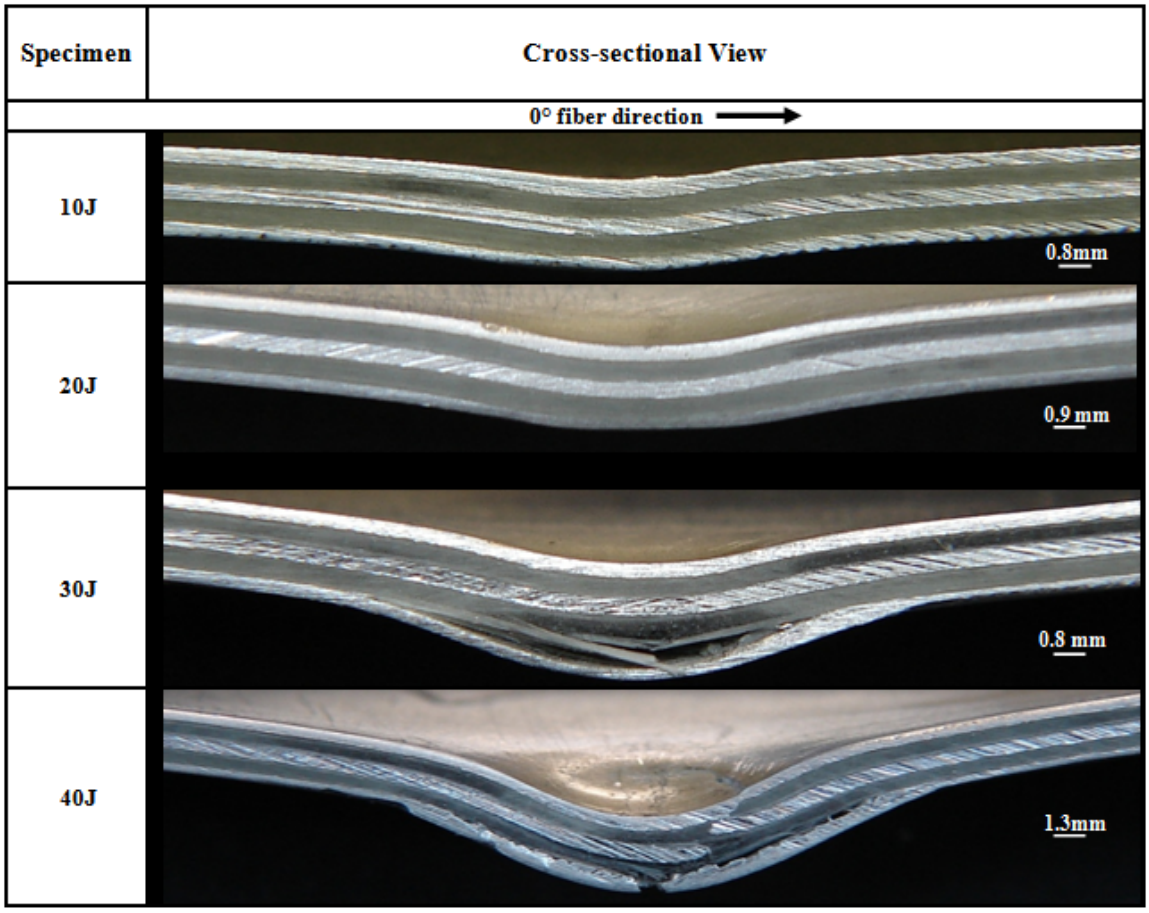

Fig.4.20. Cross-sectional view of the cross-ply GLARE 5 (3/2) FMLs under various impact energies.

For the cases of 10 and 20J impact energies, fairly smooth contact force history and contact stiffness curves were obtained (Figs. 4.18(c) and (d)). By referring to Figs. 4.19 and 4.20 no major damage could be seen except a small indent, slightly bent of the specimen and almost invisible debonding between the lower aluminum layer and its adjacent S2-glass/epoxy laminate. There was no crack on both the impacted and non-impacted sides (Table 4.3). As the impact energy further increased, oscillatory behavior could be seen in both contact-force and contact-stiffness curves. This behavior became very obvious under 40J impact energy, indicating more damage induced in the specimen and as confirmed in Table 4.3, Figs 4.19 and 4.20. For the 30J impact energy case,

damages induced were fiber breakage/splitting, delamination, matrix cracking, impact indent and permanent plastic deformation. At this impact energy, there was also no crack on either the impacted or the non-impacted side of the specimen. By increasing the impact energy to 40J, more pronounced damage could also be seen, including through-specimen cracks and severe delamination (Figs. 4.19 and 4.20). These observations are similar to those reported in Ref. [21].

With increasing the impact energy, the resultant strains also increased (Fig 4.18(e)). This was because the central deflection of the panel increased (Table 4.3). As indicated by the initial portions of the strain histories in Fig. 4.18(e), i.e. the time interval between 0 and 2 ms, the strain rate increased as the impact energy raised from 20 to 40J. Based on Fig. 4.18(e), strain results in the ±45° directions were higher than those in the 0° and 90° direction. The reason for this is believed to be the influence of the fiber direction with regard to the strain gage locations. That is, since the top aluminum layer, where the strain gages were mounted, was very thin and had a very good bonding with the adjacent prepreg layer, therefore the strains were influenced by the fiber direction. For the cross-ply GLARE 5 (3/2) both 0° and 90° are fiber directions. Due to the fact that fibers can resist more to stretching, the strains along these 0°/90° fiber directions were lower in comparison with those measured at ±45°.

As shown in Figs. 4.19 and 4.20, the area of the entire damage zone and local indentation increased with increasing impact energy. The presence of a small dot in the C-scan results for the cases of 10 and 20J impact energies indicates the material at that spot did not separate. This was a direct result of the compression/compaction effect right underneath the impact site.

Because under 40J impact energy major type of damages, i.e. fiber breakage/splitting, through-specimen crack and significant delamination, could be detected for the GLARE 5 (3/2) cross-ply panels; hence, 40J impact energy was chosen in this investigation to study the impact responses and damage patterns of the GLARE 5 (3/2) panels with different stacking sequences.

4.6.1. GLARE 5 (3/2) square specimens with various lay-up configurations

Figure 4.21 shows the histories of the absorbed energy, central displacement, contact force, contact stiffness and strains for the square GLARE 5 (3/2) specimens with cross-ply, unidirectional, angle-ply and quasi-isotropic lay-up sequences. The associated C-scan results, back-side (non-impacted) views and the cross-sectional views are shown in Figs. 4.22 and 4.23.

The absorbed energy history revealed that under the same impact condition, the unidirectional panel released less energy whereas the quasi-isotropic released the most. The peak value of central deflection was the highest for the unidirectional panel while the lowest was for the quasi-isotropic. For the GLARE 5 (3/2) cross-ply and angle-ply, this peak was approximately the same. Hence, the quasi-isotropic panel offered more resistance to indentation than other types of lay-up configuration. The unidirectional panel was the worst panel to sustain the impact. By comparing the contact force histories, the unidirectional panel had the lowest peak contact force and the longest contact time duration. The quasi-isotropic panel offered the highest peak contact force among the other panel types. It is worth noting that although the contact-stiffness and the contact-force histories for the GLARE 5 (3/2) panels with cross-ply, angle-ply and quasi-isotropic lay-up configurations were similar (Fig. 4.21c and d), their corresponding

damage patterns were quite different (Figs. 4.22 and 4.23). From Fig. 4.21(d), it could be observed that contact stiffness curves started to deviate at 4.1 mm of the central deflection, which corresponding to contact time at 1.16 ms (Fig. 4.21(c)). Similar observation had also been reported by Liu et al. [24] when comparing the unidirectional GLARE 2 versus the cross-ply GLARE 3.

C-scan and mechanical-sectioning results revealed that the major types of damage for the GLARE 5 (3/2) cross-ply panels were through-specimen crack, fiber breakage/splitting and delamination (Figs. 4.22 and 4.23). The major delamination occurred between the non-impacted side aluminum layer and the adjacent glass-epoxy layer. Some smaller regional delamination around the middle aluminum layer was also found. An elliptical-shaped damage zone was induced with the major diagonal perpendicular to the 0° fiber direction. For the unidirectional panel, long visible through-the-thickness cracks extended almost to the clamped edge were generated (Fig. 4.22). There was not much delamination besides fracture of aluminum layers and the splitting of the glass-epoxy layers for the unidirectional panel (Fig. 4.23). Since there was no bending stiffness mismatch in a unidirectional prepreg layer, no delamination was expected in the interface of the unidirectional prepreg layer. The fracture of aluminum in the non-impacted side resulted from bending while the stress concentration induced the crack in the impacted face. Its damage zone observed from C-scan (Fig. 4.22) looked like a lip-shaped rhombus with the major axis aligning along the fiber direction.

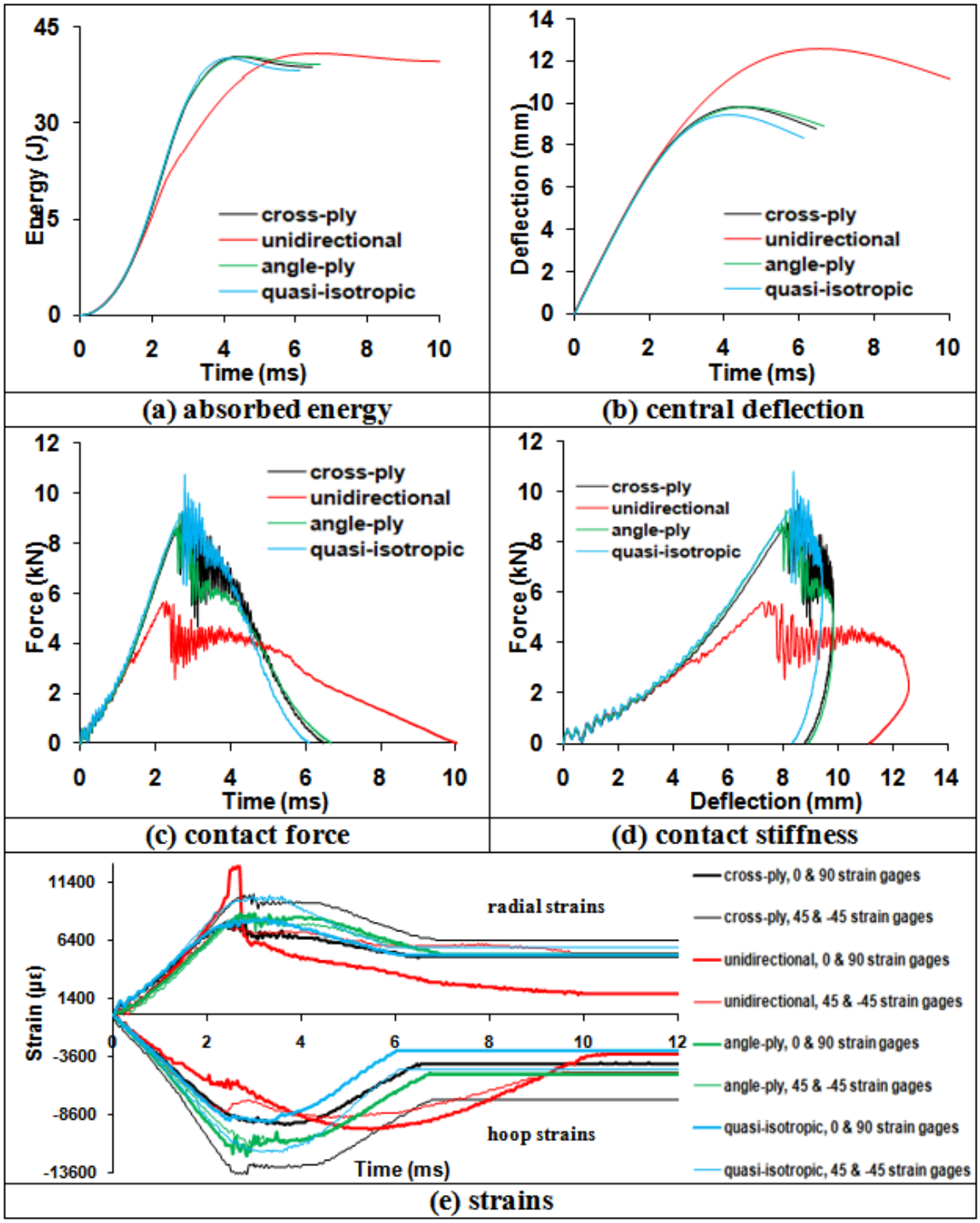

Fig.4.21. Impact responses of the GLARE 5 (3/2) square specimens with various stacking sequences under 40J impact energy.

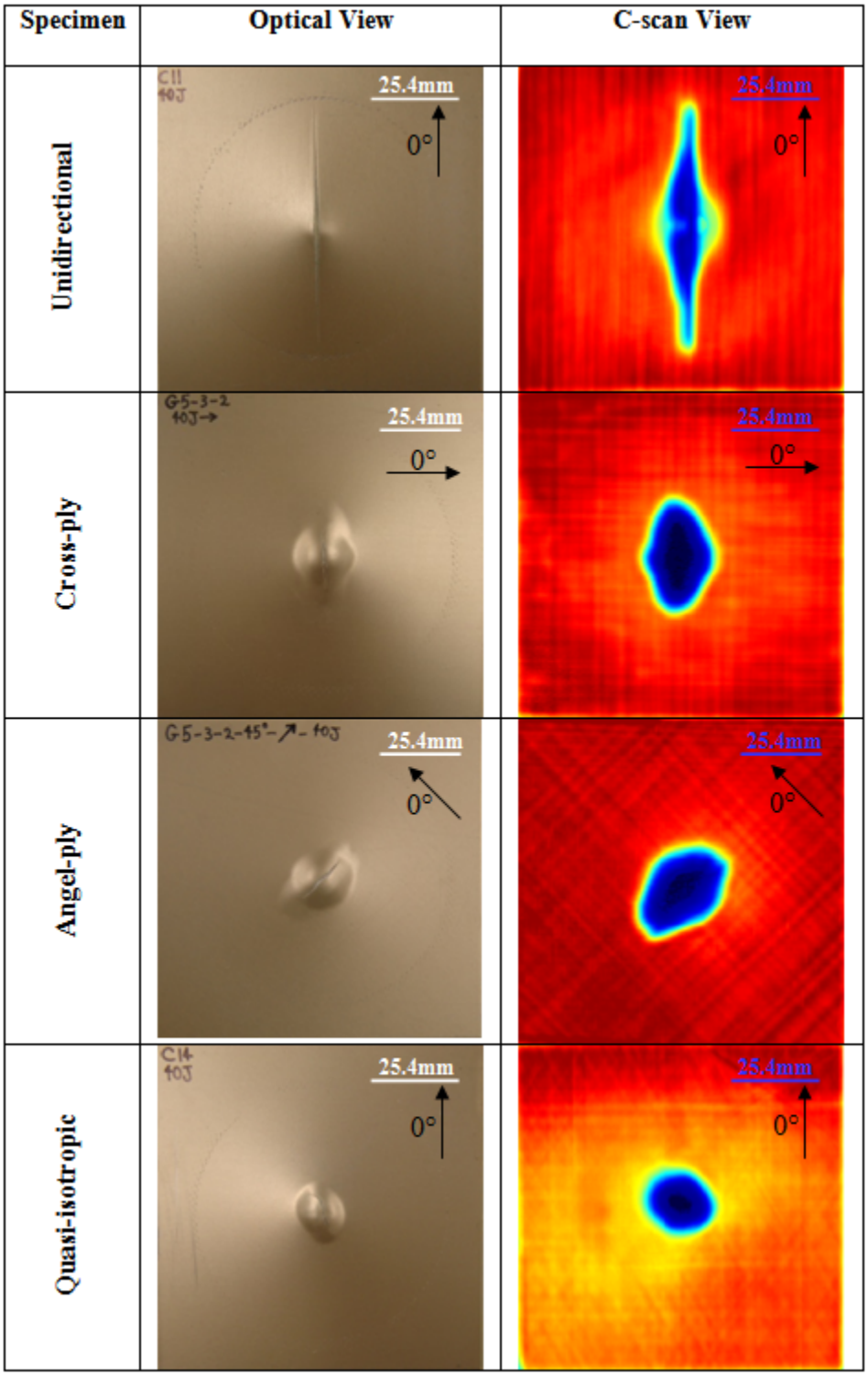

Fig.4.22. Back-side (non-impacted) view and corresponding C-scan view of the GLARE 5 (3/2) square specimens with various stacking sequences under 40J impact energy.

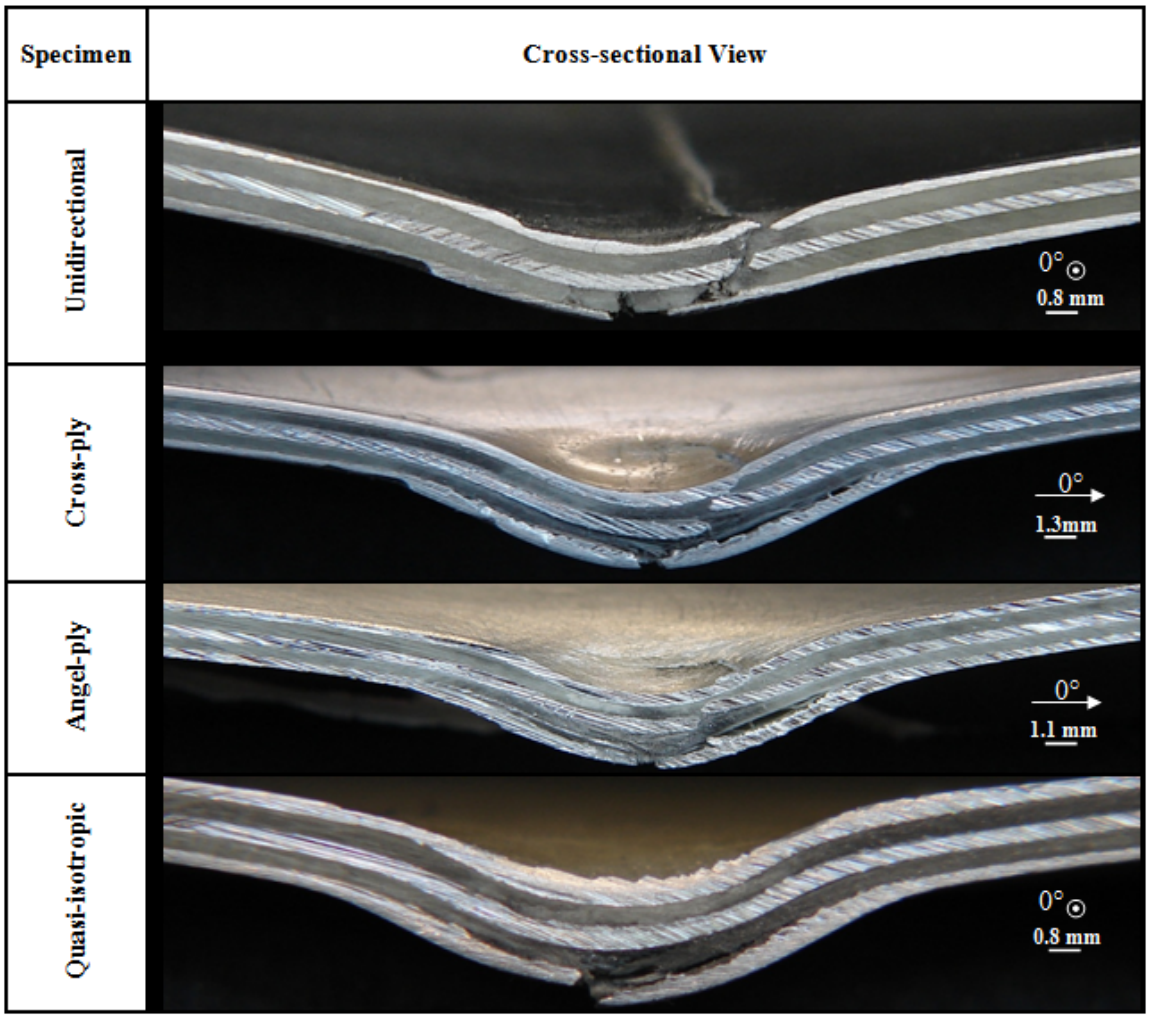

Fig.4.23. Cross-sectional view of the GLARE 5 (3/2) square specimens with various stacking sequences under 40J impact energy. The symbol ⊙ means that the fiber direction is out of the plane.

The damage pattern for the angle-ply panel was very close to the cross-ply panel except for the orientation of the damage contour (Fig. 4.22). In short, the major and minor axes of the elliptical-shaped damage zone coincided with the fiber directions. Furthermore, the major diagonal, i.e. perpendicular to the 0° fiber direction, within the elliptical-shaped damage contour was relatively shorter for the angle-ply panels compared to the cross-ply panels (Fig. 4.22). It should be noted that by circumferentially clamping a square specimen inside the specimen fixture, the total clamping area on each face of the

specimen, i.e. bottom and top, is equal to 8.93 in^2 (57.62 cm^2). Due to the stacking sequence of the angle-ply specimens, i.e. $[\pm 45°]_s$, with respect to the specimen geometry, there would be more fibers that were clamped compared to the cross-ply square specimens. It is believed that mainly because of this reason, the angle-ply specimens offered slightly more resistance to impact compared to the cross-ply specimens. For the quasi-isotropic panels, major types of damage, as shown in Figs. 4.22 and 4.23, were crack in the non-impacted side aluminum, damage in the bottom [0°/±45°/90°] quasi-isotropic prepreg layer as well as significant delamination between the –45° and 90° layers (due to mismatch in bending stiffness). A near circular damage zone was detected by ultrasonic C-scan for the quasi-isotropic panel. It is worth noting that at 40J impact energy, a visible crack appeared in all specimens on the non-impacted side. The crack was straight for the cross-ply, unidirectional and angle-ply GLARE 5 (3/2) specimens whereas it became curvy for the quasi-isotropic specimen (Fig. 4.22).

As is apparent from Fig. 4.21(e), the radial strain along the 0° fiber direction for the unidirectional panel exhibited a peak value followed by a sudden drop. The reason for this is due to the fact that the unidirectional panel experienced the most central deflection compared to other types of the panels (Fig. 4.21(b)) and hence the strain value increased dramatically. It also cracked sooner (at around 3 ms) than other panel types. The sudden drop was the ensuring result of the panel fracture. This crack passed underneath the location where the strain gage was mounted, causing the strain to release suddenly. Figure 4.21(e) shows that the strain results in the ±45° directions were higher than 0° and 90° directions. Again, as mentioned earlier, the reason is due to the influence of the fiber direction with respect to the strain gage locations.

Based on the discussion above, GLARE 5 (3/2) of unidirectional lay-up offered the worst impact resistance, followed by cross-ply and angle-ply configurations, while the quasi-isotropic stacking sequence showed the best resistance to the impact. The reason for this is that the specimen stiffness decreased as the lay-up configuration changed from the quasi-isotropic to the unidirectional stacking sequence. This conclusion is also reported in Refs. [34,37,38].

4.6.2. GLARE 5 (3/2) circular vs. square specimens with various lay-up configurations

Figure 4.24 shows the histories of the absorbed energy, central displacement, contact force, contact stiffness and strains for the circular GLARE 5 (3/2) specimens with cross-ply, unidirectional, angle-ply and quasi-isotropic lay-up sequences. Figures 4.25 through 4.28 compare the impact responses between the square and circular GLARE 5 (3/2) specimens with unidirectional, cross-ply, angle-ply and quasi-isotropic lay-up sequences under 40J impact energy. Figures 4.29 and 4.30 depict the corresponding C-scan results, back-side (non-impacted) and cross-sectional views of the specimens with the unidirectional, cross-ply, angle-ply and quasi-isotropic lay-up sequences. Table 4.4 summarizes experimental results of the impact-induced crack lengths measured on the impacted side (the top aluminum sheet) and the non-impacted side (the bottom aluminum sheet), respectively, along with the post-impact permanent central deflection in the GLARE 5 (3/2) composite materials with different stacking sequences and geometries subjected to 40J impact energy. Comparing these results to those of the square specimens, the following remarks can be found.

The energy history curves had a pattern very close to those of the square specimens. The central deflection curves for the circular unidirectional specimens increased noticeably in

comparison with the corresponding panels of square specimens. This enhancement was almost negligible for the cross-ply, angle-ply and quasi-isotropic panels. The peak force for the unidirectional circular specimen was lower than that of the corresponding square specimen. However, for the cross-ply, angle-ply and quasi-isotropic specimens, the difference in the peak force values was insignificant. The contact time was also raised when changing the geometry from square to circular. This difference was quite noticeable for the unidirectional panel; but it was relatively negligible for the cross-ply, angle-ply and quasi-isotropic panels. The contact stiffness decreased by changing the geometry from square to circular. There was no significant difference in the strain results by changing the geometry. This was very apparent for the cross-ply and quasi-isotropic specimens (Figs. 4.26 and 4.28). The effect of the above mentioned differences could be revealed by comparing the C-scan, back side and cross sectional views of the specimens with the ones for the square specimens. For the unidirectional panels of the two geometries, both C-scanned damage images were almost the same with the exception that for the circular specimen, the length of the damage along the 0° fiber direction was longer (Table 4.4, Figs. 4.22 and 4.29). In fact, the induced crack in the unidirectional circular specimens passed the grip area of the specimen. The C-scan results revealed that the damage size decreased for the cross-ply and angle-ply circular specimens. It is apparent from Figs. 4.22 and 4.29 that damage area was bigger for the quasi-isotropic circular specimen compared to its square counterpart. In addition, the circular damage shape became more rounded for the circular specimen. Based on Table 4.4, quasi-isotropic panels offered the minimum crack lengths in the outer layers, i.e. impacted and non-

impacted sides, as well as the least permanent deflection in their own geometrical categories.

The cross sectional views suggested that for the circular unidirectional specimen, the induced damage pattern was different from its square counterpart. Prepreg damages among the aluminum layers were noticeably increased. Also unlike the unidirectional square specimens, in which the prepreg close to the non-impacted side were broken into several pieces by through-the-thickness cracks, it did not happen for the circular specimen. Comparing the cross-sectional views of the two different geometries for the cross-ply specimen, the overall damage patterns were similar except in circular geometry there was no debonding between the non-impacted aluminum and the adjacent prepreg layer. For the circular angle-ply specimen, the overall damage pattern was almost similar to the angle-ply square specimen. By evaluating the cross-sectional views for the quasi-isotropic square and circular specimens, some change in the induced damages could be seen. The bottom aluminum layer failed in a step-like mode for the square specimen, whereas there was a smooth transition for the circular specimen. Moreover, further prepreg damage was exhibited by the circular specimen. That is, by transition from square to circular geometry, the damage in the bottom prepreg composite layer, i.e. farther from the impacted face, was noticeably enhanced and extended. In addition, based on this transition, localized damage in the prepreg layers underneath the impactor was induced.

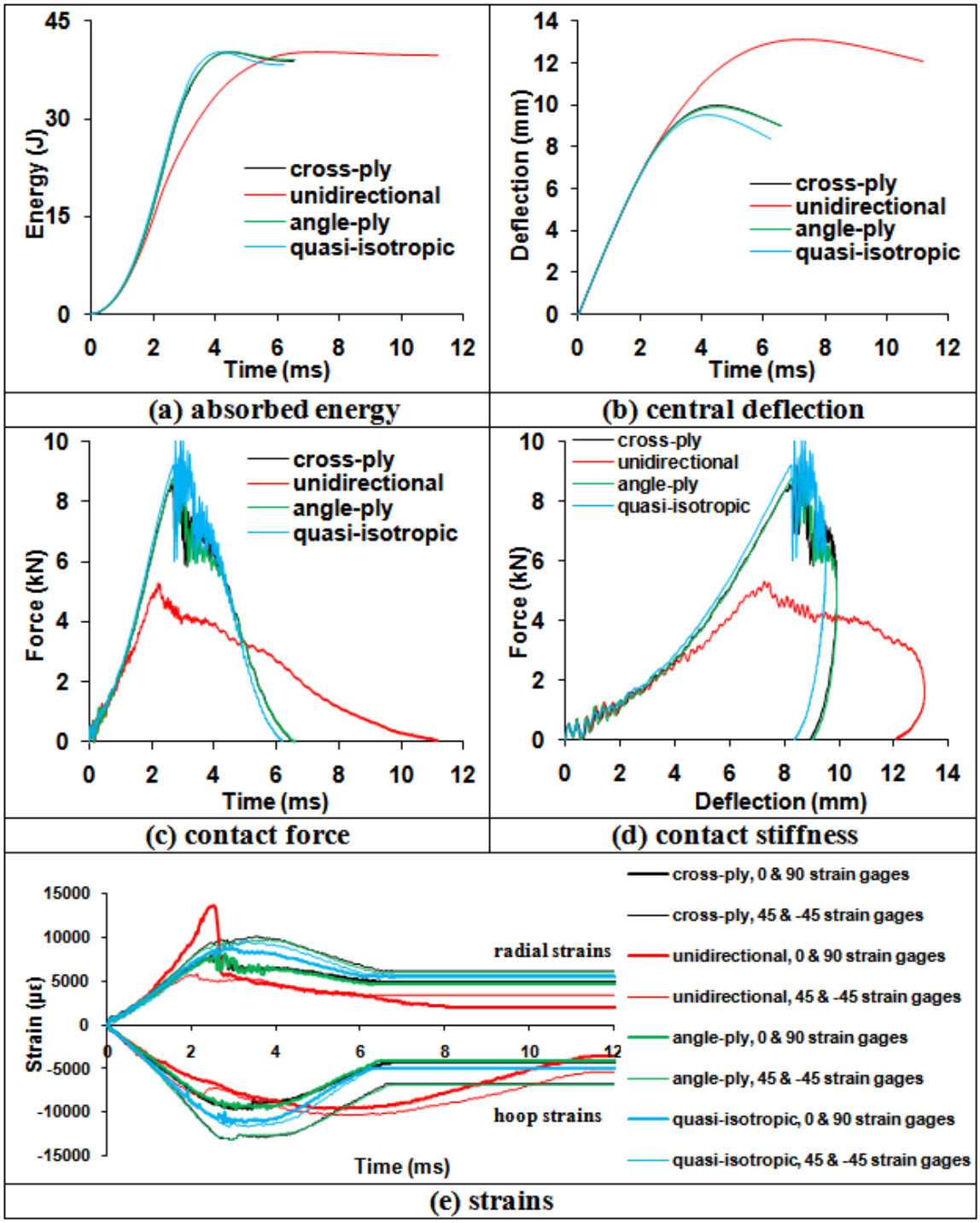

Fig.4.24. Impact responses of the GLARE 5 (3/2) circular specimens with various stacking sequences under 40J impact energy.

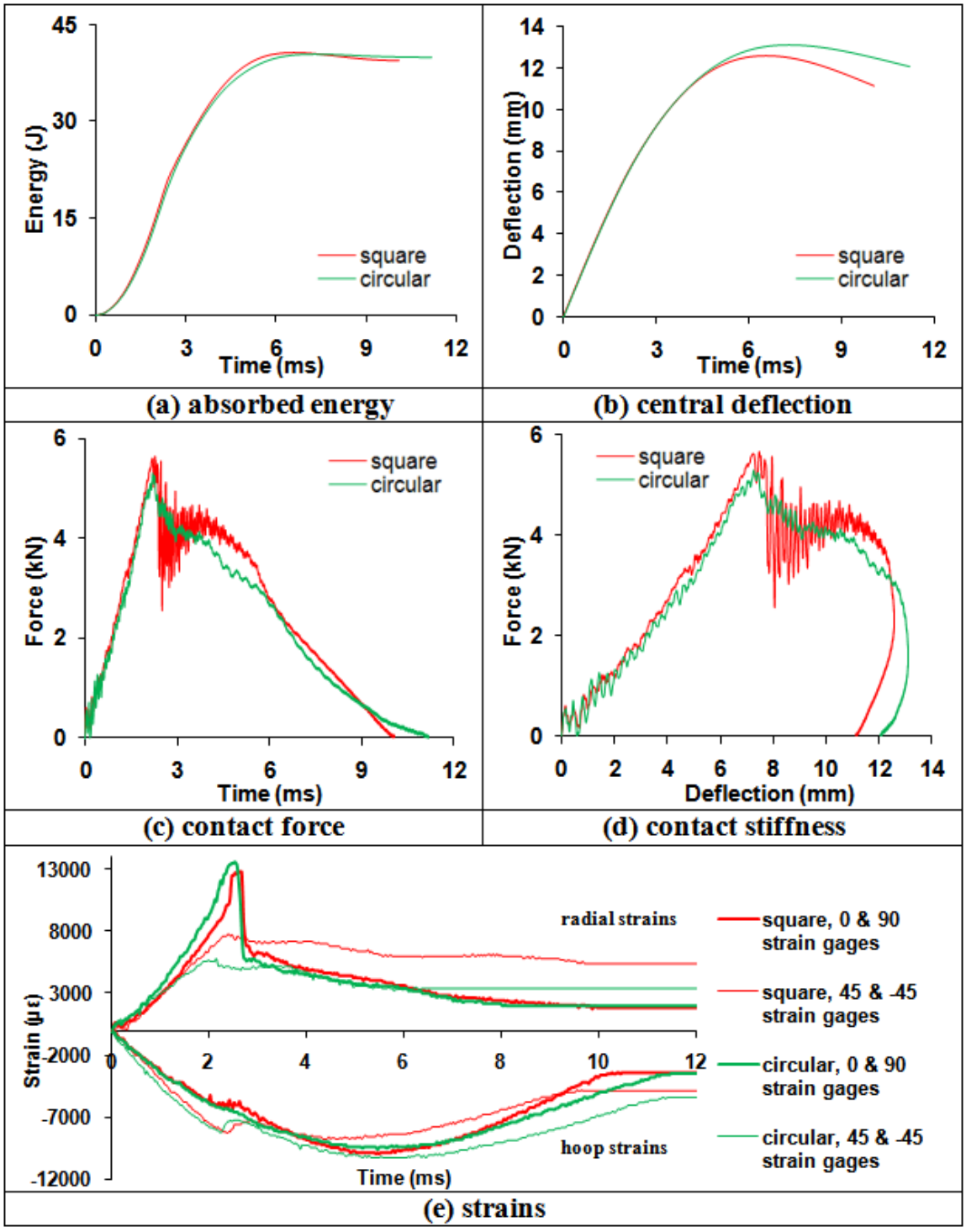

Fig.4.25. Comparison of the Impact responses between the square and circular unidirectional GLARE 5 (3/2) specimen under 40J impact energy.

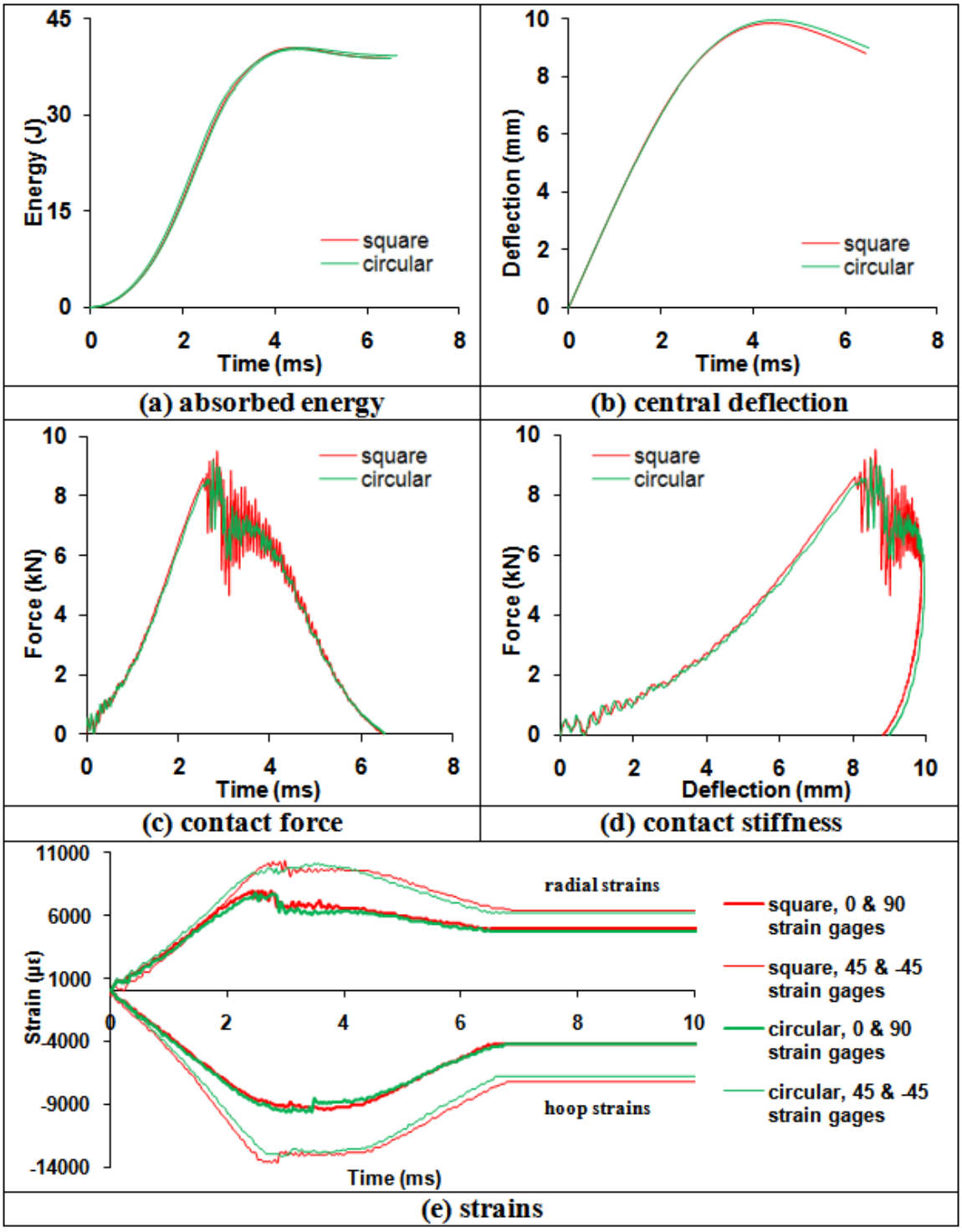

Fig.4.26. Comparison of the Impact responses between the square and circular cross-ply GLARE 5 (3/2) specimen under 40J impact energy.

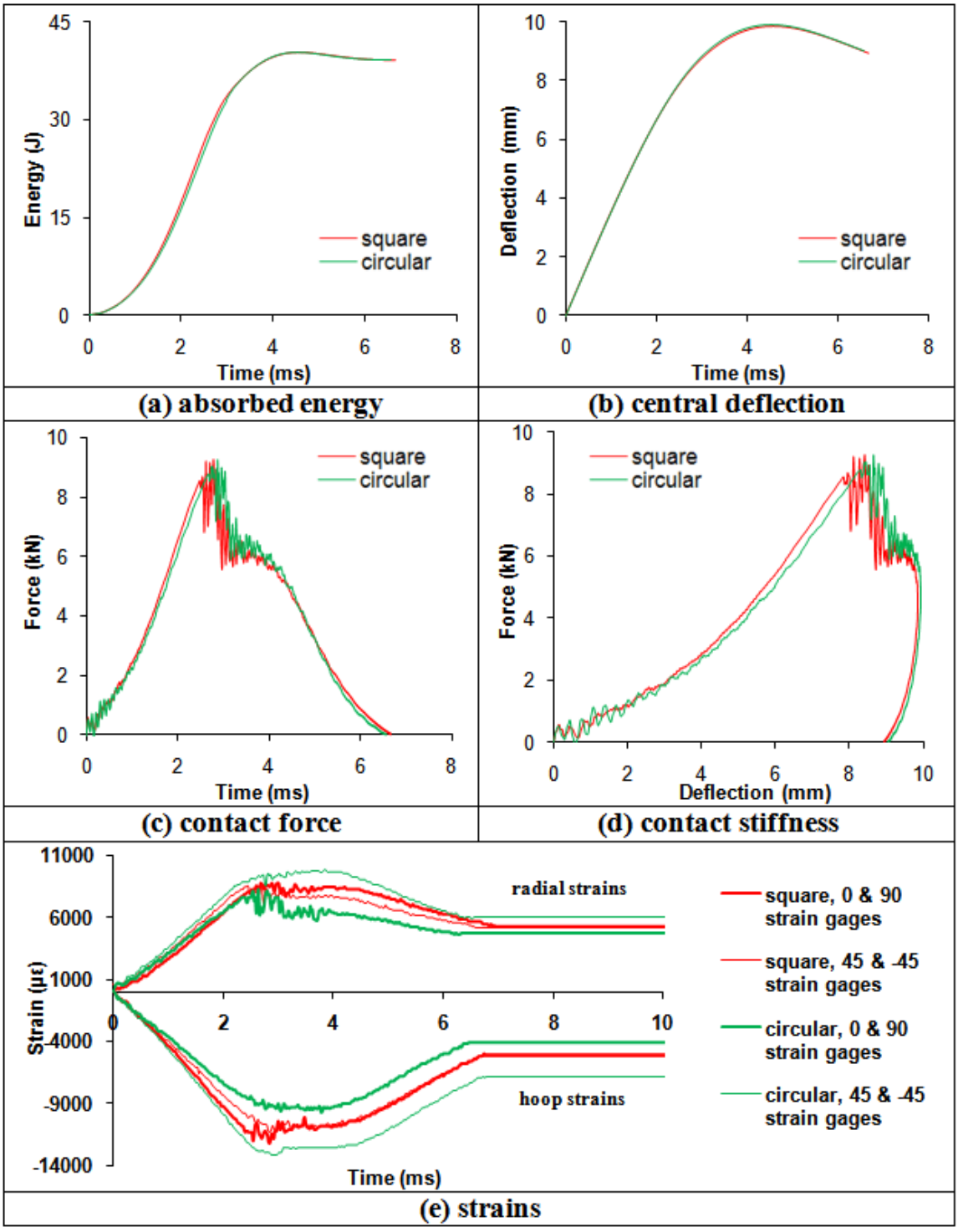

Fig.4.27. Comparison of the Impact responses between the square and circular angle-ply GLARE 5 (3/2) specimen under 40J impact energy.

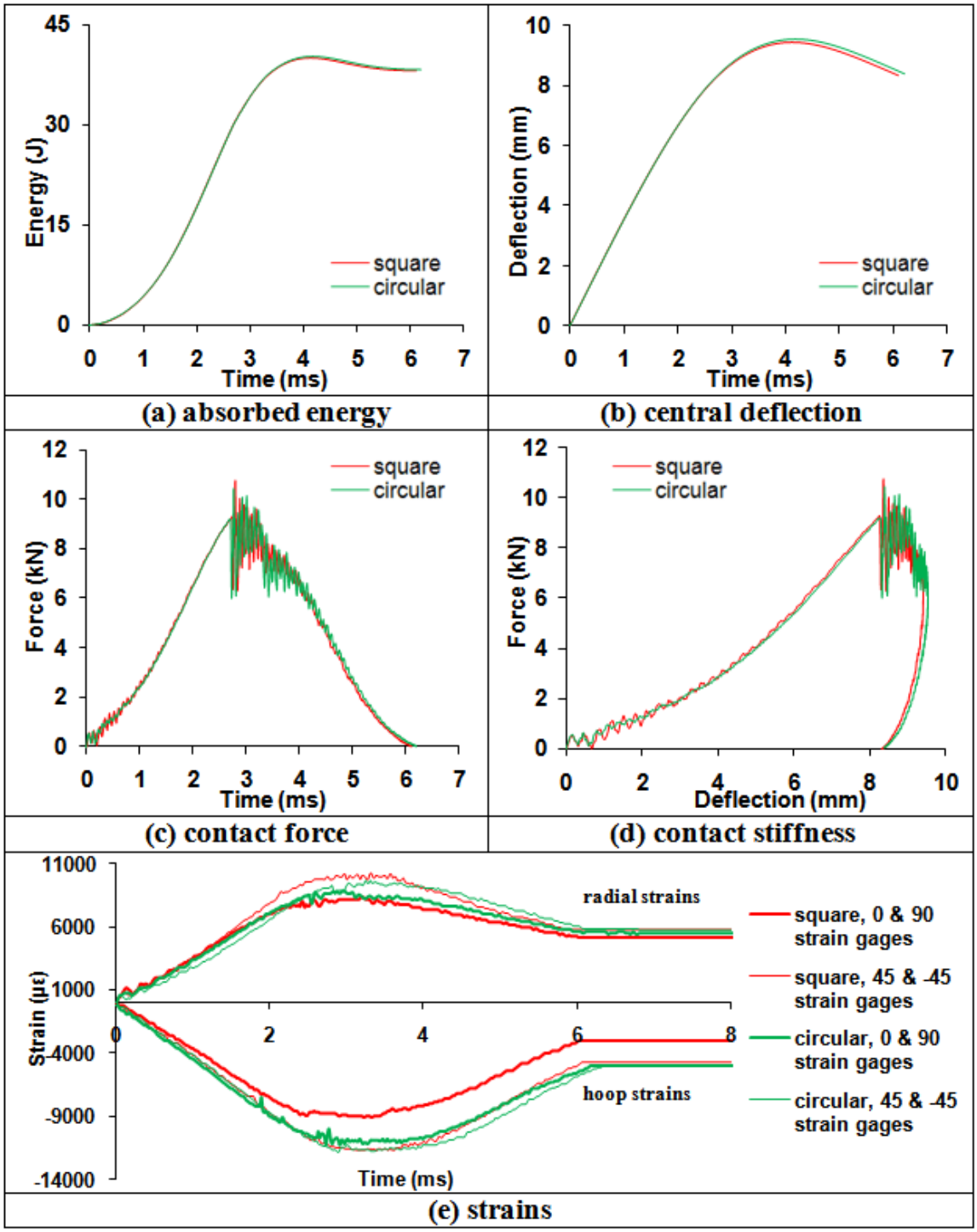

Fig.4.28. Comparison of the Impact responses between the square and circular quasi-isotropic GLARE 5 (3/2) specimen under 40J impact energy.

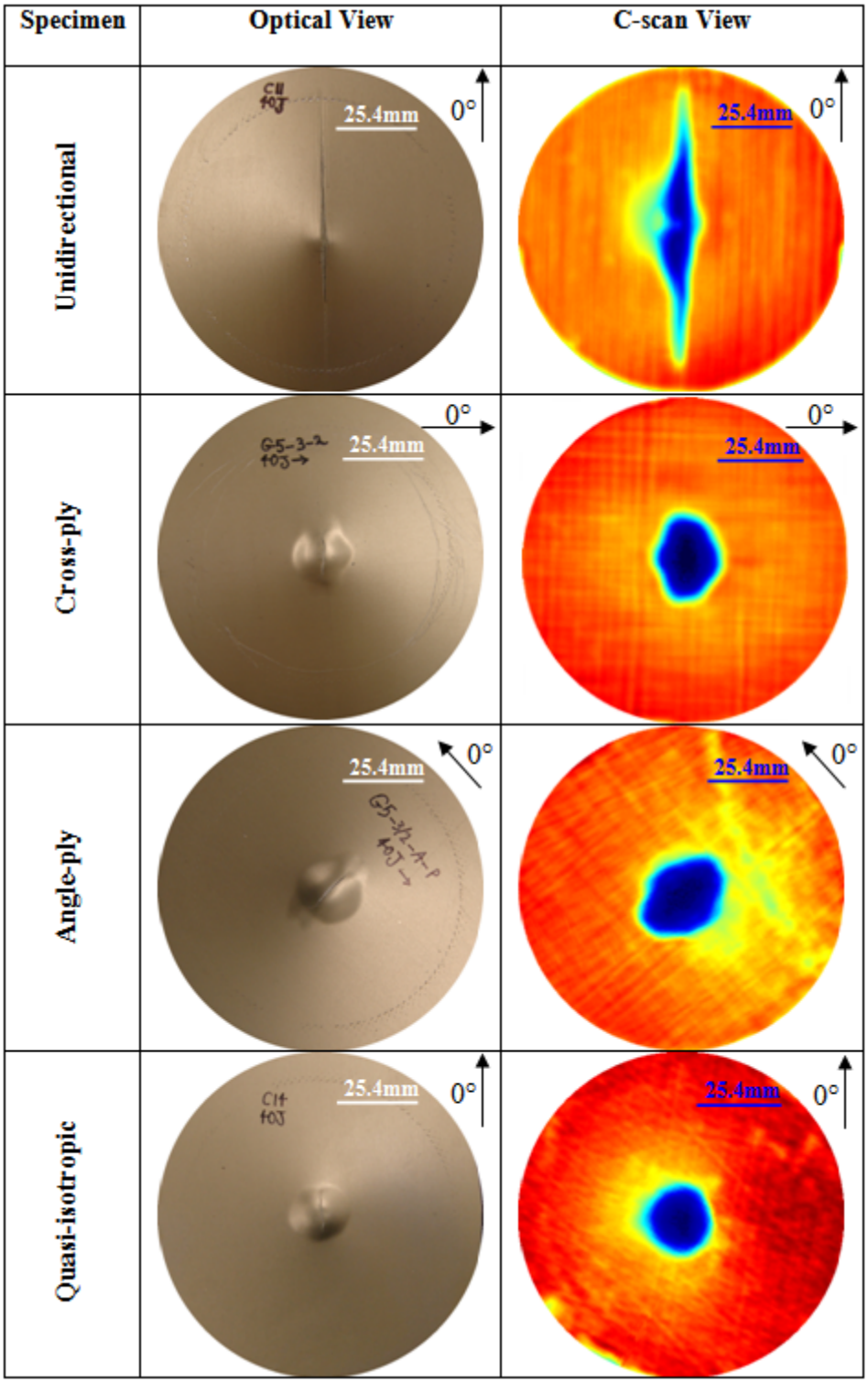

Fig.4.29. Back side (non-impacted) view and corresponding C-scan view of the GLARE 5 (3/2) circular specimens with various stacking sequences under 40J impact energy.

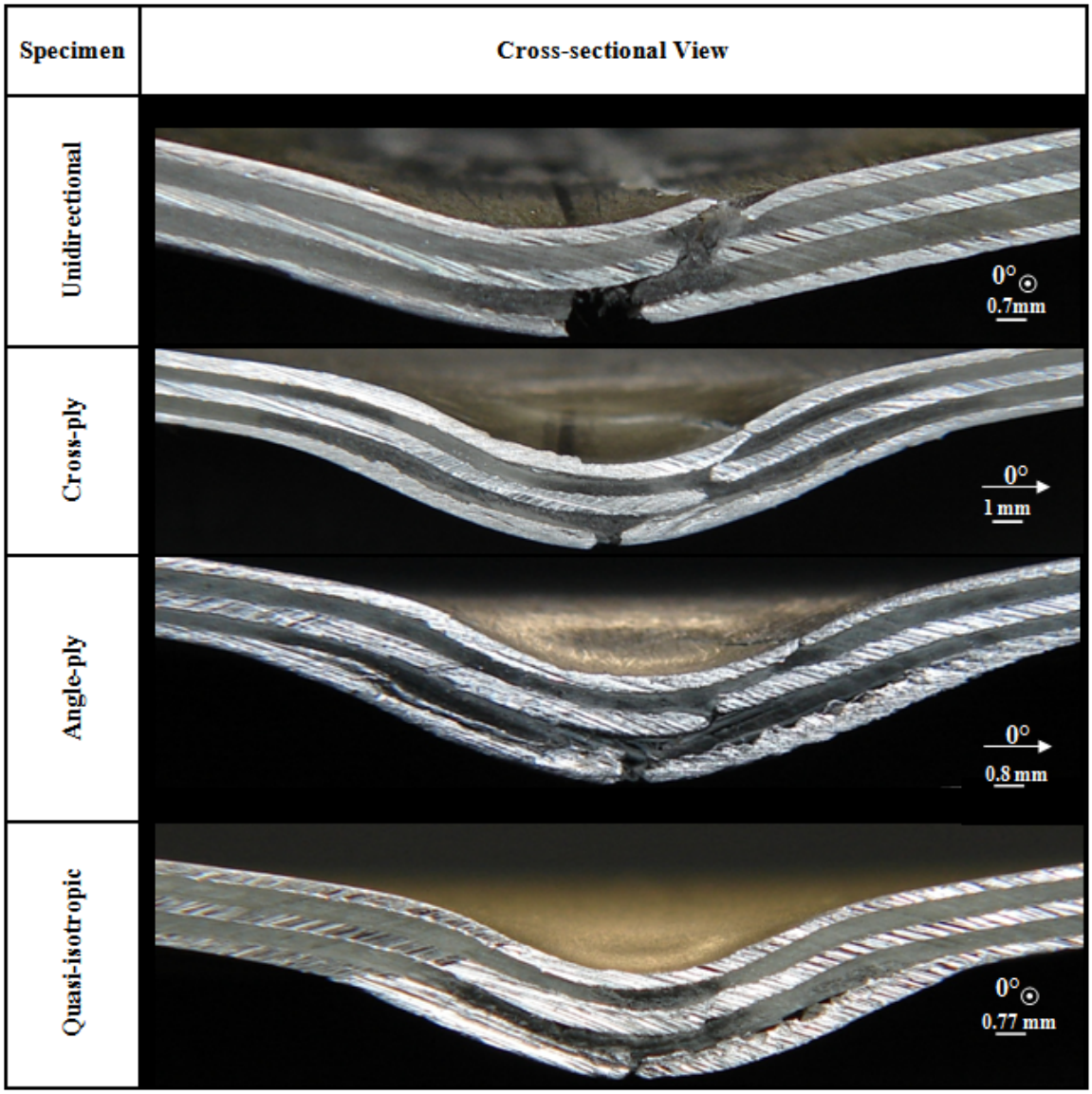

Fig.4.30. Cross-sectional view of the GLARE 5 (3/2) circular specimens with various stacking sequences under 40J impact energy. The symbol ⊙ means that the fiber direction is out of the plane.

Table4.4. Crack lengths and permanent deflections of the GLARE 5 (3/2) FMLs with various stacking sequences under 40J impact energy.

Stacking Sequence	Geometry	Crack Length in Outer Layer (mm)		Permanent Deflection (mm)
		Impacted Side	Non-impacted Side	
Unidirectional $[0°_4]$	Square	69	75	7.65
Cross-ply $[0°/90°]_s$	Square	9	18	6.75
Angle-ply $[\pm45°]_s$	Square	7	16	6.65
Quasi-isotropic [0°/±45°/90°]	Square	0	12	5.3
Unidirectional $[0°_4]$	Circular	83	83	7.7
Cross-ply $[0°/90°]_s$	Circular	8.5	16	6.8
Angle-ply $[\pm45°]_s$	Circular	8.5	16	6.8
Quasi-isotropic [0°/±45°/90°]	Circular	0	12	6.1

Based on the discussion above, by introducing circular, rather than square, geometry as the outer perimeter of the specimens, some differences were induced in the damage patterns as well as impact behaviors. These were due to the geometry and the relative anisotropy of the specimen with respect to the specimen clamping.

4.7. Conclusions

This study presented an experimental investigation on the impact response of the GLARE 5 composite materials considering the effects of thickness, impactor mass, stacking sequence and geometry using a drop weight impact tester. The following remarks can be concluded from this study.

- Failure modes changed by increasing the panel thickness. Both fiber critical and aluminum critical behaviors were seen depending on the thickness of the panel. For the thinner GLARE 5 specimens, i.e. with the (3/2) configuration, the major failure type was debonding in the non-impacted side followed by fiber breakage and splitting, as well as the aluminum layers fracture; whereas for GLARE 5 (2/1) after debonding, aluminum failure occurred. For the thicker GLARE 5 specimens, i.e. with (5/4) and (6/5) configurations, delaminations occurred near the impacted side at relatively lower impact energies. More severe damage including failure in the bottom aluminum layers as well as fiber breakage/splitting in the prepreg composite lamina were induced on the non-impacted side when higher impact energies were applied. Also due to localized stress concentrations under the higher impact energies, cracks were created on the impacted face.

- The area of the entire damage contour increased with increasing impact energies. Typically under the same impact energy as the specimen became thicker the area of the entire damage contour increased. By thickening the panel, its capability of absorbing impact energy enhanced while the maximum central deflection abated. In addition, the peak contact force as well as the force rate increased while the

duration of contact shortened. Under the same impact energy, by reducing the impactor mass, the contact force escalated and also the initial slope of the force deflection stiffened. For the same panel with the same thickness, the damage pattern would be different under the same impact energy but with different impactor mass.

- Only the profile of entire damage zone could be detected through ultrasonic C-scan. The cross sectioning technique can provide the details of damage inside of the GLARE 5 composite materials. Under the same impactor shape, impact energy cannot be used as the sole parameter to scale damage. Impactor mass or velocity also has to be taken into account.

- Threshold cracking energy varied parabolically with respect to the impact velocity, MVF and the specimen thickness.
- By increasing the metal volume fraction of the panels, the threshold cracking energy decreased parabolically. Furthermore, for the same MVF value, the cracking energy increased as the impactor mass increased. However this was relatively negligible for the thinner panels, i.e. (2/1) and (3/2).
- By increasing the panel configuration, the velocity required to meet the threshold cracking energy condition increased parabolically for both impactor masses. In addition, under the same impact velocity, the threshold cracking energy increased by increasing the impactor mass.
- The threshold cracking energy increased as the thickness of the specimen increased. Moreover, for a given panel thickness, the energy required to induce a

crack in the bottom aluminum layer increased by increasing the impactor mass. This was relatively pronounced for the panels with thicknesses above 2 mm.

- By reducing the mass of the impactor, but maintaining the same impact energy, the permanent central deflection increased. This means that the panel with lighter impactor mass will reach the perforation limit faster than the heavier one.

- GLARE 5 made of unidirectional fibers had the worst impact resistance; followed by cross-ply and angle-ply configurations, while the quasi-isotropic lay-up showed the best resistance to impact.

- The damage patterns and impact behaviors were almost invariant to the change in the specimen geometry. However, when conducting a drop-weight test using the conventional specimen geometry of a square outer perimeter and a circular inner clamp, the result will be affected by the fiber orientation of the specimen due to the relative material anisotropy with respect to the clamp fixture of the drop-weight apparatus. It is recommended that composite specimens with a circular outer perimeter and a circular inner clamp should be used instead to avoid the problem.

CHAPTER 5: MEASUREMENT OF PROJECTILE VELOCITIES IN A HIGH-SPEED GAS GUN

The ballistic impact tests were conducted using a high-speed gas gun (Fig. 3.5). Helium and compressed air were used as the propellants. Target inside the specimen container was placed at two different positions away from the gun muzzle (Fig. 3.6). As described in Chapter 3, three different techniques, namely: diode-laser/amplified-photodiode, chronograph and high-speed camera, were used for measuring the projectile velocities.

5.1. Effect of target position from the gun muzzle

In order to study the effect of target position from the gun muzzle on velocity measurement, two different target positions were chosen: 50.8 cm (20″) and 93.98 cm (37″) away from the gun muzzle (Fig. 3.6).

Figure 5.1 shows the comparison of the incident speeds of the bullet measured using the optoelectronic technique versus the high-speed camera method for both setup configurations. As the test results suggested, they were best fitted with linear regression lines (Fig. 5.1). As is obvious from the figure, the bullet speed obtained from the high-speed camera was relatively higher than the one measured by the optoelectronic technique near the end of the gun barrel for both configurations. In other words, it could be stated that as the bullet emerged from the gun barrel, it was further accelerated along its trajectory before hitting the target. This phenomenon could be explained by intermediate ballistics, which is the study of the transition from internal to external ballistics occurred in the vicinity of the gun muzzle [58].

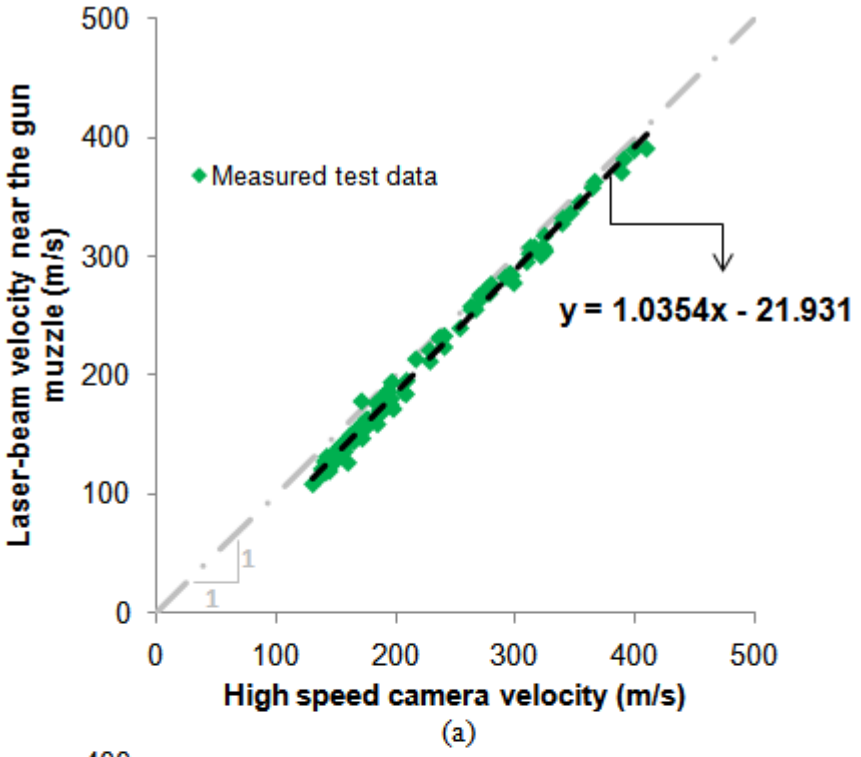

Fig.5.1. Comparison of the incident projectile speed measured at the optoelectronic paths near the gun muzzle *vs.* the high-speed camera for: (a) setup configuration #1, (b) setup configuration #2. In the equations, x and y stand for the high-speed camera and laser beams near the gun muzzle velocity, respectively.

Figure 5.2 depicts the superimposed experimental-results obtained from the two setup configurations. As is apparent, the experimental trends of both configurations coincided with each other with negligible differences despite the fact that different propellants and target distances were used. This implies that the amount by which the projectile was accelerated was invariant with respect to changes in target distance and propellant gas.

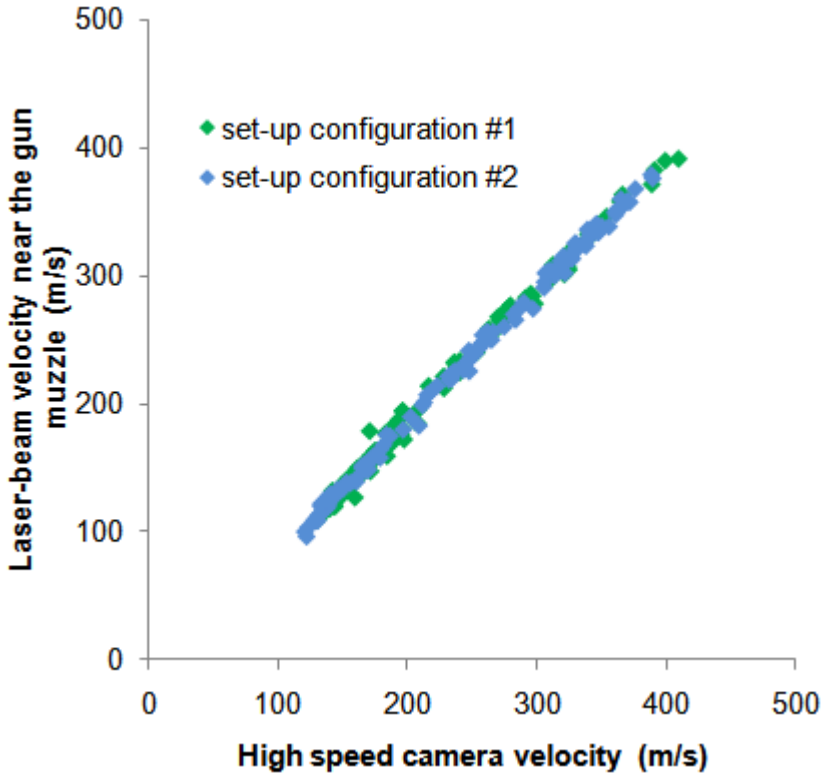

Fig.5.2. Superposed experimental-results of the incident projectile speed measured at the optoelectronic paths near the gun muzzle *vs.* the high-speed camera for both setup configurations.

Figure 5.3 shows the comparison between the projectile speed measured from the chronograph #1 and the high-speed camera before hitting the target. In the figure, the resultant trend line implies that the bullet strike speed determined by the chronograph was higher than that obtained from the high-speed camera. Furthermore, most of the test data were along the bisection line, i.e. y=x, implying that both high-speed camera and

chronograph techniques yielded in approximately close values in measuring the bullet speed. However, scattering of the results obtained from the chronography suggests that chronography may not be always trustable. As mentioned before, a set of chronograph was not used for the setup configuration #2 due to the lack of space between the muzzle and the target.

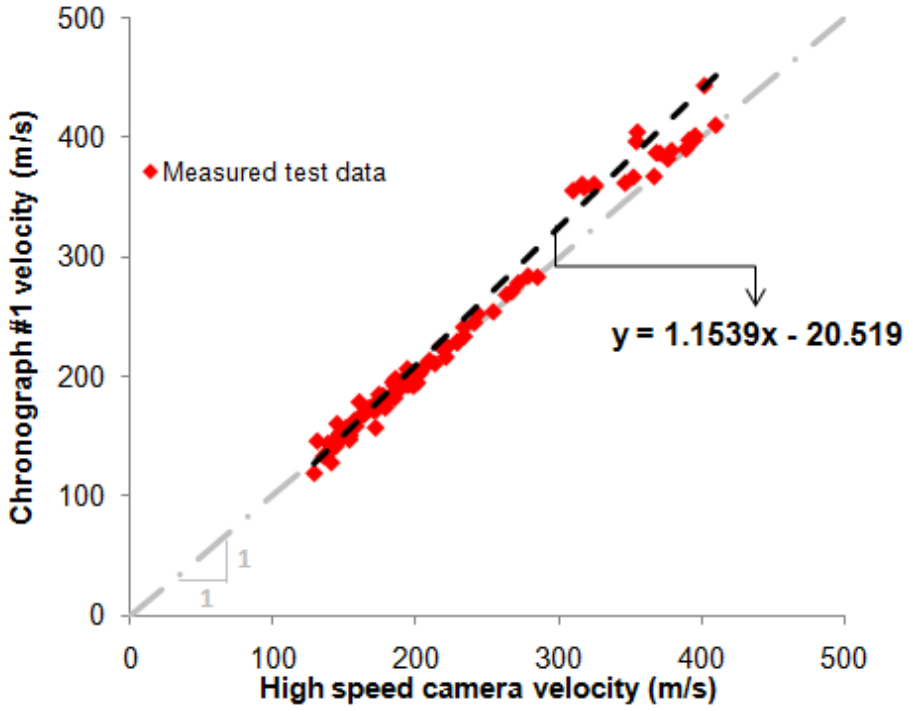

Fig.5.3. Comparison of the projectile-speed measurements using the chronograph #1 *vs.* the high-speed camera (setup configuration #1). In the equation, x stands for the high-speed camera velocity while y stands for the chronograph #1 velocity.

The bullet residual velocity was determined by the high-speed camera and the chronograph which was located after the target for both configurations (Fig.3.11). The chronograph #2 in the setup configuration #1 failed to measure the speed of the bullet in 90% of the tests conducted in this study. The remaining 10% are not plotted here. The failure was mainly due to the pre-mature triggering of the chronograph caused by the disturbance of some suspensions, e.g. dust. Figure 5.4 depicts the comparison of the

residual speed of the bullet measured from the chronograph versus the high-speed camera for the setup configuration #2.

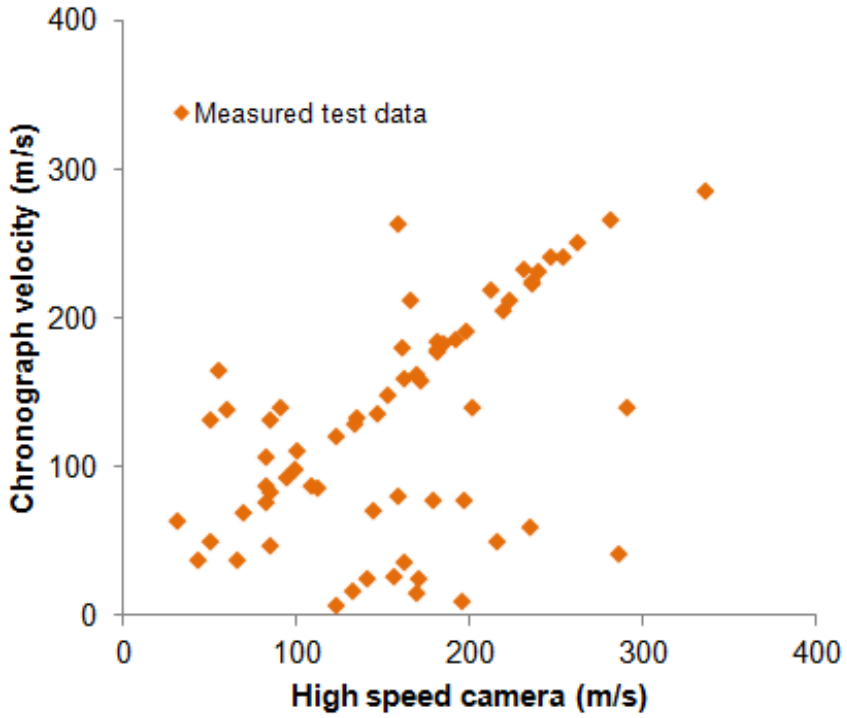

Fig.5.4. Projectile-residual-velocity measurements using the chronograph and high-speed camera (setup configuration #2). In the equation, x stands for the high-speed camera velocity while y stands for the chronograph velocity.

The correlation between the chronograph and high-speed camera data is quite scatter, indicating that the chronograph might be triggered by an object other than the bullet. In addition, the bullet may show different motions after impacting the target. This would cause some errors in measuring the velocity of a projectile as discussed in Section 5.3 later. For instance, as shown in Fig. 5.6, the chronograph was triggered by an ejected plug from the target despite the fact that the projectile did not perforate the target. It can be concluded that chronographs do not always yield in reliable results for determining the velocity of a projectile, especially for obtaining the residual velocities.

5.2. Intermediate ballistics

It was experimentally shown above that as the bullet emerged from the gun barrel, it was further accelerated along its trajectory before hitting the target. This phenomenon can be explained by intermediate ballistics which is the study of the transition from internal to external ballistics occurred in the vicinity of the gun muzzle [58].

Figure 5.5 illustrates shock wave formation before and after projectile exit. As the projectile accelerated along the bore, it pushed ahead of it a column of air augmented by any leakage of propellant gases past the projectile. A shock wave formed just ahead of the projectile, traveled along the bore, and was released as a near-spherical precursor blast shock at the muzzle, as shown in Fig. 5.5(a). Once the outflowing air velocity was sufficient, a small bottle shock would form about the muzzle. The projectile would then emerge, and once the projectile gas seal had passed the muzzle, the high pressure propellant gases would be released into the atmosphere generating a powerful blast shock, which was initially highly non-spherical due to the presence of the projectile and the high velocity flow of the propellant gases. The propellant gases rapidly expanded, accelerating to velocities much greater than that of the projectile, so that shock waves formed around the base of the projectile, rather as though the projectile was moving backwards (Fig. 5.5(b)). This apparent reverse gas flow provided slight additional acceleration of the projectile for several calibers distance beyond the muzzle.

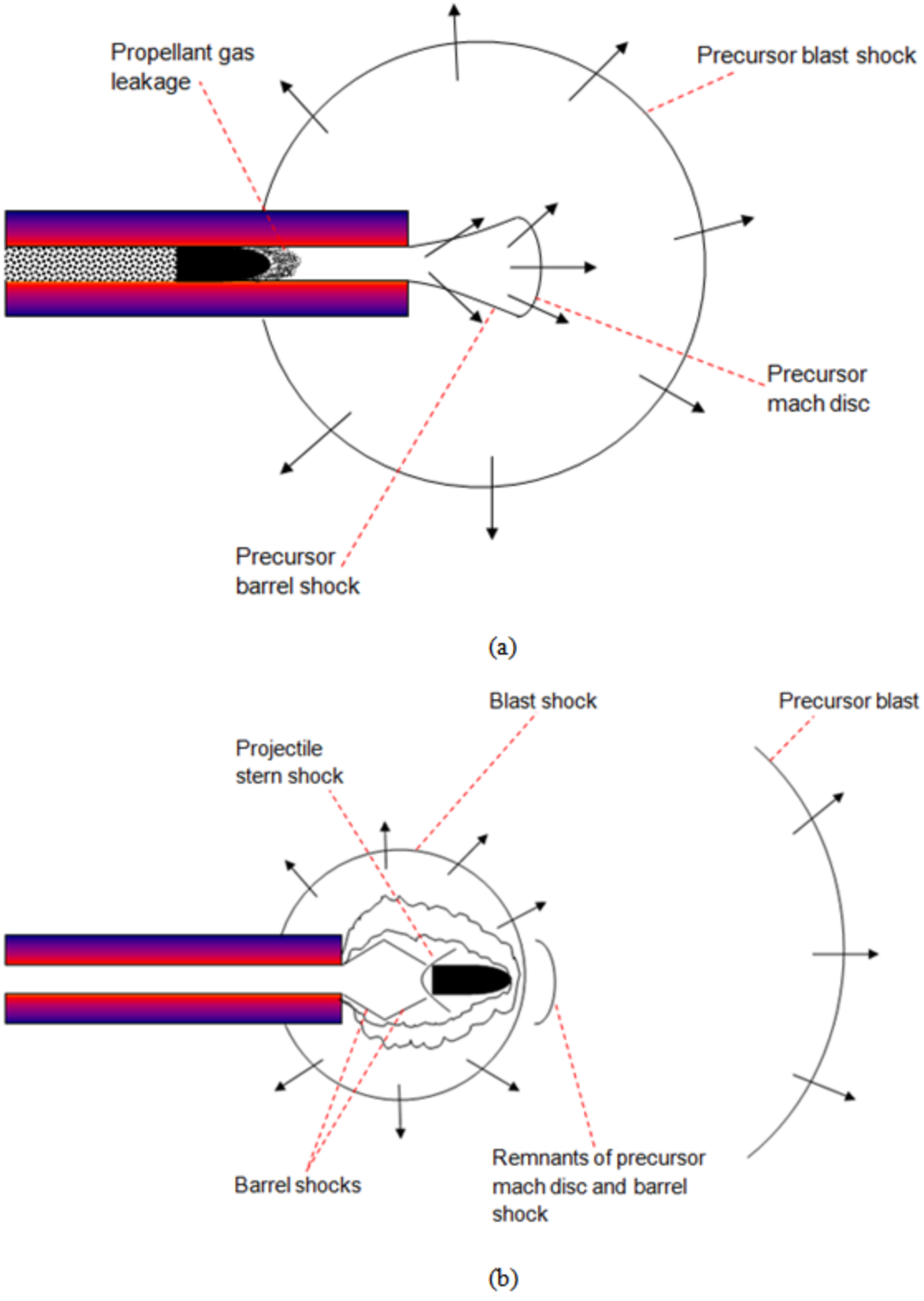

Fig.5.5. (a) Shock wave formation before projectile exit, (b) the initial formation of shock waves shortly after projectile exit.

5.3. Possible errors in measuring the projectile velocity

As mentioned before, it is necessary to observe the bullet motion along its ballistic trajectory before and after hitting the target in order to determine the strike and residual velocities accurately. Depending on the projectile incident velocity, there are two cases that were observed, namely: (a) partial penetration and (b) full penetration. In the case of partial penetration, the bullet either rebounded off the target or got stuck in it. If the bullet got stuck in the target it is apparent that its residual speed was zero. In the case of bullet rebounding off the target, chronograph would fail in measuring the speed of the bullet since it was already triggered by measuring the incident speed of the bullet. On the other hand, if it had the capability of triggering, the results obtained would not be always reliable. There are three reasons for this. First, if the bullet rebounding speed was not enough, then the bullet could not traverse the chronograph infrared optical screens and hence the chronograph would not trigger. Secondly, a particle rather than the bullet might cause the triggering of the chronograph. Thirdly, the rebounding motion of the bullet was not always along a straight line, e.g. it could be tilted, tumbled, dropped steeply, moved along a curved path due to the gravity, etc. For instance, Fig. 5.6 shows a typical example of the projectile rebounding off the target in a tumbling motion. As is apparent, the necessity of recording the projectile motion is obvious in accurate determination of a projectile rebound velocity.

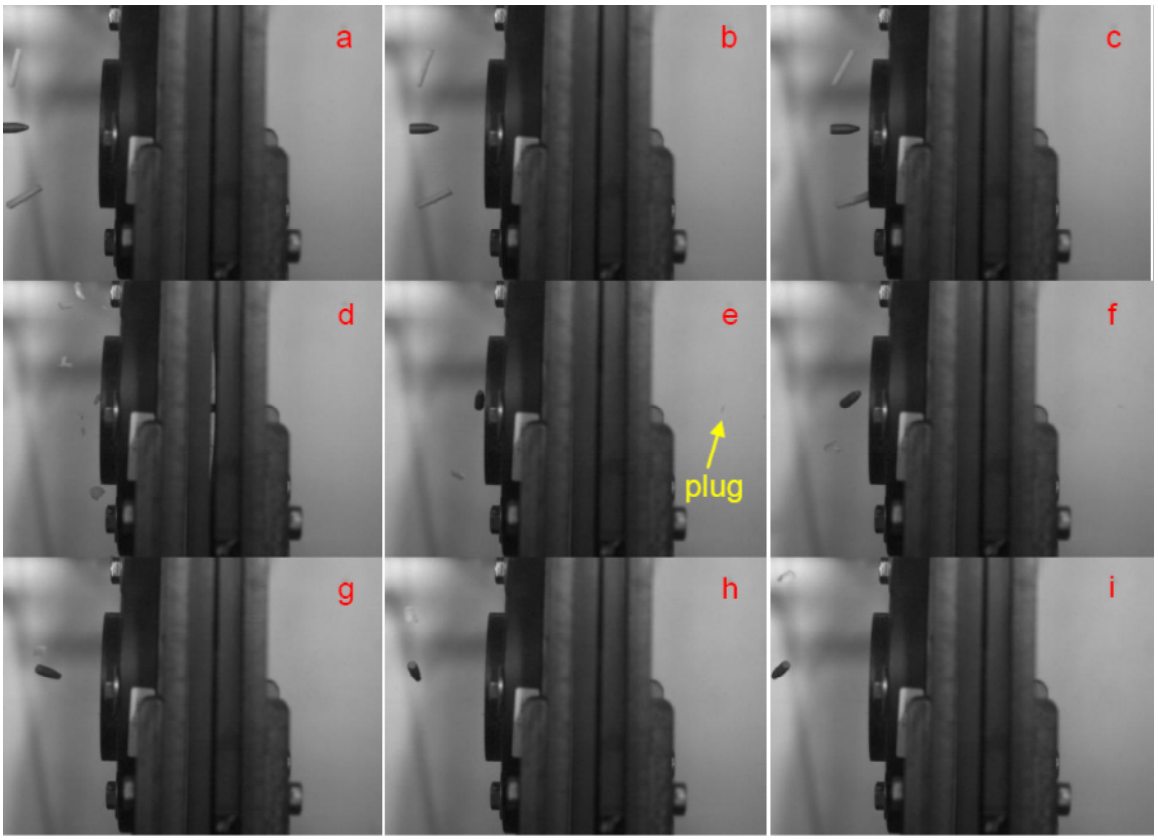

Fig.5.6. A typical example of the projectile rebounding off the target in a tumbling motion.

Figures 5.7 through 5.10 illustrate some different bullet positions in which it might take after perforating a target. An example of a bullet exiting a target along a straight line, i.e. the angle of yaw≈0, is given in Fig. 5.7. Figures 5.8 and 5.9 depict the bullet emerging the target with two different yaw angles, i.e. 2.73° and 15.20°, respectively. It is evident from the figures that as the angle of yaw increases, the magnitude of the V_x component of the velocity vector V decreases. As a consequence the magnitude of the V_y component increases. It should be mentioned that by relying only on chronographs for the determination of projectile velocities, the obtained values would not be accurate for the cases in which the projectile perforated the target. Since chronographs would trigger based on the first object passed through its infrared screens regardless of what the type of

the object was. In other words, the obtained values are insensitive to the projectile states, e.g. yaw angle, tumbling, etc.

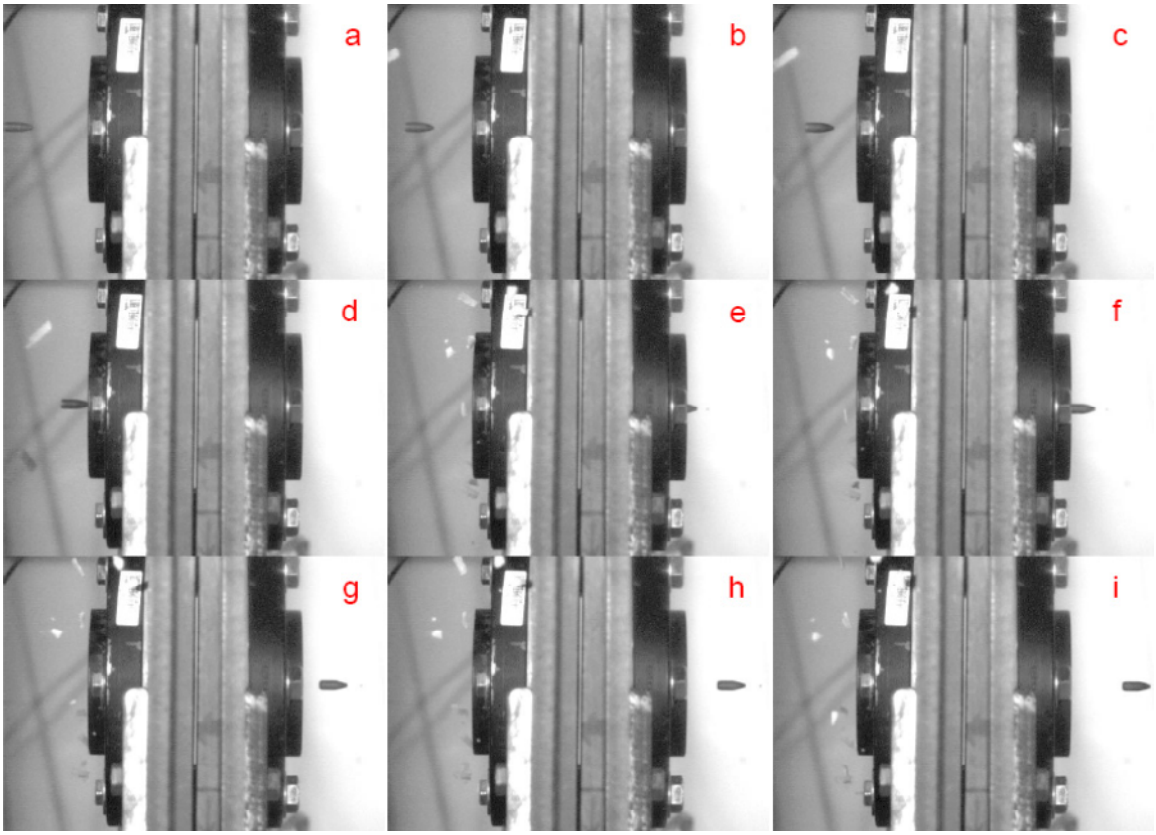

Fig.5.7. An example of the bullet exiting a target along a straight line.

In addition, by considering the values obtained from chronographs, the ballistic limit velocities, kinetic energies, etc. would not be estimated correctly. For instance, in the study by Goldsmith et al. [93], they reported that the ballistic limit increased with increasing yaw angle. Figure 5.10 depicts the bullet departing the target in a tumbling motion.

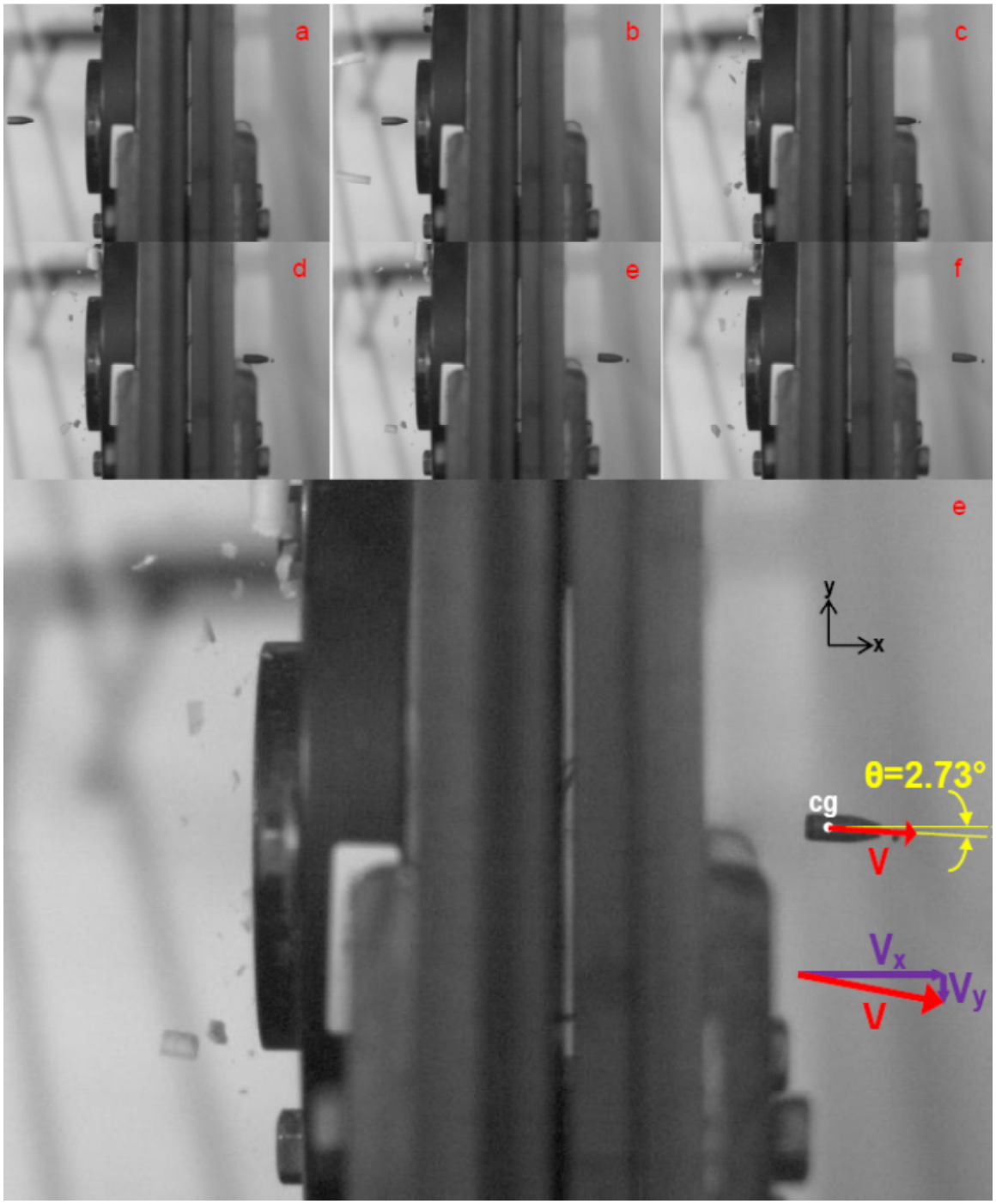

Fig.5.8. An example of the bullet emerging the target with a smaller yaw-angle of 2.73°.

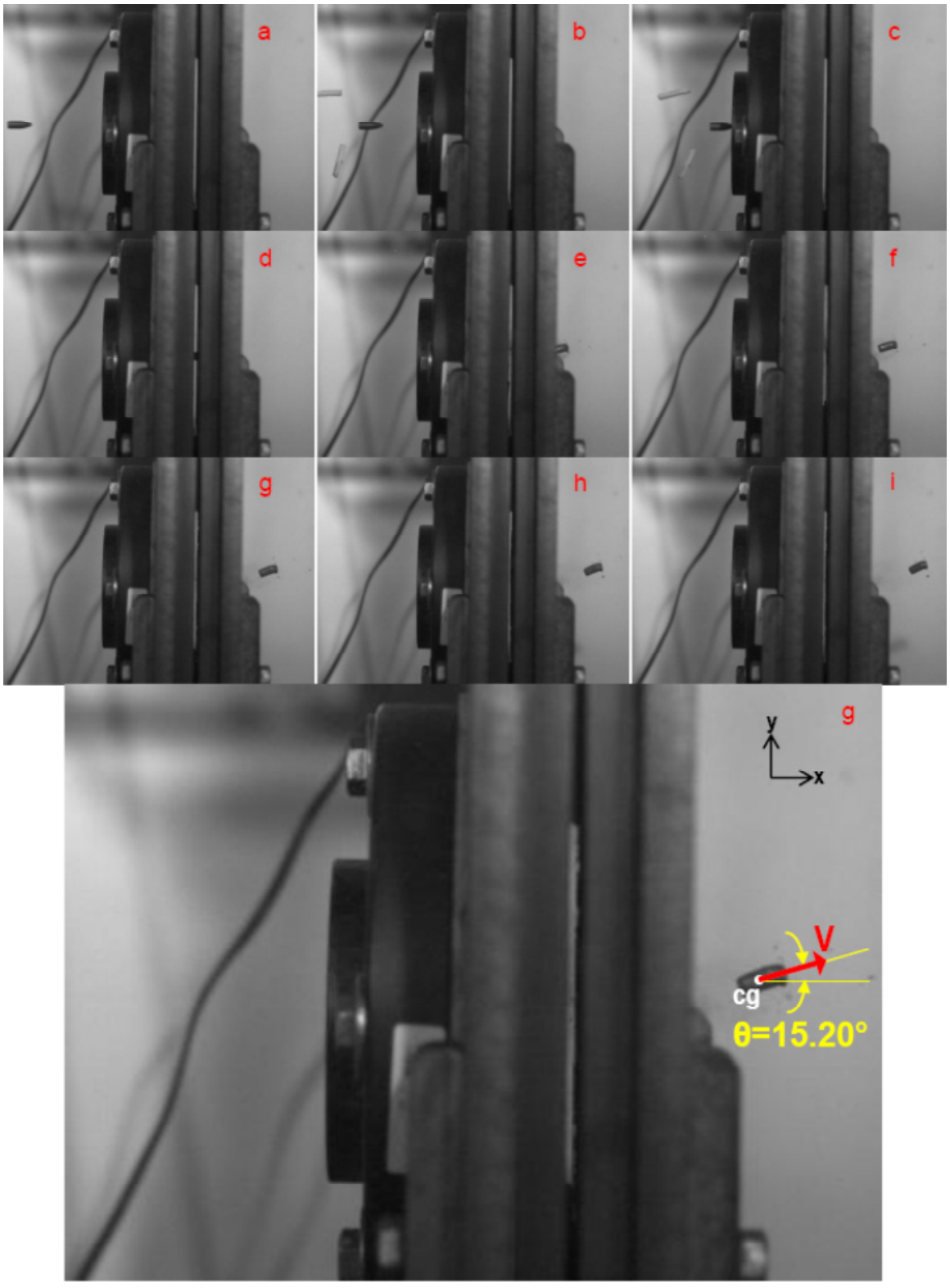

Fig.5.9. An example of the bullet exiting the target with a larger yaw-angle of 15.20°.

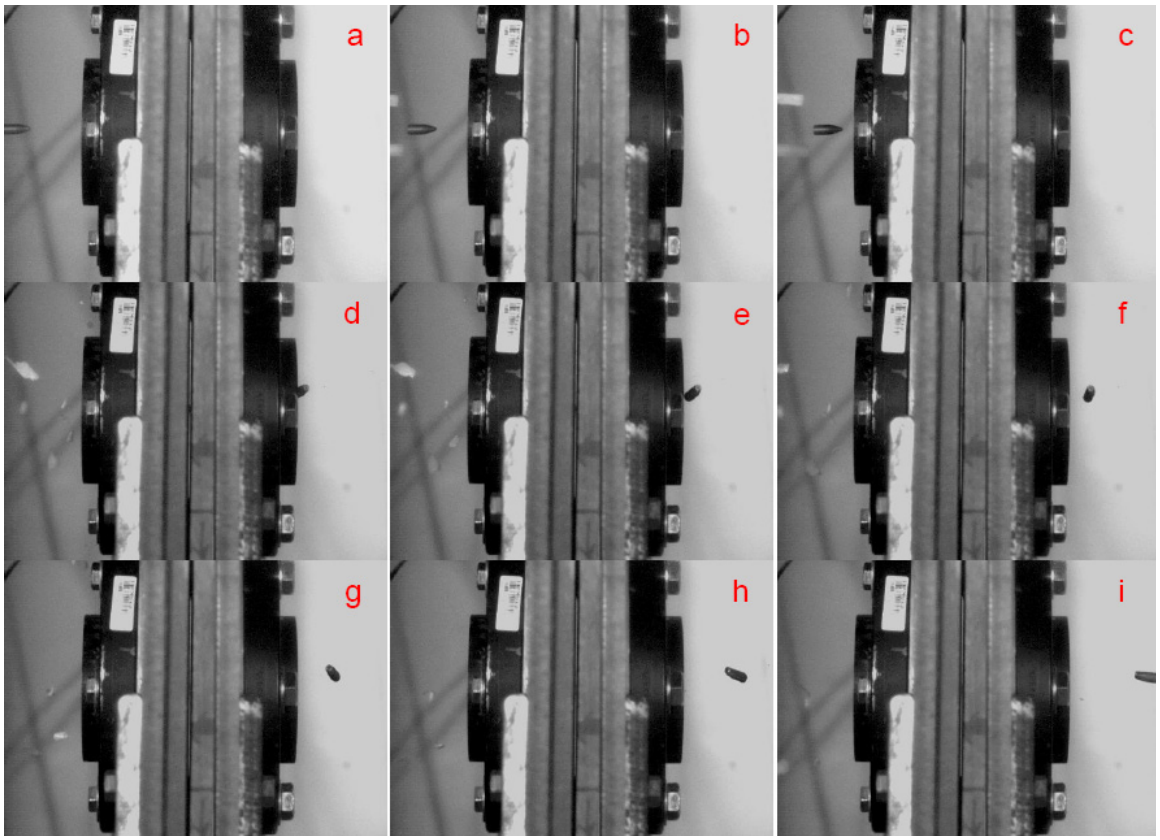

Fig.5.10. An example of the bullet departing the target in a tumbling motion.

Based on Figs. 5.7 through 5.10, the significance of using the high-speed camera can be revealed in the determination of the residual velocities and subsequently accurately obtaining the residual kinetic energy. Moreover, the degree of complexity in the determination of velocity of a projectile would increase for non-normal impact studies, e.g. oblique impact studies, due to the increase in the sophistication of the projectile motion. Therefore, monitoring the projectile motion becomes very important. As a consequence, high-speed camera would be very helpful in such situations.

5.4. Determination of the ballistic limit velocity (V_{50})

After determining the speeds of the bullet before and after impact, the incident projectile velocity (before impact) was plotted versus the residual velocity (after impact) for each

type of the specimen according to Table 3.1 (refer to Chapter 6 for more ditails). The experimental data could then be fitted by least-square regression according to the classical Lambert-Jonas' equation [94] for the positive residual velocity values:

$$V_R^P = A(V_I^P - V_{50}^P) = A \cdot V_I^P - B \tag{5.1}$$

where A and B are two regression coefficients and P is a power. V_R and V_I are residual and incident velocity of the projectile, while V_{50} is the ballistic limit velocity, which is defined as the velocity required for a projectle to perforated a piece of armor 50% of the time. Equation (5.1) is the generlized form of an equation obtained from the work-energy principle for the ballistic impact of a rigid projectile and the equivalent mass of the ejecta. It should be noted that when P = 2, Eq. (5.1) is known as the Recht-Ipson's equation [95]. In the study by Ben-Dor et al. [96], they showed that the accuracies of both Lambert-Jonas and Recht-Ipson's model were approximetly the same.

For each specimen type (Table 3.1), several P values were chosen according to its V_I~V_R experimental trend. Subsequently, the ballistic limit velocity (V_{50}) was determined based on the specimen experimental trend and classical Lambert–Jonas' equation, Eq. (5.1). These issues are addressed in Chapter 6.

5.5. Conclusions

This study presented an experimental investigation on different techniques for measuring the velocity of a projectile. The effects of the target position, propellant gases and possible errors in velocity measurements of a projectile were discussed. The following remarks can be concluded from this study.

- It was found that the projectile was further accelerated along the ballistic trajectory after emerging from the gun barrel. The amount of the acceleration was negligible by changing the target position from the gun muzzle and the type of propellants (helium or compressed air). Without considering the further acceleration of the projectile along the projectile trajectory, the projectile speed and in general ballistic limit velocities would be underestimated.
- In general, chronography did not give consistent and reliable results for measuring the speed of a projectile. This was due to the triggering of the chronograph caused by some suspensions, e.g. dust, other than the bullet itself. On the other hand, in the case of triggering the chronograph by the projectile, the velocity measurements obtained would not be reliable due to the possibility of different projectile orientations after hitting the specimen. Hence, monitoring the projectile motion became very important in the calculation of residual kinetic energy.
- Based on this study, the high-speed camera technique yielded the most reliable and accurate results in measuring the projectile speed. On the contrary, chronographs failed most of the time to accurately measure the projectile speed; while the laser-based optical technique gave lower estimates of impact velocity.
- The classical Lambert-Jonas' equation was very useful in obtaining the ballistic limit velocities, especially for the cases where obtaining lower incident velocity experimentally was difficult.

CHAPTER 6: BALLISTIC IMPACT TESTS ON GLARE 5 FMLS

High-velocity impact is dominated by inertial forces, wave propagation and changes in material stiffness, strength and fracture energy due to high strain rate [97]. Figure 6.1 shows three distinct types of impact regimes for monolithic panels. In low-velocity impact, the panel span (shown with radius a) and boundary conditions affect the amount of energy that is absorbed before perforation (Fig. 6.1(a)). In high-velocity impact, the panel span and boundary conditions are irrelevant in the impact analysis because perforation occurs during wave propagation and before stress waves can reach the panel boundaries.

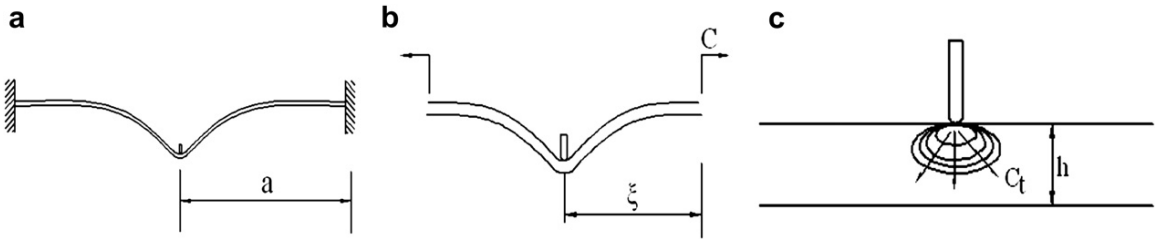

Fig.6.1. Classification of impact regimes: a) low-velocity, b) high-velocity and c) ballistic impact [97].

As indicated in Fig. 6.1(b), the panel deformation is localized to a region (radius ξ) determined by the propagation speed of waves C. Some of the initial kinetic energy of the projectile is consumed in panel deformation and fracture. The remaining initial kinetic energy of the projectile results in residual velocities of the projectile and debris after panel perforation. With increasing projectile speed, the extent of panel deformation ξ decreases because of panel perforation. If the impact velocity is very high, perforation of the panel may occur without any panel deformation. This situation is termed ballistic impact and as shown in Fig. 6.1(c), is dominated by the propagation of through-thickness

waves. The through-thickness wave speed C_t and plate thickness h are important parameters in ballistic impact studies [97].

In this study, the ballistic impact tests were conducted at room temperature using a high-speed gas gun (Fig. 3.5). Helium and compressed air were used as the propellants. As described in Chapter 5, three different techniques were considered for measuring the projectile velocities at different locations.

Ballistic impact tests were conducted on the GLARE 5 FMLs with two different geometrical shapes, namely: 254 mm by 25.4 mm (10″×1″) beam and 152.4 mm by 101.6 mm (6″×4″) plate. The specimens with various thicknesses and stacking sequences (Table 3.1) were impacted by a 0.22 caliber copper bullet at the center. The plate specimens were secured by clamping 25.4 mm (1″) of each end (Fig 3.7(a)), while the beam specimens clamped over a length of 50.8 mm (2″) from each side (Fig. 3.7(b)). It should be noted that the specimen fixture was extra supported by four C-clamps inside the specimen container (Fig.3.6). This would provide a fixed-fixed boundary condition at both ends of the clamped specimen. Two strain gages, marked as SG-1 (strain gage #1) and SG-2 (strain gage #2) were mounted on the impact side of the beam specimen. The strain gages were located at 25.4 mm (1″) and 38.1 mm (1.5″) away from the center (Fig. 6.2). Once an experiment was completed, only the plate specimens were ultrasonically C-scanned. The optical pictures of impacted specimens were taken. Finally, the specimens were cut transversely along the center to reveal the internal damage.

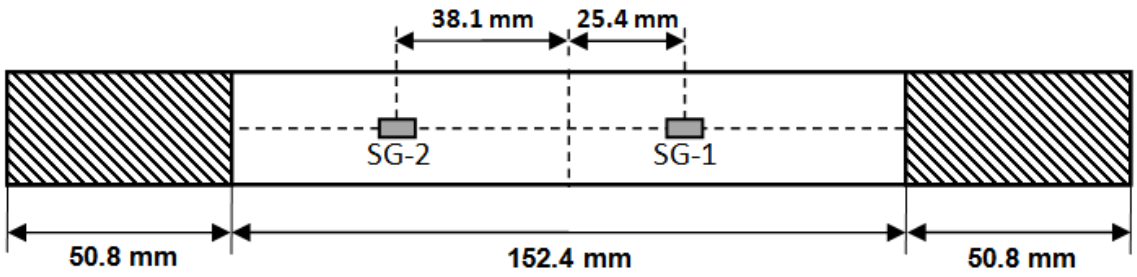

Fig.6.2. A typical composite beam specimen mounted with two strain gages on the ballistic impact side.

6.1. Ballistic impact tests on GLARE 5 FML beams

In this section, the impact response of the GLARE 5 FML beams was studied. The effects of specimen thickness and stacking sequence were considered. These effects are discussed in the following subsections.

6.1.1. Effect of specimen thickness

The cross-ply GLARE 5 panels with different thicknesses were cut into 254 mm by 25.4 mm (10″×1″) beam specimens to assess the thickness effect. The range of thickness is from 1.117 mm (0.044″) of GLARE 5 (2/1) up to 4.368 mm (0.172″) of GLARE 5 (6/5). After determining the speeds of the bullet before and after impact, the incident projectile velocity (before impact) was plotted versus the residual velocity (after impact) for each specimen type according to Table 3.1. The experimental data was then fitted by least-square regression according to the classical Lambert-Jonas' equation (Eq. 5.1) for the positive residual velocity values. Figures 6.3 through 6.7 depict variation of residual velocity versus incident velocity for the GLARE 5 FML beams with (2/1), (3/2), (4/3), (5/4) and (6/5) configurations, respectively. In the figures, experimental data are specified by a solid diamond symbol and the Lambert-Jonas' curves with different P values are shown by dashed lines. The intersection of the Lambert-Jonas' curve with the incident-

velocity axis was considered as V_{50} for a given P value. Then, the average V_{50} value and its variations were calculated. As is apparent from the figures, by increasing the specimen thickness, V_{50} also increased. The resultant V_{50} for each specimen configuration is shown in Fig. 6.8, which depicts variation of ballistic limit with respect to the panel thickness for the cross-ply GLARE 5 beam specimens. In the plot, the average ballistic limit and its variation range are denoted by a solid diamond and deviation bar for each panel thickness, respectively. It is apparent that by increasing the panel thickness, the ballistic limit also increased with a parabolic trend. This was different from the findings in Refs. [72,73] that the ballistic limit varied linearly with panel thickness. However, within the velocity range tested in this study, the curvy parabolic trends do not deviate too much from a linear line. Metal volume fraction versus ballistic limit for the cross-ply GLARE 5 specimens with different thicknesses is given in Fig. 6.9. It is worth noting that as the number of prepreg laminated layers increased, the ballistic limit also escalated.

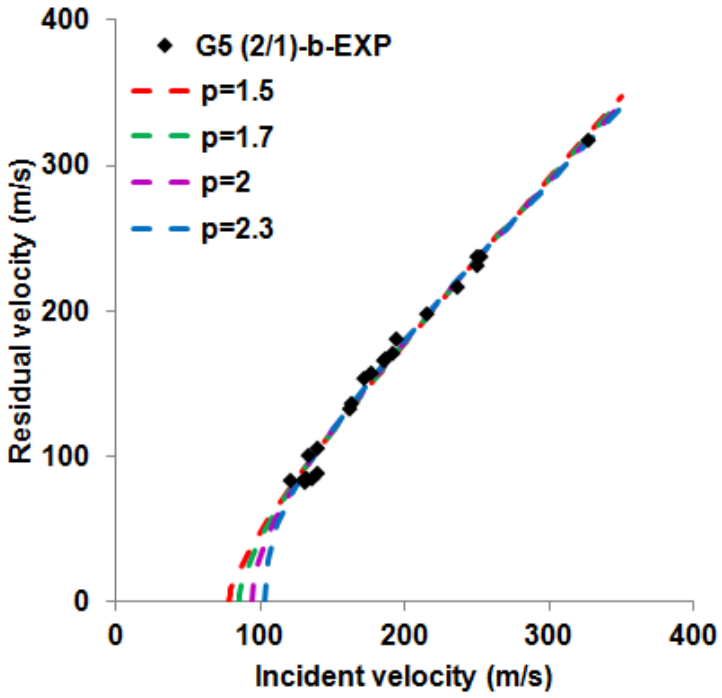

Fig.6.3. Experimental residual velocity *vs*. incident velocity fitted with Lambert-Jonas' equation using different P values for the GLARE 5 (2/1) beam specimen.

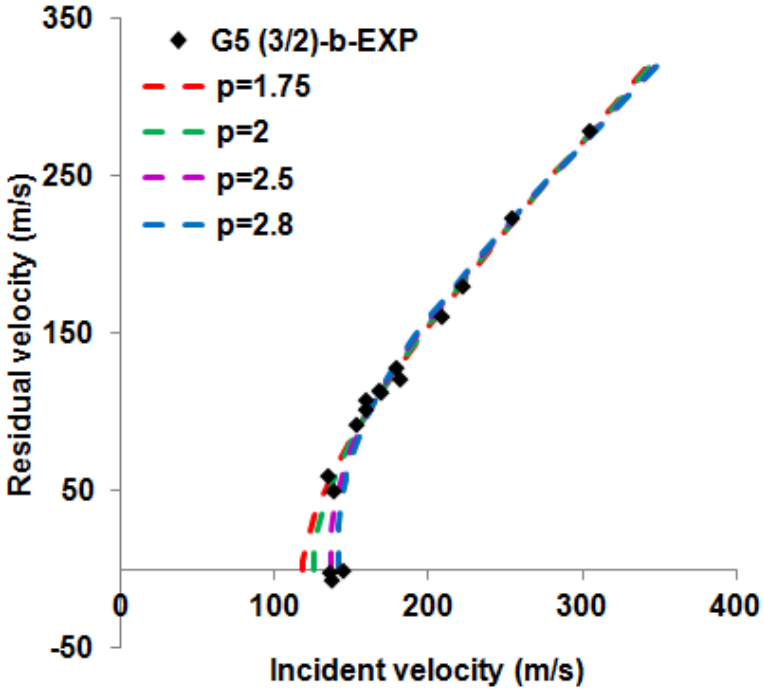

Fig.6.4. Experimental residual velocity *vs*. incident velocity fitted with Lambert-Jonas' equation using different P values for the GLARE 5 (3/2) beam specimen.

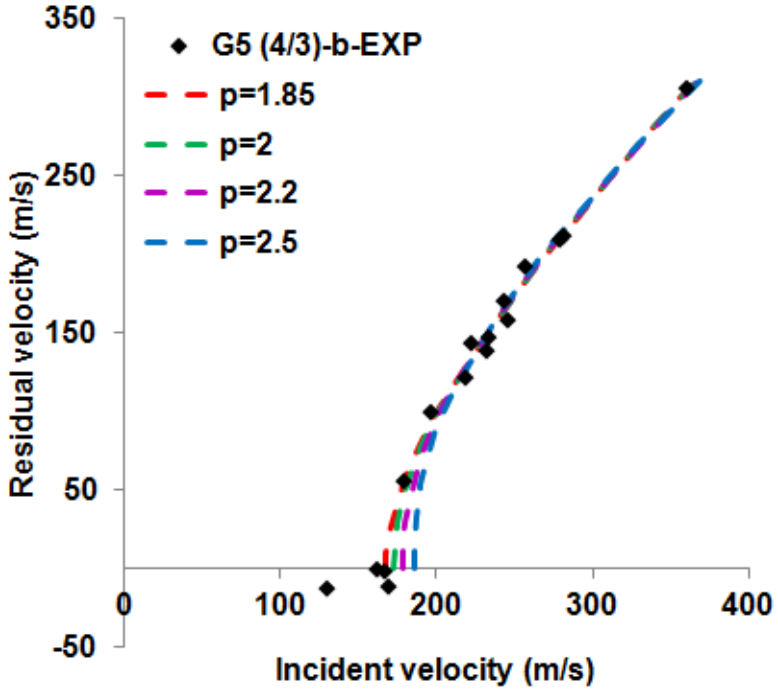

Fig.6.5. Experimental residual velocity *vs*. incident velocity fitted with Lambert-Jonas' equation using different P values for the GLARE 5 (4/3) beam specimen.

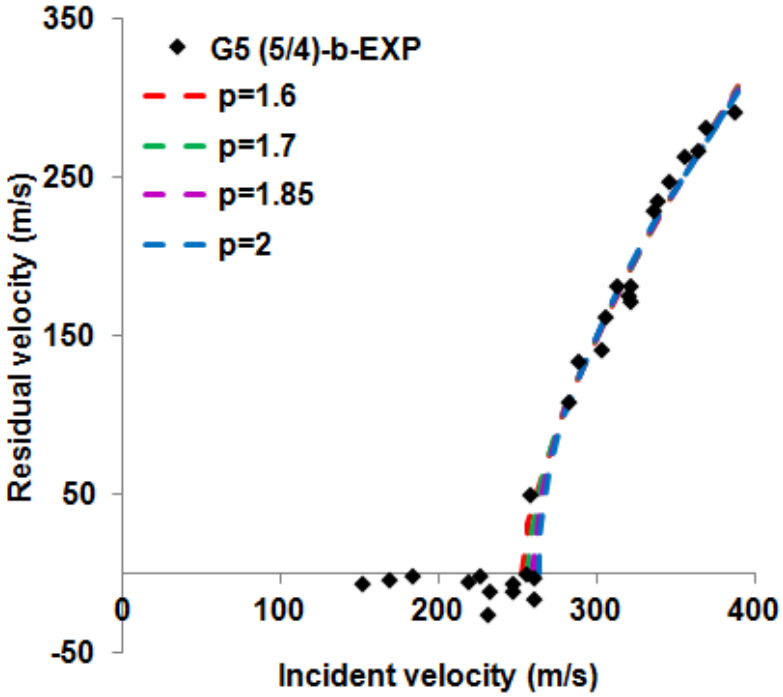

Fig.6.6. Experimental residual velocity *vs*. incident velocity fitted with Lambert-Jonas' equation using different P values for the GLARE 5 (5/4) beam specimen.

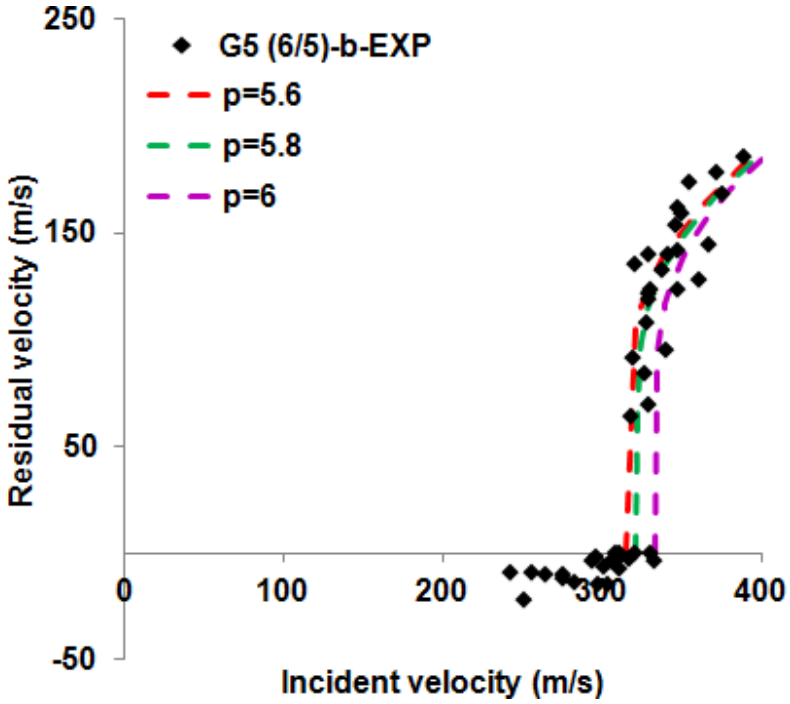

Fig.6.7. Experimental residual velocity *vs*. incident velocity fitted with Lambert-Jonas' equation using different P values for the GLARE 5 (6/5) beam specimen.

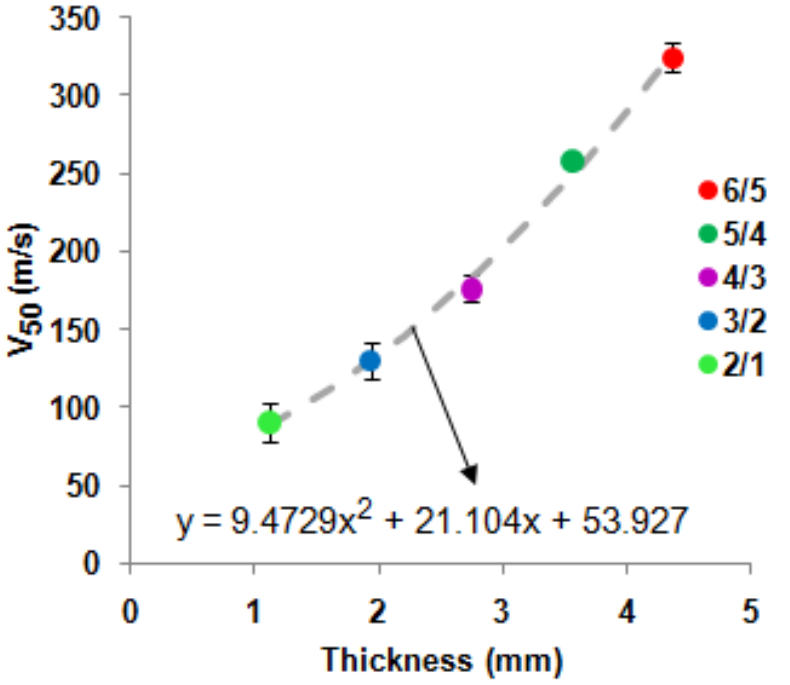

Fig.6.8. Variation of ballistic limit with thickness for the cross-ply GLARE 5 beam specimens. In the equation x stands for thickness and y for V_{50}.

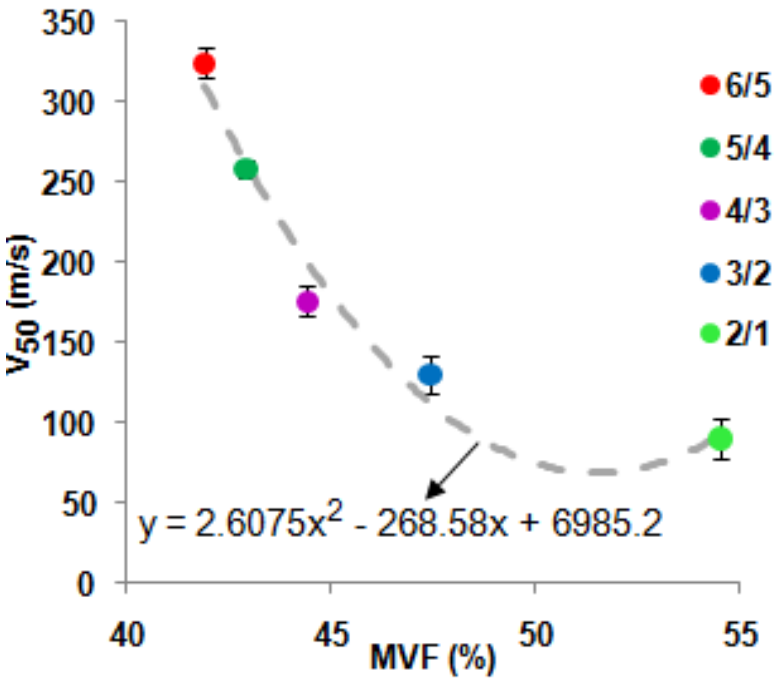

Fig.6.9. Variation of ballistic limit with metal volume fraction for the cross-ply GLARE 5 beam specimens with different thicknesses. In the equation x stands for MVF and y for V_{50}.

Figure 6.10 exhibits the impacted, non-impacted and side views of the GLARE 5 FML beams with various configurations impacted ballistically at various incident velocities. The cross-sectional views of these specimens are shown in Fig. 6.11. The typical damage induced in polymer-based composite materials, i.e. matrix cracking, fiber breakage/splitting/pullout and delamination, can also be observed in the GLARE 5 FMLs (Figs. 6.10 and 6.11). The fibers could break under shear, e.g. Fig.6.11(d), and tension, e.g. Fig. 6.10(b) with the (6/5) configuration. One major aspect that makes FMLs so unique compared to the traditional composite materials is that they contain additional metal layers. Therefore, besides the damage created in the prepreg layers (which is similar to the damage in the traditional composites), two extra failure mechanisms were also introduced in FMLs: (1) damage in the aluminum layers and (2) interfacial fracture between the aluminum and the prepreg layer. As Figs. 6.10 and 6.11 suggest, the

aluminum layers failed through bulging, petalling and plugging (caused mainly by shear). Plastic hinging as well as localized thinning around the impact point occurred in the aluminum layers. The localized thinning of aluminum layers around the impact point is believed as results of their stretching and yielding, which was also reported in Ref. [16]. The creation of plastic hinges in the aluminum layers was another mechanism to absorb energy. The interfacial failure between two dissimilar materials, also known as debonding, was observed in the specimens. Debonding and delamination are important factors in keeping the structural integrity. They were also part of the mechanisms in dissipating energy. As shown in Figs. 6.10 and 6.11, specimens with different configurations dissipated the kinetic energy of the bullet-specimen system also by the progression of debonding/delamination in different locations. For instance, Fig. 6.11(h) reveals that the bottom aluminum layer located at the non-impacted side of the panel, peeled off as a result of debonding growth between the aluminum and the adjacent prepreg layer. This will be confirmed later using the high-speed-camera footage. The specimen local/global bending deformations (Figs. 6.10 and 6.11) are considered to be important parameters in dissipating energy. The aluminum layers embedded in the FMLs increased the amount of energy absorbed by the specimens through their bending and stretching (e.g. Fig. 6.10(a) with the (6/5) configuration). It should be mentioned that, in general, non-FML based composite materials do not deform plastically. Hence, this type of energy-absorption mechanism does not contribute any significant effect on their energy dissipation. Based on the above-mentioned experimental observations of the induced impact damage in the FMLs, the uniqueness of this type of laminated specimens in dissipating impact energy was evident. That is to say, they developed damage similar

to both monolithic aluminum alloy and polymer composite laminate. The internal impact damage created in the GLARE 5 specimens was mostly confined to a relatively small area surrounding the point of impact and its size was always smaller than a visible, plastically deformed dent on the non-impacted side of the specimens. The same behavior for the GLARE FMLs is also reported in Ref. [8]. Moreover, it is believed that the interfacial debonding as well as the aluminum layers bending and stretching are the most important factors in dissipating the impact energy in the GLARE 5 FML beams.

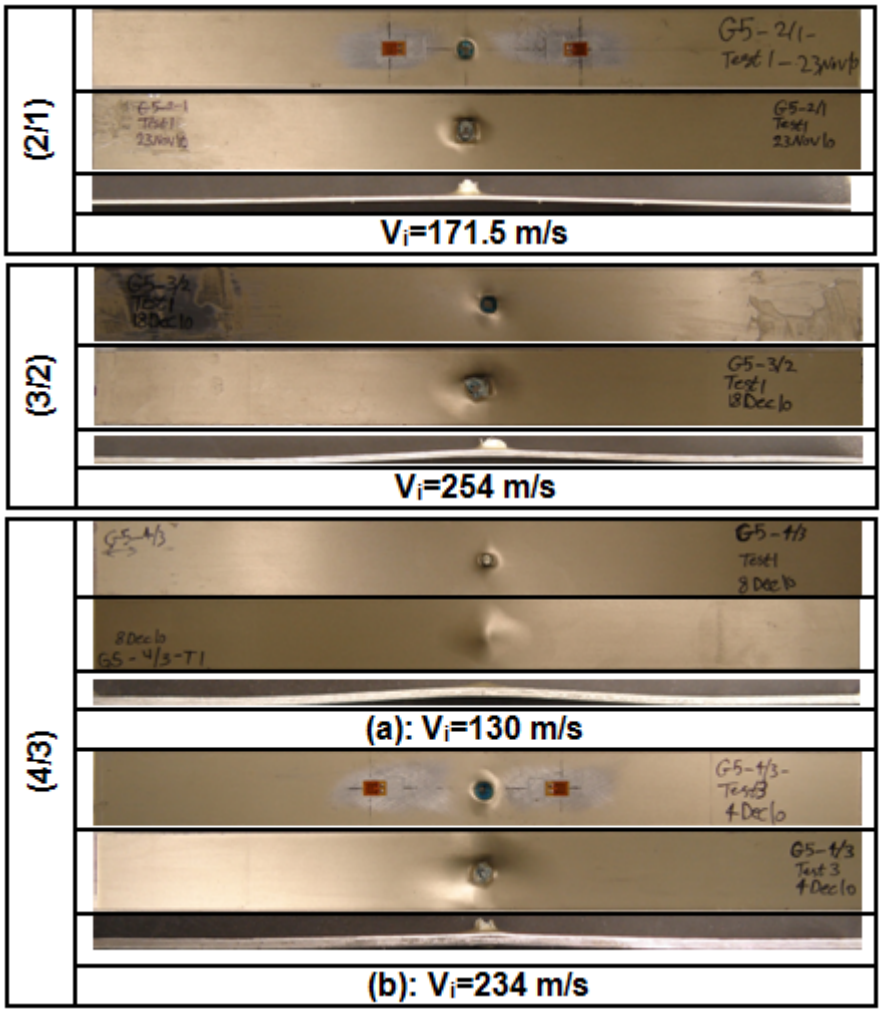

Fig.6.10. Damage induced in the GLARE 5 FML beams with various thicknesses impacted at different incident velocities. Impacted-side (top), non-impacted-side (middle), and side (bottom) views.

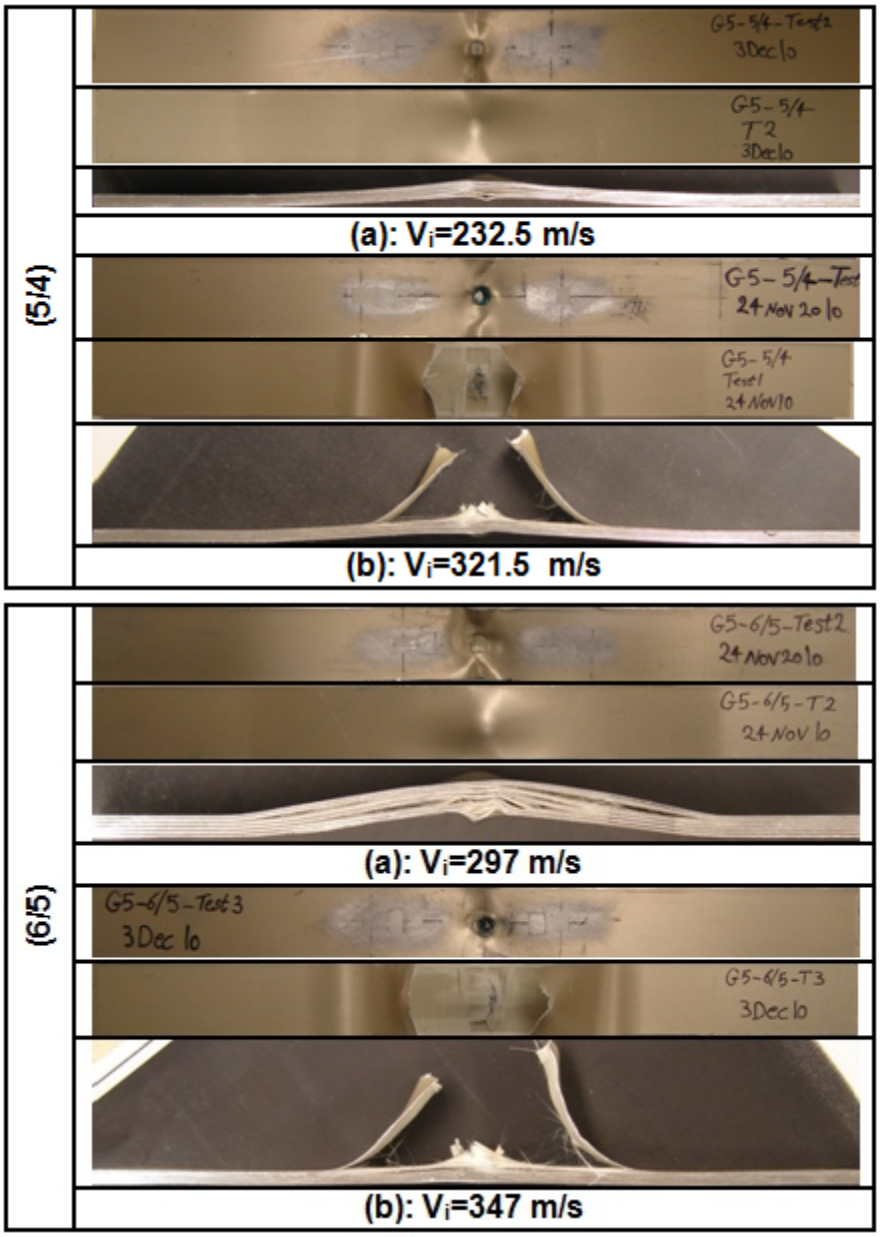

Fig.6.10. (Continued)

Figures 6.12 and 6.13 exhibit damage progression on the non-impacted side of GLARE 5 (2/1) and (6/5) FML beams impacted at 269 m/s and 340 m/s, respectively. These pictures were obtained using a high-speed camera. For both specimens, bulging initiated during the first 12.6 μs of contact time. As is obvious from Fig. 6.12, during the first approximately 25 μs, a diamond-shaped damage contour was created and enlarged

towards the edges of the beam specimen. This was followed by the piercing and perforating of the target by the bullet within the time interval of 25-100 μs. The specimen bending started after 38 μs after the contact established. The petalling in the bottom aluminum layer as well as the visible-plastically-deformed zone were quite obvious. A circular-shaped damage contour was taken place on the non-impacted side of the (6/5) specimen. It propagated toward the edges of the specimen in the form of an elliptical-shaped damage contour. Between the time interval of 37.90 μs and 50.53 μs the damage contour reached the specimen edges along the width. The initial crack on the bottom aluminum layer was created at around 37.90 μs and progressed along the aluminum transverse direction, causing the aluminum layer to split into two parts at 113.70 μs. As time passed by, some broken fibers and debris were expelled out of the specimen and bullet. The two tear-off pieces of the aluminum layer continued to deflect due to their residual kinetic energy. They reached their temporary stationary position at about 1.30 ms of the contact time. Some part of their initial kinetic energy was mainly absorbed by further progression of debonding between the aluminum layer and the adjacent prepreg layer. The remaining energy was dissipated by means of vibration. It is also clear from the figure that the damage induced in the prepreg layers was relatively small and localized compared to the plastic indent created in the aluminum layer. The same phenomenon was also reported by other researchers for the GLARE laminates, e.g. [8,21].

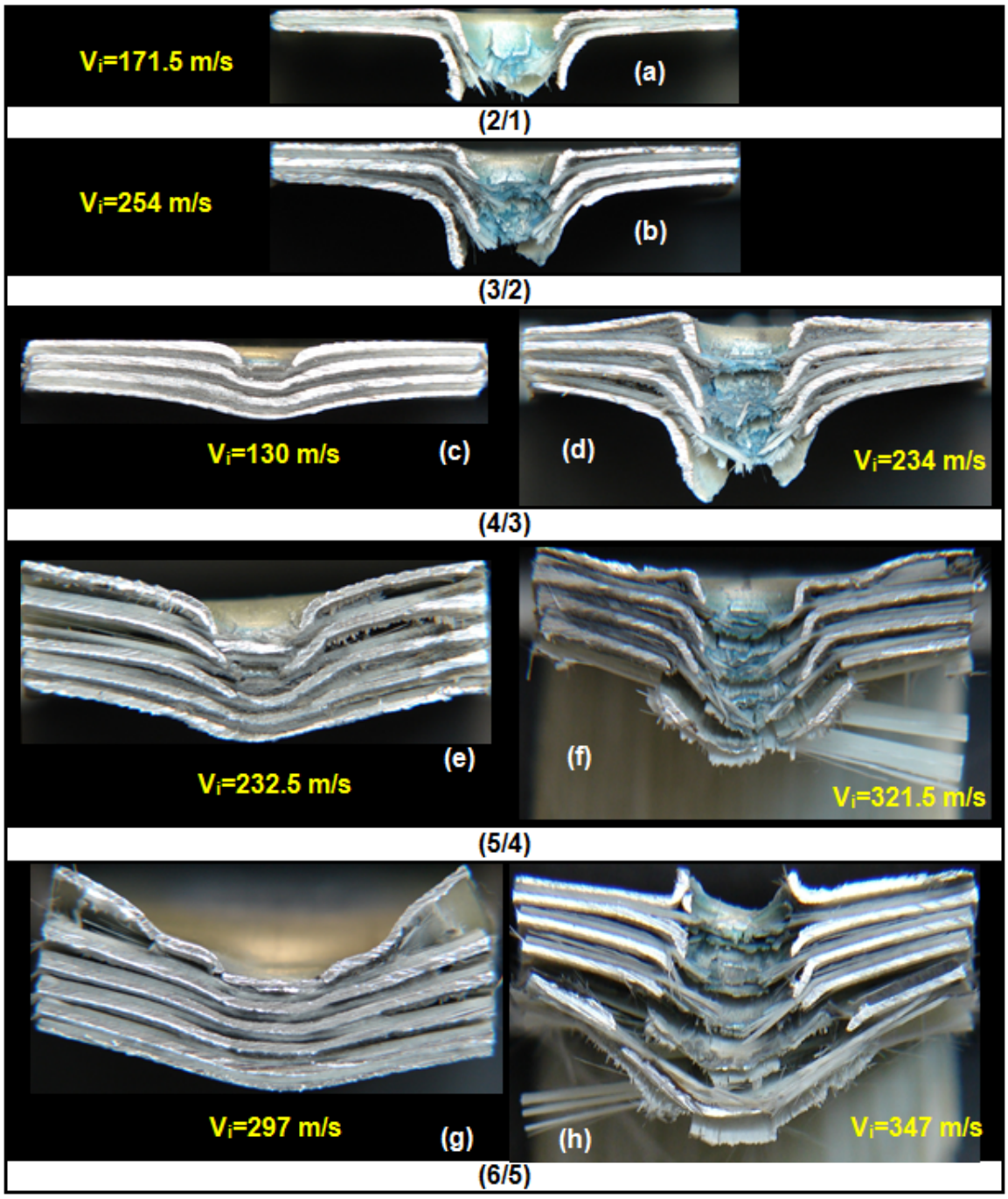

Fig.6.11. Cross-sectional views of the GLARE 5 FML beams with various thicknesses impacted at different incident velocities.

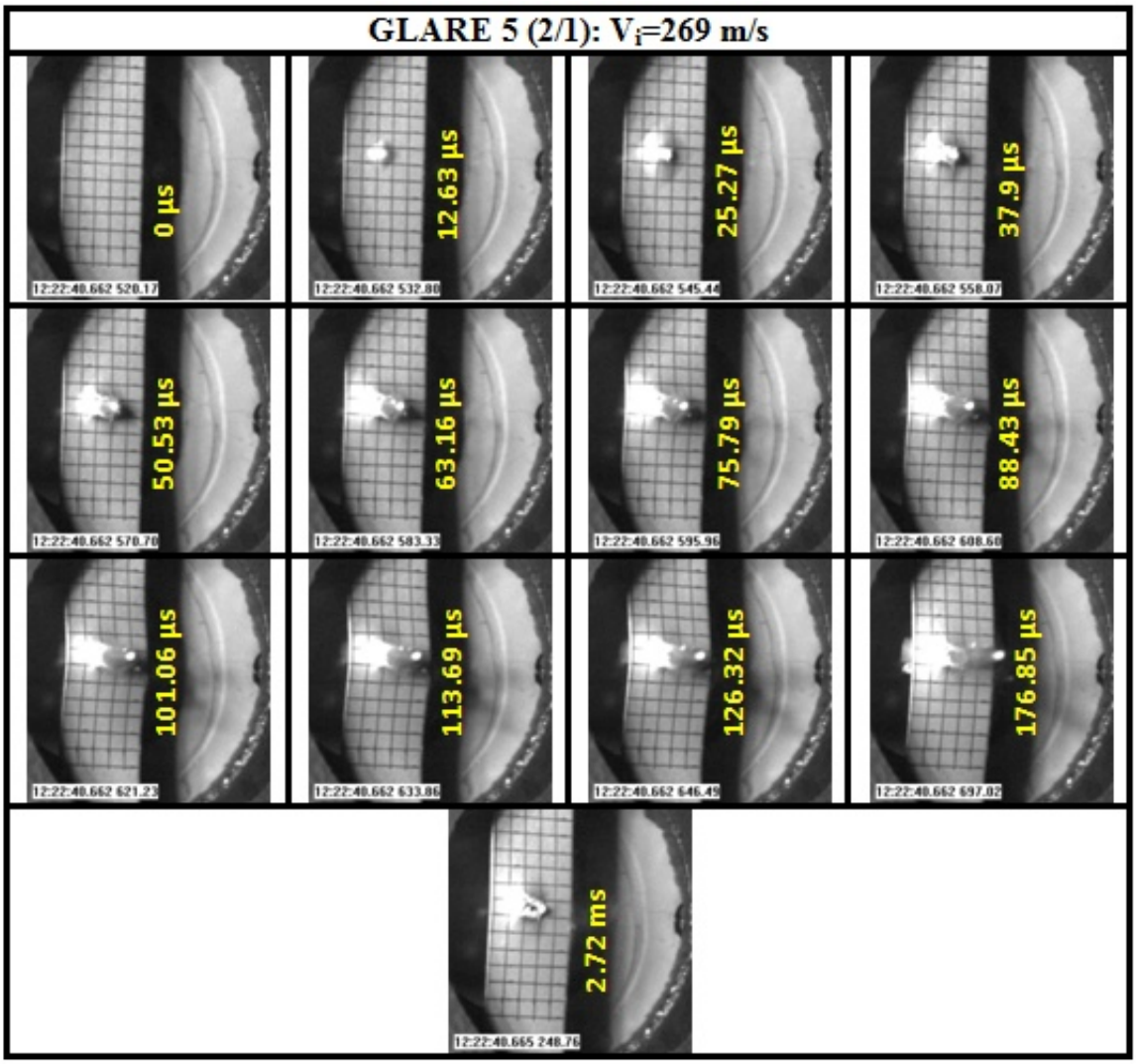

Fig.6.12. High-speed camera footage of the GLARE 5 (2/1) FML beam impacted at 269 m/s.

Experimental observations implied that bullet residual length was affected by the specimen thickness under a given impact velocity. In other words, for a given impact velocity, the bullet length was shortened after impact as the specimen thickness increased. This was due to an increase in contact resistance as a function of specimen thickness.

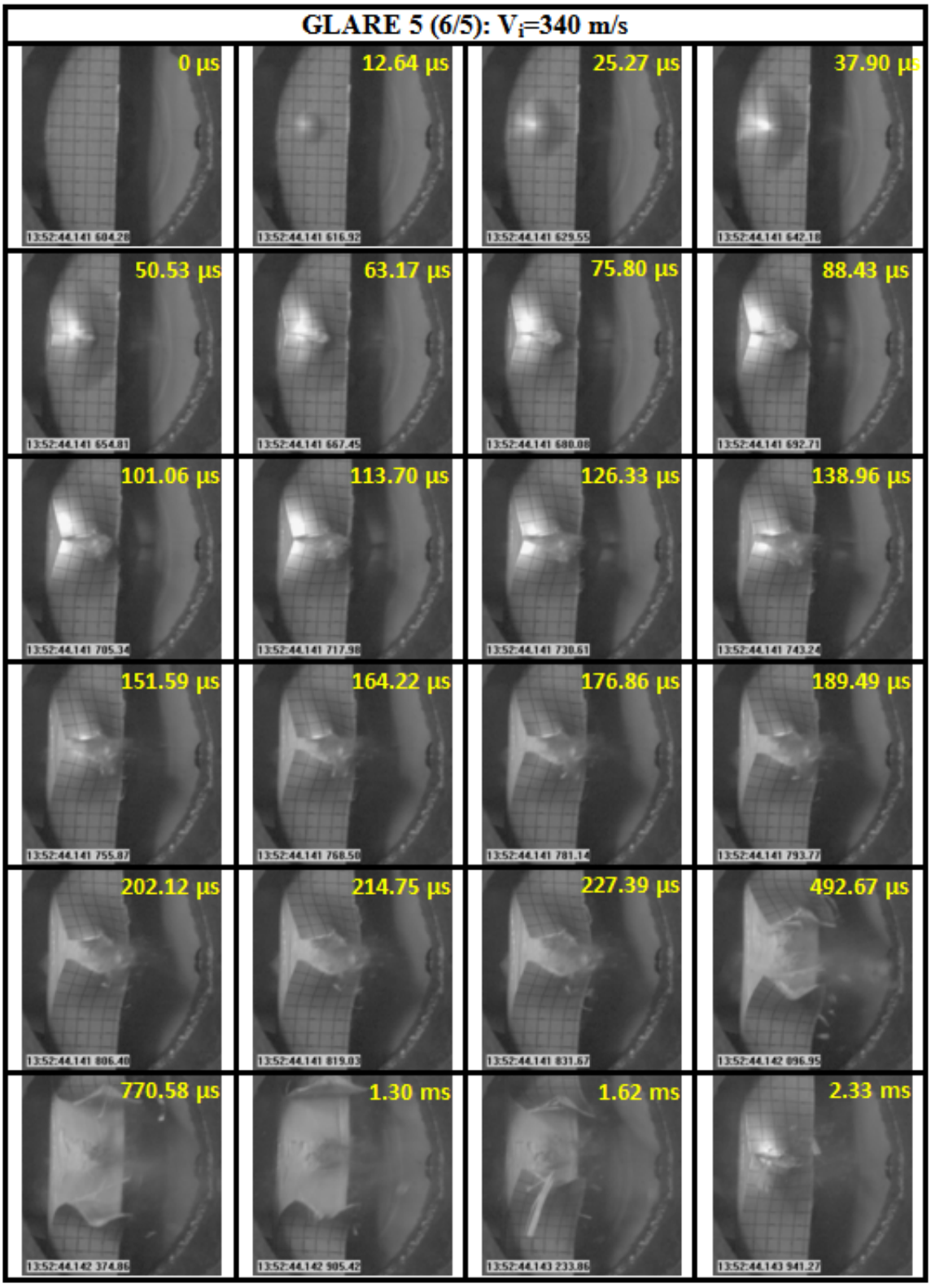

Fig.6.13. High-speed camera footage of the GLARE 5 (6/5) FML beam impacted at 340 m/s.

6.1.2. Effect of specimen stacking sequence

The effect of stacking sequence was studied on the GLARE 5 (3/2) beam specimens with unidirectional $[0°_4]$, unidirectional $[90°_4]$, cross-ply $[0°/90°]_s$ and quasi-isotropic $[0°/\pm45°/90°]$ lay-up orientations.

Figures 6.14 through 6.17 depict variation of residual velocity versus incident velocity for the GLARE 5 (3/2) FML beams with unidirectional $[0°_4]$, unidirectional $[90°_4]$, cross-ply $[0°/90°]_s$ and quasi-isotropic $[0°/\pm45°/90°]$ stacking sequences, respectively. In the figures, experimental data are specified by a solid diamond symbol and the Lambert-Jonas' curves with different P values are shown by dashed lines. Figure 6.18 depicts variations of the ballistic limit velocity as a function of specimen stacking sequence. For each individual specimen type, the variation range in its V_{50} is denoted by a deviation bar. It is apparent from Fig. 6.18 that the unidirectional $[90°_4]$ specimen offered the least resistance to the projectile perforation. In addition, the quasi-isotropic specimen showed slightly higher ballistic limit velocity compared to the unidirectional $[0°_4]$ and cross-ply $[0°/90°]_s$ specimens. Except for the unidirectional $[90°_4]$ specimen, the ballistic limit was almost invariant with respect to change in stacking sequence.

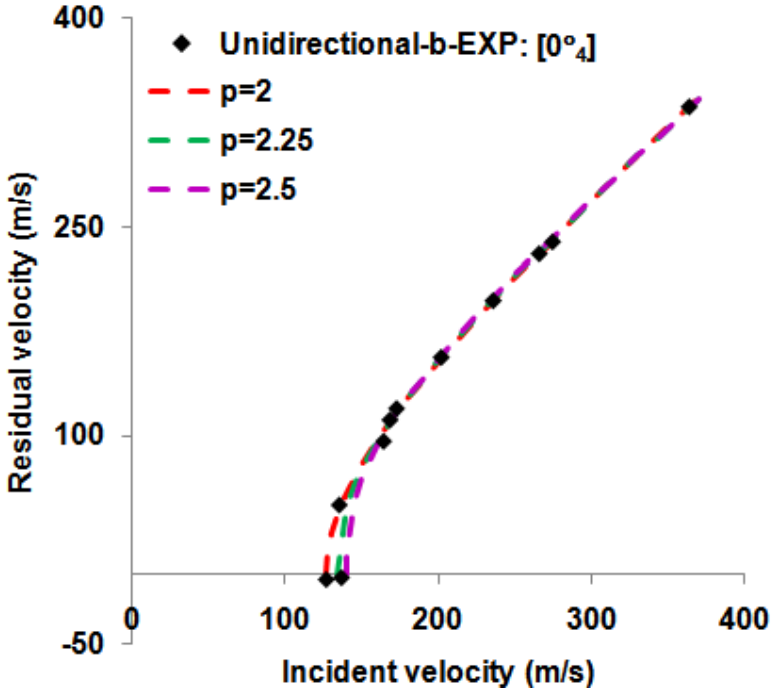

Fig.6.14. Experimental residual velocity *vs*. incident velocity fitted with Lambert-Jonas' equation using different P values for the unidirectional [0°$_4$] GLARE 5 (3/2) beam specimen.

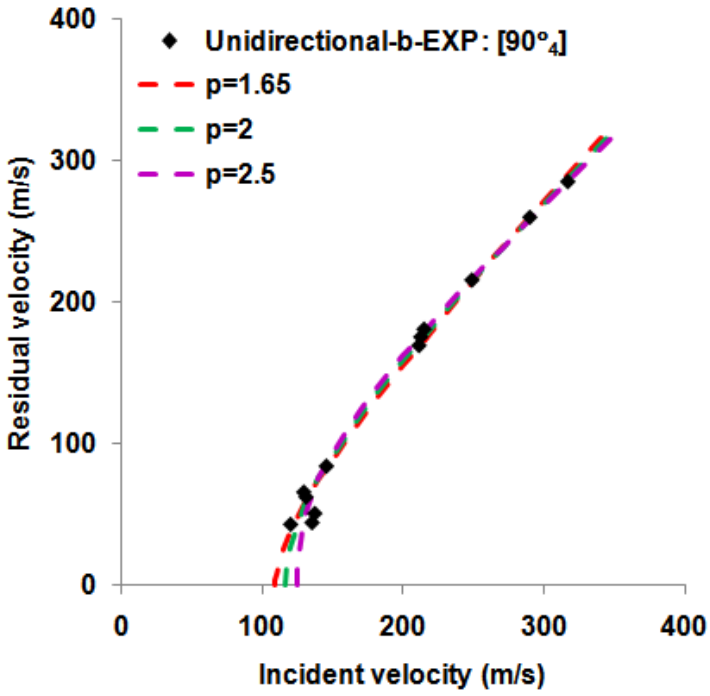

Fig.6.15. Experimental residual velocity *vs*. incident velocity fitted with Lambert-Jonas' equation using different P values for the unidirectional [90°$_4$] GLARE 5 (3/2) beam specimen.

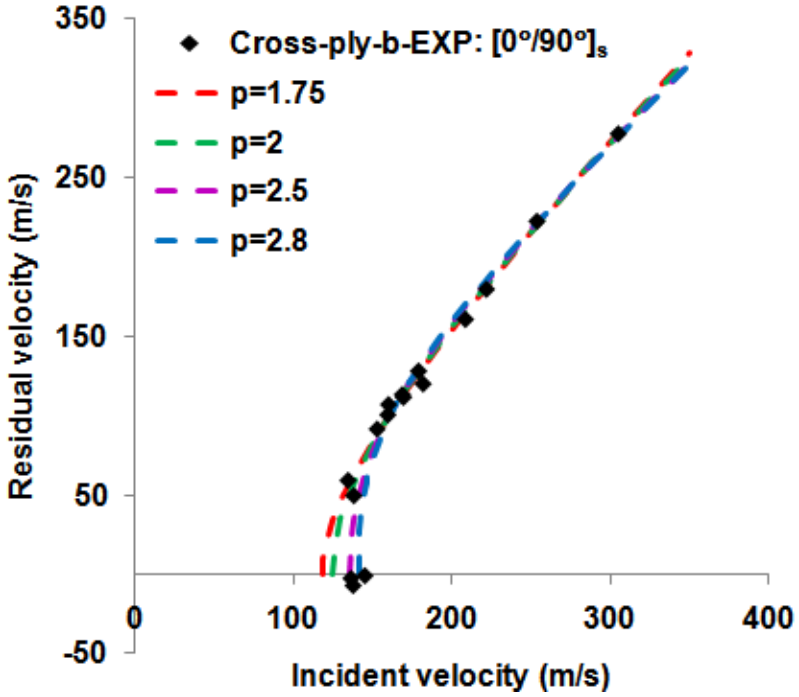

Fig.6.16. Experimental residual velocity *vs*. incident velocity fitted with Lambert-Jonas' equation using different P values for the cross-ply $[0°/90°]_s$ GLARE 5 (3/2) beam specimen.

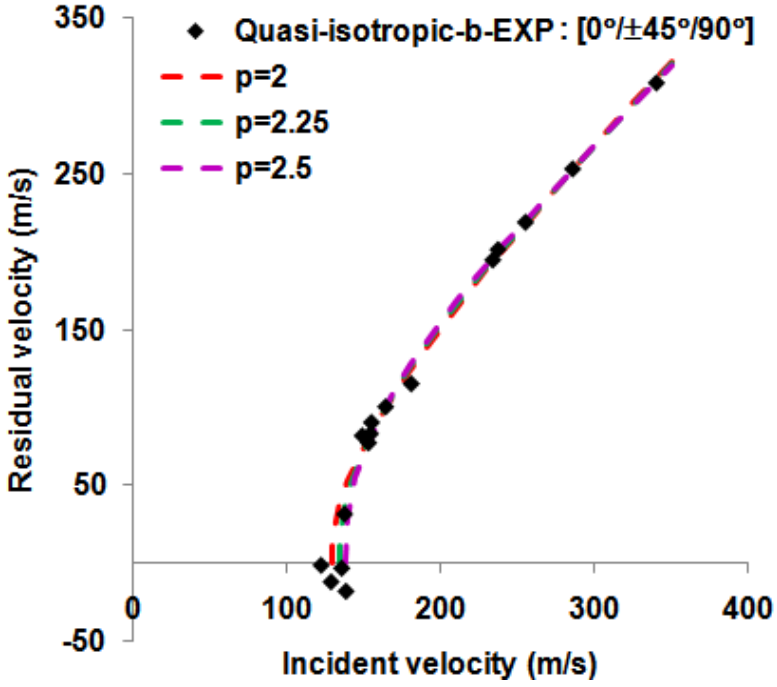

Fig.6.17. Experimental residual velocity *vs*. incident velocity fitted with Lambert-Jonas' equation using different P values for the quasi-isotropic [0°/±45°/90°] GLARE 5 (3/2) beam specimen.

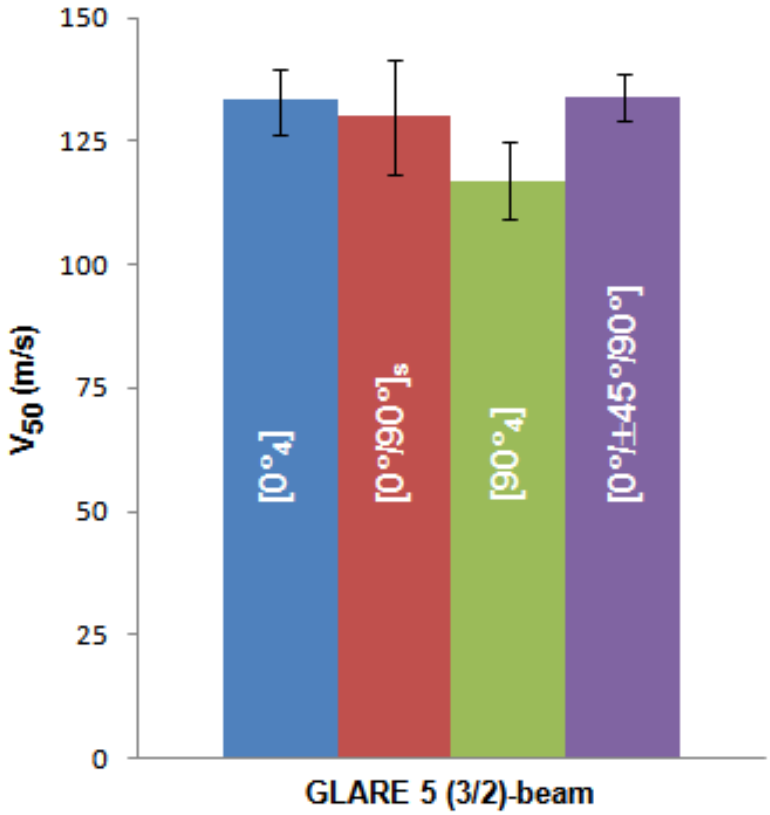

Fig.6.18. Variations of ballistic limit velocity as a function of stacking sequence for the GLARE 5 (3/2) FML beams.

Figure 6.19 shows damage induced in the GLARE 5 (3/2) FML beams with unidirectional $[0°_4]$, unidirectional $[90°_4]$, cross-ply $[0°/90°]_s$ and quasi-isotropic [0°/±45°/90°] stacking sequences impacted at 274.5 m/s, 215 m/s, 254 m/s and 234 m/s, respectively. As the figure implies, the aluminum layers failed through petalling and plugging. Plastic hinging as well as localized thinning around the impact point occurred in the aluminum layers. As mentioned before, the localized thinning of aluminum layers around the impact point is believed resulting from their stretching and yielding. The creation of plastic hinges in the aluminum layers was another mechanism to absorb energy. In general, matrix cracking, fiber breakage/splitting/pullout, delamination in prepreg layers and debonding between aluminum and adjacent prepreg layers were

observed. The specimen local/global bending deformations were considered to be important parameters in dissipating energy (Fig. 6.19). The aluminum layers implanted in the FMLs increased the amount of energy absorbed by the specimens through their bending and stretching. As mentioned earlier, in general, non-FML based composite materials do not deform plastically. Hence, this type of energy-absorption mechanism does not contribute any significant effect on their energy dissipation. A visible crack occurred along the 0° fiber direction for both unidirectional specimens (Fig. 6.19). For the $[90°_4]$ specimen a through-the-thickness crack took place. The initiation and progression of the crack towards the specimen edges caused the specimen to split into two halves. This was not seen in the $[0°_4]$ specimen, which could be explained by the orientation of the fibers with respect to the specimen geometry. There was not much delamination for the unidirectional panels (Fig. 6.19(d)). This was expected in the interface of the unidirectional prepreg layers since there was no bending stiffness mismatch in a unidirectional prepreg layer. Severe debonding was observed in both unidirectional specimens. However, this was more pronounced in the $[90°_4]$ specimen. For the cross-ply and quasi-isotropic specimen debonding/delamination was obvious. Fiber breakage took place in both unidirectional specimens mainly under tension (Fig. 6.19(c) and (d)). However, this was under shear and tension for the cross-ply and quasi-isotropic specimens (Fig. 6.19(d)).

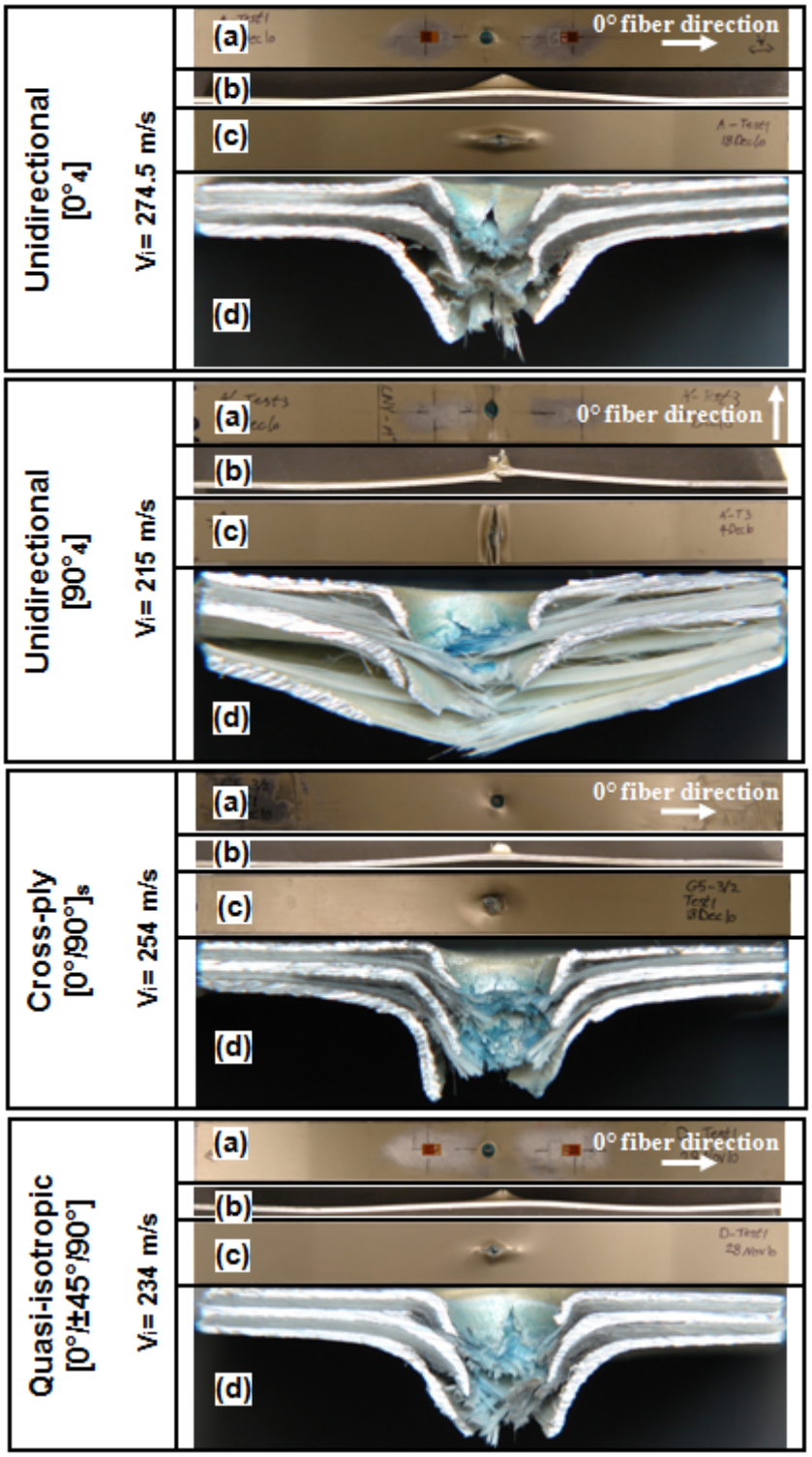

Fig.6.19. Damage induced in the GLARE 5 (3/2) FML beams with various stacking sequences impacted at different incident velocities. (a) impacted-side view, (b) side view, (c) non-impacted-side view and (d) cross-sectional view.

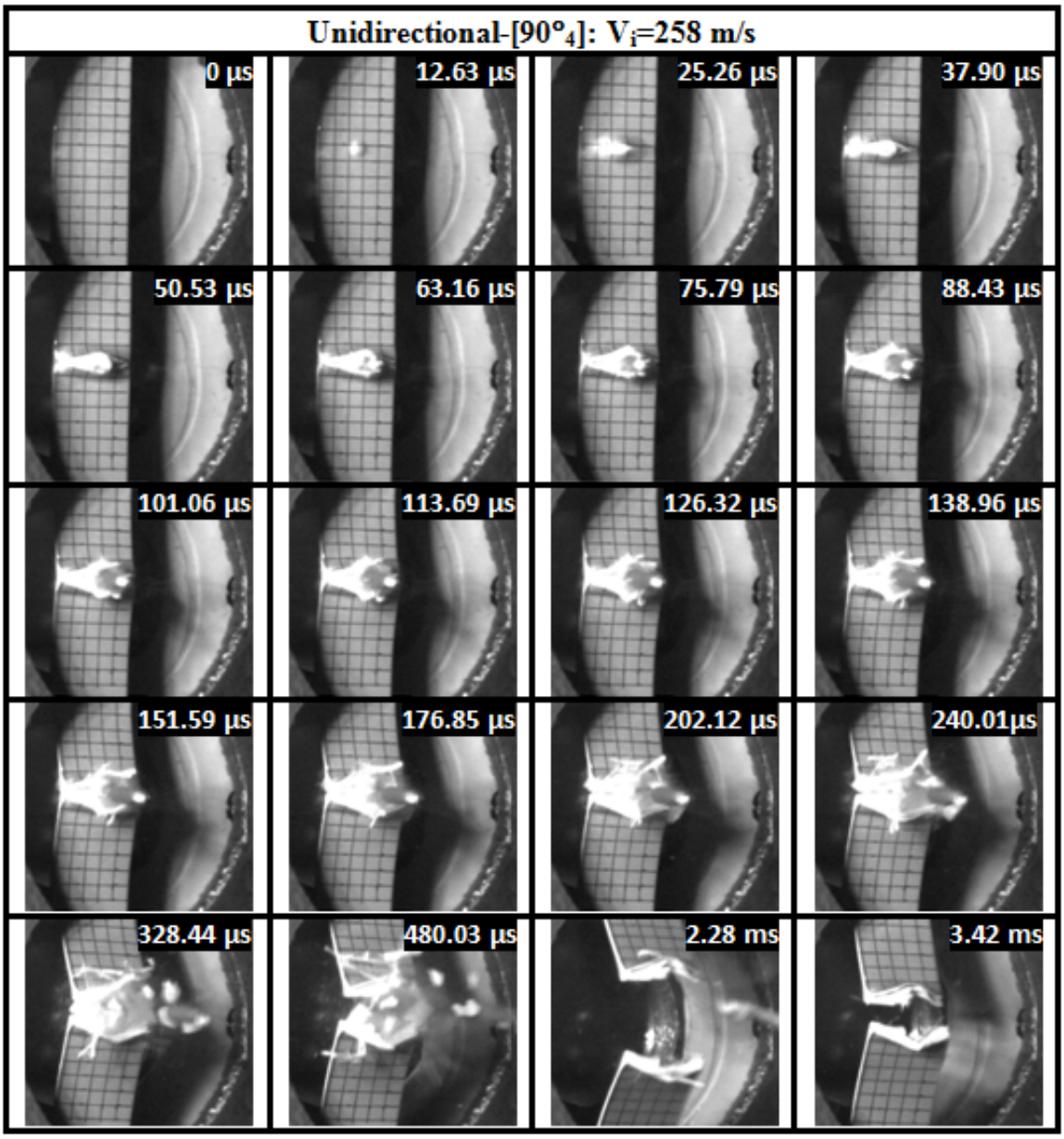

Fig.6.20. High-speed camera footage of the GLARE 5 (3/2)-[90°$_4$] FML beam impacted at 258 m/s.

Based on the aforementioned experimental remarks of the induced impact damage in the FMLs, the uniqueness of this type of laminated specimens in dissipating impact energy was evident. That is to say, they developed damage similar to both monolithic aluminum alloy and polymer composite laminate. Moreover, it is believed that the interfacial debonding, which was influenced by the prepreg stacking sequence, as well as the

aluminum layers bending and stretching are the most important factors in dissipating the impact energy in the GLARE 5 (3/2) FML beams.

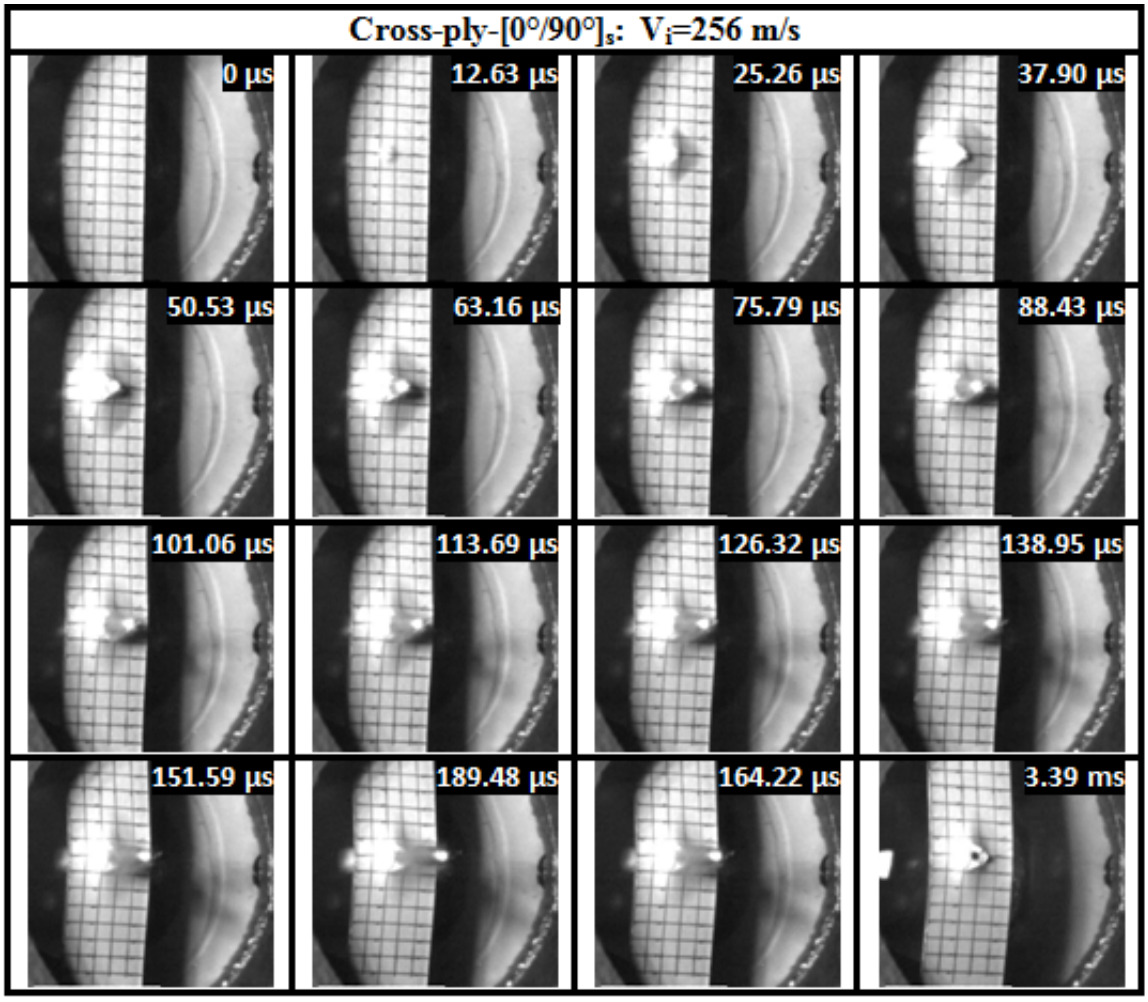

Fig.6.21. High-speed camera footage of the GLARE 5 (3/2)-$[0°/90°]_s$ FML beam impacted at 256 m/s.

Figures 6.20 and 6.21 display damage progression on the non-impacted side of the GLARE 5 (3/2) FML beams with unidirectional $[90°_4]$ and cross-ply stacking sequences impacted at 258 m/s and 256 m/s, respectively. These pictures were acquired using a high-speed camera. For both specimens, bulging initiated during the first 12.63 µs of contact time. As is obvious from Fig. 6.20, during the first approximately 50.53 µs, a lip-shaped damage contour was created and propagated along the 0° fiber direction

towards the specimen edges. This was followed by the piercing and perforating of the target by the bullet. The damage development in the unidirectional [$90_4°$] FMLs caused the specimens to split into two halves (Fig. 6.20). The induced damage on the non-impacted side of the cross-ply specimen propagated in the form of a diamond-shaped damage zone (Fig. 6.21). The transition from partial to full penetration occurred during the time interval of 50.53-75.79 μs. The petalling in the bottom aluminum layer as well as the visible-plastically-deformed zone were quite obvious.

6.2. Ballistic impact tests on GLARE 5 FML plates

In this section, the impact response of the GLARE 5 FML plates was considered. The effects of specimen thickness and stacking sequence were examined. These effects are investigated in the following subsections.

6.2.1. Effect of specimen thickness

The cross-ply GLARE 5 panels with various thicknesses were cut into152.4 mm by 101.6 mm (6″×4″) plate specimens to evaluate the thickness effect. The range of thickness is from 1.117 mm (0.044″) of GLARE 5 (2/1) up to 4.368 mm (0.172″) of GLARE 5 (6/5). As mentioned before, after determining the speeds of the bullet before and after impact, the incident projectile velocity (before impact) was plotted versus the residual velocity (after impact) for each type of the specimen (Table 3.1). The experimental data could then be fitted by least-square regression according to the classical Lambert-Jonas' equation (Eq. 5.1) for the positive residual velocity values. Figures 6.22 through 6.26 depict variation of residual velocity versus incident velocity for the GLARE 5 FML plates with (2/1), (3/2), (4/3), (5/4) and (6/5) configurations, respectively. In the figures, experimental data are specified by a solid diamond symbol and the Lambert-Jonas'

curves with different P values are shown by dashed lines. The intersection of the Lambert-Jonas' curve with the incident-velocity axis was considered as V_{50} for a given P value. Then, the average V_{50} value and its variations were calculated. As is apparent from the figures, by increasing the specimen thickness, V_{50} also increased. The resultant V_{50} for each specimen configuration is shown in Fig. 6.27, which depicts variation of ballistic limit with respect to the panel thickness for the cross-ply GLARE 5 FML plates. In the plot, the average ballistic limit and its variation range are denoted by a solid diamond and deviation bar for each panel thickness, respectively. It is apparent that by increasing the panel thickness, the ballistic limit also increased with a parabolic trend. Metal volume fraction versus ballistic limit for the cross-ply GLARE 5 specimens with different thicknesses is given in Fig. 6.28. It is worth noting that as the number of prepreg laminated layers increased, the ballistic limit also increased.

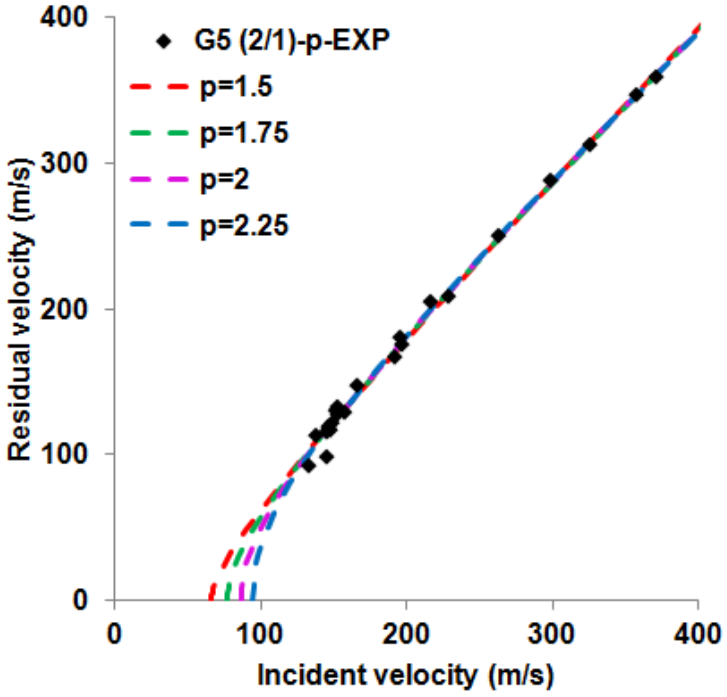

Fig.6.22. Experimental residual velocity *vs*. incident velocity fitted with Lambert-Jonas' equation using different P values for the GLARE 5 (2/1) plate specimen.

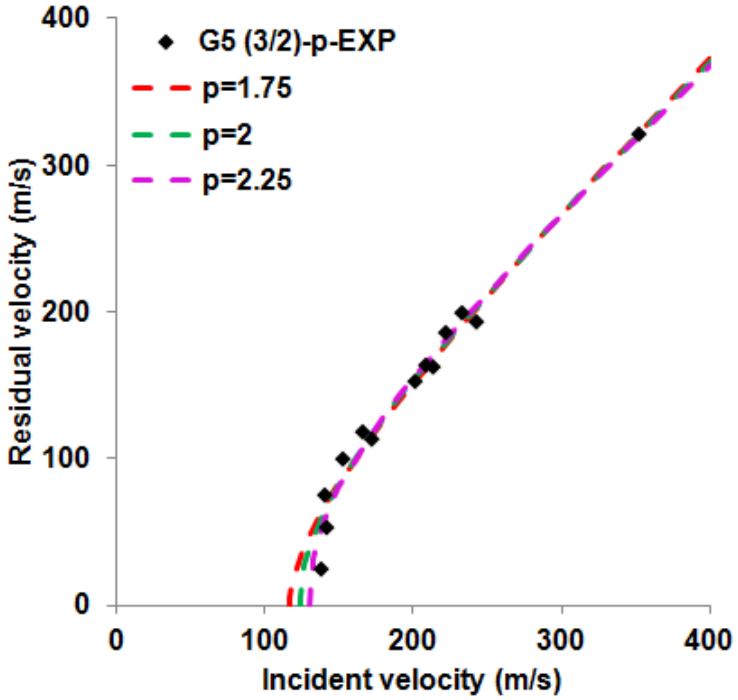

Fig.6.23. Experimental residual velocity *vs*. incident velocity fitted with Lambert-Jonas' equation using different P values for the GLARE 5 (3/2) plate specimen.

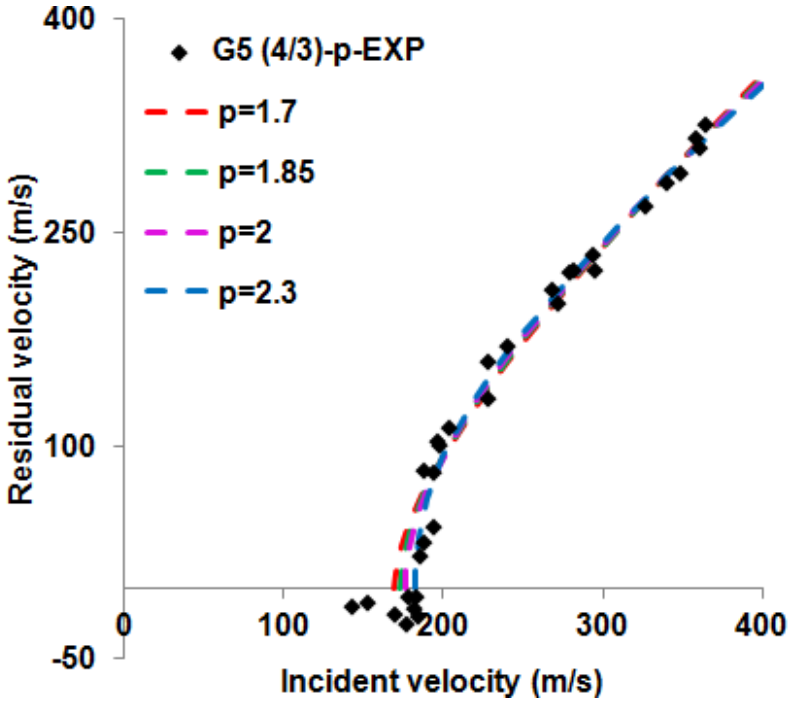

Fig.6.24. Experimental residual velocity *vs*. incident velocity fitted with Lambert-Jonas' equation using different P values for the GLARE 5 (4/3) plate specimen.

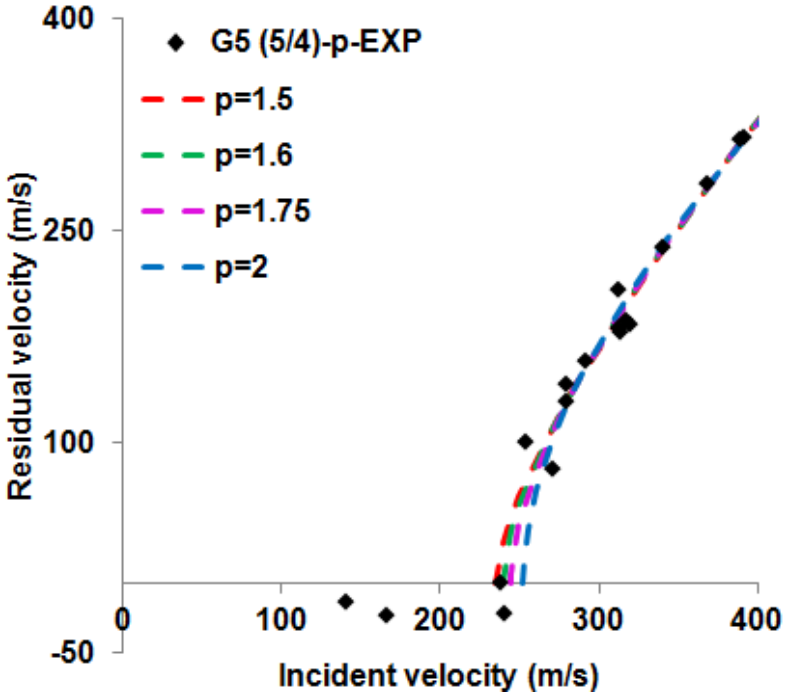

Fig.6.25. Experimental residual velocity *vs*. incident velocity fitted with Lambert-Jonas' equation using different P values for the GLARE 5 (5/4) plate specimen.

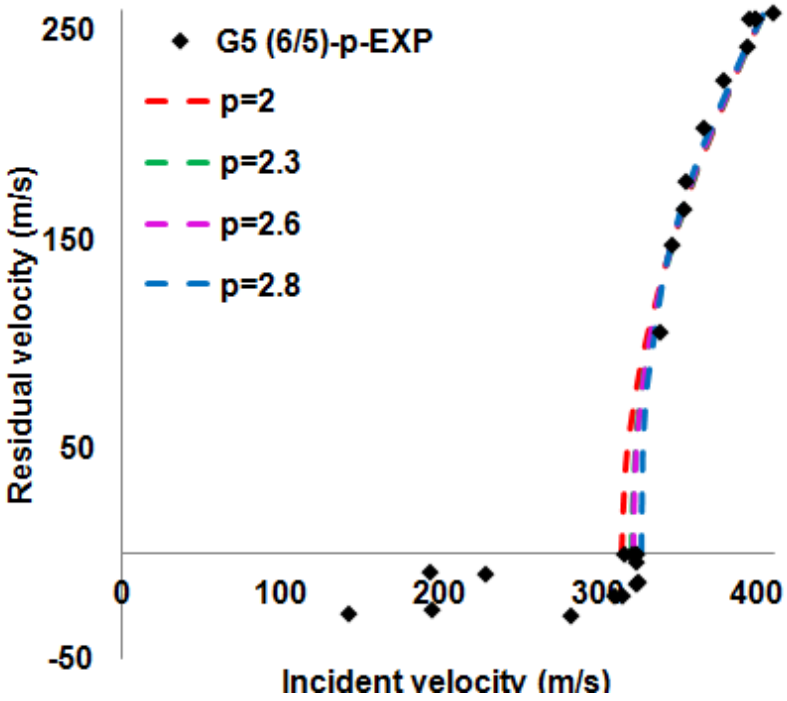

Fig.6.26. Experimental residual velocity *vs*. incident velocity fitted with Lambert-Jonas' equation using different P values for the GLARE 5 (6/5) plate specimen.

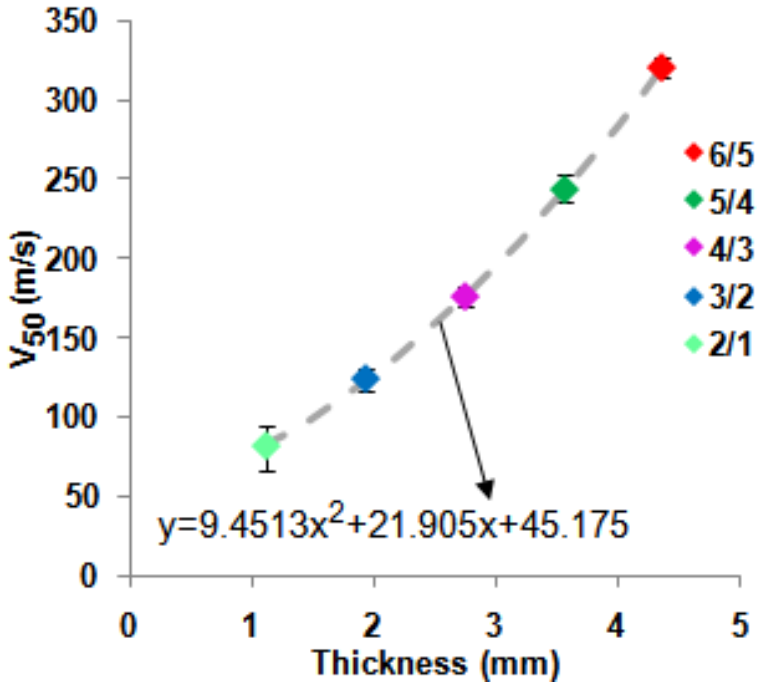

Fig.6.27. Variation of ballistic limit with thickness for the cross-ply GLARE 5 plate specimens. In the equation x stands for thickness and y for V_{50}.

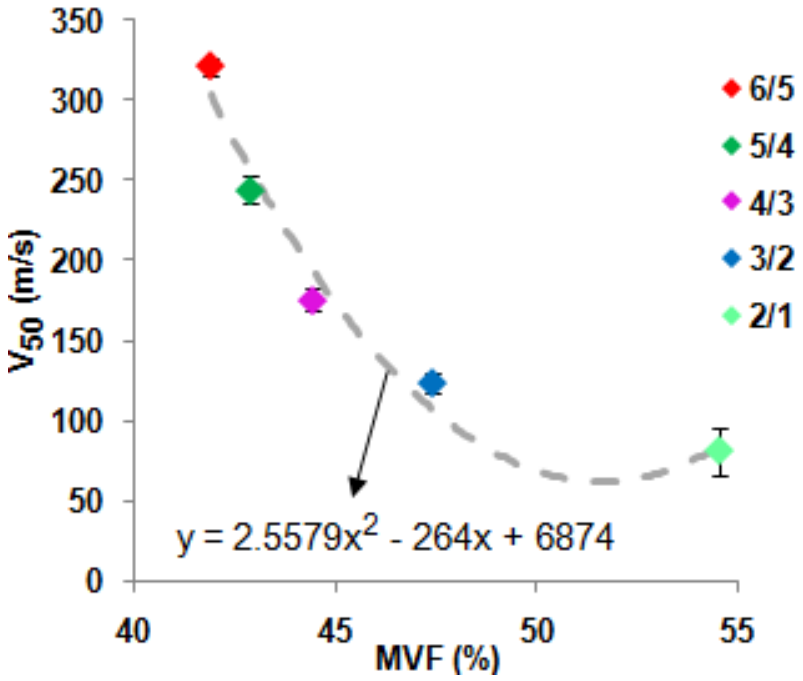

Fig.6.28. Variation of ballistic limit with metal volume fraction for the cross-ply GLARE 5 plate specimens with different thicknesses. In the equation x stands for MVF and y for V_{50}.

Figures 6.29 and 6.30 illustrate front/back side and C-scan views of the GLARE 5 FML plates with various configurations impacted ballistically at different incident velocities, respectively. The cross-sectional views and some examples of the side views of the specimens impacted at various incident velocities are shown in Fig. 6.31. Similar damage pattern that was seen for the FML beams was also observed for the FML plates. That is, matrix cracking, fiber breakage/splitting/pullout, delamination, damage in the aluminum layers and interfacial fracture between the aluminum and the prepreg layer (Figs. 6.29 and 6.31). The aluminum layers failed through bulging, petalling and plugging (Figs. 6.29 and 6.31). Plastic hinging as well as localized thinning around the impact point occurred in the aluminum layers. As was mentioned earlier, the localized thinning of aluminum layers around the impact point is believed as results of their stretching and yielding. The creation of plastic hinges in the aluminum layers as well as the progression of debonding/delamination in different locations within the specimens were additional mechanisms to absorb energy. As was shown in Fig. 6.13, the debonding/delamination growth reached the specimen edges causing the aluminum layer separated from the adjacent prepreg layer. This type of damage mode is not expected in the 6″x4″ specimen. This is because the ratio of the bullet diameter to the 10″x1″ specimen width is much higher compared to the ratio with respect to the 6″x4″ specimen. Moreover, the 6″x4″ specimen has higher bending stiffness. As a result, the permanent global bending deformation in the plate specimens was less pronounced when impacted ballistically compared to the beam specimens (Fig. 6.31(c)).

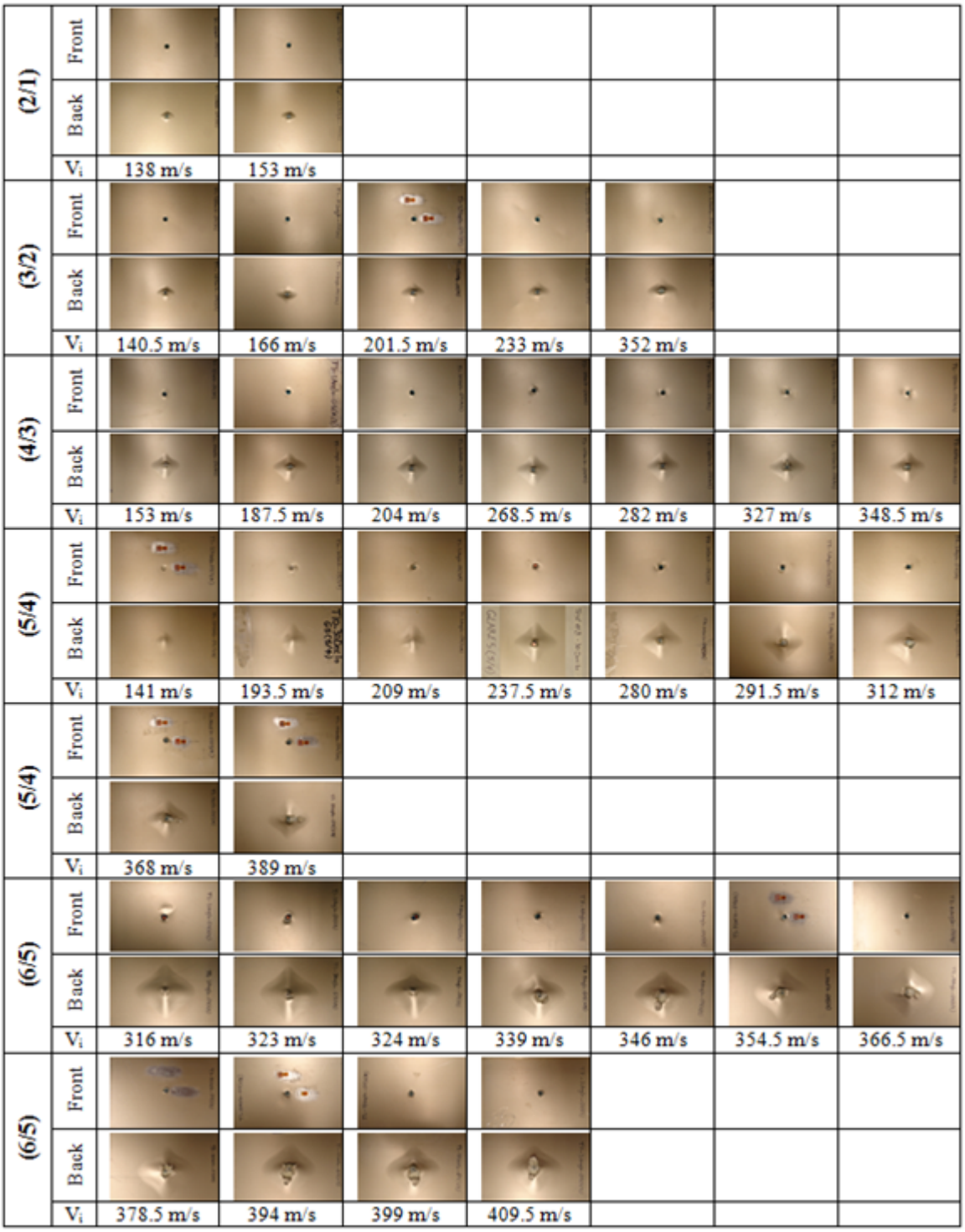

Fig.6.29. Front and back side views of the GLARE 5 FML plates with various thicknesses impacted at different incident velocities.

Figure 6.29 suggests that for a given impact velocity range, the visible plastically deformed dent appeared on the non-impacted side of the specimen increased by increasing the specimen thickness. This was also confirmed by referring to Fig. 6.30, which illustrates that by increasing the panel thickness for a given impact velocity range, the damage contour also increased.

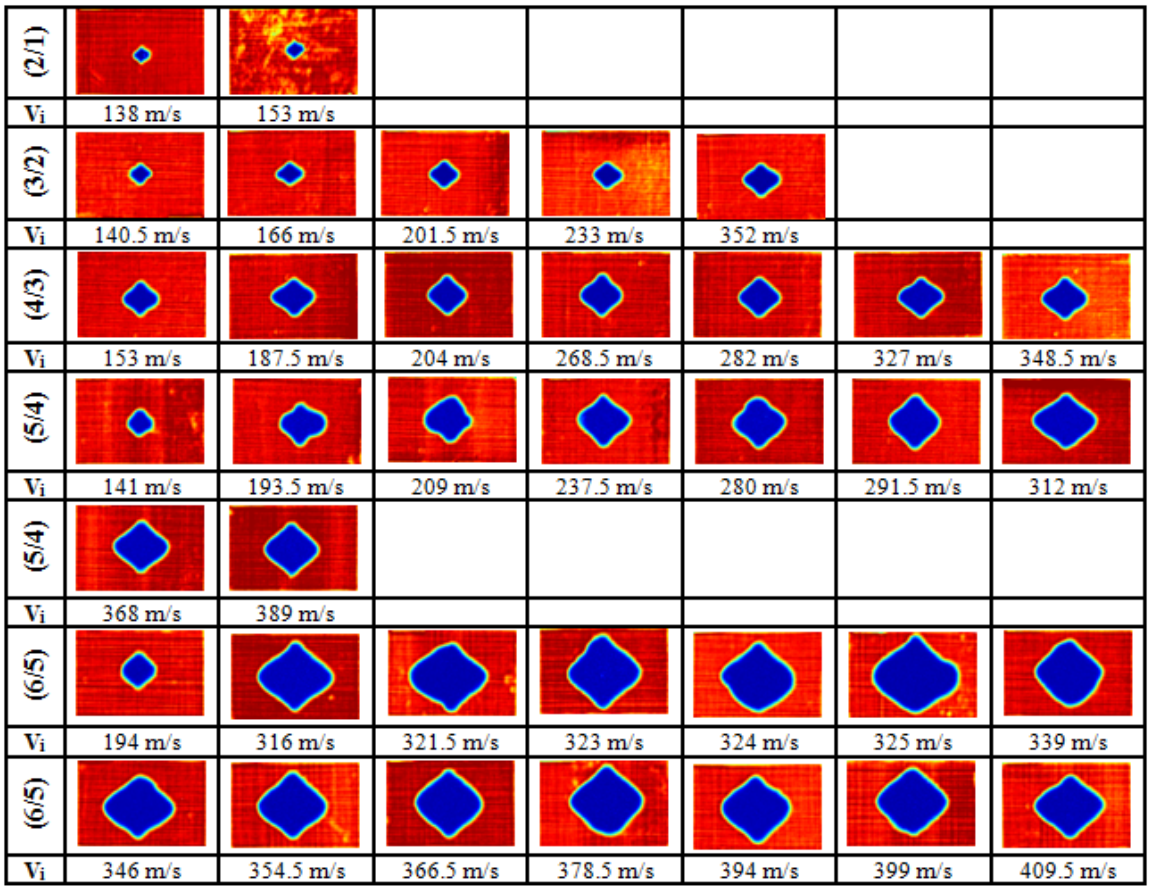

Fig.6.30. Ultrasonic C-scan images of the GLARE 5 FML plates with various thicknesses impacted at different incident velocities.

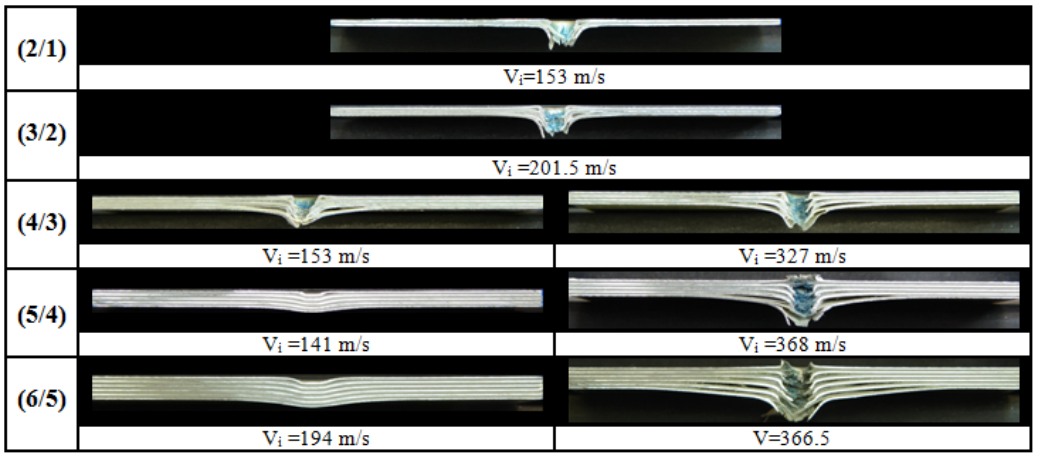

(a) Zoomed-out

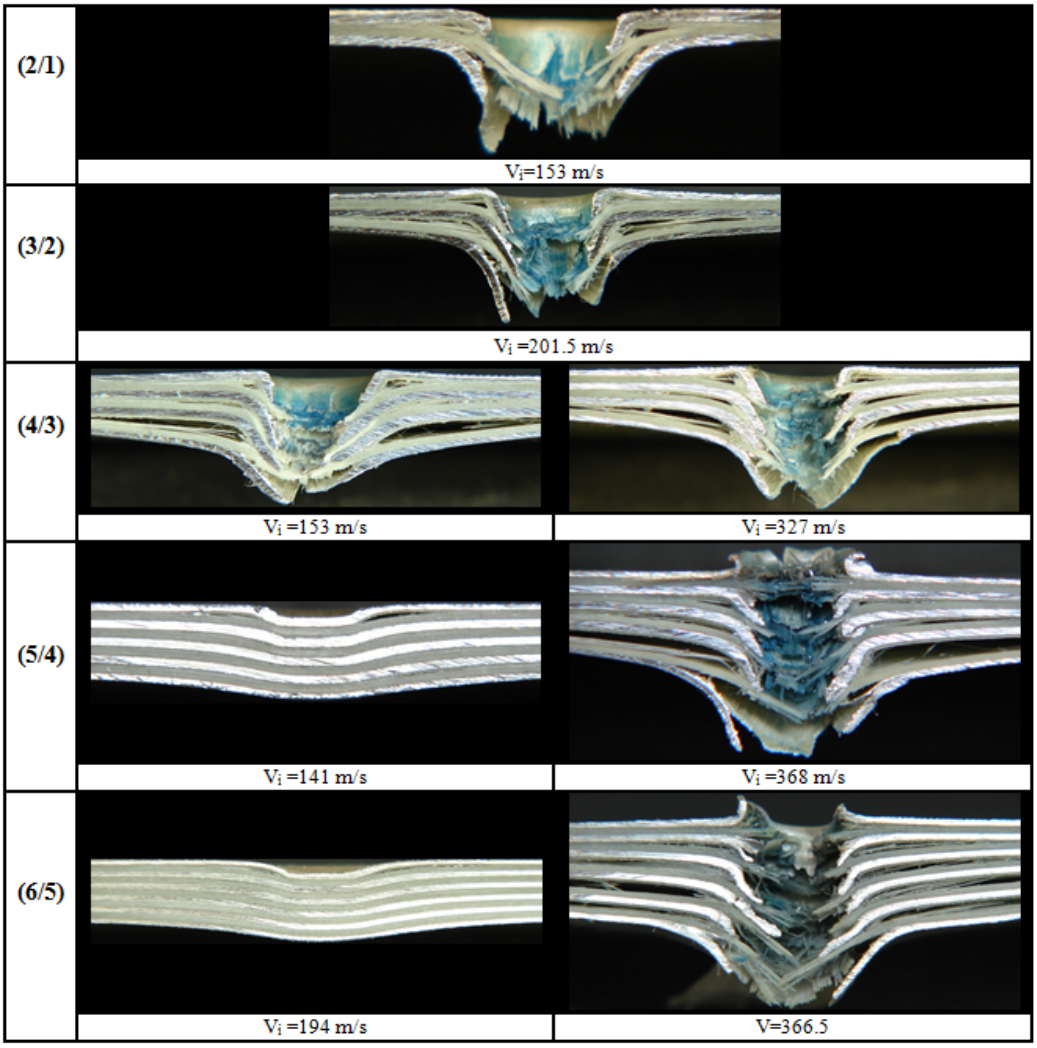

(b) Zoomed-in

Fig.6.31. Cross-sectional (a,b) and side (c) views of the GLARE 5 FML plates with various thicknesses impacted at different incident velocities.

Cross-ply	V_i (m/s)	Side View
(2/1)	157	
	195	
(3/2)	153	
	213	
(4/3)	193	
	295	
	357	
(5/4)	254	
	263	
	283	
(6/5)	196	
	324	
	353	
	400	

(c)

Fig.6.31. (Continued)

The reason for this can be explain by a similar concept as in Ref. [2]. As the specimen became thicker, their relative bending deformation reduced compared to a thinner specimen. Due to the high, localized contact stresses, for the thicker specimen the damage initiated from top and progress toward the bottom of the specimens in a pine tree form (Fig. 6.31(a)). By referring to Fig. 6.30 it is evident that, in general, the damage contour increased as the impact velocity reached its V_{50} value for a given specimen configuration and then it slightly decreased for impact velocity above the V_{50} value. Based on the above-mentioned experimental observations, the FML plates developed damage similar to both monolithic aluminum alloy and polymer composite laminate. It is believed that the interfacial debonding as well as the aluminum layers bending and

stretching are the most important factors in dissipating the impact energy in the GLARE 5 FML plates.

6.2.2. Effect of specimen stacking sequence

The effect of stacking sequence was investigated on the GLARE 5 (3/2) plate specimens with unidirectional $[0°_4]$, cross-ply $[0°/90°]_s$, angle-ply $[\pm45°]_s$ and quasi-isotropic $[0°/\pm45°/90°]$ lay-up orientations.

Figures 6.32 through 6.35 illustrate variation of residual velocity versus incident velocity for the GLARE 5 (3/2) FML plates with unidirectional $[0°_4]$, cross-ply $[0°/90°]_s$, angle-ply $[\pm45°]_s$ and quasi-isotropic $[0°/\pm45°/90°]$ stacking sequences, respectively. Once again, in the figures, experimental data are specified by a solid diamond symbol and the Lambert-Jonas' curves with different P values are shown by dashed lines. Figure 6.36 represents variations of the ballistic limit velocity as a function of specimen stacking sequence for the GLARE 5 (3/2) FML plates. For each individual specimen type, the variation range in its V_{50} is denoted by a deviation bar.

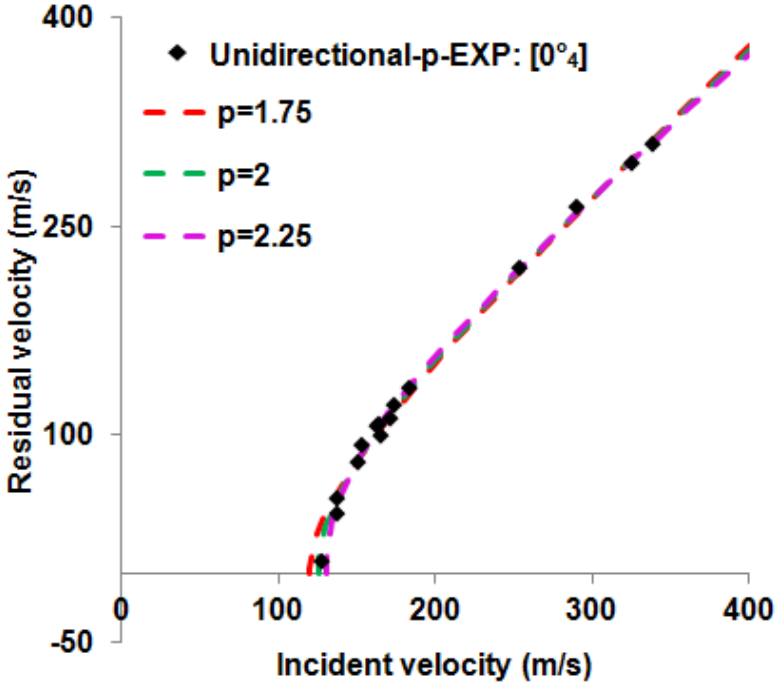

Fig.6.32. Experimental residual velocity *vs*. incident velocity fitted with Lambert-Jonas' equation using different P values for the unidirectional $[0°_4]$ GLARE 5 (3/2) plate specimen.

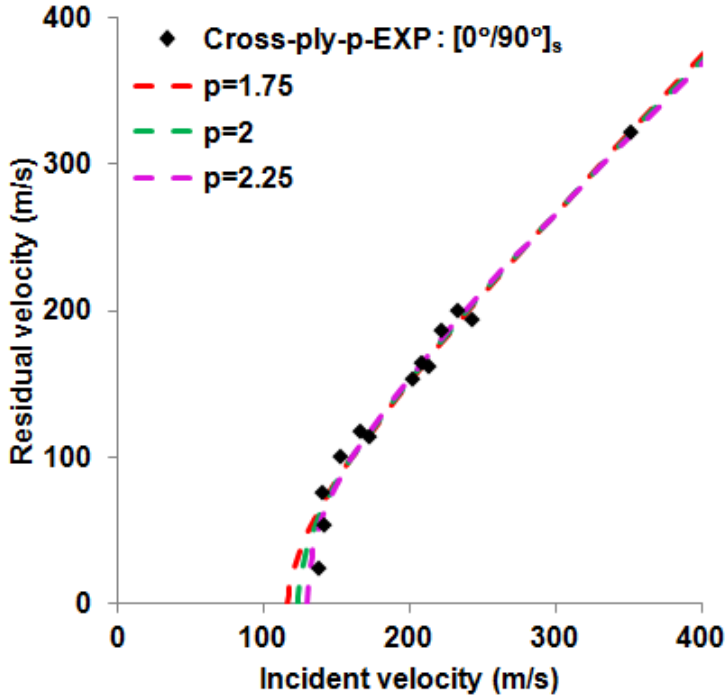

Fig.6.33. Experimental residual velocity *vs*. incident velocity fitted with Lambert-Jonas' equation using different P values for the cross-ply $[0°/90°]_s$ GLARE 5 (3/2) plate specimen.

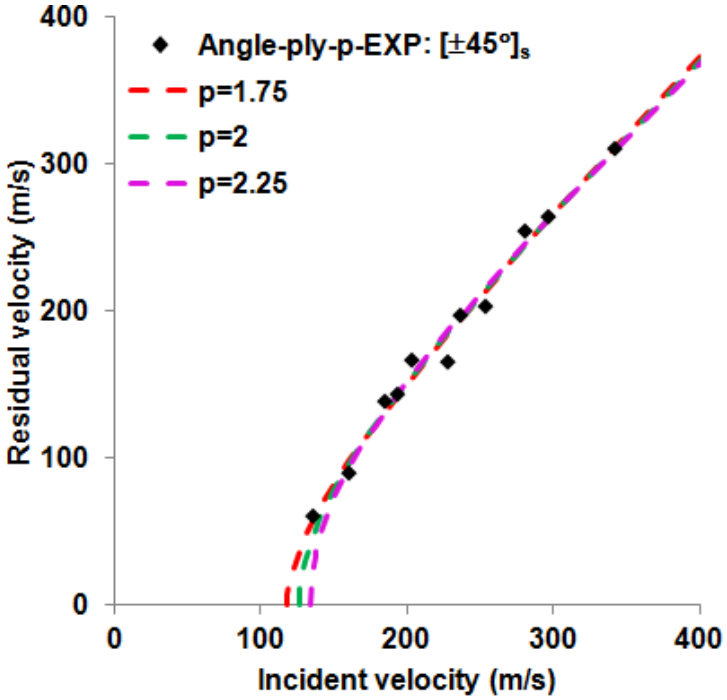

Fig.6.34. Experimental residual velocity *vs*. incident velocity fitted with Lambert-Jonas' equation using different P values for the angle-ply $[\pm 45°]_s$ GLARE 5 (3/2) plate specimen.

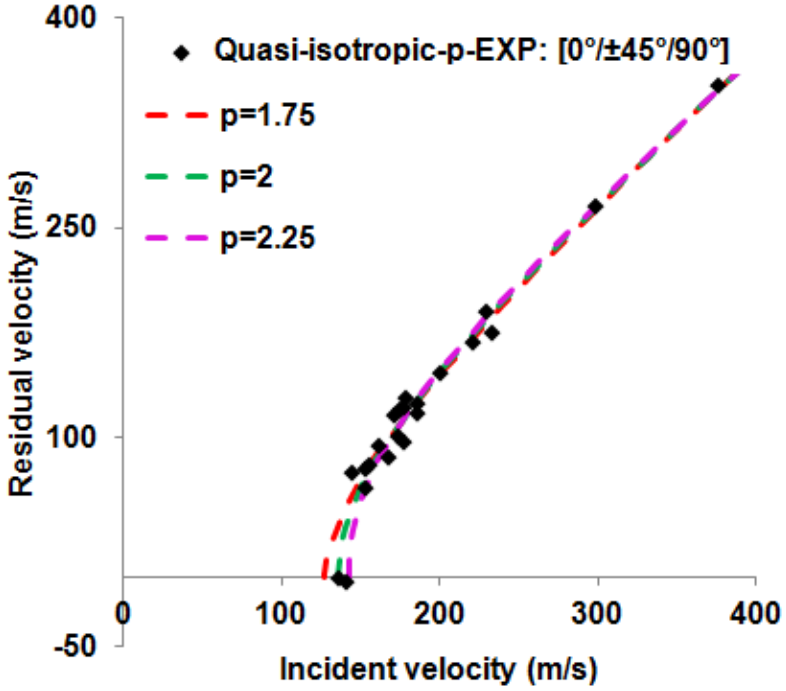

Fig.6.35. Experimental residual velocity *vs*. incident velocity fitted with Lambert-Jonas' equation using different P values for the quasi-isotropic [0°/±45°/90°] GLARE 5 (3/2) plate specimen.

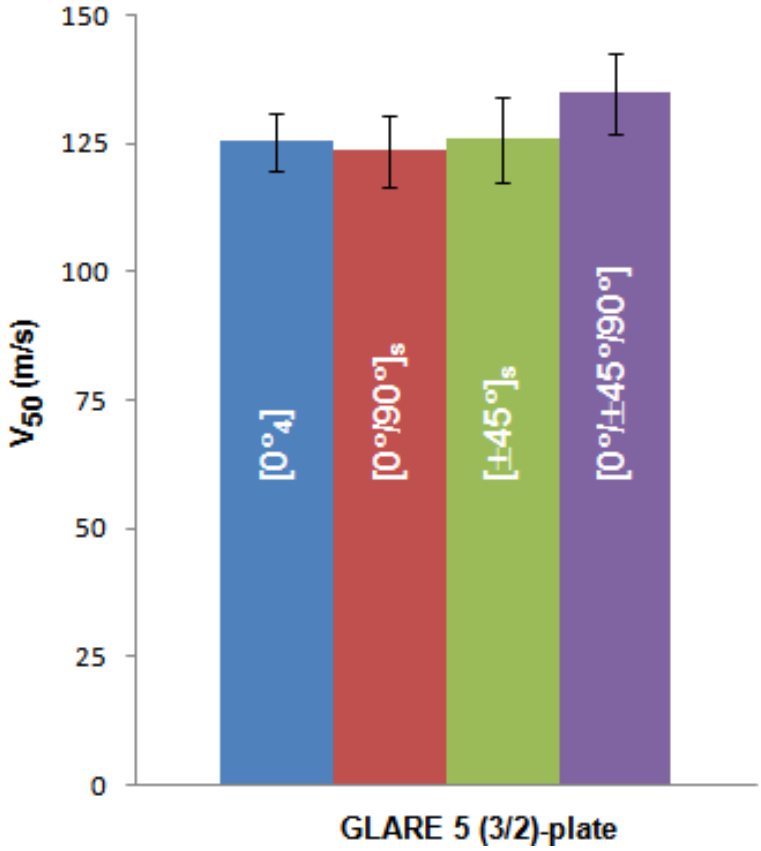

Fig.6.36. Variations of ballistic limit velocity *vs*. stacking sequence for the GLARE 5 (3/2) FML plates.

Among these panel types, the quasi-isotropic specimen offered more resistant to impact, while the ballistic limit was almost the same for the other three types of stacking sequences (Fig. 6.36). Figures 6.37 and 6.38 show front/back side and C-scan views of the GLARE 5 FML plates with various lay-up orientations impacted ballistically at different incident velocities, respectively. The cross-sectional views and some examples of the specimen side views impacted at different incident velocities are given in Fig. 6.39.

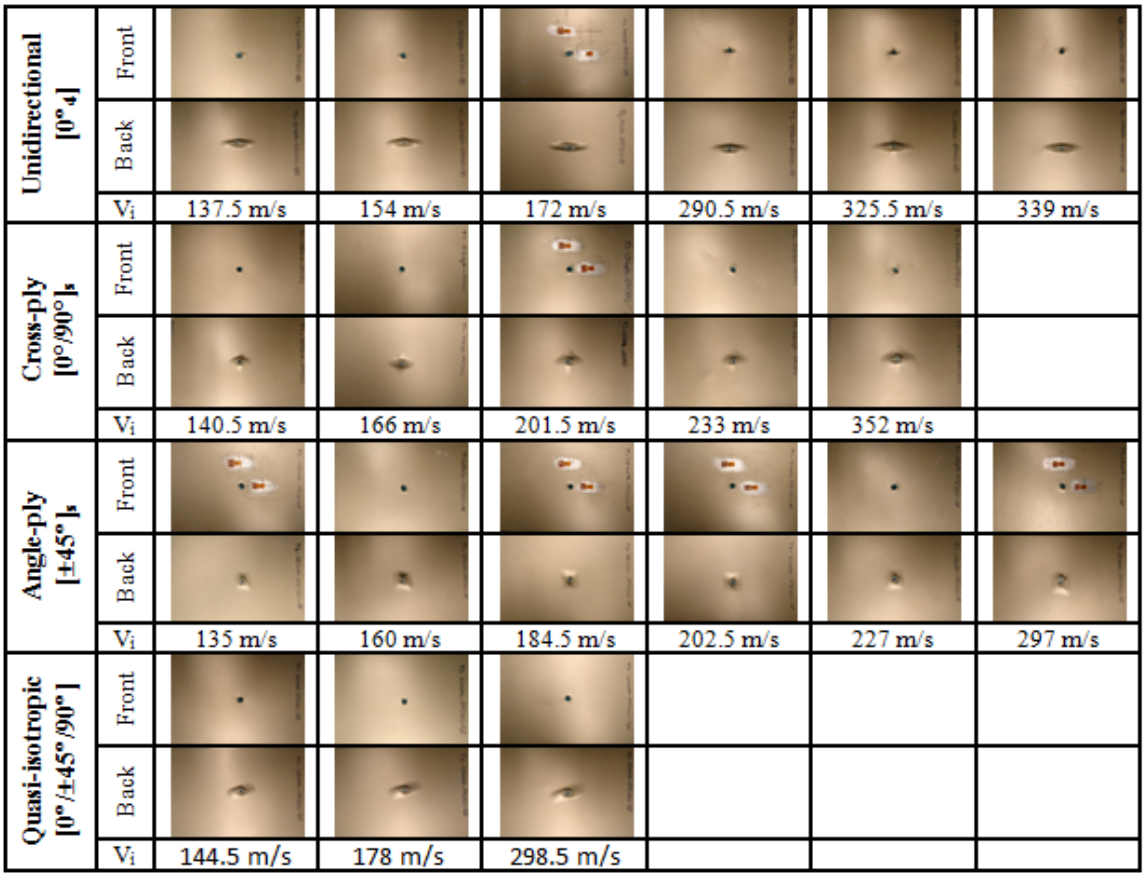

Fig.6.37. Front and back side views of the GLARE 5 FML plates with various stacking sequences impacted at different incident velocities.

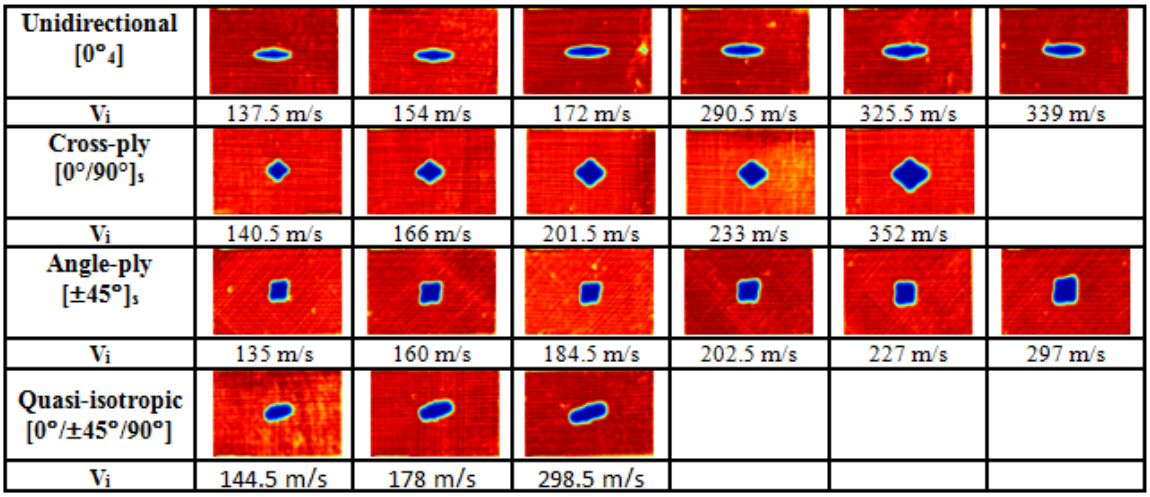

Fig.6.38. Ultrasonic C-scan images of the GLARE 5 FML plates with various stacking sequences impacted at different incident velocities.

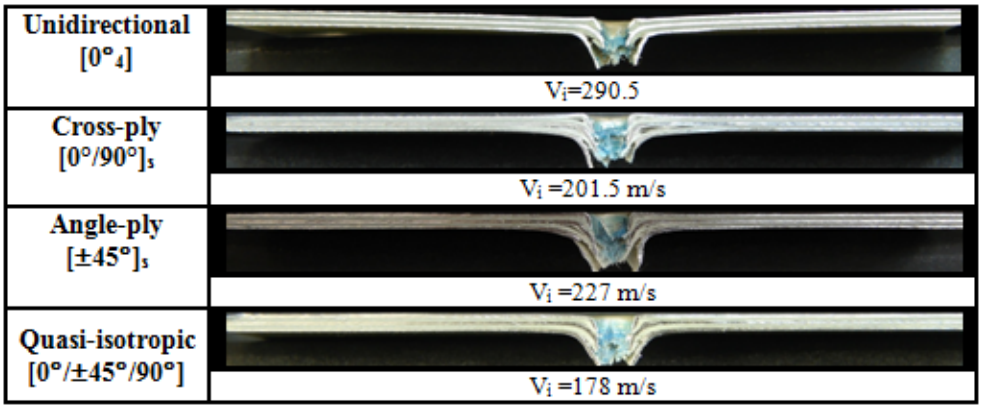

(a) Zoomed-out

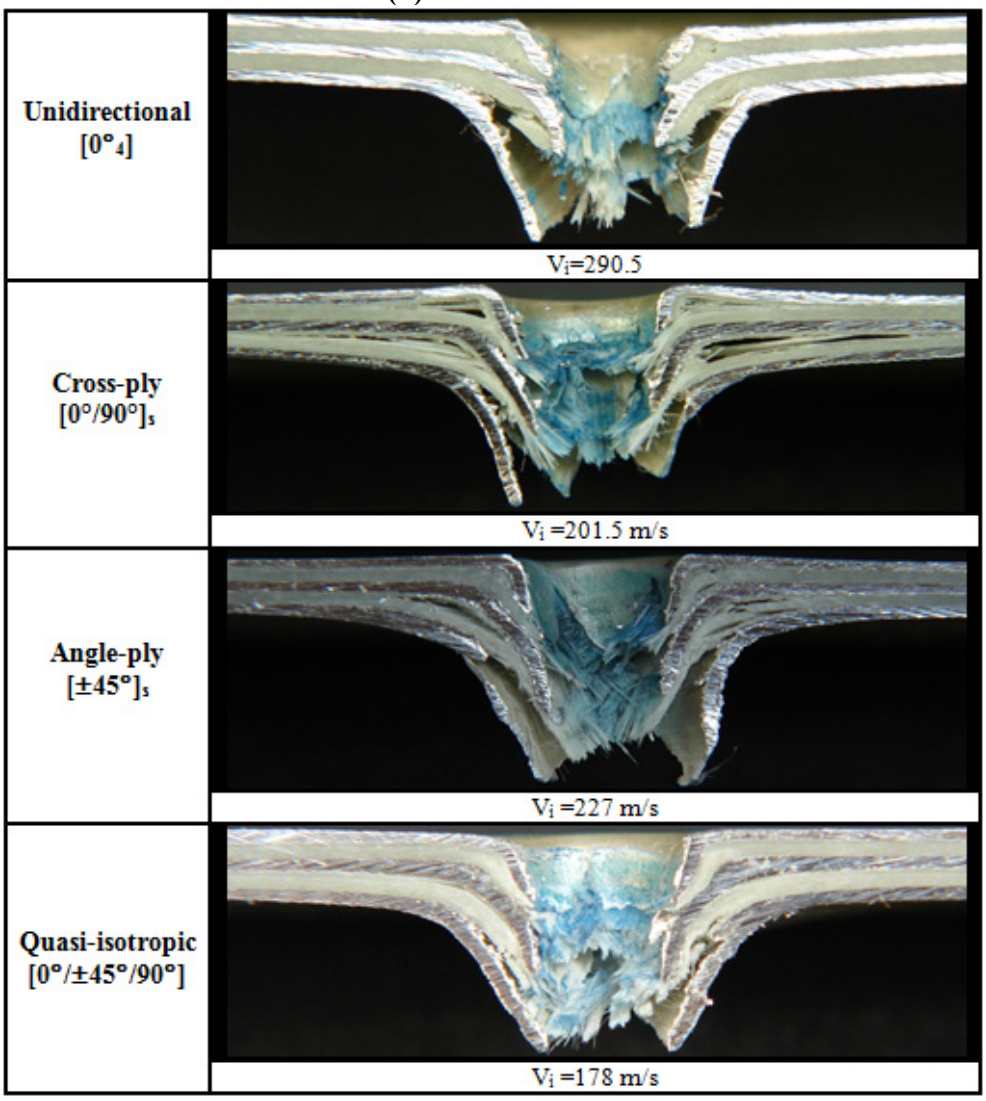

(b) Zoomed-in

Fig.6.39. Cross-sectional (a,b) and side (c) views of the GLARE 5 FML plates with various stacking sequences impacted at different incident velocities.

(3/2)	V_i (m/s)	Side View
Unidirectional $[0°_4]$	150	
cross-ply $[0°/90°]_s$	153	
	213	
angle-ply $[\pm45°]_s$	193	
	253	
Quasi-isotropic [0°/±45°/90°]	167	
	233	

(c)

Fig.6.39. (Continued).

Based on Figs. 6.37 and 6.39, the aluminum layers failed through petalling and plugging. Plastic hinging, as well as localized thinning around the impact point occurred in the aluminum layers. In general, matrix cracking, fiber breakage/splitting/pullout, delamination in prepreg layers and debonding between aluminum and adjacent prepreg layers were observed. Subjected to ballistic impact, the specimen permanent global bending deformations were less pronounced compared to their counterpart beam specimens (Fig. 6.39(c)). Figure 6.38 reveals that an elliptical damage zone occurred for both of unidirectional and quasi-isotropic specimens. On the other hand, the damage zone was in the form of a diamond shape for the cross-ply specimen. The damage pattern for the angle-ply panel was very close to the cross-ply panel except for the orientation of the damage contour. Different damage orientations were expected to take place in the specimens due to the existence of different lay-up orientations. There was not much delamination for the unidirectional specimen (Fig. 6.39(a,b)). This was expected in the interface of the unidirectional prepreg layers since there was no bending stiffness

mismatch in a unidirectional prepreg layer. The occurrence of debonding/delamination was obvious for cross-ply, angle-ply and quasi-isotropic specimens (Fig. 6.39(a,b)).

6.3. Effect of geometry on ballistic impact tests on GLARE 5 FMLs

Figure 6.40 compares the ballistic limit velocities between the cross-ply GLARE 5 plate and beam specimens with different configurations. Both plate and beam specimens had similar V_{50}-thickness trends. As is evident, by transferring from a plate to a beam geometry, the ballistic limit increased slightly. In other words, the ballistic limit velocity was relatively insensitive with respect to change in specimen geometry.

The effect of variation in MVF on ballistic limit for the cross-ply GLARE 5 plate and beam specimen is given in Fig. 6.41. The V_{50}-MVF trends for both geometries were almost similar. Based on the results, for a given number of prepreg laminated layers, there was a slight increase in the ballistic limit velocity as specimen geometry changed from a plate- to a beam-type. It should be mentioned that the representative polynomial equations for Figs. 6.40 and 6.41 were given in Figs. 6.8, 6.9, 6.27 and 6.28.

Figure 6.42 compares the ballistic limit velocities of GLARE 5 (3/2) with various stacking sequences between plate and beam specimens. As is clear from the figure, unidirectional and cross-ply beam specimens offered more resistance to the projectile perforation compared to their plate counterparts. On the other hand, quasi-isotropic plate and beam specimens showed practically the same ballistic limit.

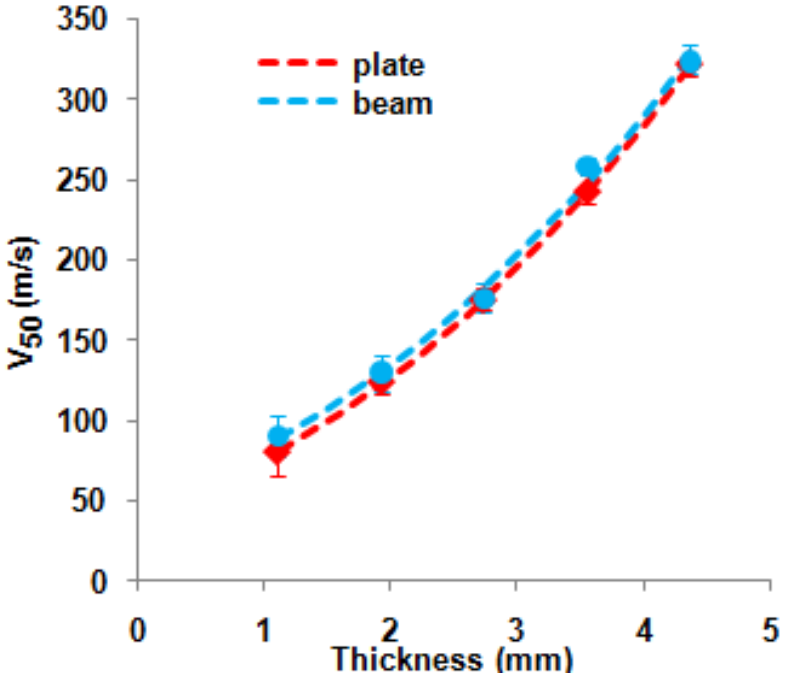

Fig.6.40. Comparison of ballistic limit velocity *vs*. thickness between cross-ply GLARE 5 plate and beam specimens.

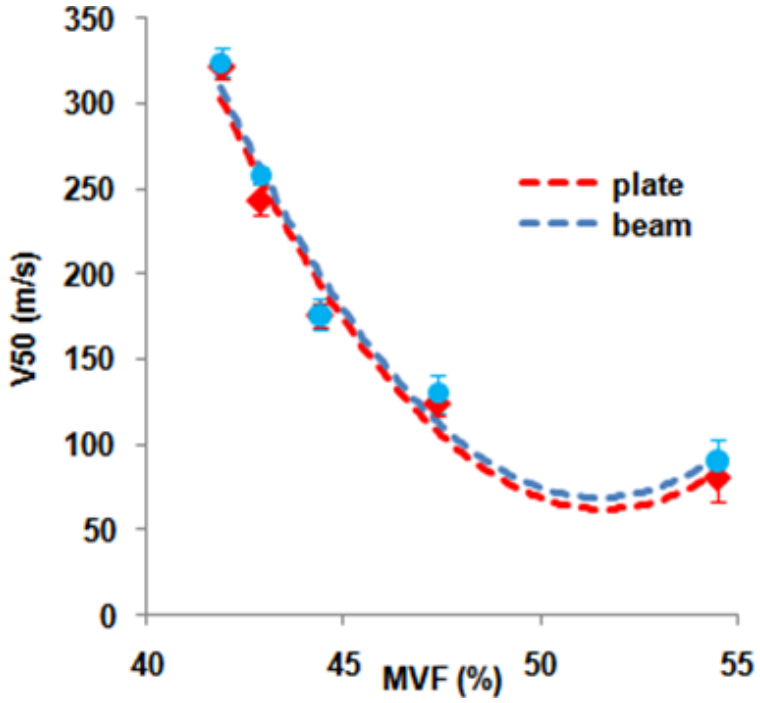

Fig.6.41. Comparison of ballistic limit velocity *vs*. metal volume fraction between cross-ply GLARE 5 plate and beam specimens.

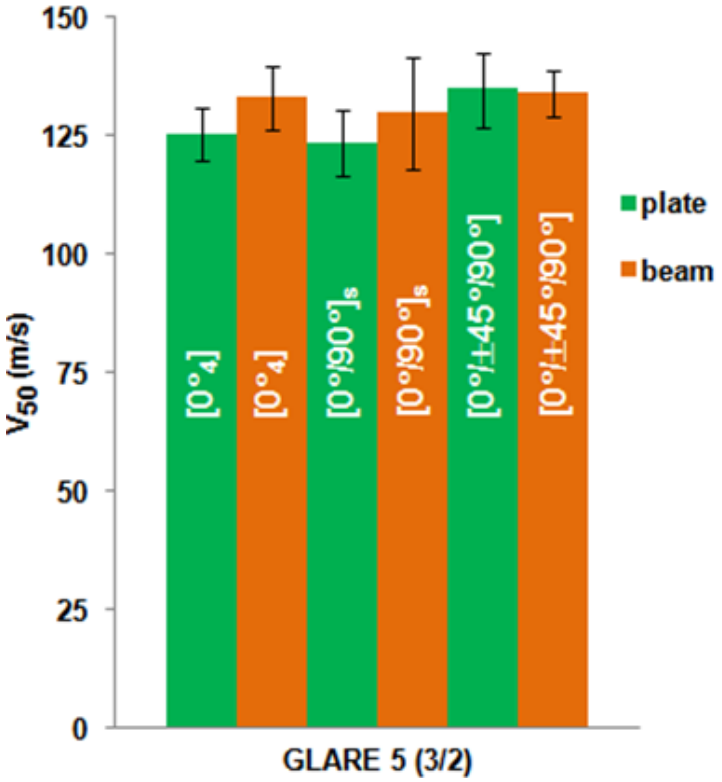

Fig.6.42. Comparison of ballistic limit velocity *vs*. stacking sequence between GLARE 5 (3/2) plate and beam specimens.

It should be mentioned that there are always some uncertainties involved in experimental techniques which would influence the results. In this study, since high velocity is involved, these parameters mainly are related to ballistic impact, namely: picture resolutions obtained from the high-speed camera for determining bullet velocities, data acquisition rate for measuring strains, etc.

6.4. Conclusions

This study presented an experimental investigation on ballistic impact behaviors of the GLARE 5 FML beams and plates of various thicknesses and stacking sequences. The following remarks can be concluded from this study.

- GLARE 5 beam and plate specimens developed damage similar to both monolithic aluminum alloy and polymer composite laminate. The induced internal impact

damage was mostly confined to a relatively small area surrounding the point of impact and its size was smaller than a visible plastically deformed dent on the non-impacted side of the specimens. Moreover, the interfacial debonding as well as the aluminum layers bending and stretching were considered to be the major aspects in dissipating the impact energy in the specimens. However, the permanent global bending deformation of the FML plates was less pronounced compared to the FML beams.

- The classical Lambert-Jonas' equation was very useful in obtaining the ballistic limit velocities, especially for the cases where obtaining lower incident velocity was experimentally difficult.
- For both unidirectional beam specimens, i.e. $[0°_4]$ and $[90°_4]$, a lip-shaped damage contour was induced; whereas it had a diamond shape for the cross-ply specimen. For the quasi-isotropic specimen, the damage zone on the non-impacted side of the specimen was a mixture of the damages introduced in the unidirectional and cross-ply specimens.
- For the FML beams, the unidirectional $[90°_4]$ specimen offered the least resistance to the projectile perforation. In addition, the quasi-isotropic specimen offered slightly higher V_{50} compared to the unidirectional $[0°_4]$ and cross-ply $[0°/90°]_s$ specimens. Except for the unidirectional $[90°_4]$ specimen, ballistic limit was almost invariant with respect to change in stacking sequence.
- The optical images from the non-impacted side of the FML plates revealed that the plastically deformed damage zone appeared on the non-impacted side of the specimens increased by increasing the specimen thickness for a given velocity range.

- The ultrasonic C-scan results of the plate specimens suggested that the damage contour increased as the impact velocity reached its V_{50} value for a given specimen thickness and then it slightly decreased above its V_{50} value. On the other hand, by increasing the panel thickness for a given impact velocity range, the damage contour also increased.
- For the FML plates, an elliptical damage zone occurred for both unidirectional and quasi-isotropic specimens. On the other hand, the damage zone was in the form of a diamond shape for the cross-ply specimen. The damage pattern for the angle-ply panel was similar to the cross-ply panel except for the orientation of the damage contour.
- For the FML plates, the quasi-isotropic specimen offered relatively more resistant to ballistic impact compared to other type of stacking sequences. Also based on the results, the ballistic limit was almost insensitive with stacking sequence variation for the (3/2) configuration.
- For both plate and beam specimens, the ballistic limit velocity increased parabolically as the thickness increased and decreased as the metal volume fraction increased.
- By changing from the plate to the beam geometry, the ballistic limit increased slightly. For a given number of prepreg laminated layers, there was a slight increase in the ballistic limit velocity as specimen geometry switched from the plate to the beam.
- The unidirectional and cross-ply beam specimens offered more resistance to the projectile perforation compared to their plate counterparts. On the other hand, quasi-isotropic plate and beam specimens had almost the same ballistic limit.

CHAPTER 7: FINITE ELEMENT ANALYSIS

In this chapter, the ballistic impact on the GLARE 5 FMLs with various thicknesses, stacking sequences and geometries was modeled and analyzed using the finite element (FE) software, LS-DYNA. To validate the reliability of the model, the FE results were compared to those obtained experimentally. These results include the incident projectile impact velocity versus the residual velocity (V_I~V_R), damage patterns, and bullet residual length. The validated FE model was then used to extract some useful information in which experimental results were not available.

7.1. Material models

(a) MAT_SIMPLIFIED_JOHNSON_COOK (MAT_98)

Johnson and Cook express the flow stress as (MAT_15) [98]:

$$\sigma_y = \left(A + B\bar{\varepsilon}^{p^n}\right)(1 + C \ln \dot{\varepsilon}^*)\left(1 - T^{*m}\right) \tag{7.1}$$

where

A, B, C, n and m are user-defined input constants, and:

$\bar{\varepsilon}^p$ effective (equivalent) plastic strain

$\dot{\varepsilon}^* = \frac{\dot{\bar{\varepsilon}}}{\dot{\varepsilon_0}}$ dimensionless plastic strain rate for $\dot{\varepsilon_0} = 1\ \mathrm{s}^{-1}$

$T^* = \frac{T - T_{room}}{T_{melt} - T_{room}}$ homologous temperature

The strain at fracture is given by:

$$\varepsilon^f = [D_1 + D_2 \exp D_3\sigma^*][1 + D_4 \ln \varepsilon^*][1 + D_5\, T^*] \tag{7.2}$$

where D_i, i=1,...,5 are input constants and σ^* is the ratio of pressure (mean stress) divided by effective (Von-Mises) stress:

$$\begin{cases} \sigma^* = \dfrac{P}{\sigma_{eff}} \\ \sigma_{eff} = \left(\dfrac{3}{2} S_{ij} S_{ij}\right)^{\frac{1}{2}} \end{cases} \tag{7.3}$$

where S_{ij} is the deviatoric stress tensor.

Fracture occurs when the damage parameter (D) given in Eq. (7.4) reaches the value 1.

$$D = \sum \frac{\Delta \bar{\varepsilon}^P}{\varepsilon^f} \tag{7.4}$$

For the simplified Johnson-Cook material model (Mat_98), Eq. (7.1) reduces to:

$$\sigma_y = \left(A + B\bar{\varepsilon}^{p^n}\right)(1 + C \ln \dot{\varepsilon}^*) \tag{7.5}$$

In the simplified model, thermal effects and damage are ignored [98].

(b) MAT_COMPOSITE_DAMAGE (MAT_22)

It is also called the Chang-Chang composite damage model [99,100]. This model is a linear-orthotropic material model with brittle failure. For this model, five material parameters are used:

S_1= Longitudinal tensile strength

S_2= Transverse tensile strength

S_{12}= Shear strength

C_2= Transverse compressive strength

α= Nonlinear shear stress parameter

S_1, S_2, S_{12}, and C_2 are obtained from material strength measurements and α is defined by a material shear stress-strain measurements. In this model three failure criteria are possible, namely: matrix cracking, compression and fiber breakage failures. These criteria are described below [101].

(1) Matrix cracking failure: the matrix cracking failure criterion is determined from

$$\begin{cases} F_{matrix} = \left(\frac{\sigma_2}{S_2}\right)^2 + \bar{\tau} \\ \bar{\tau} = \dfrac{\frac{{\tau_{12}}^2}{2G_{12}} + \frac{3}{4}\alpha {\tau_{12}}^4}{\frac{{S_{12}}^2}{2G_{12}} + \frac{3}{4}\alpha {S_{12}}^4} \end{cases} \tag{7.6}$$

here σ_2 is the tensile stress in the transverse direction whereas τ_{12} is the in-plane shear stress between fibers and matrix. Failure is assumed whenever $F_{matrix}>1$. Once $F_{matrix}>1$, then the material constants E_2 (Young's modulus in the transverse direction), G_{12} (in-plane shear modulus in the 1-2 plane), ν_{12} and ν_{21} (generalized Poisson's ratios in the 1-2 plane) are set to zero.

(2) Compression failure: the compression failure criterion is given as

$$F_{comp} = \left(\frac{\sigma_2}{2S_{12}}\right)^2 + \left[\left(\frac{C_2}{2S_{12}}\right)^2 - 1\right]\frac{\sigma_2}{C_2} + \bar{\tau} \tag{7.7}$$

Failure is assumed when $F_{comp}>1$. When this type of failure occurs, the material constants E_2, ν_{12} and ν_{21} are all set to zero.

(3) Fiber breakage failure: the fiber breakage failure criterion is defined as

$$F_{fiber} = \left(\frac{\sigma_1}{S_1}\right)^2 + \bar{\tau} \tag{7.8}$$

where σ_1 is the tensile stress in the longitudinal direction. Failure is assumed whenever $F_{fiber}>1$. If $F_{fiber}>1$, then the constants E_1 (Young's modulus in the longitudinal direction), E_2, G_{12}, ν_{12} and ν_{21} are set to zero.

(c) MAT_ADD_EROSION (MAT_00)

Many of the constitutive models in LS-DYNA do not allow failure and erosion. Hence, MAT_ADD_EROSION failure criteria were adapted to all the materials used here. In this

study a strain-based failure criterion was used for element erosion; that is, when $\varepsilon \geq \varepsilon_{erosion}$, the element was eroded and removed from the calculations.

The aluminum layers as well as the 0.22 caliber copper bullet were modeled using the simplified Johnson-Cook material model. Their material parameters are given in Table 7.1 [102,103]. The Chang-Chang damage model was employed for the prepreg layers. The mechanical properties of unidirectional S2-glass/epoxy composite are described in Table 7.2 (some data were provided by the Structural Laminates Company). The shear modulus, i.e. G_{23}, was assumed to be the same as the other two shear moduli, G_{12} and G_{31}, as suggested in Ref. [104].

Table7.1. Material model parameters used for the 2024-T3 aluminum-alloy layers and 0.22 copper bullet.

Parameter	**Notation**	**2024-T3 Aluminum-Alloy [102]**	**0.22 Copper Bullet [103]**
Density [kg/m^3]	ρ	2770	–
Poisson's ratio	ν	0.33	0.33
Young's modulus [GPa]	E	73.084	117.21
Static yield limit [MPa]	A	369	4.36
Strain hardening modulus	B	684	457.81
Strain hardening exponent	n	0.73	0.37575
Strain rate coefficient	C	0.0083	0

Vlot et al. [105] attributed the increase in energy absorption of GLARE to the significant increase of tensile strength of glass fibers at very high-strain rate. It was reported by Armenakas et al. [106] that the stiffness of unidirectional glass/epoxy laminates increased by about 50% when loaded to strain rates of about 500 s^{-1}. One of the drawbacks of the

Chang-Chang damage model is that there is no strain rate effect involved in it. Hence, in order to capture the rate effect in the prepreg layers, Young's moduli and longitudinal tensile strength, i.e. along the fiber direction, were varied up to a factor of 1.5 of their static values. These modifications were only made for the (6/5) configuration under higher impact velocities.

Table7.2. Material model parameters used for the unidirectional S2-glass/epoxy prepreg layers.

Parameter	Notation	UD S2-Glass/Epoxy Prepreg
Density [kg/m^3]	ρ	2000
Poisson's ratio	PRBA(ν_{21})	0.0575
	PRCA(ν_{31})	0.0575
	PRCB(ν_{32})	0.33
Young's modulus [GPa]	EA(E_1)	54
	EB(E_2)	9.4
	EC(E_3)	9.4
Shear modulus [GPa]	GAB(G_{12})	5.6
	GBC(G_{23})	5.6
	GCA(G_{31})	5.6
Shear strength [MPa]	SC(S_{12})	76
Longitudinal tensile strength [MPa]	XT(S_1)	1900
Transverse tensile strength [MPa]	YT(S_2)	57
Transverse compressive strength [MPa]	YC(C_2)	285
Nonlinear shear stress parameter	α	–

7.2. Contact and delamination/debonding model

The contact between adjacent layers in the FML was defined using the option, CONTACT_AUTOMATIC_SURFACE_TO_SURFACE_TIEBREAK. This contact

definition was particularly chosen to allow delamination/debonding between adjacent layers. Furthermore, it was assumed that delamination/debonding between the layers were governed by the criterion [98]:

$$\left[\frac{\sigma_n}{NFLS}\right]^2 + \left[\frac{\sigma_s}{SFLS}\right]^2 \geq 1 \tag{7.9}$$

where σ_n and σ_s are normal and shear stresses acting on the layer interface, respectively; while NFLS and SFLS are normal and shear strengths of interface, respectively. It was also assumed that delamination/debonding occurred mainly by shear failure. Hence, NFLS was set to a very large number and therefore delamination/debonding in the model was governed by SFLS. Since SFLS was not obtained experimentally, it was varied in order to fit experimental results.

ERODING_SURFACE_TO_SURFACE contact model was defined between the projectile and FML. This model allows elements to be eroded from both projectile and target when certain failure criteria are met.

7.3. FE modeling of ballistic impact tests on GLARE 5 FML beams

Figure 7.1 exhibits perspective views of the composite beam and bullet. Several attempts were made to optimize the FE model based on the number of elements and mesh size using the available computational power. The results indicated that by refining the mesh size, smoother results were obtained. In order to ensure that by further decreasing the mesh size the result would not change, an additional mesh with very fine elements was created using a super-power computer and compared to the one shown in Fig. 7.1. The results suggested that the FE obtained V_I~V_R data were invariant with respect to the change in mesh size. As a result, the mesh shown in Fig. 7.1 was considered in this study. To reduce computational time, finer mesh was used around the impact area, which is the

critical location; while coarser mesh was considered as moving away from the impact center. In order to further decrease computational time, only a quarter-symmetric model was considered in this study due to the double symmetry of the specimen-projectile system. Two elements were used in the through-thickness direction for each aluminum layer; whereas 1 element was considered for each ply in the prepreg composite layer. That is, a total of 4 elements was used to simulate the assembly of each $[0°/90°]_s$ lamina in its through-thickness direction.

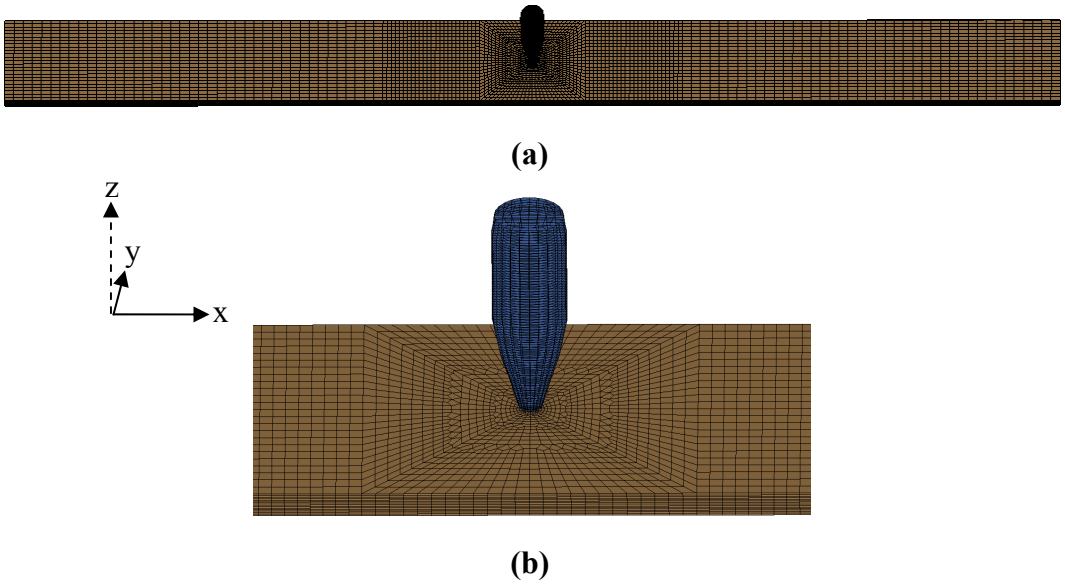

Fig.7.1. Perspective views of the finite element simulation model: (a) far-off view, (b) close-up view.

For instance, the GLARE 5 (2/1) was model with 8 elements in the thickness direction. The quarter of the projectile was modeled using 1,125 solid elements. The mesh density for the projectile was chosen in such a way that good contact between the specimen and projectile was maintained during impact (Fig. 7.1). The GLARE 5 (2/1) quarter-symmetric specimen model consisted of 8,880 one-point-integration 8-node solid brick elements. It should be mentioned that the prepreg in-plane material directions, i.e. 1

(corresponds to the 0° fiber direction) and 2 (corresponds to the 90° fiber direction), were aligned with the global x and y axes, and the through-thickness material direction 3 was aligned with the global z axis, respectively. In addition, a fixed-fixed boundary condition was used in this study.

7.3.1. Model validation of GLARE 5 FML beams: thickness effect

Figures 7.2 through 7.6 compare the FE predictions with experimental V_I~V_R data for the cross-ply GLARE 5 FML beams with various configurations. The FE results are shown by a circular symbol. As is apparent, the FE predictions are in excellent agreement with the experimental results. The comparison between experimental and FE results of ballistic limit as a function of specimen thickness is illustrated in Fig. 7.7. The variations in the results are demonstrated by deviation bars. The FE prediction is in good agreement with its experimental counterpart.

Next, post-impact damage prediction from the FE analysis was compared to its experimental counterpart. The results are shown in Figs. 7.8 through 7.12 for various specimen thicknesses impacted at different speeds. There is good agreement in damage pattern between the FE models and experiments. Moreover, it should be noted that the broken/split fibers, which appeared around the impact area of the specimens, were not seen that much in the FE predictions. This was due to the strain-based-element-erosion criterion used in the FE models. The failed elements were eroded and removed from the FE calculations. Therefore, they are not presented in the comparisons. Another factor, which was considered to validate the FE models, was the bullet residual length. This is depicted in Fig. 7.13. It is evident that the bullet residual length obtained from the experiments and FE is also in good agreement.

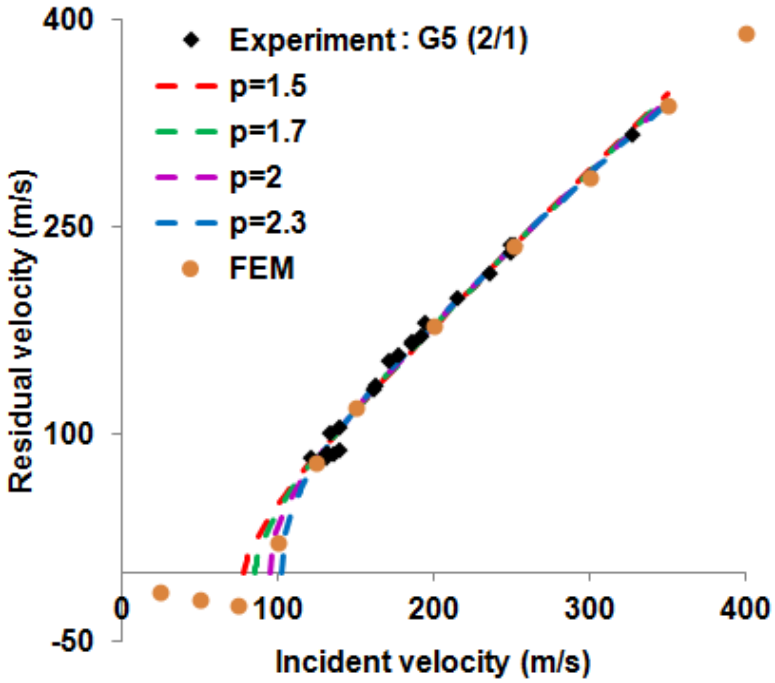

Fig.7.2. Comparison between experimental and FEM residual-incident velocity trend for the GLARE 5 (2/1) beam specimen.

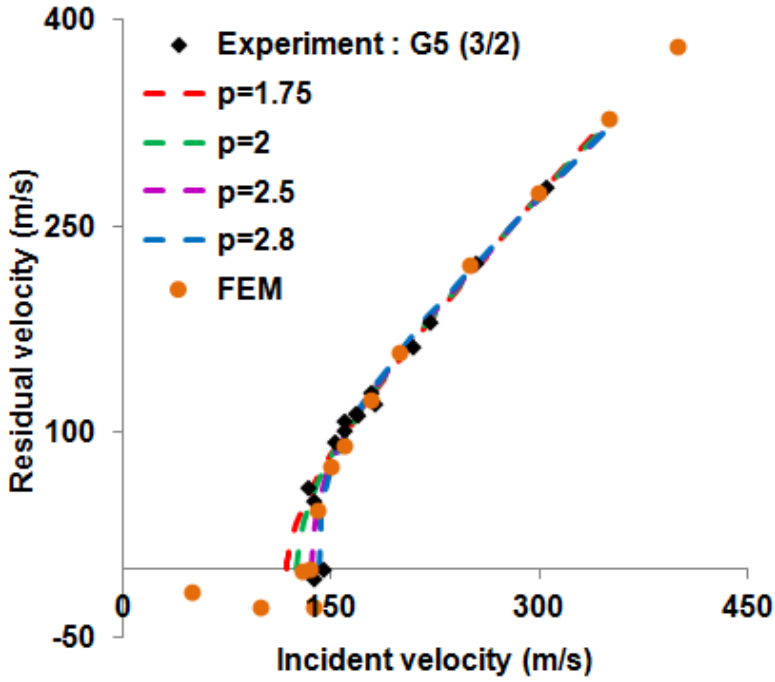

Fig.7.3. Comparison between experimental and FEM residual-incident velocity trend for the GLARE 5 (3/2) beam specimen.

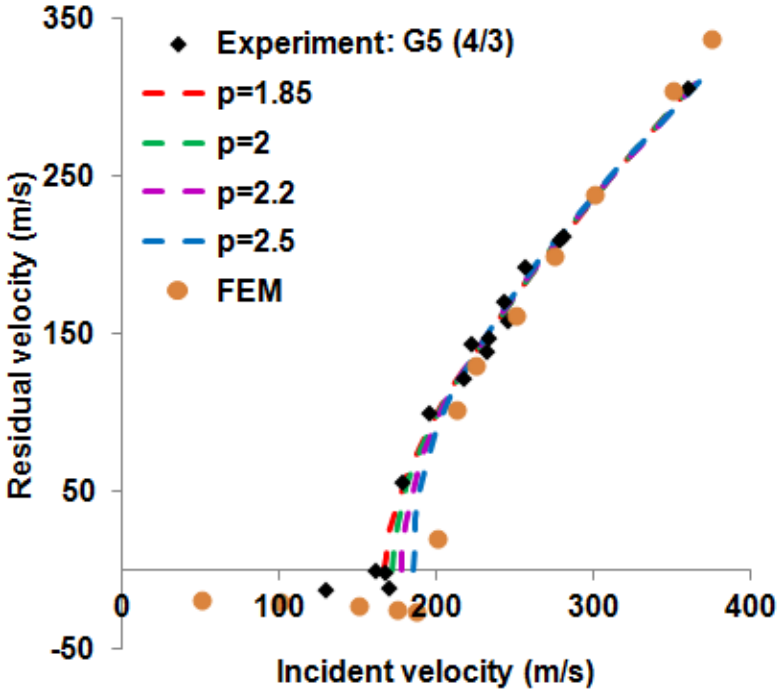

Fig.7.4. Comparison between experimental and FEM residual-incident velocity trend for the GLARE 5 (4/3) beam specimen.

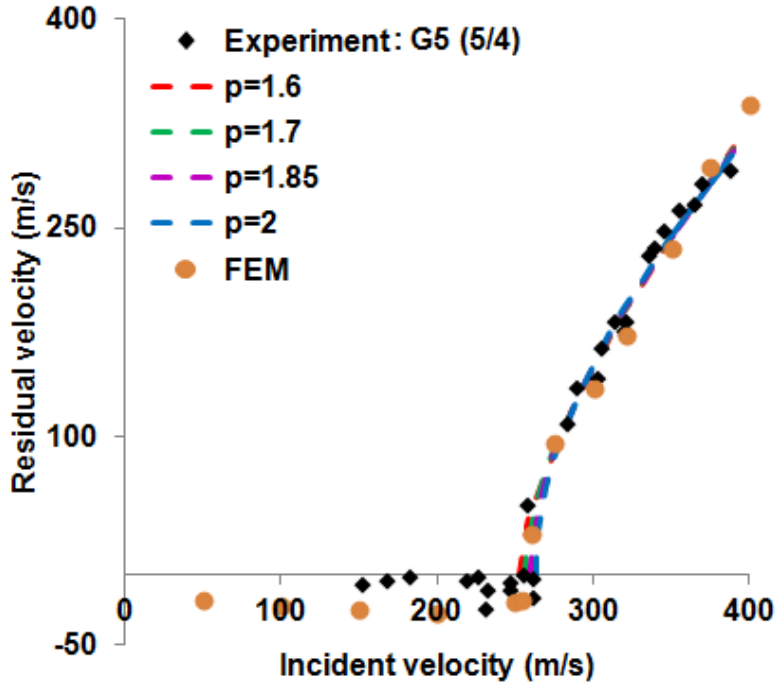

Fig.7.5. Comparison between experimental and FEM residual-incident velocity trend for the GLARE 5 (5/4) beam specimen.

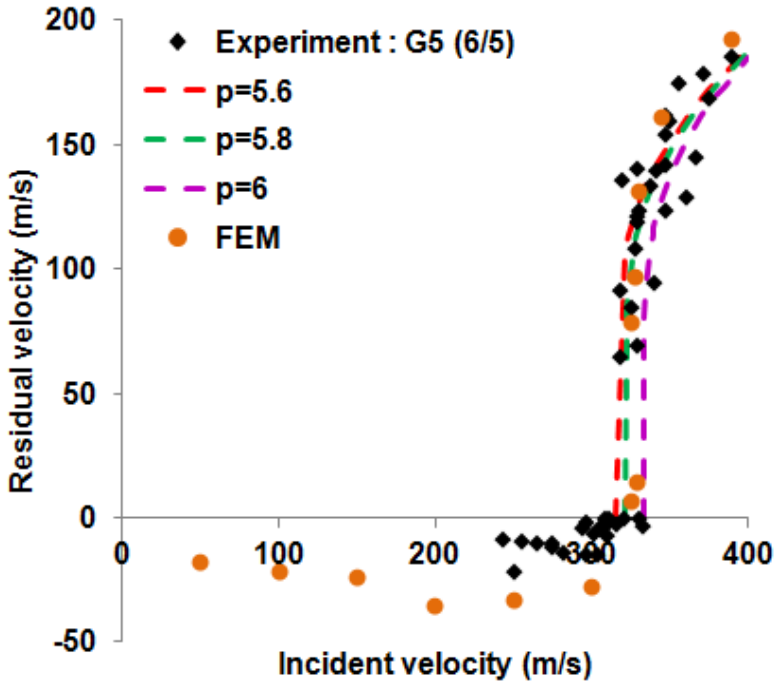

Fig.7.6. Comparison between experimental and FEM residual-incident velocity trend for the GLARE 5 (6/5) beam specimen.

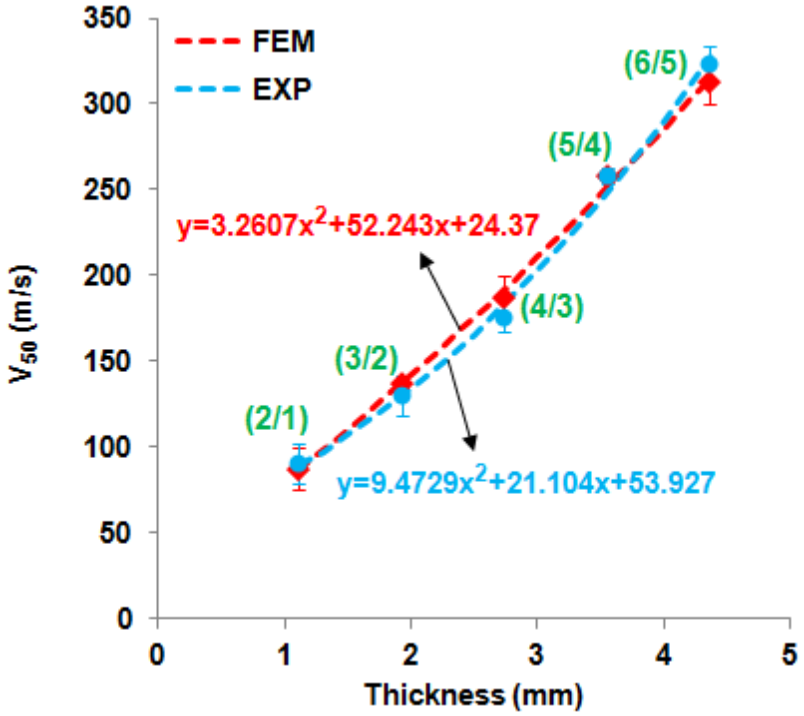

Fig.7.7. Comparisons between experimental and FE results of ballistic limit velocity (V_{50}) as a function of beam-specimen thickness. In the equations x stands for thickness and y for V_{50}.

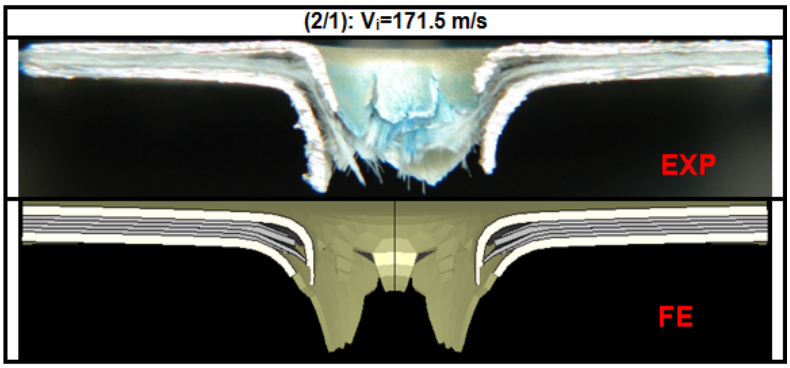

Fig.7.8. Comparisons of post-impact damage patterns for the GLARE 5 (2/1) beam specimen impacted at 171.5 m/s.

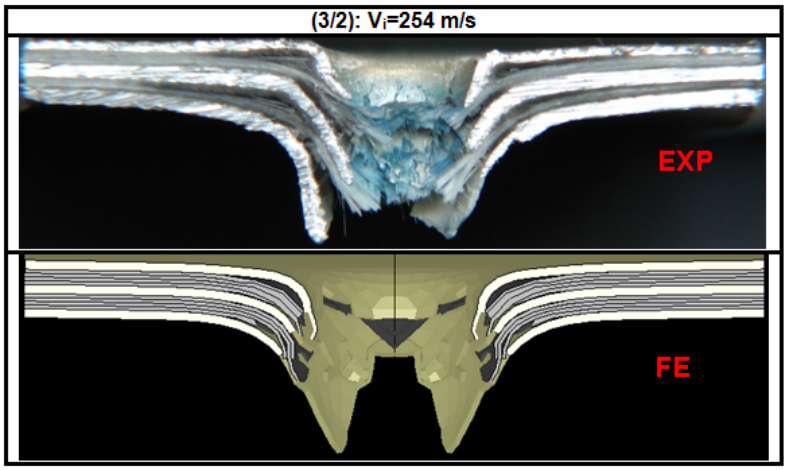

Fig.7.9. Comparisons of post-impact damage patterns for the GLARE 5 (3/2) beam specimen impacted at 254 m/s.

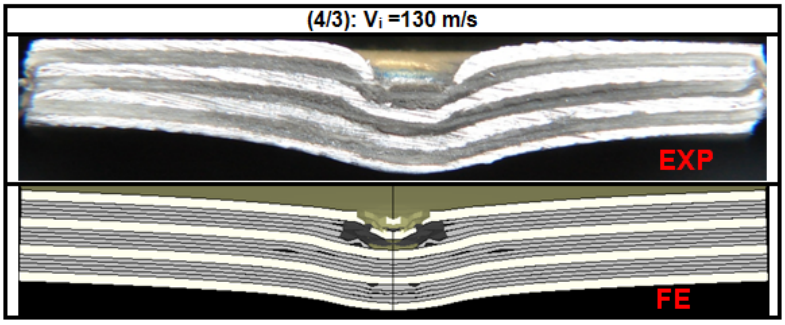

(a)

Fig.7.10. Comparisons of post-impact damage patterns for the GLARE 5 (4/3) beam specimen impacted at: (a) 130 m/s and (b) 234 m/s.

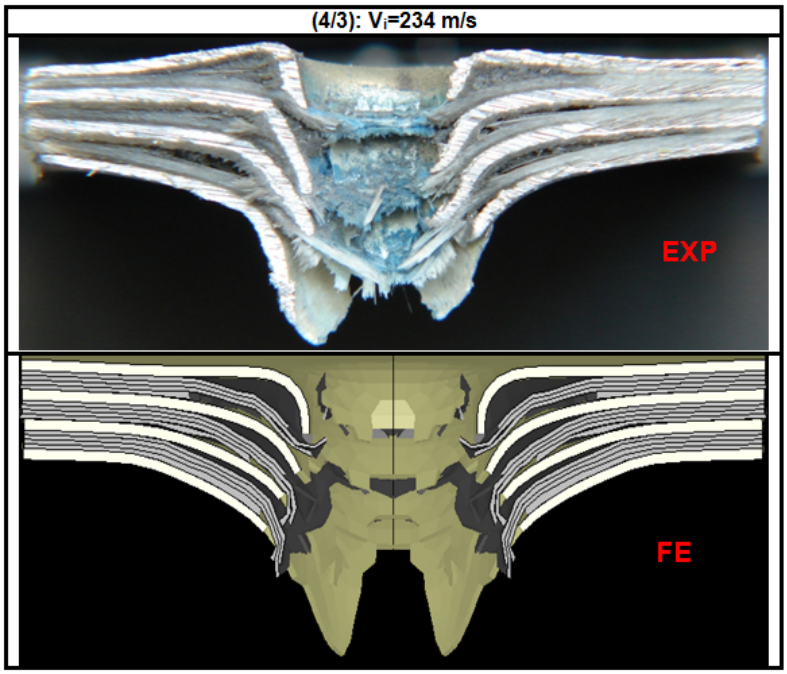

(b)

Fig.7.10. (Continued).

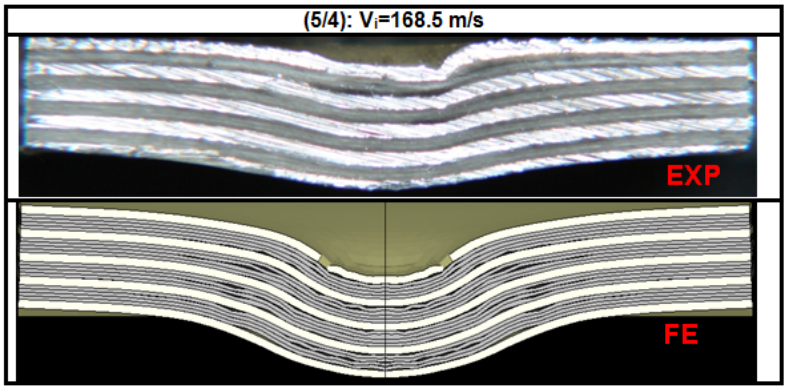

(a)

Fig.7.11. Comparisons of post-impact damage patterns for the GLARE 5 (5/4) beam specimen impacted at: (a) 168.5 m/s and (b) 321.5 m/s.

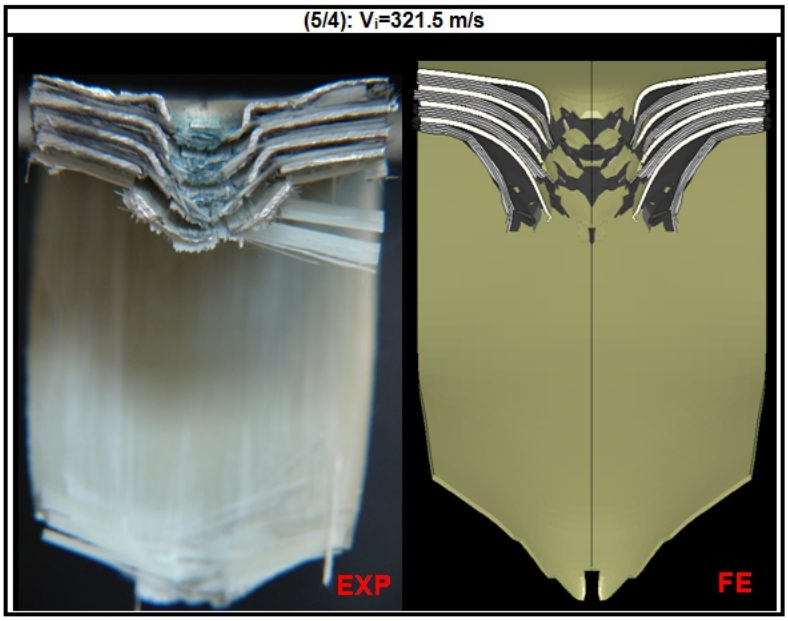

(b)

Fig.7.11. (Continued).

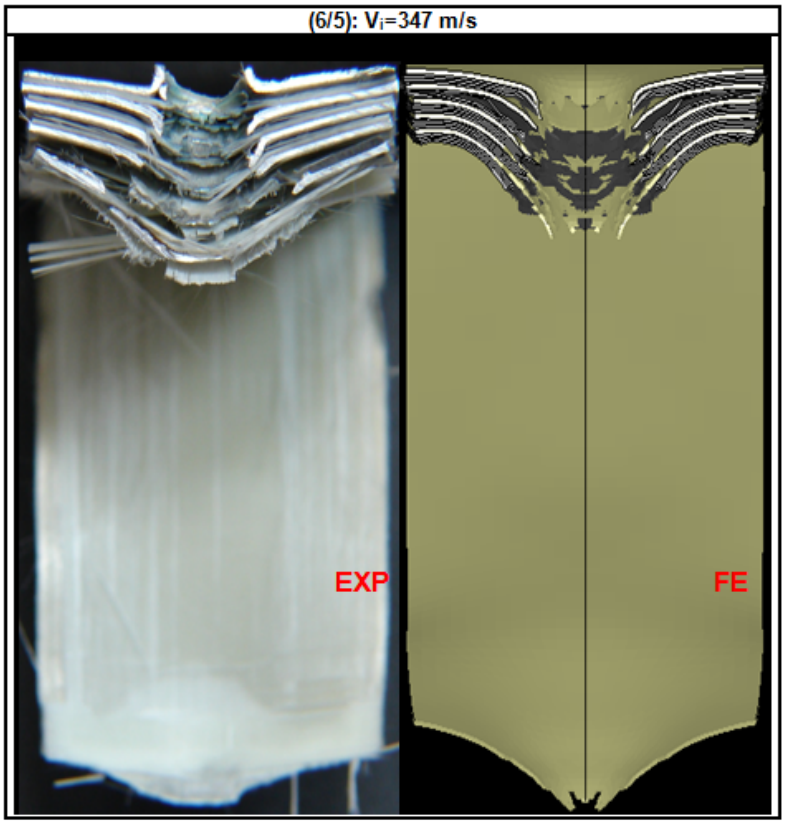

Fig.7.12. Comparisons of post-impact damage patterns for the GLARE 5 (6/5) beam specimen impacted at 347 m/s.

GLARE 5 [beam]	Experiment		Finite Element Model		ΔL
	Bullet Residual Length (mm)	Bullet	Bullet Residual Length (mm)	Bullet	Length Difference (mm)
(2/1) V_i=171.5 m/s	16.52		16.43		0.09
(3/2) V_i=254 m/s	15.88		15.16		0.72
(4/3) V_i=130 m/s	15.56		13.54		2.02
(4/3) V_i=234 m/s	14.76		14.22		0.54
(5/4) V_i=321.5 m/s	12.95		12.79		0.16
(6/5) V_i=347 m/s	12.35		9.83		2.52

Fig.7.13. Experiment and FE comparisons of bullet residual length of the GLARE 5 beam specimens with various thicknesses at different incident velocities.

7.3.1.1. Numerical prediction: thickness effect

After validating the FE model based on the abovementioned criteria, namely: the V_I~V_R relation, damage patterns and bullet residual length, it is now reasonable to extract some useful information, e.g. penetration resistance force, in which experimental results were not available. All results presented in this study were based on a full material model, i.e. not a quarter model.

The force histories could not be captured during experiments. However, the FE model provided the force histories of the ballistic tests. As an example, two different incident velocities, i.e. 50 m/s and 350 m/s, were chosen in such a way that both partial and full penetrations occurred for all the specimens with different configurations. Figure 7.14 compares the FE predicted contact force as a function of time for the GLARE 5 FML beams with various thicknesses under 50 m/s and 350 m/s impact velocities. In both

cases, the maximum contact force was the highest for the (6/5) configuration; whereas it was the lowest for the (2/1). In other words, for a given incident velocity, the thicker the specimen became the higher the maximum contact force was.

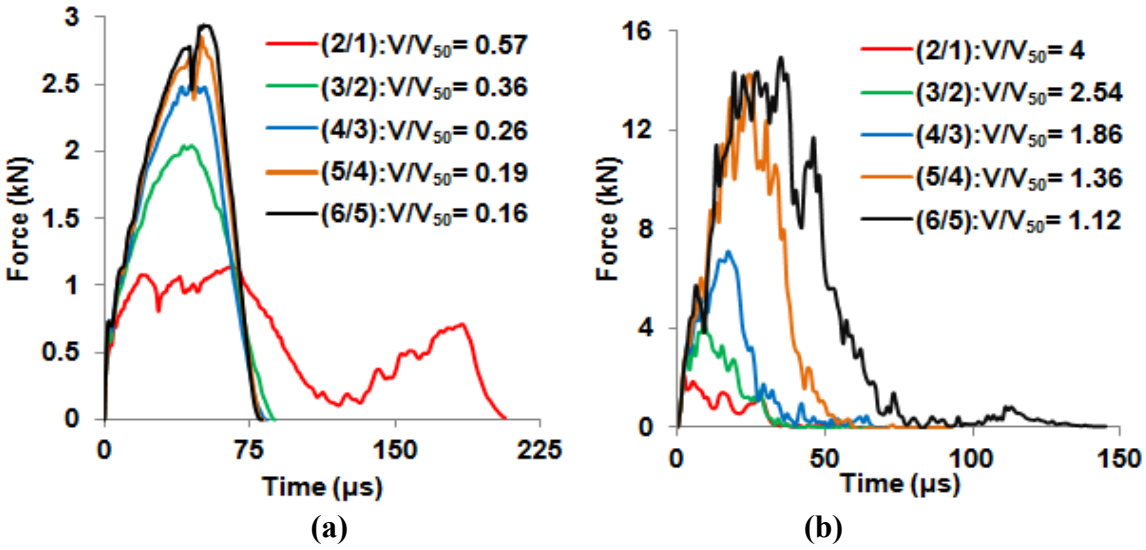

Fig.7.14. FE predictions of contact history for the cross-ply GLARE 5 FML beams with various thicknesses impacted at: (a) 50 m/s, and (b) 350 m/s.

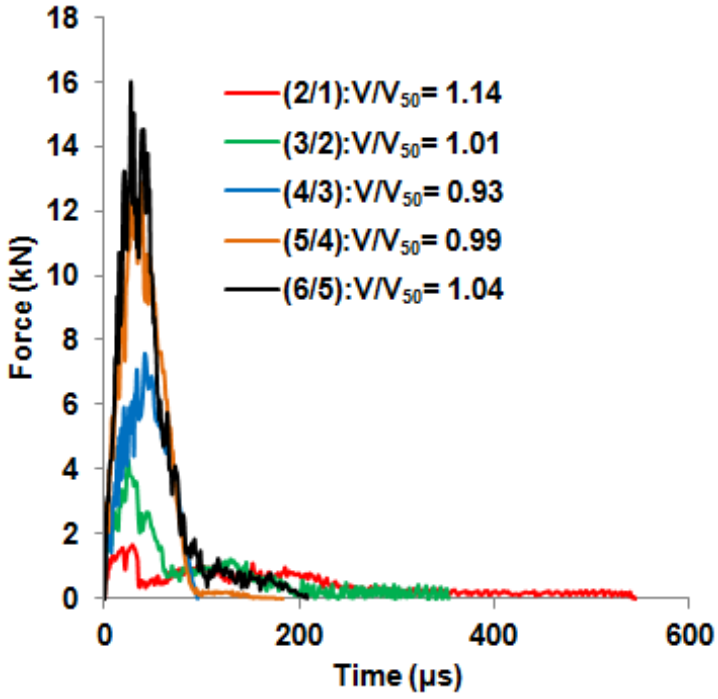

Fig.7.15. FE predictions of contact history for the cross-ply GLARE 5 FML beams with various thicknesses near their ballistic limit velocities.

The FE predictions of contact history for the same specimens near their ballistic limit velocities are shown in Fig 7.15. As Figs. 7.14 and 7.15 suggest, the maximum contact force is a function of the projectile incident velocity. Furthermore, for a given specimen configuration, by increasing the projectile incident velocity up to near its V_{50}, the maximum contact force increased. By further increasing the projectile speed above its ballistic limit velocity, the maximum contact force was relatively insensitive with respect to an increase in the projectile speed. The reason for this could be explained by different damage mechanism in the specimen when impacted ballistically below and above the ballistic limit velocity, V_{50}. Since the ballistic limit velocity was a constant value for a given specimen thickness, it implied that the penetration resistant energy should be constant. As the projectile was penetrating the target, it pushed the material ahead of it, which counteracted with resistance to the projectile motion until the projectile arrested. This would provide some extra time for further damage to develop. The penetration resistance force increased up to a point where the projectile pierced the target. In other words, the specimen integrity would be optimized for the condition where the residual exit velocity of the projectile was zero. Hence, for a given specimen configuration, the contact resistance force would increase up to its ballistic limit velocity, i.e. $V_I/V_{50} \leq 1$.

In the case where $V_I/V_{50} > 1$, the damage mechanism was different. Since there would be not enough time for the damage to progress in the specimen and thus the induced damage would be much more localized compared to the case of $V_I/V_{50} \leq 1$. In addition, at velocities above V_{50} due to the higher stresses created at the point of impact, the material around the perimeter of the projectile was sheared and pushed inward causing a cavity/plug to be created. The cavity size in the specimen, which was influenced by the

incident projectile velocity, would increase as the projectile penetrated through the target. Hence, the penetration resistance force would be reduced as compared to the condition where $V_I/V_{50} \leq 1$.

Figure 7.16 compares the variation of FE predicted contact force versus the projectile displacement for the GLARE 5 specimens with various thicknesses impacted at 350 m/s. As expected, the initial slopes of the contact force-displacement, known as contact stiffness, were almost the same for all the specimens until the point where damage initiated in the specimens (Fig. 7.16(b)).

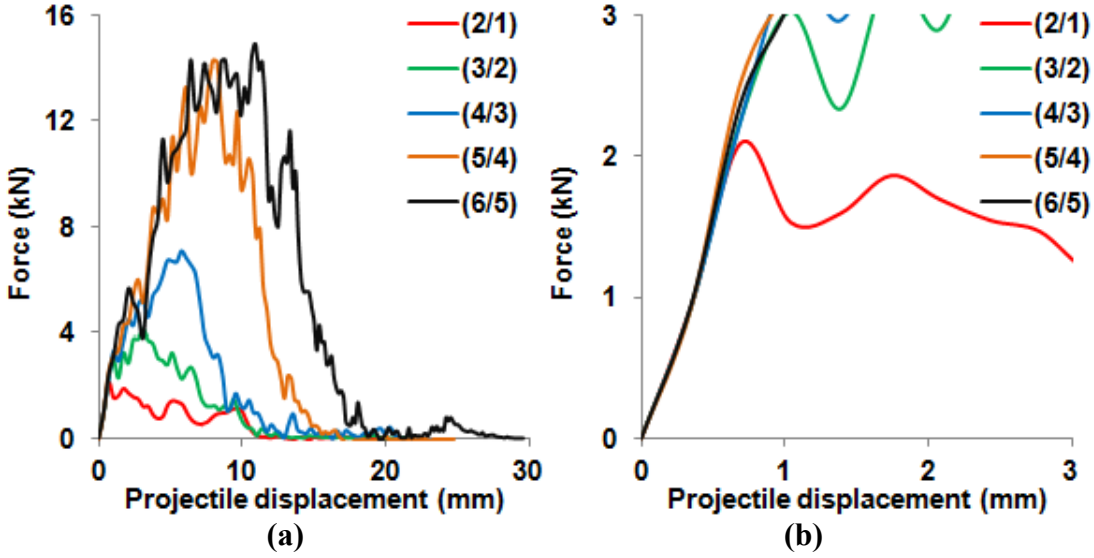

Fig.7.16. FE predictions of contact force as a function of projectile displacement for the cross-ply GLARE 5 FML beams with various thicknesses impacted at 350 m/s: (a) zoomed-out, (b) zoomed-in.

It would be more illustrative to compare damage progression as a function of contact force history. Such comparison is depicted in Fig. 7.17 for the (6/5) FML beam given in Fig. 7.12. It is apparent that specimen bulging occurred around 6 μs; whereas full penetration took place at around 140 μs. There was an increase in contact force between time intervals 106 and 124 μs after contact force dropped to zero. The reason for this

could be explained by the frictional resistance force that existed between the projectile and specimen.

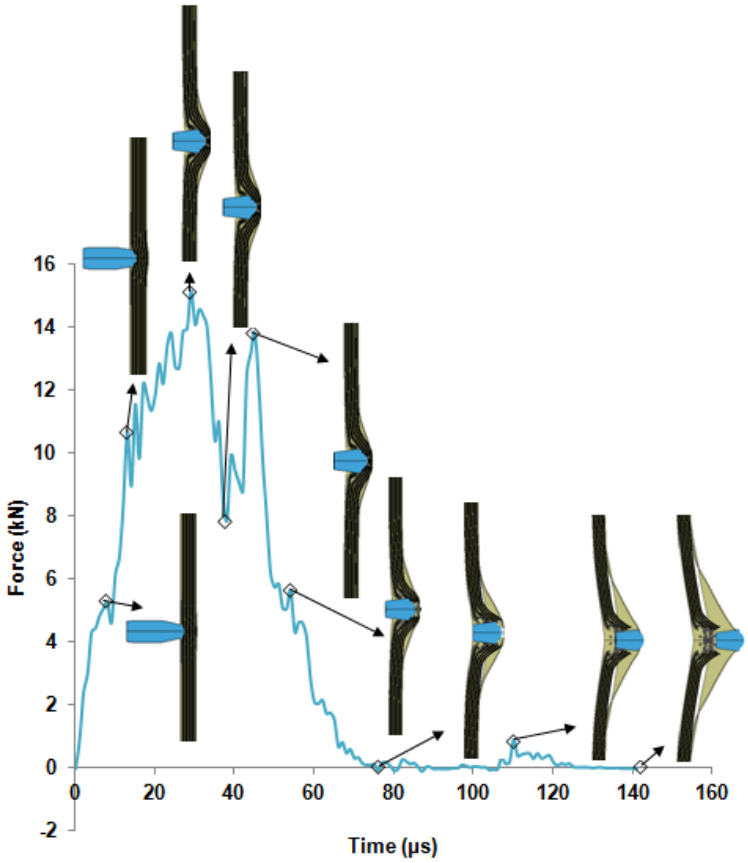

Fig.7.17. Comparison of the FE predicted force-history and damage progression for the cross-ply GLARE 5 (6/5) FML beam impacted at 347 m/s.

In addition, Fig. 7.18 exhibits the developments of in-plane axial ($\varepsilon_x = \varepsilon_1$) and transverse ($\varepsilon_y = \varepsilon_2$) strain waves along with the through-thickness strain wave ($\varepsilon_z = \varepsilon_3$) as a function of time for the same specimen given in Fig. 7.17. Once the contact between the projectile and FML beam initiated at time t=0.99 μs, a 3D strain/stress wave front developed and propagated from the impact site. A tensile strain wave propagated in the x-direction, whereas a compressive wave propagated in the y-axis as well as the through-thickness direction. It should be noted that the amplitude of strains in all directions is ±0.001 and hence the maximum axial stress corresponding to the maximum strain in the prepreg is,

54 GPa × ±0.001= ±54 MPa. In the same way, the maximum transverse/through-thickness stress in the prepreg is, 9.4 GPa × ±0.001= ±9.4 MPa.

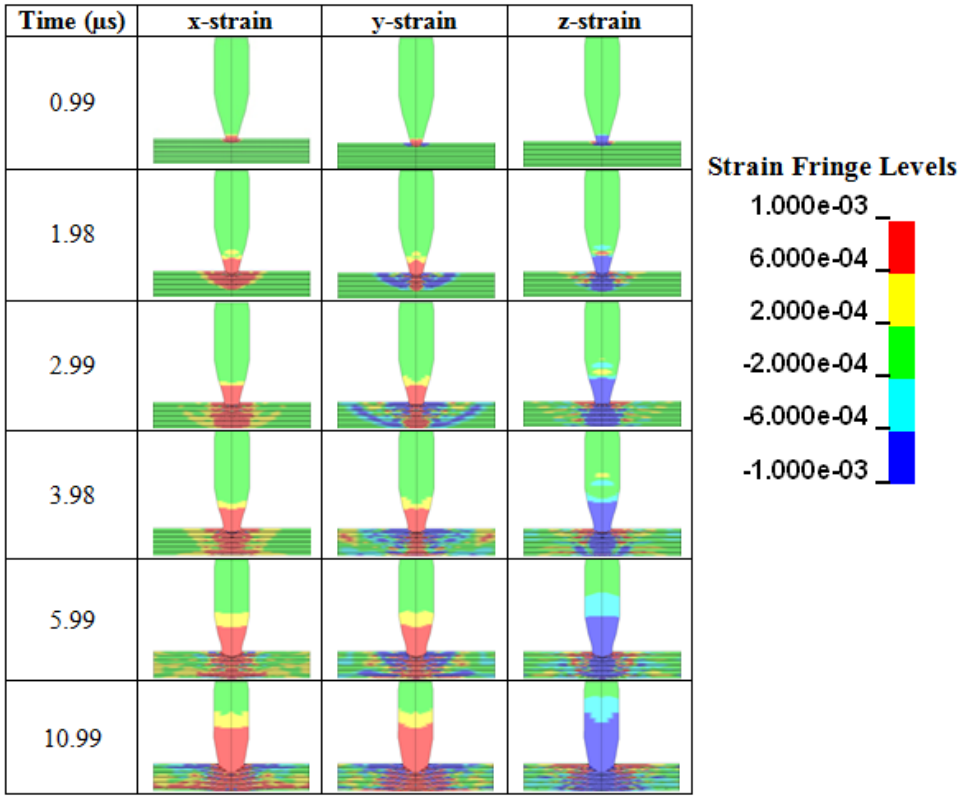

Fig.7.18. Strain contours of the GLARE 5 (6/5) FML beam impacted at 347 m/s.

Figure 7.19 illustrates the transient dynamic strain histories obtained from the experiments and FE analyses for (2/1) and (6/5) configurations impacted at 177 m/s and 347 m/s, respectively. It should be noted that no filter was applied to acquire the strain results. The only purpose of this figure was to show that the general trend of the transient strain histories obtained from the FE models were in agreement with the corresponding experimental results.

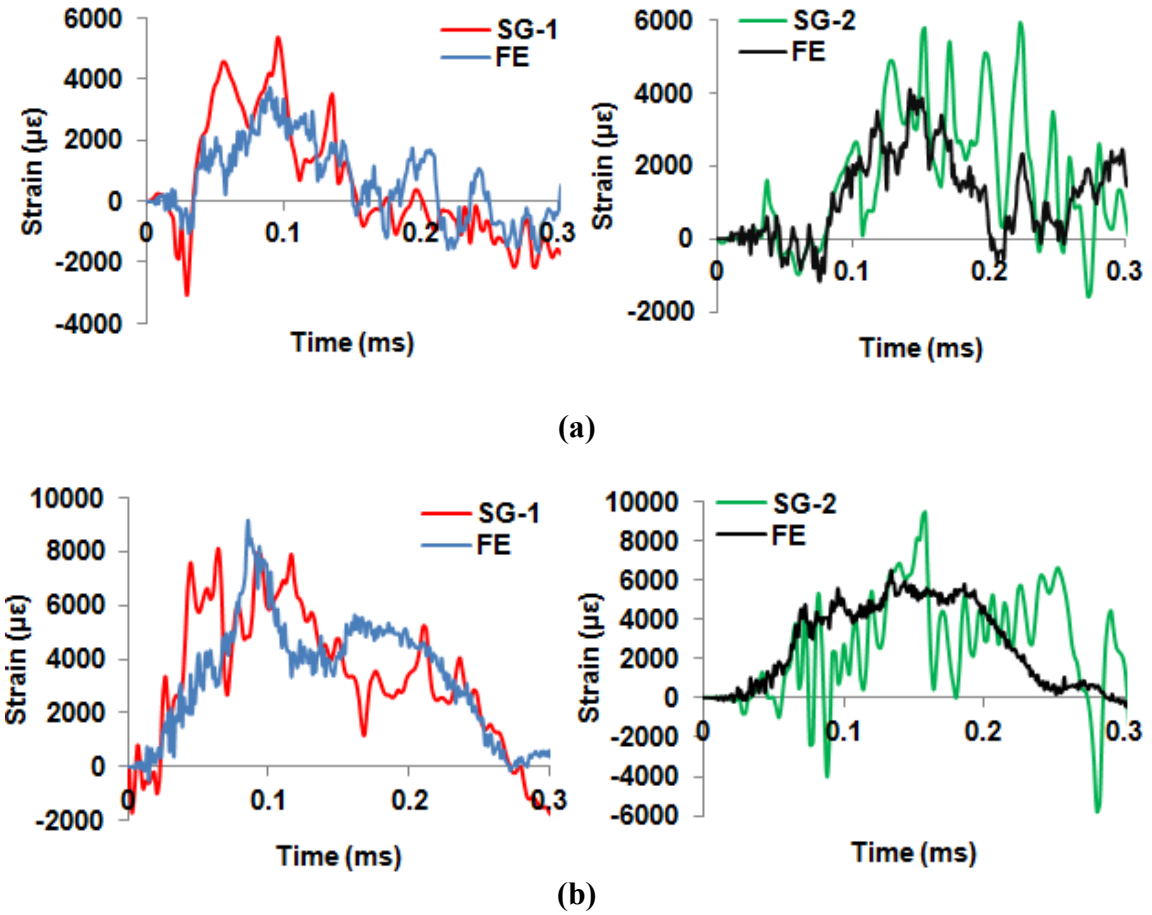

Fig.7.19. Comparisons of transient dynamic strain histories between the experiment and FE prediction for: (a) GLARE 5 (2/1) impacted at 177 m/s, and (b) GLARE 5 (6/5) impacted at 347 m/s.

Just before impact, entire energy was in the form of kinetic energy of the projectile. Upon impact, this energy was dissipated in various ways: (1) different damage mechanisms in the target, (2) projectile deformation and (3) kinetic energy of the ejecta. As the projectile penetrated the target, its kinetic energy reduced while the internal energy of the system increased causing the target energy to rise. As an example, Fig. 7.20 depicts the system kinetic, internal, total, hourglass and frictional sliding energy histories of the GLARE 5 (4/3) FML beam impacted at 150 m/s. The system total energy which is the summation of its kinetic, internal, hourglass and sliding energies remained constant. As the bullet

stopped by the target, the kinetic energy of the system reduced to zero and once the bullet rebounded off the target it increased again (Fig. 7.20). Moreover, it should be noted that the internal energy of the system increased and reached its maximum around 0.7 ms of contact time which was when the system became temporarily stationary. By further advancing in contact time, the internal energy decreased. This was because some of the stored internal energy in the system was released causing the bullet and target to bounce back. Sliding and hourglass energies were quite low compared to the other energies.

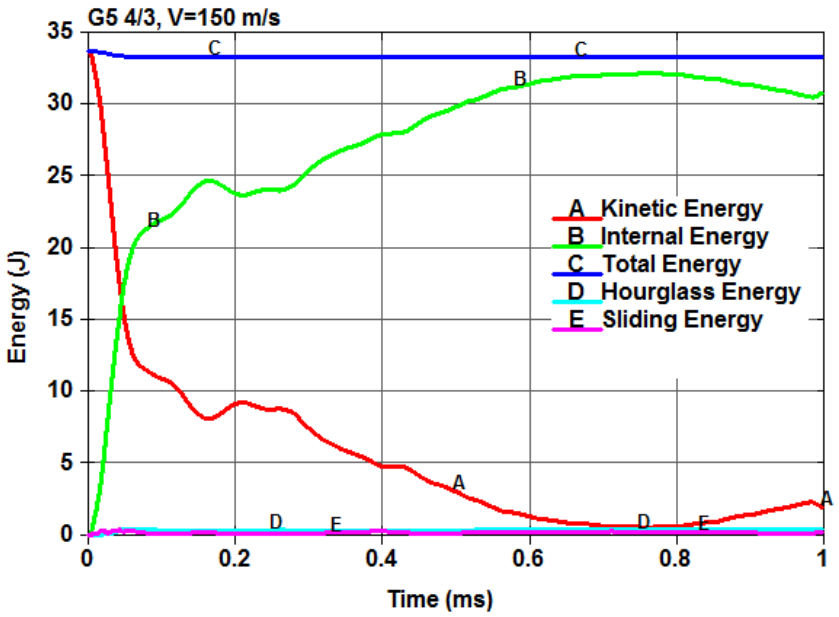

Fig.7.20. Energy history of the GLARE 5 (4/3) FML beam impacted at 150 m/s.

7.3.2. Model validation of GLARE 5 FML beams: stacking sequence effect

Figures 7.21 through 7.24 illustrate the FE predictions with experimental V_I~V_R data for the GLARE 5 (3/2) FML beams with various stacking sequences. The FE results are displayed by a circular symbol. As is apparent, the FE predictions are in excellent agreement with the experimental results. The comparison between experimental and FE results of ballistic limit as a function of specimen lay-up orientation is depicted in

Fig. 7.25. The variations in the results are demonstrated by deviation bars. The FE prediction is in good agreement with its experimental counterpart.

Figures 7.26 through 7.29 show the post-impact damage prediction obtained from FE analysis and experimental results for various specimen stacking sequences impacted at different speeds. There is good agreement in damage pattern between the FE models and experiments. The broken/split fibers, which appeared around the impact area of the specimens, were not seen that much in the FE predictions. This was due to the strain-based-element-erosion criterion used in the FE models. The bullet residual length was also considered to verify the FE models. As is evident from Fig. 7.30, the bullet residual length obtained from the experiments and FE is also in good agreement.

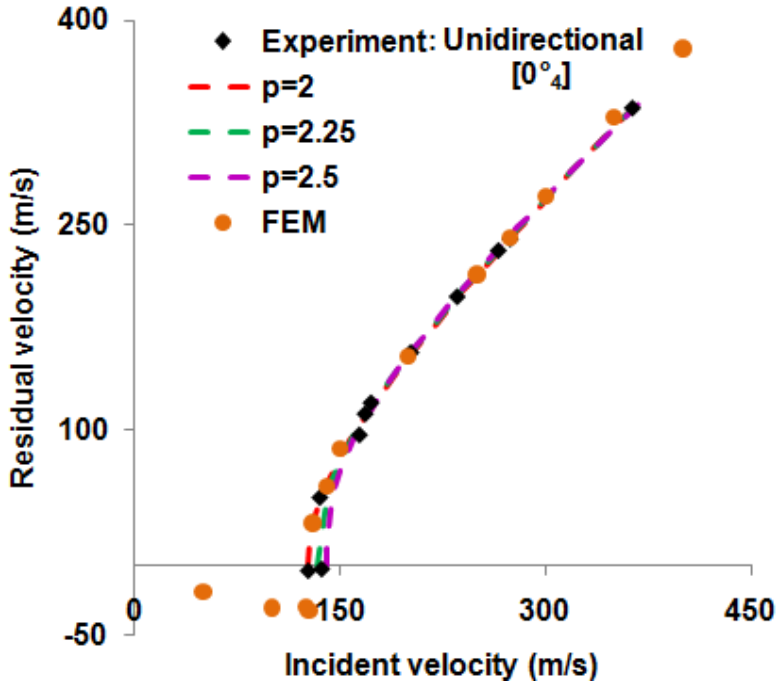

Fig.7.21. Comparison between experimental and FEM residual-incident velocity trend for the unidirectional [$0°_4$] GLARE 5 (3/2) beam specimen.

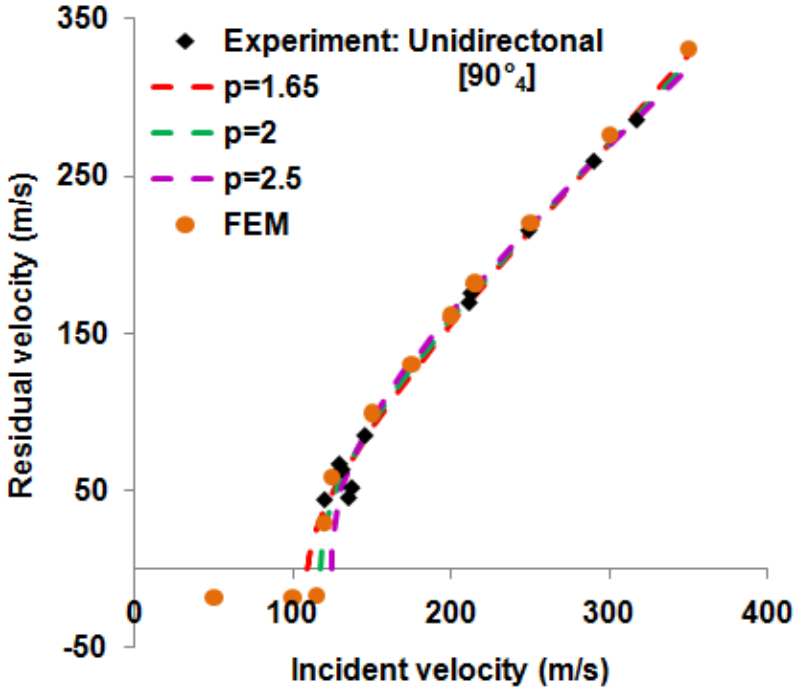

Fig.7.22. Comparison between experimental and FEM residual-incident velocity trend for the unidirectional [90°$_4$] GLARE 5 (3/2) beam specimen.

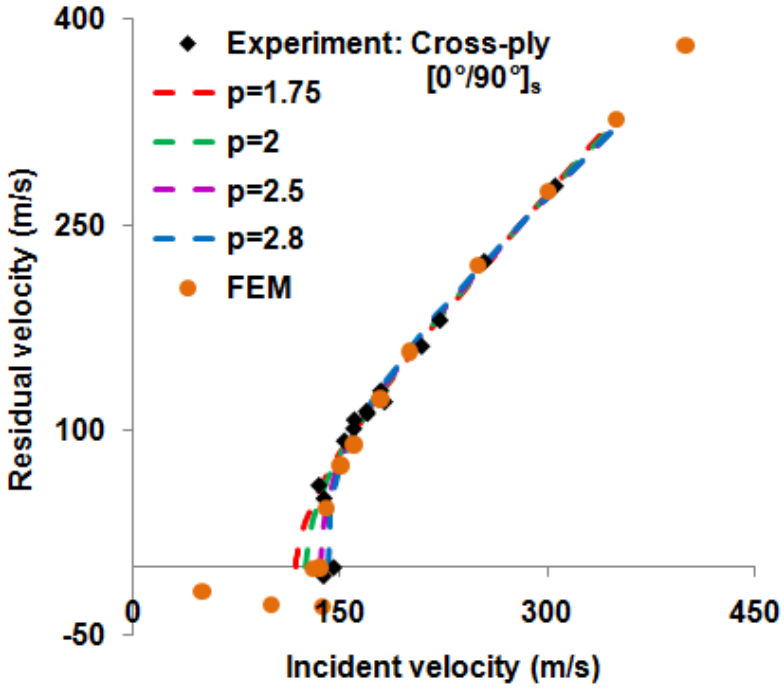

Fig.7.23. Comparison between experimental and FEM residual-incident velocity trend for the cross-ply [0°/90°]$_s$ GLARE 5 (3/2) beam specimen.

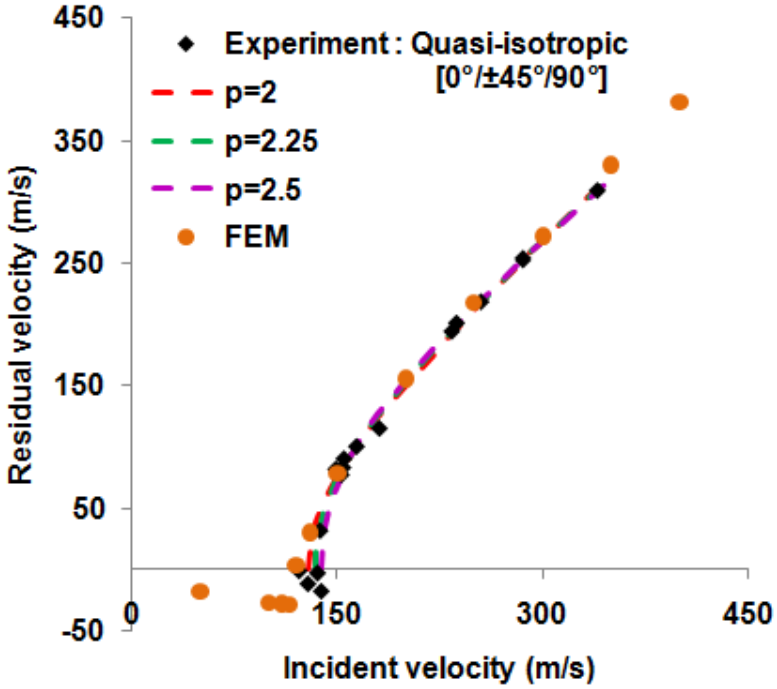

Fig.7.24. Comparison between experimental and FEM residual-incident velocity trend for the quasi-isotropic [0°/±45°/90°] GLARE 5 (3/2) beam specimen.

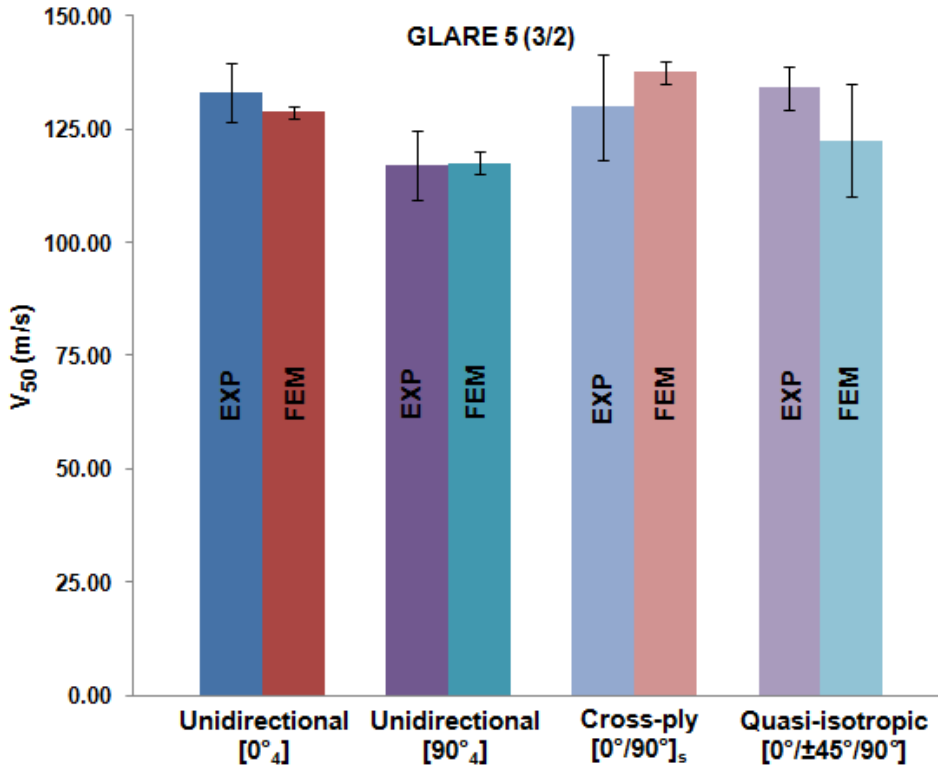

Fig.7.25. Comparisons between experimental and FE results of ballistic limit velocity (V_{50}) as a function of beam-specimen stacking sequence.

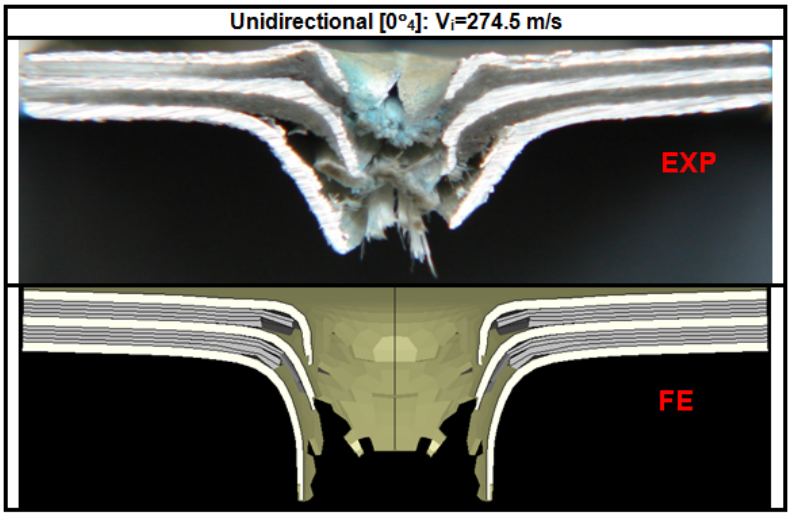

Fig.7.26. Comparisons of post-impact damage patterns for the unidirectional [$0°_4$] GLARE 5 (3/2) beam specimen impacted at 274.5 m/s.

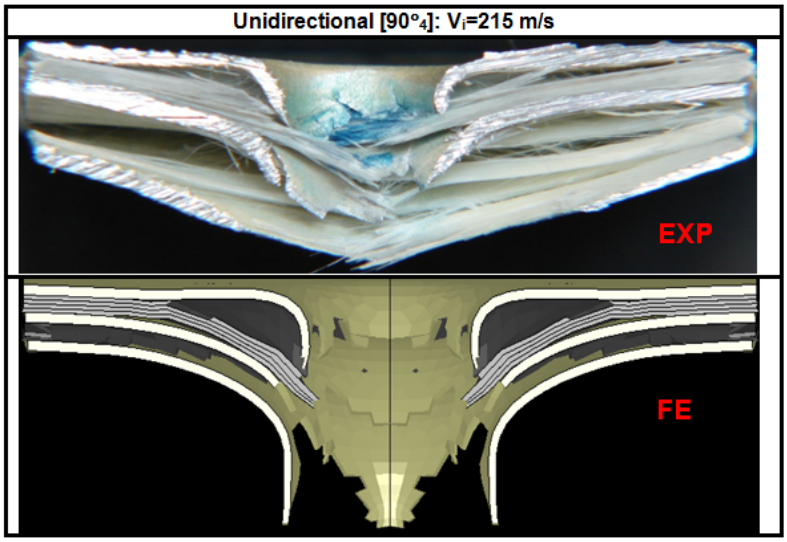

Fig.7.27. Comparisons of post-impact damage patterns for the unidirectional [$90°_4$] GLARE 5 (3/2) beam specimen impacted at 215 m/s.

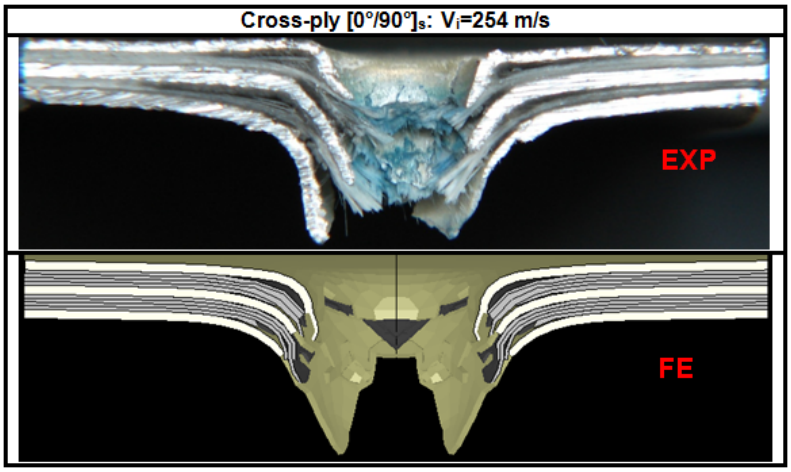

Fig.7.28. Comparisons of post-impact damage patterns for the cross-ply $[0°/90°]_s$ GLARE 5 (3/2) beam specimen impacted at 254 m/s.

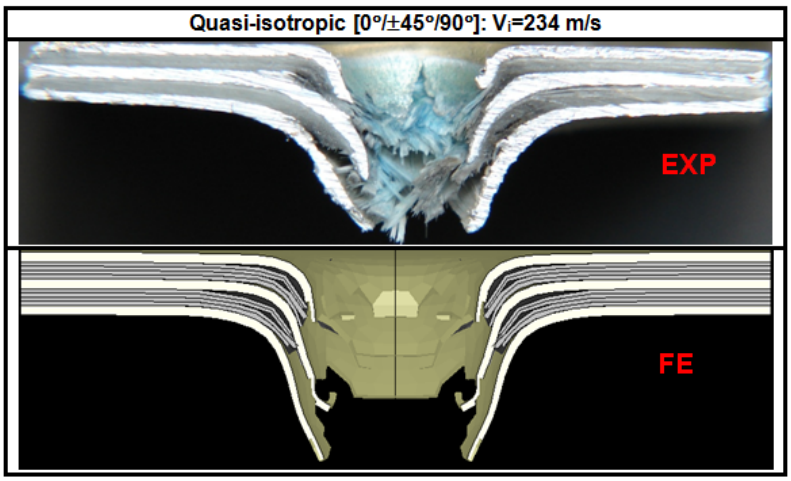

Fig.7.29. Comparisons of post-impact damage patterns for the quasi-isotropic [0°/±45°/90°] GLARE 5 (3/2) beam specimen impacted at 234 m/s.

GLARE 5 (3/2) [beam]	Experiment		Finite Element Model		ΔL
	Bullet Residual Length (mm)	Bullet	Bullet Residual Length (mm)	Bullet	Length Difference (mm)
$[0°_4]$ V_i=274.5 m/s	15.82		15.17		0.65
$[90°_4]$ V_i=215 m/s	15.95		15.33		0.62
$[0°/90°]_s$ V_i=254 m/s	15.88		15.16		0.72
[0°/±45°/90°] V_i=234 m/s	15.75		15.42		0.33

Fig.7.30. Experiment and FE comparisons of bullet residual length of the GLARE 5 (3/2) beam specimens with various stacking sequences at different incident velocities.

7.3.2.1. Numerical prediction: stacking sequence effect

Two examples were regarded here to study the contact resistance force. They are namely: (1) non-perforated case with an impact velocity of 100 m/s, and (2) perforated case with an impact velocity of 250 m/s. These examples are depicted in Figs. 7.31 and 7.32, respectively. The figures exhibit the FE predicted contact force as functions of time and projectile displacement for the unidirectional $[0°_4]$, unidirectional $[90°_4]$, cross-ply $[0°/90°]_s$ and quasi-isotropic $[0°/\pm45°/90°]$ lay-up orientation. As shown in Figs. 7.31 and 7.32, the cross-ply specimen offered the highest contact resistance force while the unidirectional $[90°_4]$ specimen showed the lowest. The maximum contact forces for the unidirectional $[0°_4]$ and quasi-isotropic FML beams were almost the same. For a given impact velocity, the initial slope of contact force-displacement, known as contact stiffness, was the same for all the stacking sequence types.

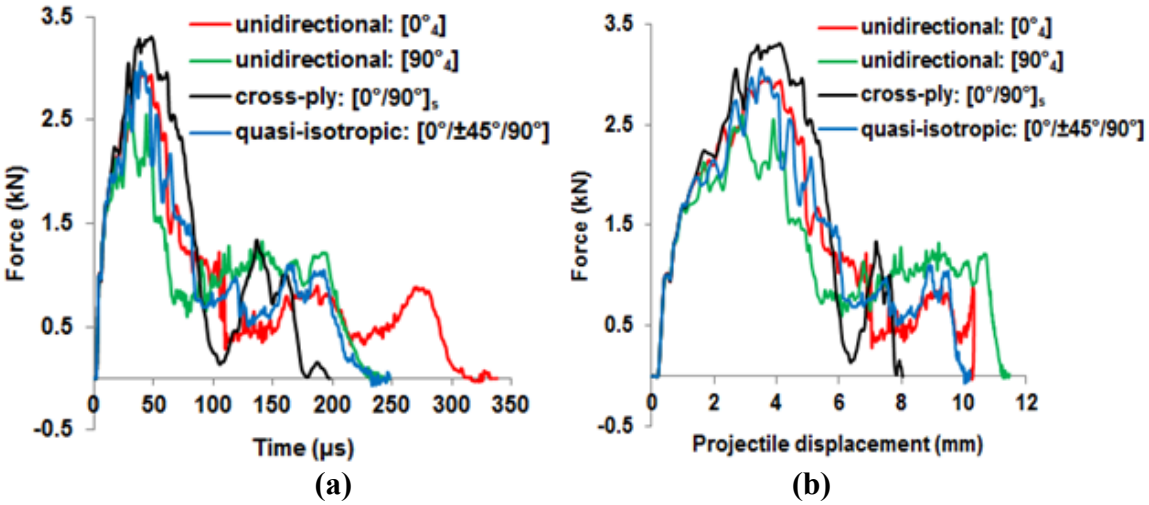

Fig.7.31. FE prediction of contact force as a function of time (a), and projectile displacement (b), for the GLARE 5 (3/2) FML beams with various stacking sequences impacted at 100 m/s.

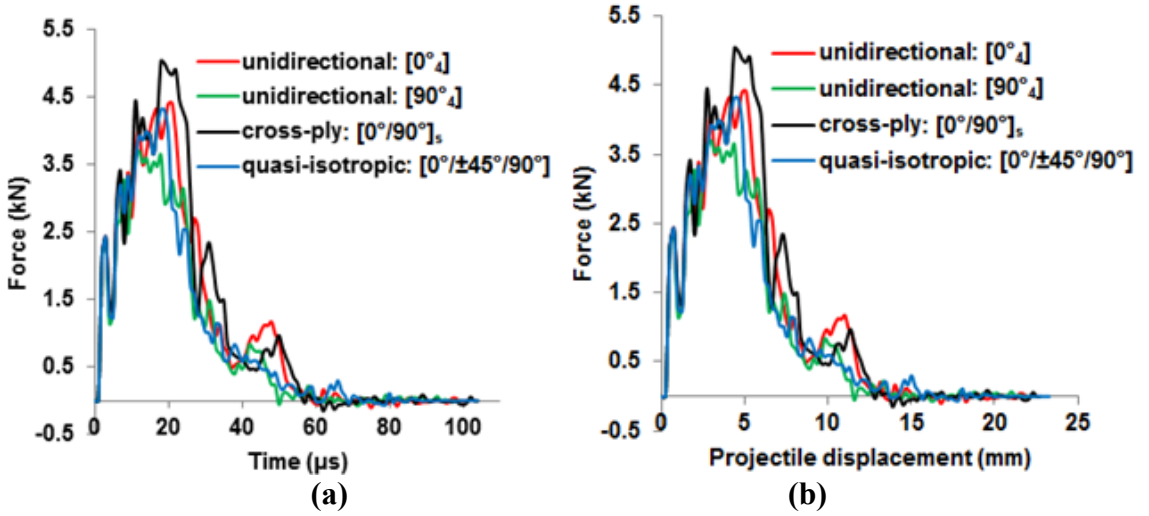

Fig.7.32. FE prediction of contact force as a function of time (a), and projectile displacement (b), for the GLARE 5 (3/2) FML beams with various stacking sequences impacted at 250 m/s.

The contact resistance force would directly influence the residual length of a deformable projectile. Hence, it was expected that the more the contact force was the least the bullet residual length would be. This statement is validated in Fig. 7.33 which compares bullet residual length as a function of specimen stacking sequence under incident speeds of 100 m/s and 250 m/s. For a given velocity, the bullet residual length was the smallest for the

cross-ply lay-up orientation; whereas, it was the largest for the unidirectional [90°$_4$] specimen. The bullet residual length for quasi-isotropic and unidirectional [0°$_4$] FML beams was in between the cross-ply and unidirectional [90°$_4$] lay-up orientation results.

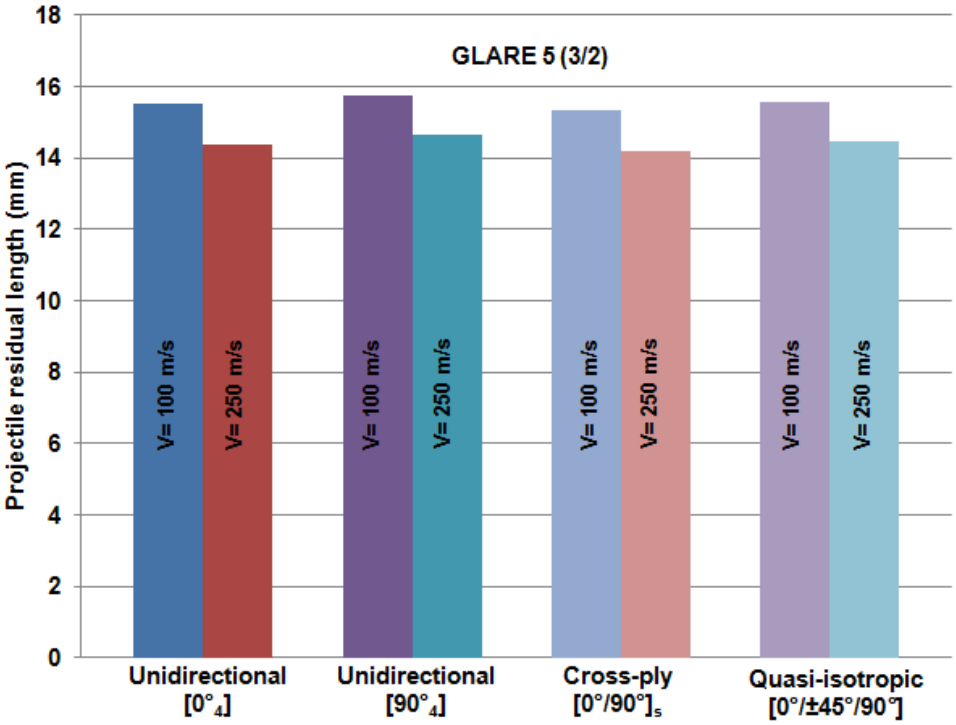

Fig.7.33. FE predicted bullet residual length versus specimen stacking sequence impacted at 100 m/s and 250 m/s.

Furthermore, since the variation in the bullet residual length for a given impact velocity was relatively invariant with respect to change in stacking sequence (Fig. 7.33); thus, it was reasonable to assume that the energy required to deform the bullet was the same for all the specimen types under a given impact velocity. As a result, it was useful to compare the total transferred energy to the specimens. This is shown in Fig. 7.34, which represents the FE predicted projectile kinetic energy history of the GLARE 5 (3/2) FML beams with various stacking sequences impacted at 250 m/s. The total transferred energy was the highest for the cross-ply specimen and the lowest for the unidirectional [90°$_4$]

stacking sequence. Moreover, the dissipated energy was reduced by changing the stacking sequence in the following order: cross-ply $[0°/90°]_s$, unidirectional $[0°_4]$, quasi-isotropic [0°/±45°/90°] and unidirectional $[90°_4]$, respectively.

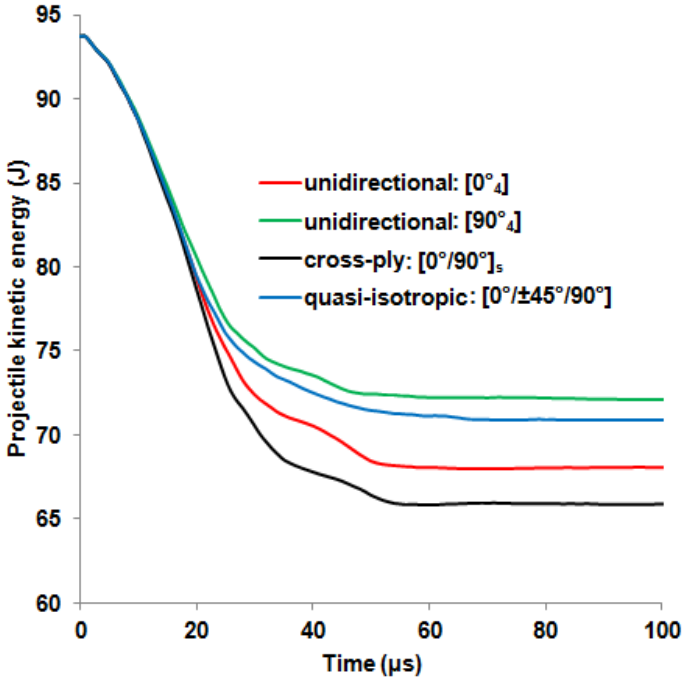

Fig.7.34. FE predicted projectile kinetic energy as a function of time for the GLARE 5 (3/2) FML beams with various stacking sequences impacted at 250 m/s.

Figure 7.35 illustrates the transient dynamic strain histories obtained from the experiments and FE analyses for the cross-ply lay-up orientation FML beam impacted at 179 m/s. It should be noted that no filter was applied to acquire the strain results. The only purpose of this figure was to show that the general trend of the transient strain histories obtained from the FE model was in agreement with the corresponding experimental results.

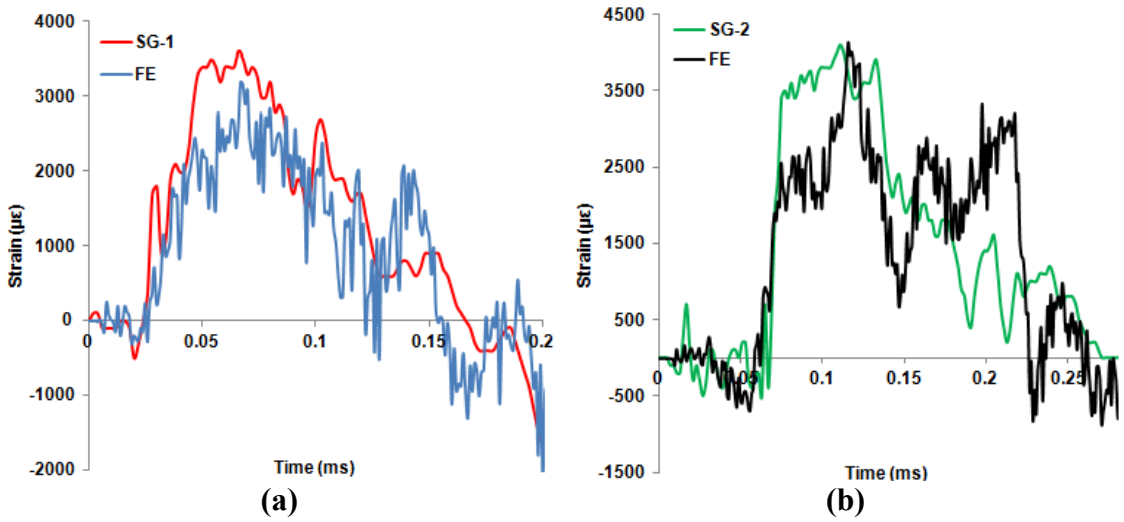

Fig.7.35. Comparisons of the transient dynamic strain histories between the experiment and FE prediction result for the GLARE 5 (3/2)-[0°/90°]$_s$ impacted at 179 m/s: (a) strain gage #1, (b) strain gage #2.

7.4. FE modeling of ballistic impact tests on GLARE 5 FML plates

Figure 7.36 illustrates perspective views of the composite plate and bullet. Several attempts were made to optimize the FE model based on the number of elements and mesh size using the available computational power. The results showed that by refining the mesh size, smoother results were achieved. In order to ensure by further reducing the mesh size the result would not change, an additional mesh with very fine elements was created using a super-power computer and compared to the one shown in Fig. 7.36. The results revealed that the FE obtained V_I~V_R data were invariant with respect to the change in mesh size. As a result, the mesh shown in Fig. 7.36 was considered. To reduce computational time, finer mesh was used around the impact area, which is the critical location; while coarser mesh was considered as moving away from the impact center. In order to further decrease computational time, only a quarter-symmetric model was considered in this study due to the double symmetry of the specimen-projectile system. Two elements were used in the through-thickness direction for each aluminum layer;

whereas 1 element was considered for each ply in the prepreg composite layer. That is, a total of 4 elements was used to simulate the assembly of each $[0°/90°]_s$ lamina in its through-thickness direction.

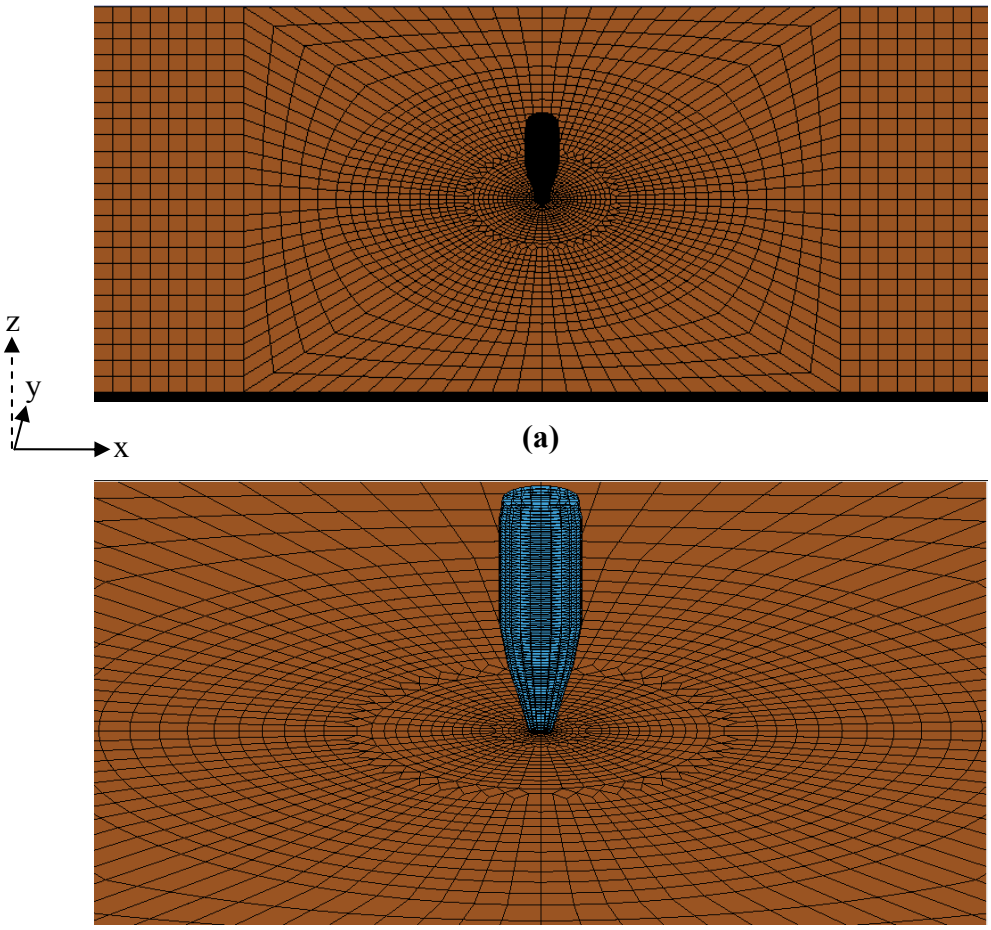

Fig.7.36. Perspective views of the finite element simulation model: (a) far-off view, (b) close-up view.

For instance, the GLARE 5 (2/1) was model with 8 elements in the thickness direction. The quarter of the projectile was modeled using 1,125 solid elements. The mesh density for the projectile was chosen in such a way that good contact between the specimen and projectile was maintained during impact (Fig. 7.36). The GLARE 5 (2/1) quarter-symmetric specimen model consisted of 5,720 one-point-integration 8-node solid brick

elements. It should be mentioned that the prepreg in-plane material directions, i.e. 1 (corresponds to the 0° fiber direction) and 2 (corresponds to the 90° fiber direction), were aligned with the global x and y axes, and the through-thickness material direction 3 was aligned with the global z axis, respectively. Moreover, a fixed-fixed boundary condition was used in this study.

7.4.1. Model validation of GLARE 5 FML plates: thickness effect

Figures 7.37 through 7.41 compare the FE predictions with experimental V_I~V_R data for the cross-ply GLARE 5 FML plates with various configurations. The FE results are illustrated by a circular symbol. As is apparent, the FE predictions are in excellent agreement with the experimental results. The comparison between experimental and FE results of ballistic limit as a function of specimen thickness is shown in Fig. 7.42. The variations in the results are represented by deviation bars. The FE prediction is in good agreement with its experimental counterpart.

Next, post-impact damage prediction from the FE analysis was compared to its experimental counterpart. The results are given in Figs. 7.43 through 7.47 for various specimen thicknesses impacted at different speeds. There is good agreement in damage pattern between the FE models and experiments. Furthermore, as was mentioned earlier, the broken/split fibers were not seen that much in the FE predictions due to the strain-based-element-erosion criterion used in the FE models. The failed elements were eroded and removed from the FE calculations. Therefore, they are not presented in the comparisons.

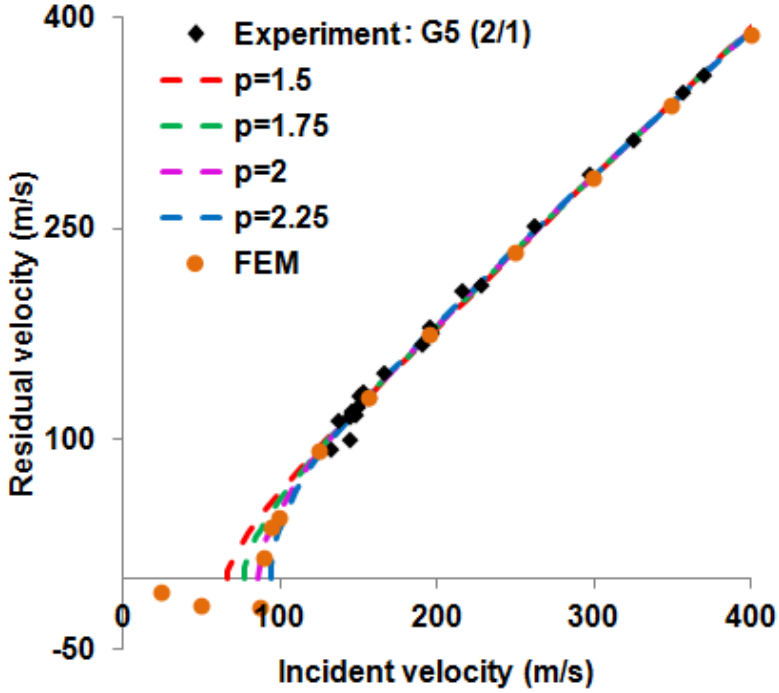

Fig.7.37. Comparison between experimental and FEM residual-incident velocity trend for the GLARE 5 (2/1) plate specimen.

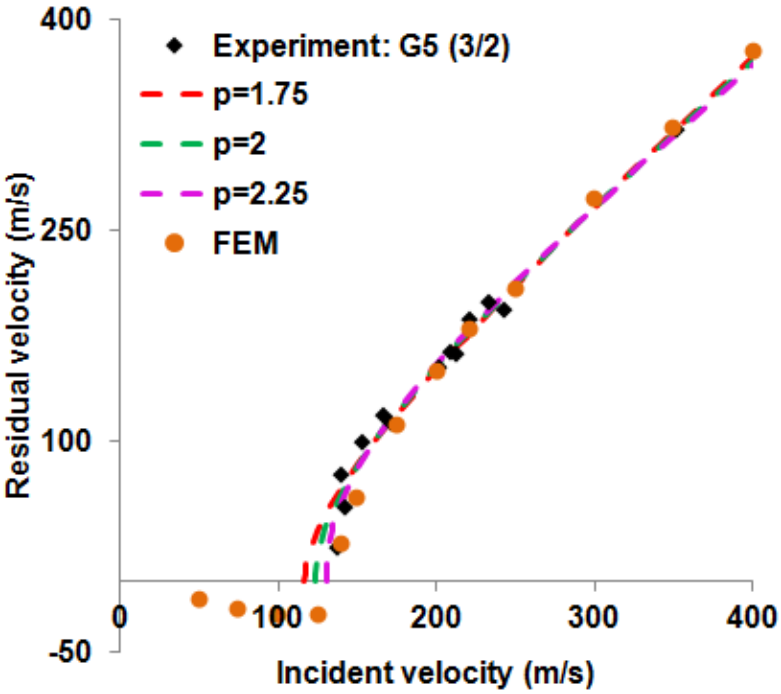

Fig.7.38. Comparison between experimental and FEM residual-incident velocity trend for the GLARE 5 (3/2) plate specimen.

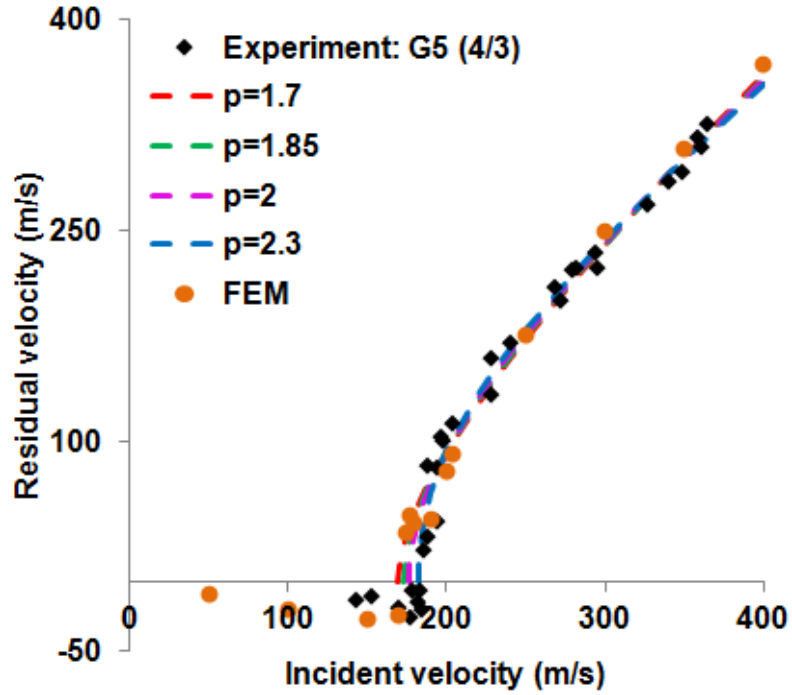

Fig.7.39. Comparison between experimental and FEM residual-incident velocity trend for the GLARE 5 (4/3) plate specimen.

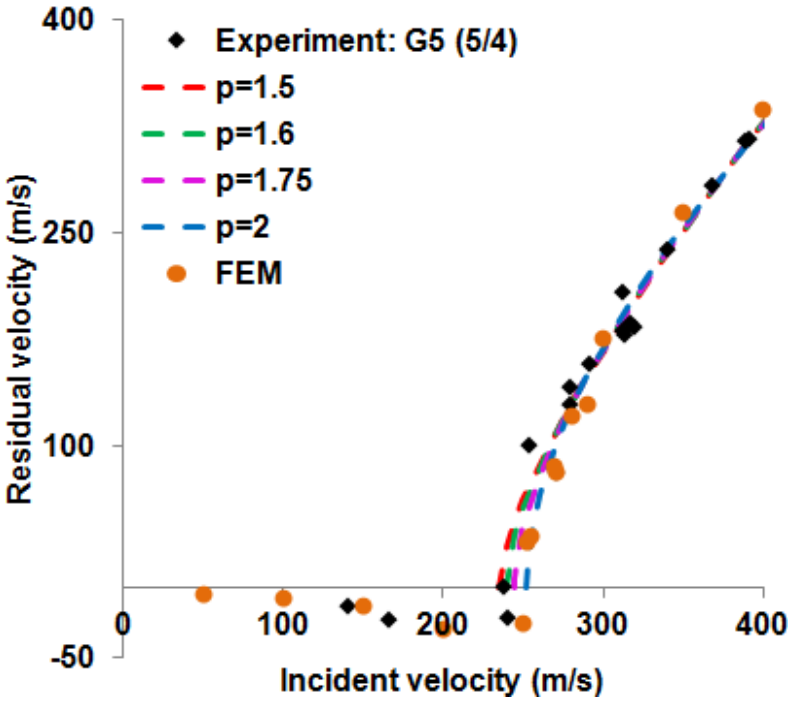

Fig.7.40. Comparison between experimental and FEM residual-incident velocity trend for the GLARE 5 (5/4) plate specimen.

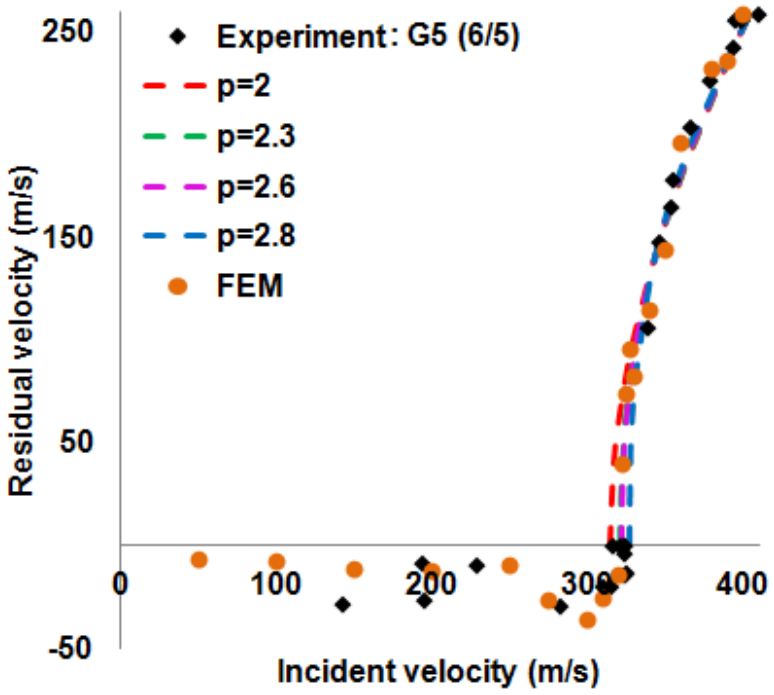

Fig.7.41. Comparison between experimental and FEM residual-incident velocity trend for the GLARE 5 (6/5) plate specimen.

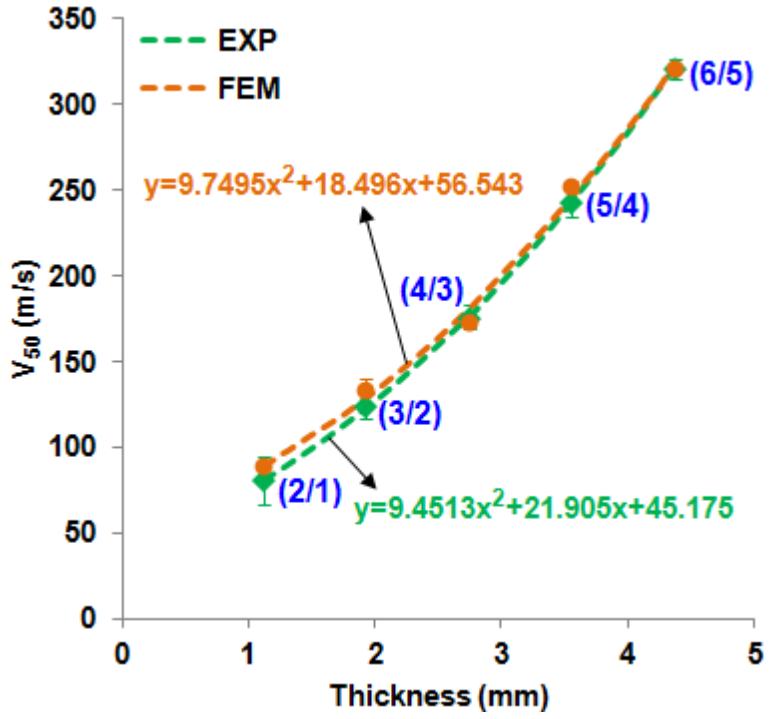

Fig.7.42. Comparisons between experimental and FE results of ballistic limit velocity (V_{50}) as a function of plate-specimen thickness. In the equations x stands for thickness and y for V_{50}.

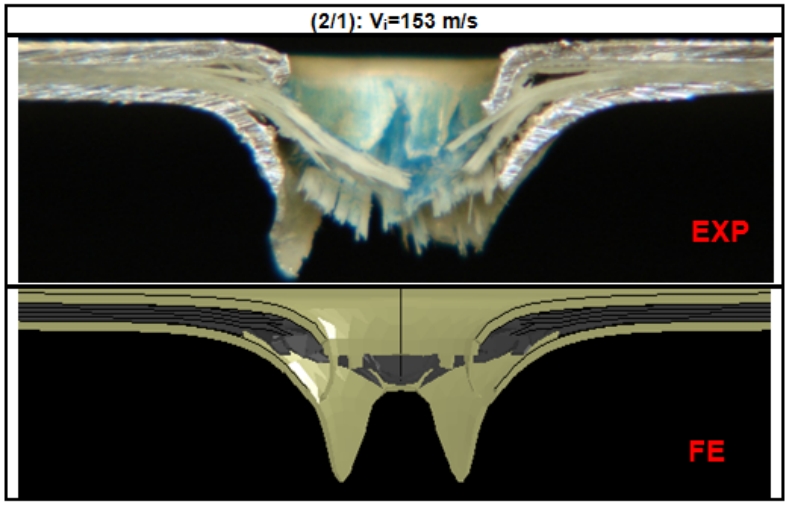

Fig.7.43. Comparisons of post-impact damage patterns for the GLARE 5 (2/1) plate specimen impacted at 153 m/s.

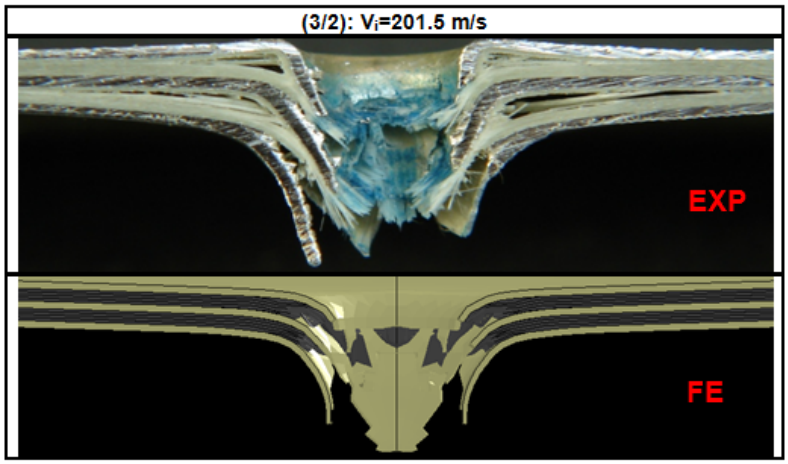

Fig.7.44. Comparisons of post-impact damage patterns for the GLARE 5 (3/2) plate specimen impacted at 201.5 m/s.

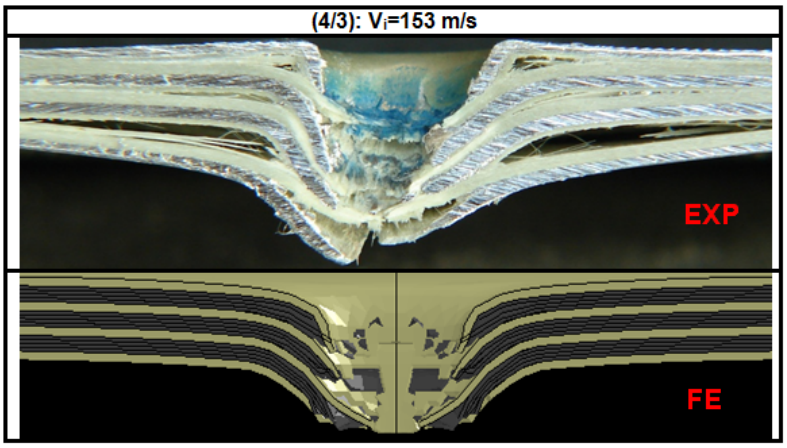

(a)

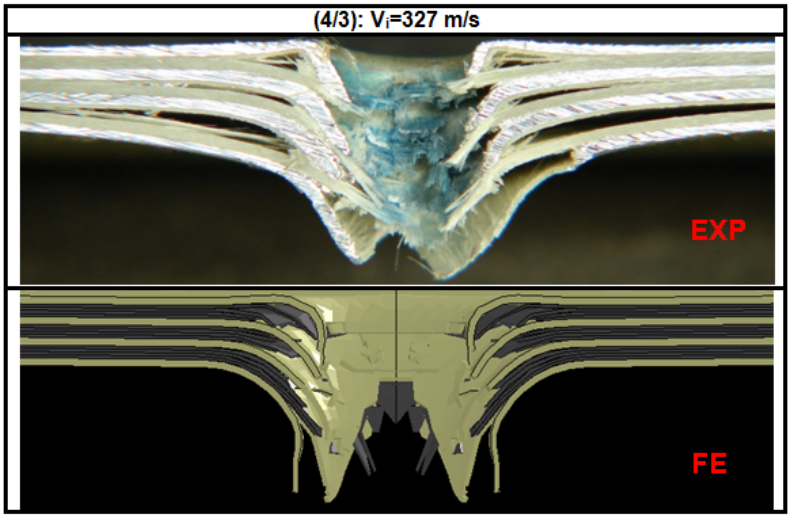

(b)

Fig.7.45. Comparisons of post-impact damage patterns for the GLARE 5 (4/3) plate specimen impacted at: (a) 153 m/s and (b) 327 m/s.

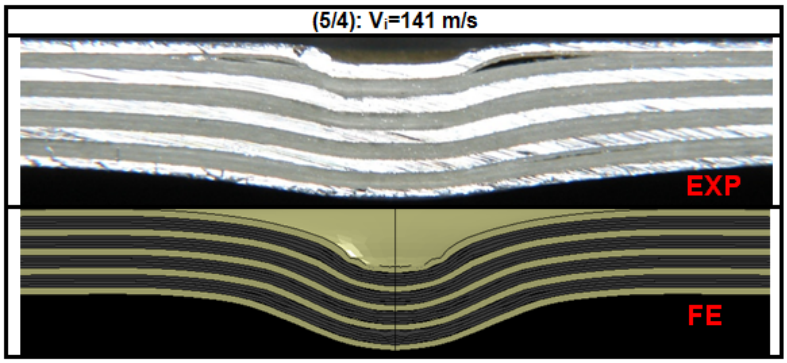

(a)

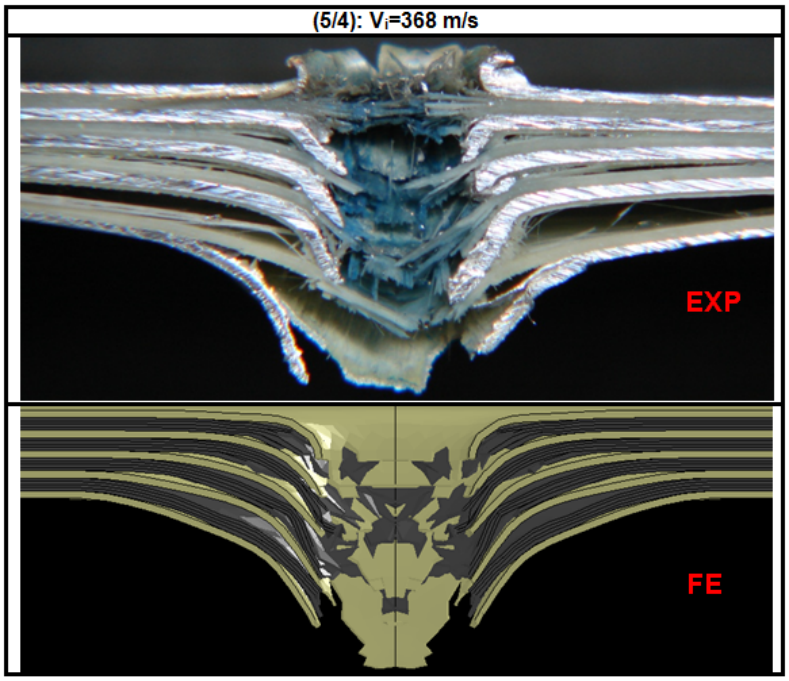

(b)

Fig.7.46. Comparisons of post-impact damage patterns for the GLARE 5 (5/4) plate specimen impacted at: (a) 141 m/s and (b) 368 m/s.

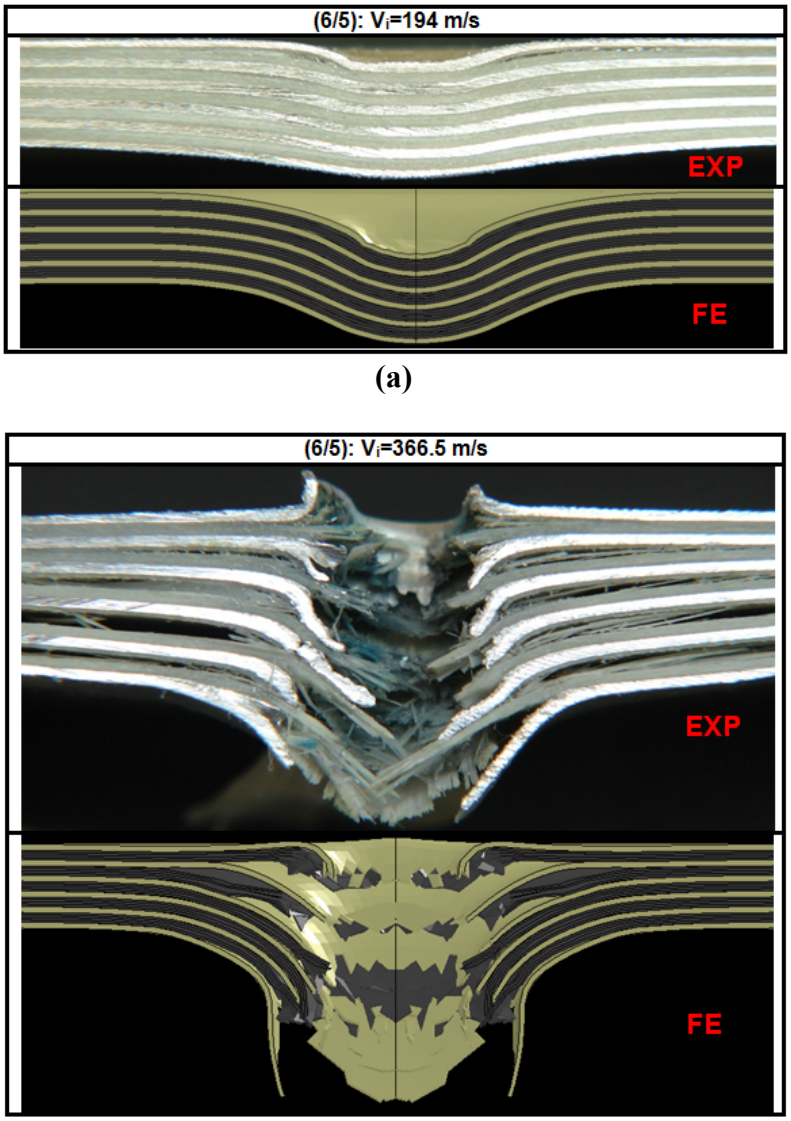

Fig.7.47. Comparisons of post-impact damage patterns for the GLARE 5 (6/5) plate specimen impacted at: (a) 194 m/s and (b) 366.5 m/s.

Another factor, which was considered to validate the FE models, was the bullet residual length. This is shown in Fig. 7.48. It is obvious that the bullet residual length obtained from the experiments and FE is also in good agreement.

GLARE 5 [plate]	Experiment		Finite Element Model		ΔL
	Bullet Residual Length (mm)	Bullet	Bullet Residual Length (mm)	Bullet	Length Difference (mm)
(2/1) V_i=153 m/s	16.67		16.56		0.11
(3/2) V_i=201.5 m/s	15.80		15.74		0.06
(4/3) V_i=327 m/s	14.70		14.16		0.54
(5/4) V_i=141 m/s	14.78		13.49		1.29
(5/4) V_i=368 m/s	13.97		13.59		0.38
(6/5) V_i=366.5 m/s	11.98		10.00		1.98

Fig.7.48. Experiment and FE comparisons of bullet residual length of the GLARE 5 plate specimens with various thicknesses at different incident velocities.

7.4.1.1. Numerical prediction: thickness effect

Two different incident velocities, i.e. 50 m/s and 350 m/s, were chosen in such a way that both partial and full penetrations occurred for all the specimens with different configurations. Figure 7.49 compares the FE predicted contact force as a function of time for the GLARE 5 FML plates with various thicknesses under 50 m/s and 350 m/s impact velocities. In both cases, the maximum contact force was the highest for the thickest specimen, i.e. the (6/5) configuration; whereas it was the lowest for the thinnest specimen, i.e. the (2/1) configuration. The FE predictions of contact history for the same specimens near their ballistic limit velocities are illustrated in Fig 7.50. As Figs. 7.49 and 7.50 reveal, for a given specimen configuration, by increasing the projectile incident velocity up to near its V_{50}, the maximum contact force increased. By further increasing

the projectile speed above its ballistic limit velocity, the maximum contact force was relatively insensitive with respect to an increase in the projectile speed. The reason for this was mentioned earlier in Section 7.3.1.1.

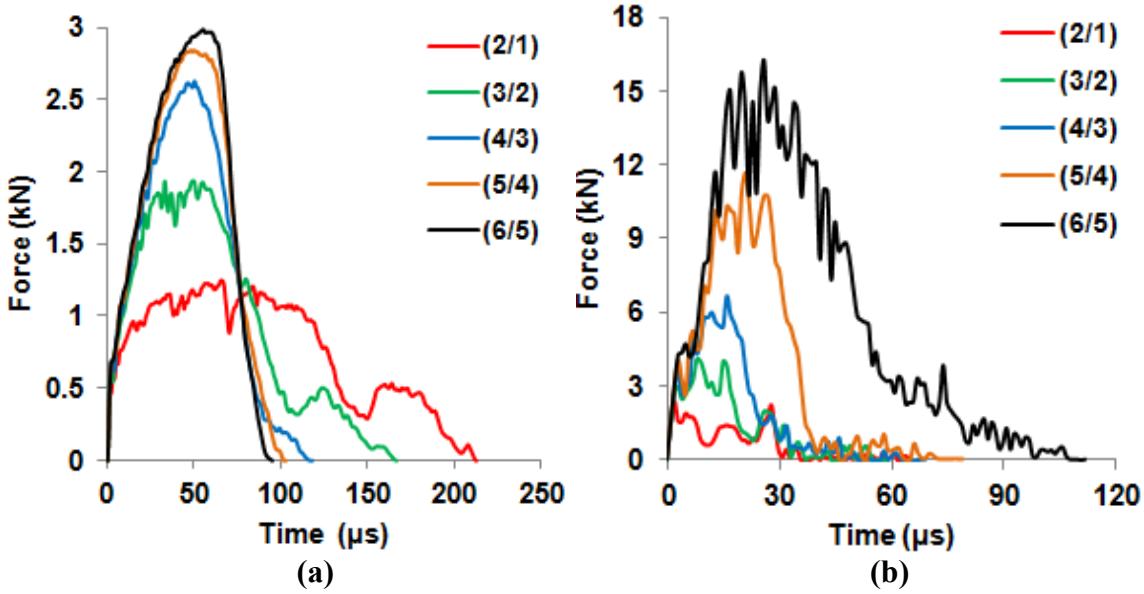

Fig.7.49. FE predictions of contact history for the cross-ply GLARE 5 FML plates with various thicknesses impacted at: (a) 50 m/s, and (b) 350 m/s.

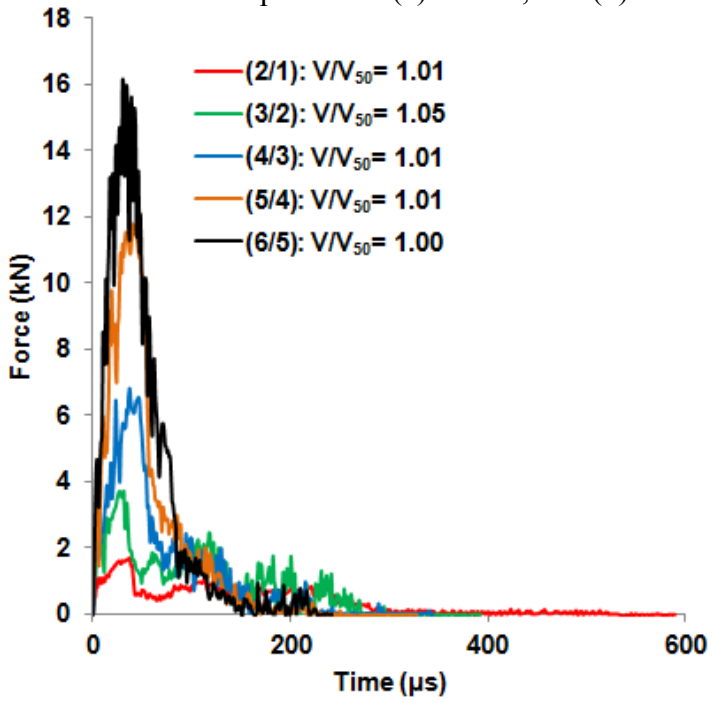

Fig.7.50. FE predictions of contact history for the cross-ply GLARE 5 FML plates with various thicknesses near their ballistic limit velocities.

Furthermore, by comparing the force histories of the cross-ply beam and plate specimen, it was observed that the force histories were nearly insensitive with respect to change in specimen geometry.

7.4.2. Model validation of GLARE 5 FML plates: stacking sequence effect

Figures 7.51 through 7.54 demonstrate the FE predictions with experimental V_I~V_R data for the GLARE 5 (3/2) FML plates with various stacking sequences. The FE results are shown by a circular symbol. As is obvious, the FE predictions are in excellent agreement with the experimental results. The comparison between experimental and FE results of ballistic limit as a function of specimen lay-up orientation is illustrated in Fig. 7.55. The variations in the results are represented by deviation bars. The FE prediction is in good agreement with its experimental counterpart.

Figures 7.56 through 7.59 depict the post-impact damage prediction obtained from FE analysis and experimental results for various specimen stacking sequences impacted at different speeds. There is good agreement in damage pattern between the FE models and experiments. Once again, as mentioned before, the broken/split fibers, which appeared around the impact area of the specimens, were not seen that much in the FE predictions due to the strain-based-element-erosion criterion used in the FE models. The bullet residual length was also considered to verify the FE models. This is shown in Fig. 7.60. The bullet residual length obtained from the experiments and FE is also in good agreement.

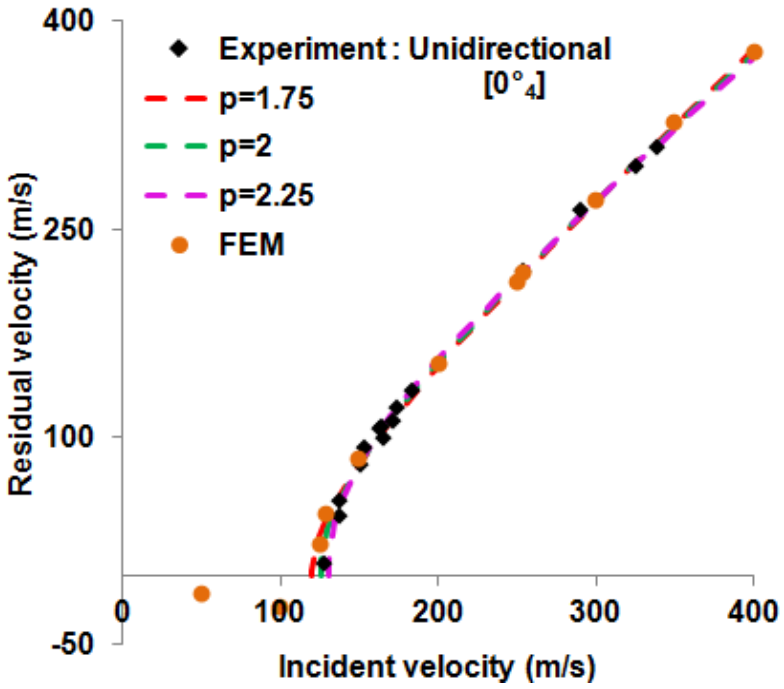

Fig.7.51. Comparison between experimental and FEM residual-incident velocity trend for the unidirectional $[0°_4]$ GLARE 5 (3/2) plate specimen.

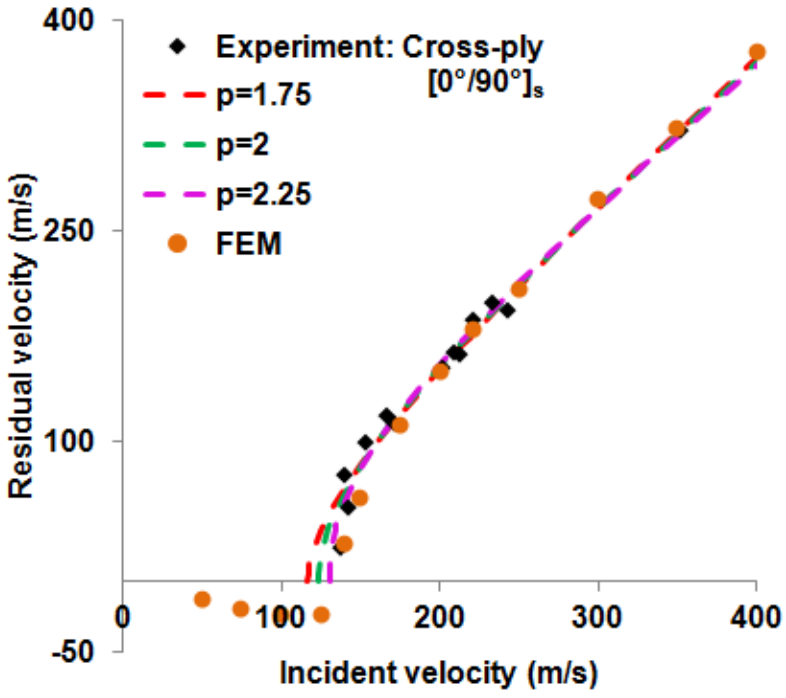

Fig.7.52. Comparison between experimental and FEM residual-incident velocity trend for the cross-ply $[0°/90°]_s$ GLARE 5 (3/2) plate specimen.

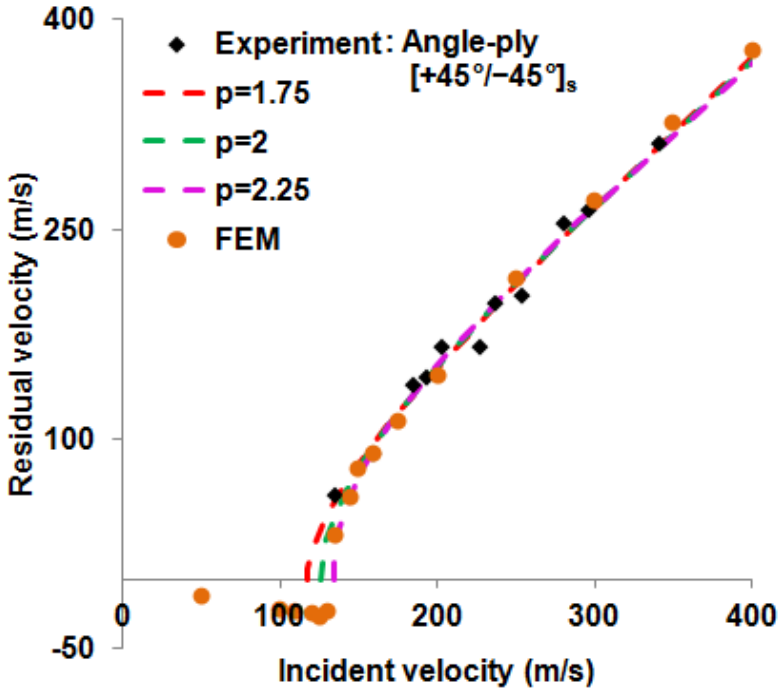

Fig.7.53. Comparison between experimental and FEM residual-incident velocity trend for the angle-ply $[\pm 45°]_s$ GLARE 5 (3/2) plate specimen.

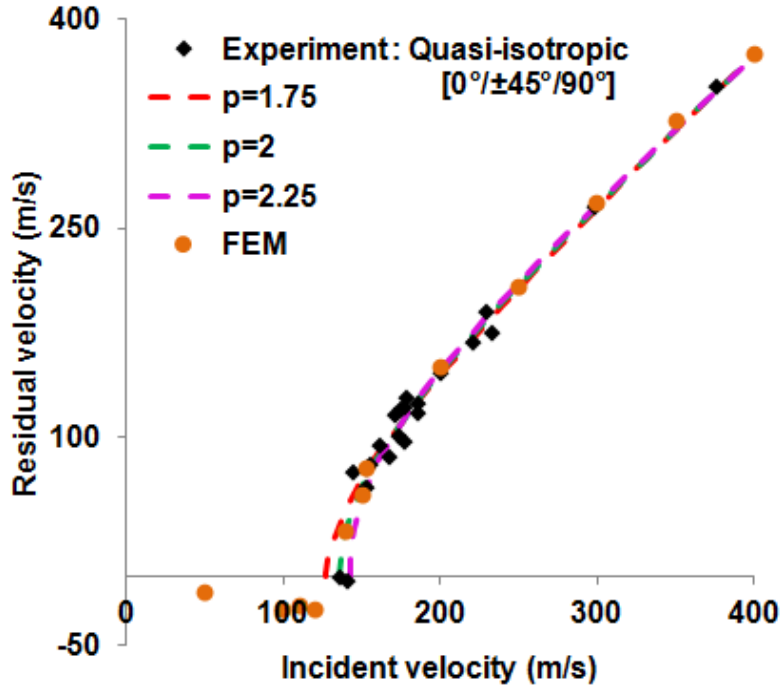

Fig.7.54. Comparison between experimental and FEM residual-incident velocity trend for the quasi-isotropic [0°/±45°/90°] GLARE 5 (3/2) plate specimen.

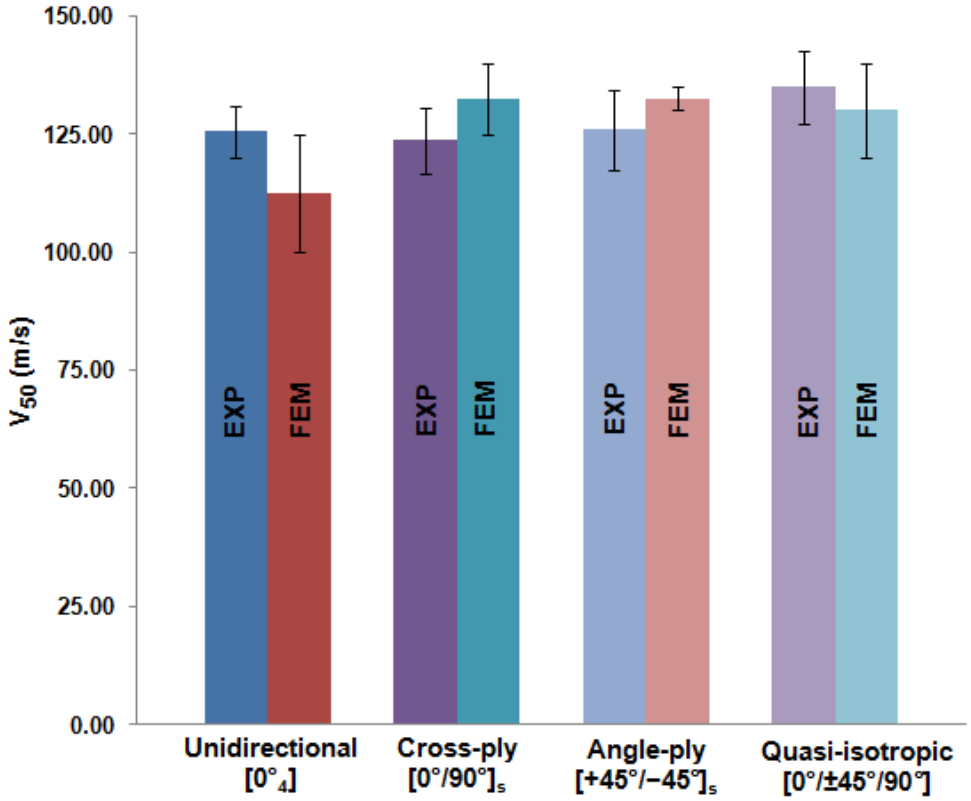

Fig.7.55. Comparisons between experimental and FE results of ballistic limit velocity (V_{50}) as a function of plate-specimen stacking sequence.

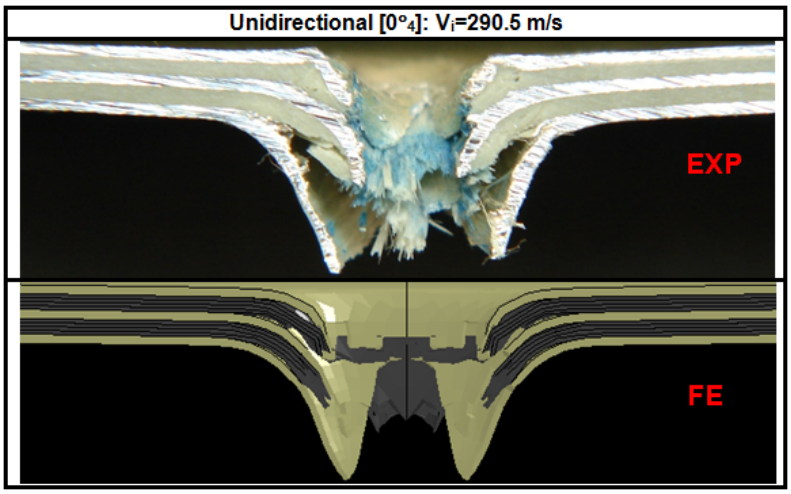

Fig.7.56. Comparisons of post-impact damage patterns for the unidirectional [$0°_4$] GLARE 5 (3/2) plate specimen impacted at 290.5 m/s.

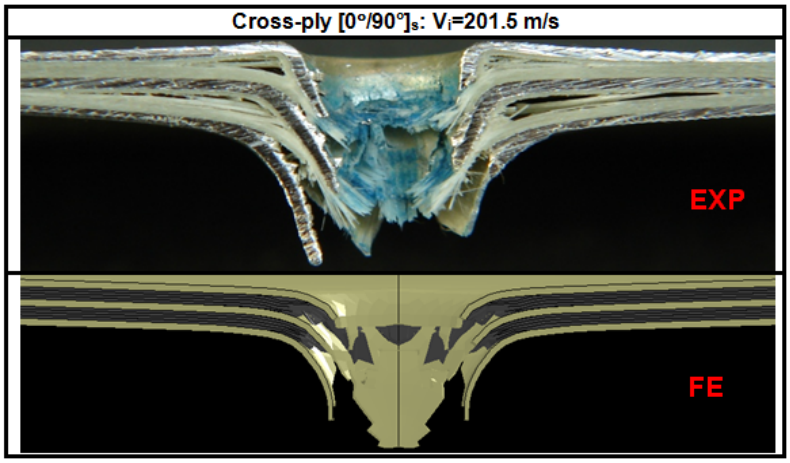

Fig.7.57. Comparisons of post-impact damage patterns for the cross-ply $[0°/90°]_s$ GLARE 5 (3/2) plate specimen impacted at 201.5 m/s.

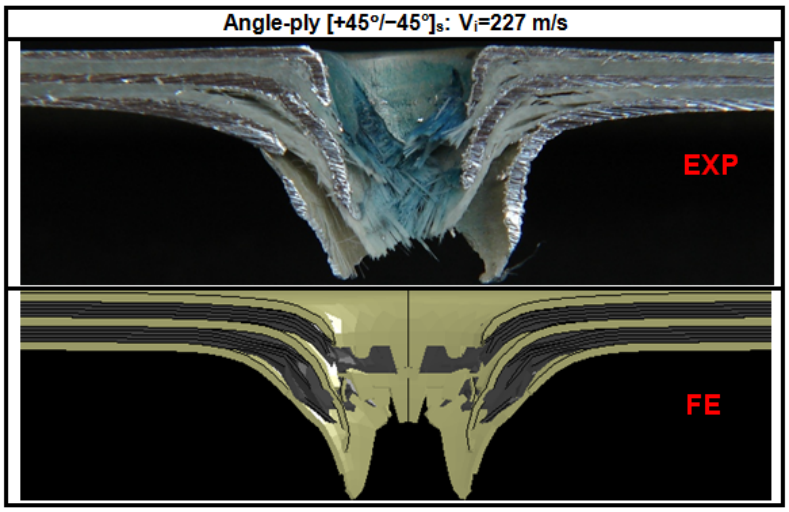

Fig.7.58. Comparisons of post-impact damage patterns for the angle-ply $[\pm 45°]_s$ GLARE 5 (3/2) plate specimen impacted at 227 m/s.

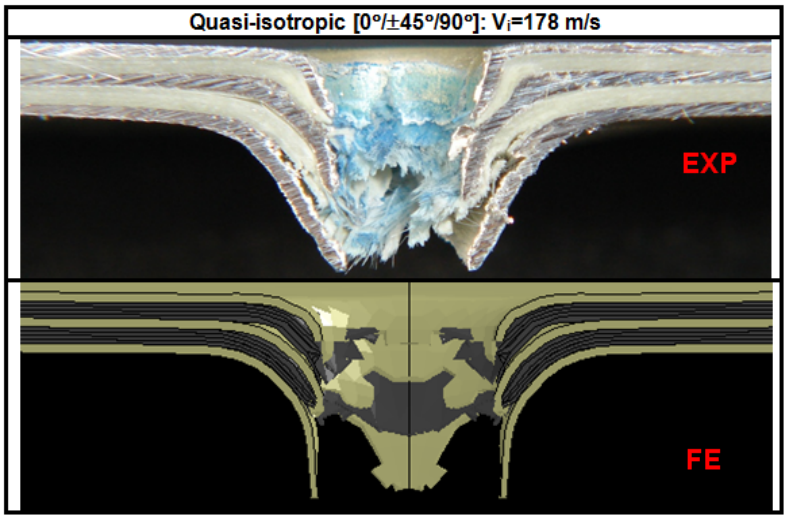

Fig.7.59. Comparisons of post-impact damage patterns for the quasi-isotropic [0°/±45°/90°] GLARE 5 (3/2) plate specimen impacted at 178 m/s.

GLARE 5 (3/2) [plate]	*Experiment*		*Finite Element Model*		ΔL
	Bullet Residual Length (mm)	Bullet	Bullet Residual Length (mm)	Bullet	Length Difference (mm)
$[0°_4]$ V_i=290.5 m/s	15.95		15.28		0.67
$[0°/90°]_s$ V_i=201.5 m/s	15.80		15.74		0.06
$[+45°/-45°]_s$ V_i=227 m/s	15.90		15.45		0.45
[0°/±45°/90°] V_i=178 m/s	15.95		15.92		0.03

Fig.7.60. Experiment and FE comparisons of bullet residual length of the GLARE 5 (3/2) plate specimens with various stacking sequences at different incident velocities.

7.4.2.1. Numerical prediction: stacking sequence effect

In this section, two examples were considered to study the contact resistance force. They are namely: (1) non-perforated case with an impact velocity of 50 m/s, and (2) perforated case with an impact velocity of 350 m/s. These examples are shown in Fig. 7.61, which displays the FE predicted contact force as a function of time for the unidirectional $[0°_4]$,

cross-ply $[0°/90°]_s$, angle-ply $[+45°/-45°]_s$ and quasi-isotropic $[0°/\pm45°/90°]$ lay-up orientation. As is apparent from the figure, the contact force histories had the same trend for all the lay-up orientations. The FE predictions of contact history for the same specimens near their ballistic limit velocities are depicted in Fig 7.62.

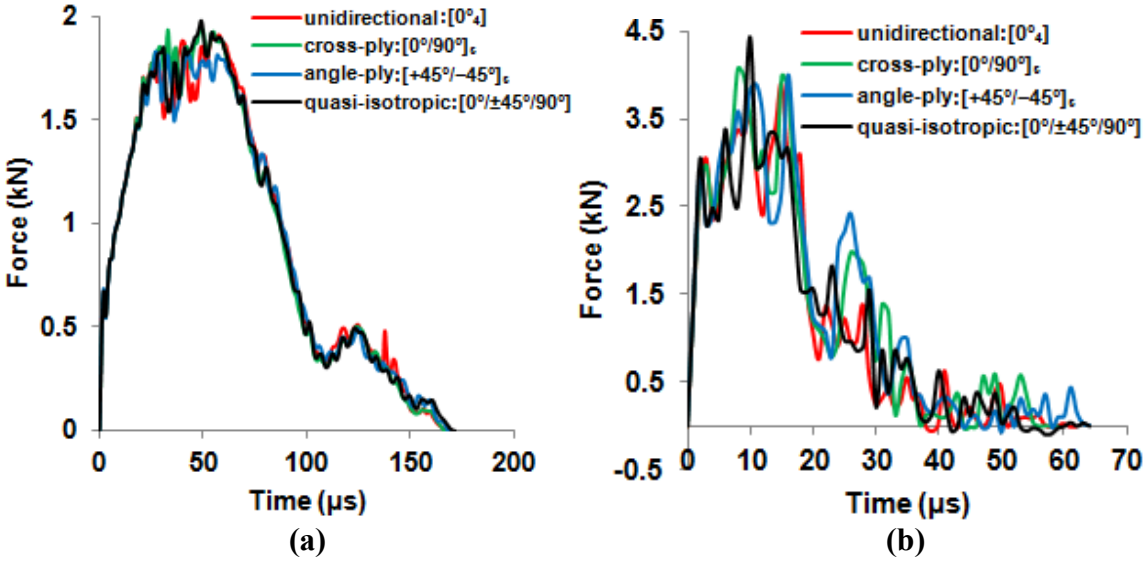

Fig.7.61. FE prediction of contact force as a function of time for the GLARE 5 (3/2) FML plates with various stacking sequences impacted at: (a) 50 m/s, (b) 350 m/s.

As Figs. 7.61 and 7.62 suggest, for a given specimen lay-up orientation, by increasing the projectile incident velocity up to near its V_{50}, the maximum contact force increased. By further increasing the projectile speed above its ballistic limit velocity, the maximum contact force was relatively insensitive with respect to an increase in the projectile speed. The reason for this was explained before in Section 7.3.1.1.

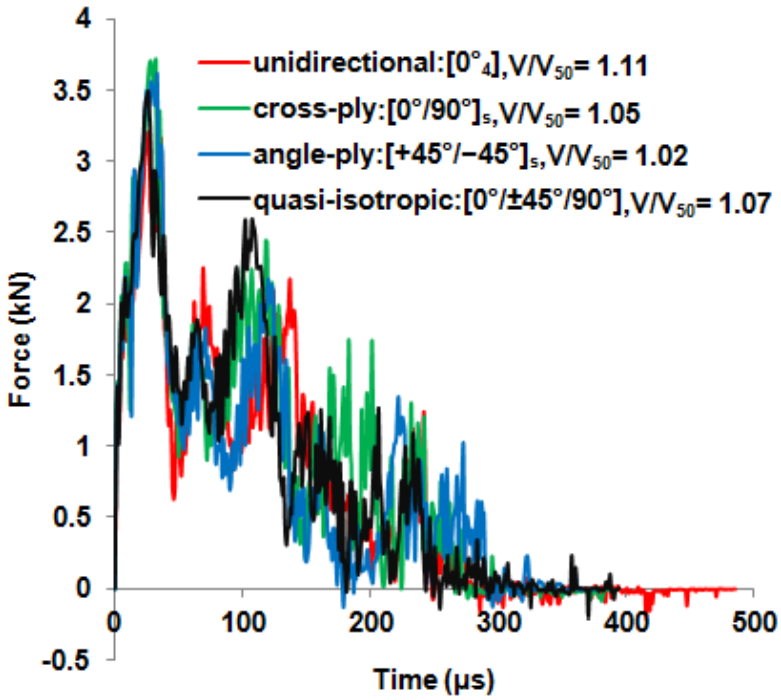

Fig.7.62. FE predictions of contact history for the GLARE 5 (3/2) FML plates with various stacking sequences near their ballistic limit velocities.

7.5. Conclusions

This study presented a numerical investigation on ballistic impact behaviors of the GLARE 5 FML beam and plate specimens of various thicknesses and stacking sequences. The following remarks can be concluded from this study.

- The FE model incorporated with MAT_22 (Chang-Chang material model) and MAT_98 (Simplified Johnson-Cook material model) was successfully used to simulate the ballistic impact tests on GLARE 5 FMLs.
- Good agreement between FE and experimental results namely: the V_I~V_R relation, damage patterns and bullet residual length was obtained for both beam and plate FMLs of various thicknesses and lay-up orientations, and hence the model was validated.

- For both beam and plate FMLs, the FE predicted V_{50}-thickness trend was in good agreement with the experimental results. Moreover, the FE predicted V_{50} as a function of specimen lay-up orientation was also in good agreement with the experimental results.
- For the cross-ply beam and plate specimens, the maximum contact force was the highest for the thickest specimen, i.e. the (6/5) configuration; whereas it was the lowest for the thinnest one, i.e. the (2/1) configuration. It was found that for a given specimen configuration, by increasing the projectile incident velocity up to near its V_{50}, the maximum contact force increased. By further increasing the projectile speed above its ballistic limit velocity, the maximum contact force was almost insensitive with respect to an increase in the projectile incident impact velocity. Similar conclusion was also achieved for the beam and plate specimens with various lay-up orientations.
- The force histories of the cross-ply beam and plate specimens revealed that the force histories were almost insensitive with respect to change in specimen geometry.
- Among the (3/2) FML beams, the cross-ply specimen offered the highest contact resistance while the unidirectional $[90°_4]$ specimen offered the lowest. The maximum contact force for the unidirectional $[0°_4]$ and quasi-isotropic panels were almost the same. Subjected to a ballistic impact, the GLARE 5 (3/2) FML beams with the cross-ply stacking sequence could dissipate more energy compared to other FML beams with different lay-up orientations.

CHAPTER 8: CONCLUSIONS AND PROPOSED FUTURE WORK

8.1. Summary

In this dissertation, the low-velocity and ballistic impact responses of the GLARE 5 FMLs of various thicknesses, stacking sequences and geometries were investigated. The range of thickness was from 1.117 mm (0.044″) of GLARE 5 (2/1) up to 4.368 mm (0.172″) of GLARE 5 (6/5). The effect of stacking sequence was studied on the GLARE 5 (3/2) specimens with unidirectional $[0°_4]$, unidirectional $[90°_4]$, cross-ply $[0°/90°]_s$, angle-ply $[-45°/+45°]_s$ and quasi-isotropic $[0°/\pm45°/90°]$ lay-up orientations. The low-velocity impact tests were focused on both square- and circular-shaped specimens; whereas beam and plate geometries were used for ballistic impact tests. Both destructive cross-sectional micrographs and nondestructive ultrasonic techniques were applied to evaluate the damage induced by impact. In addition, a high-speed camera was employed to assess damage evolution in the FMLs. Results showed that only the contour of the entire damage area was obtained using ultrasonic C-scan, whereas more details of the damage were provided through the mechanical cross-sectioning technique.

In the low-velocity-impact section, it was found that thicker GLARE 5 FMLs offered higher impact resistance. The failure mode changed with varying thickness and impactor mass. By reducing the mass of the impactor, but maintaining the same impact energy, the permanent central deflection increased. This implied that the panel with lighter impactor mass reached the perforation limit faster than the heavier one. The threshold cracking energy varied parabolically with respect to the impact velocity, MVF and the specimen thickness. The impact properties of the FMLs were also affected by laminate stacking sequence. The GLARE 5 FMLs made of unidirectional fibers had the least impact

resistance; followed by cross-ply and angle-ply configurations; while the quasi-isotropic lay-up showed the best in resistance to impact. It was shown that the damage patterns and impact behaviors were almost invariant to the change in the specimen geometry. on the other hand, it was recommended that composite specimens with a circular outer perimeter and inner clamp should be used instead of using a square outer perimeter and a circular inner clamp.

In the ballistic-impact part, three different techniques, namely: laser-beam optoelectronics, chronograph and high-speed photography were utilized to measure projectile velocities along the ballistic trajectory. It was found that the bullet speed obtained from the high-speed camera was relatively higher than the one measured by the optoelectronic technique near the end of the gun barrel. In other words, as the bullet emerged from the gun barrel, it was further accelerated along its trajectory before hitting the target. This phenomenon was explained by intermediate ballistics. The results suggested that the amount of the acceleration was negligible by changing the target position from the gun muzzle and the type of propellants. The classical Lambert-Jonas' equation was very helpful in obtaining the ballistic limit velocities, especially for the cases when obtaining lower incident velocity was difficult experimentally. The ballistic limit velocity was determined based on the specimen-experimental-velocity trend and classical Lambert–Jonas' equation. It was found that by changing the geometry from a plate to a beam, the ballistic limit velocity increased. The results showed that V_{50} varied in a parabolic trend with respect to the MVF and the specimen thickness for both geometries. On the other hand, changing the stacking sequence had a less pronounced effect on V_{50} for both geometries. GLARE 5 beam and plate specimens developed

damage similar to both monolithic aluminum alloy and polymer composite laminate. The interfacial debonding as well as the aluminum layers bending and stretching were considered to be the major aspects in dissipating the impact energy in the specimens. However, the permanent global bending deformation of the FML plates was less pronounced compared to the FML beams. The optical images from the non-impacted side of the FML plates revealed that the plastically deformed damage zone appeared on the non-impacted side of the specimens increased by increasing the specimen thickness for a given velocity range.

Finally, the LS-DYNA FE code was used to perform numerical simulations of ballistic impact on the GLARE 5 FMLs of diverse thicknesses, stacking sequences and geometries. The FE models were validated based on the V_I~V_R relation, damage patterns and bullet residual lengths. Good agreement between FE and experimental results was obtained. The FE predicted V_{50} as functions of thickness and stacking sequence was also in good agreement with the experimental results. The validated FE results exhibited that for the cross-ply beam and plate specimens, the maximum contact force was the highest for the thickest specimen; whereas it was the lowest for the thinnest one. On the other hand, for a given specimen configuration, by increasing the projectile incident velocity up to near its V_{50}, the maximum contact force increased. By further increasing the projectile speed above its ballistic limit velocity, the maximum contact force was almost insensitive with respect to an increase in the projectile incident impact velocity. Similar conclusion was also achieved for beam and plate specimens with different lay-up orientations. Moreover, the force histories of the cross-ply beam and plate specimens revealed that the force histories were almost insensitive with respect to change in specimen geometry.

8.2. Contributions

The following subjects were extensively studied in this dissertation.

a) Low-velocity impact response of the GLARE 5 FMLs:

- ❖ The effects of thickness, impactor mass, stacking sequence and geometry.
- ❖ The estimation of the threshold level of cracking energy of the cross-ply GLARE 5 specimens.

b) Ballistic impact response of the GLARE 5 FMLs:

- ❖ The projectile speed along its ballistic trajectory using different techniques, namely: laser-beam optoelectronics, chronograph and high-speed photography.
- ❖ The effects of target position from the gun muzzle and propellants.
- ❖ The effects of stacking sequence, thickness and geometry.

c) FE analyses of the GLARE 5 FMLs under ballistic impact:

- ❖ Developing an FE model.
- ❖ Validating the developed FE model based on experimentally obtained results and, subsequently, extracting some useful information in which experimental results were not available.

8.3. Proposed future work

<u>For the experimental part</u>:

- Study the strain rate effect on dynamic mechanical properties using split Hopkinson bar technique.
- Study the temperature effect under ballistic impact.
- Develop a better technique to capture damage progression in the specimen using a high-speed camera and X-ray radiography.

- Study the amount of heat generation and dissipation during ballistic impact.

For the FE part:

- One of the drawbacks of the Chang-Chang damage model is that there is no strain rate effect involved in it. Hence, a better material model that can incorporate this factor will be helpful.
- A better debonding/delamination growth criterion to improve the FE predicted damage pattern.
- Consider the heat generation and dissipation during ballistic impact in the FE model.

REFERENCES

1. Daniel I.M., Ishai O., Engineering mechanics of composite materials, 2nd edition. Oxford University Press, Inc., 2006.

2. Abrate S., Impact on composite structures. Cambridge University Press, Cambridge, UK, 1998.

3. Abrate S., Modeling of impacts on composite structures. Compos. Struct., 2001, 51, 129-138.

4. Abrate S., Localized impact on sandwich structures with laminated facings. Applied Mech. Review, 1997, 50(2), 69-82.

5. Foreign object impact damage to composites. ASTM STP 568, American Society for Testing and Materials, 1975.

6. Vlot A., Glare-History of the development of a New Aircraft Material. Kluwer, Dordrecht: Kluwer Academic Publishers, 2001.

7. Vermeeren C.A.J.R., Beumler T., De Kanter J.L.C.G., Van Der Jagt O.C., Out B.C.L., Glare design aspects and philosophies. Appl. Compos. Mater., 2003, 10, 257-276.

8. Vlot A., Gunnink J.W. (Eds.). Fiber metal laminates, an introduction. Dordrecht, the Netherlands: Kluwer Academic Publishers, 2001.

9. Vogelesang L.B., Vlot A., Development of fibre metal laminates for advanced aerospace structures. Mater. Proc. Tech., 2000, 103, 1-5.

10. Lawcock G., Ye L., Mai Y.W., Novel fiber reinforced metal laminates for aerospace applications - a review: part I- background and general mechanical properties. SAMPE Journal, 1995, 31(1), 23-31.

11. Hagenbeek M., Characterisation of fibre metal laminates under thermo-mechanical loadings. Dissertation, Delft University of Technology, 2005.

12. Wu G., Yang J.M., Hahn H.T. The impact properties and damage tolerance and of bi-directionally reinforced fibre metal laminates. Mater. Sci., 2007, 42, 948–957.

13. Vlot A., Impact loading on fiber metal laminates. Impact Eng., 1996, 18(3), 291–307.

14. Alderliesten R., Rans C., The meaning of threshold fatigue in fibre metal laminates. Fatigue, 2009, 31, 213–222.

15. Sun C.T., Dicken A., Wu H.F., Characterization of impact damage in ARALL laminates. Compos. Sci. Tech., 1993, 49, 139–144.

16. Abdullah M.R., Cantwell W.J., The impact resistance of polypropylene-based fibre-metal laminates. Compos. Sci. Tech., 2006, 66, 1682–1693.

17. Langdon G.S., Nuricka G.N., Cantwell W.J., The response of fibre metal laminate panels subjected to uniformly distributed blast loading. Mech. A, Solids, 2008, 27, 107–115.

18. Vasek A., Polak J., Kozak V., Fatigue crack initiation in fiber-metal laminate GLARE 2. Mater. Sci. Eng., 1997, A234–236, 621–624.

19. Kawai M., Hachinohe A., Takumida K., Kawase Y., Off-axis fatigue behaviour and its damage mechanics modelling for unidirectional fibre-metal hybrid composite: GLARE 2. Compos. Part A, 2001, 32, 13–23.

20. Castrodeza E.M., Bastian F.L., Perez Ipiña J.E., Critical fracture toughness, J_C and δ_{5C}, of unidirectional fiber-metal laminates. Thin-Walled Struct., 2003, 41, 1089–1111.

21. Laliberté J.F., Poon C., Straznicky P.V., Fahr A., Applications of fiber-metal laminates. Polymer Compos., 2004, 21(4), 558-567.

22. Fiber-metal laminates, Advanced Structural Materials for the Aerospace Industry, Aviation Equipment Structures, INC.

23. Vlot A., Low-velocity impact loading on fiber reinforced aluminum laminates (ARALL) and other aircraft sheet materials. Dissertation, Delft University of Technology, 1991.

24. Liu Y., Liaw B., Effect of constituents and lay-up configuration on drop-weight tests of fiber-metal laminates. Appl. Compos. Mater., 2010, 17(1), 43-62.

24a. Liu Y., Impact-induced large elastoplastic damage in fiber-metal laminated panels. Dissertation, The City University of New York, 2005.

25. Reyes Villanueva G., Cantwell W.J., The mechanical properties of fibre-metal laminates based on glass fibre reinforced polypropylene. Compos. Sci. Tech., 2000, 60, 1085–1094.

26. Park R., Jang J., Effect of laminate thickness on impact behavior of aramid fiber/vinylester composites. Polym. Testing, 2003, 22, 939-946.

27. Chen P., Xiong J., Shen Z., Thickness effect on the contact behavior of a composite laminate indented by a rigid sphere. Mech. of Mater., 2008, 40, 183-194.

28. Tai N.H., Ma C.C.M., Lin J.M., Wu G.Y., Effects of thickness on the fatigue-behavior of quasi-isotropic carbon/epoxy composites before and after low energy impacts. Compos. Sci. and Tech., 1999, 59, 1753-1762.

29. Fan J., Cantwell W.J., Guan Z.W., The low-velocity impact response of fiber-metal laminates. Reinforced Plast. and Compos., 2011, 30(1), 26-35.

30. Belingardi G., Vadori R., Influence of the laminate thickness in low velocity impact behavior of composite material plate. Compos. Struct., 2003, 61, 27–38.

31. Sutherland L.S., Guedes Soares C., Effect of laminate thickness and of matrix resin on the impact of low fibre-volume, woven roving E-glass composites. Compos. Sci. and Tech., 2004, 64, 1691–1700.

32. Sutherland L.S., Soares C.G., Impact tests on woven-roving E-glass/polyester laminates. Compos. Sci. and Tech., 1999, 59(10), 1553-1567.

33. Seo H., Hundley J., Hahn H.T., Yang J.M., Numerical simulation of glass-fiber-reinforced aluminum laminates with diverse impact damage. AIAA, 2010, 48(3), 676-687.

34. Hitchen S.A., Kemp R.M.J., The effect of stacking sequence on impact damage in a carbon fiber/epoxy composite. Compos., 1995, 26, 207-214.

35. Atas C., Liu D., Impact response of woven composites with small weaving angles. Impact Eng., 2008, 35(2), 80-97.

36. Tsartsaris N., Meo M., Dolce F., Polimeno U., Guida M., Marulo F., Low-velocity impact behavior of fiber metal laminates. Compos. Mater., 2011, 45(7), 803-814.

37. Choi H.Y., Wang H.S., Chang F.K., Effect of laminate configuration and impactor's mass on the initial impact damage of graphite/epoxy composite plates due to line-loading impact. Compos. Mater., 1992, 26(6),804-827.

38. Guynn E.G., O'Brien T.K., The influence of lay-up and thickness on composite impact damage and compression strength. AIAA-85-0646, Proceedings, 26th AIAA/ASME/ASCE/AHS Structures, Structural Dynamics, and Materials Conference. Orlando, FL., April 1985, 1, 187-196.

39. Mili F., Necib B., The effect of stacking sequence on the impact-induced damage in cross-ply E-lass/epoxy composite plates. Arch. Appl. Mech., 2009, 79, 1019-1031.

40. Cantwell W.J., Morton J., Geometrical effects in the low velocity impact response of CFRP. Compos. Struct., 1989, 1, 39-59.

41. Cantwell W.J., Geometrical effects in the low velocity impact response of GFRP. Compos. Sci. and Tech., 2007, 67, 1900-1908.

42. Strait L.H., Karasek M.L., Amateau M.F., Effects of stacking sequence on the impact resistance of carbon fiber reinforced thermoplastic toughened epoxy laminates. Compos. Mater., 1992, 26(12), 1725-1740.

43. Chun L., Lam K.Y., Dynamic response of fully clamped laminated composite plates subjected to low-velocity impact of a mass. Solids Struct., 1998, 35(11), 963- 979.

44. Choi I.H., Lim C.H., Low-velocity impact analysis of composite laminates using linearized contact law. Compos. Struct., 2004, 66, 125–132.

45. Choi H.Y., Downs R.J., Chang F.K., A new approach toward understanding damage mechanisms and mechanics of laminated composites due to low-velocity impact: part I-experiments. Compos. Mater., 1991, 25, 992-1011.

46. Chang F.K., Choi H.Y., Jeng S.-T., Characterization of impact damage in laminated composites. SAMPE Journal, 1990, 26(1), 18-25.

47. Kim S.J., Goo N.S., Dynamic contact responses of laminated composite plates according to the impactor's shapes. Comput. and Struct., 1997, 65(1), 83-90.

48. Zukas J. A., High velocity impact dynamics. A Wiley-Interscience Publication, 1990.

49. Børvik T., Hopperstad O.H., Langseth M., Malo K.A., Effect of target thickness in blunt projectile penetration of Weldox 460 E steel plates. Impact Eng., 2003, 28, 413-464,.

50. Børvik T., Dey S., Clausen A.H., Perforation resistance of five different high-strength steel plates subjected to small-arms projectiles. Impact Eng., 2009, 36, 948-964.

51. Sarva S., Nemat-Nasser S., McGee J., Isaacs J., The effect of thin membrane restraint on the ballistic performance of armor grade ceramic tiles. Impact Eng., 2007, 34, 277-302.

52. Zhao G., Cho Ch., Lu Sh., Wang Zh., Experimental study on impact resistance properties of T300/epoxy composite laminates. Compos. Mater., 2010, 44(7), 857-870.

53. Nesterenko V.F., Goldsmith W., Indrakanti S.S., Gu Y., Response of hot isostatically pressed Ti-6Al-4V targets to normal impact by conical and blunt projectiles. Impact Eng., 2003, 28, 137-160.

54. Ulven C., Vaidya U.K., Hosur M.V., Effect of projectile shape during ballistic perforation of VARTM carbon/epoxy composite panels. Compos. Struct., 2003, 61, 143-150.

55. Tan V.B.C., Lim C.T., Cheong C.H., Perforation of high-strength fabric by projectiles of different geometry. Impact Eng., 2003, 28, 207-222.

56. Durmuş A., Güden M., Gülçimen B., Ülkü S., Musa E., Experimental investigations on the ballistic impact performances of cold rolled sheet metals. Mater. & Design, 2011, 32, 1356-1366.

57. Starratt D., Sanders T., Cepus E., Poursartip A., Vaziri R., An efficient method for continuous measurement of projectile motion in ballistic impact experiments. Impact Eng., 2000, 24, 155-170.

58. Farrar C.L., Leeming D.W., Military ballistics- a basic manual (Battlefield Weapons Systems & Technology). Brassey's Defence Publishers, Volume X, 1983.

59. Sevkat E., Liaw B., Delale F., Raju B.B., A combined experimental and numerical approach to study ballistic impact response of S2-glass fiber/toughened epoxy composite beams. Compos. Sci. and Tech., 2009, 69(7-8), 965-982.

60. Sevkat E., Experimental and numerical approaches for estimating ballistic limit velocities of woven composite beams. Impact Eng., 2012, 45, 16-27.

60a. Sevkat E., Hybrid carbon-glass fiber/toughened epoxy thick composites subject to drop-weight and ballistic impacts. Dissertation, The City University of New York, 2009.

60b. Budhoo Y., Effect of temperature on the damage of hybrid thick composites subject to drop-weight and ballistic impacts. Dissertation, The City University of New York, 2010.

61. Czarnecki G.J., Estimation of the V_{50} using semi-empirical (1-point) procedures. Compos. Part B, 1998, 29(3), 321-329.

62. Gellert E.P., Cimpoeru S.J., Woodward R.L., A study of the effect of target thickness on the ballistic perforation of glass-fiber-reinforced plastic composites. Impact Eng., 2000, 24, 445-456.

63. Cortes P., Cantwell W.J., The impact properties of high-temperature fiber-metal laminates. Compos. Mater., 2007, 41(5), 613-632.

64. Kim H., Welch D.A., Kedward K.T., Experimental investigation of high velocity ice impacts on woven carbon/epoxy composite panels. Compos. Part A, 2003, 34, 25–41.

65. Wu E., Chang L.C., Woven glass/epoxy laminates subject to projectile impact. Impact Eng., 1995, 16(4), 607-619.

66. Zaretsky E., DeBotton G., Perl M., The response of a glass fibers reinforced epoxy composite to an impact loading. Solids and Struct., 2004, 41, 569–584.

67. Cork C.R., Foster P.W., The ballistic performance of narrow fabrics. Impact Eng., 2007, 34, 495–508.

68. Naik N.K., Shrirao P., Reddy B.C.K., Ballistic impact behaviour of woven fabric composites: formulation. Impact Eng., 2006, 32, 1521–1552.

69. Naik N.K., Shrirao P., Reddy B.C.K., Ballistic impact behaviour of woven fabric composites: parametric studies. Mater. Sci. and Eng. A, 2005, 412, 104–116.

70. Naik N.K., Doshi A.V., Ballistic impact behavior of thick composites: parametric studies. Compos. Struct., 2008, 82, 447-464.

71. Morye S.S., Hine P.J., Duckett R.A., Carr D.J., Ward I.M., Modeling of the energy absorption by polymer composites upon ballistic impact. Compos. Sci. and Tech., 2000, 60, 2631-2642.

72. Hoo Fatt M.S., Lin C., Revilock Jr. D.M., Hopkins D.A., Ballistic impact of GLARE^{TM} fiber-metal laminates. Compos. Struct., 2003, 61, 73–88.

73. Goldsmith W., Dharan C.K.H., Chang H., Quasi-static and ballistic perforation of carbon fiber laminates. Solids Struct., 1995, 32(1), 89-103.

74. Vaidya U.K., Kulkarni M., Haque A., Hosur M.V., Kulkarni R., Ballistic performance of graphite/epoxy and S2-glass/epoxy composites with polycarbonate facing. Mat. Tech. and Adv. Perf. Mat., 2000, 15(3), 202-214.

75. Langdon G.S, Lemanski S.L., Nurick G.N., Simmons M.C., Cantwell W.J., Schleyer G.K., Behaviour of fibre-metal laminates subjected to localised blast loading: part I-experimental observation. Impact Eng., 2007, 34, 1202-1222.

76. Lemanski S.L., Nurick G.N., Langdon G.S., Simmons M.C., Cantwell W.J., Schleyer G.K., Behaviour of fibre-metal laminates subjected to localised blast loading-part II: quantitative analysis. Impact Eng., 2007, 34(7), 1223-1245.

77. Lemanski S.L., Nurick G.N., Langdon G.S., Simmons M.S., Cantwell W.J., Schleyer G.K., Understanding the behaviour of fibre metal laminates subjected to localised blast loading. Compos. Struct., 2006, 76, 82-87.

78. Langdon G.S., Cantwell W.J., Nurick G.N., The blast response of novel thermoplastic-based fibre-metal laminates-some preliminary results and observations. Compos. Sci. and Tech., 2005, 65, 861-872.

79. Li C.F., Hub N., Yina Y.J., Sekinec H., Fukunaga H., Low-velocity impact-induced damage of continuous fiber-reinforced composite laminates: part I. an FEM numerical model. Compos. Part A, 2002, 33, 1055–1062.

80. Li C.F., Hub N., Chenga J.G., Fukunagac H., Sekinec H., Low-velocity impact-induced damage of continuous fiber-reinforced composite laminates. Part II. verification and numerical investigation. Compos. Part A, 2002, 33, 1063–1072.

81. Pica A., Wood R.D., Hinton E., Finite element analysis of geometrically nonlinear plate behavior using a Mindlin formulation. Comput. and Struct., 1980, 11, 203–15.

82. Matzenmiller A., Lubliner J., Taylor R.L., A constitutive model for anisotropic damage in fiber-composites. Mech. of Mater., 1995, 20(2), 125-152.

83. William, K., Vaziri R., Finite element analysis of the impact response of CFRP composite plates. Proceedings of the ICCM-11, 1995, 532-654.

84. Van Hoof J., Woeswick M.J., Straznicky P.V., Bolduc M., Tylko S., Simulation of ballistic impact response of composite helmets. Proceedings of the 5th International LS-DYNA Users Conference, 1998.

85. Gama B.A., Gillespire Jr. J.W., Finite element modeling of impact, damage evolution and penetration of thick-section composites. Impact Eng., 2011, 38, 181-197.

86. Buyuk M., Kan S., Loikkanen M.J., Explicit finite-element analysis of 2024-T3/T351 aluminum material under impact loading for airplane engine containment and fragment shielding. Aerospace Eng., 2009, 22, 287-295.

87. Data sheets. Aviation Equipment Structures, Inc., Costa Mesa, California, 1998.

88. QA Reports B0319B-2, B1008B-1, B0904A-3. Structural Laminates Company, New Kensington, Pennsylvania, 1994.

89. Alloy 7475 Plate and Sheet, ACRP-053-B. Alcoa Mill Products, Bettendorf, Iowa.

90. Instron Dynatup 8250 Drop Weight Impact Tester. Operating Instructions, M14-13655-EN. Instron Corporation, Revision A, 1999.

91. http://www.instron.us/wa/home/default_en.aspx?ref=http%3a%2f%2fwww.google.com%2furl

92. Reid S.R., Zhou G., Impact behaviour of fibre-reinforced composite materials and structures. Woodhead Publishing Ltd and CRC Press LLC, 2000.

93. Goldsmith W., Tam E., Tomer D., Yawing impact on thin plates by blunt projectiles. Impact Eng.,1995, 16(3), 479-498.

94. Lambert J.P., Jonas G.H., Towards standardization of in terminal ballistics testing: velocity representation. Ballistic Research Laboratories, Aberdeen Proving Ground, Maryland, Report No. BRL-R-1852, 1976.

95. Recht R.F., Ipson T.W., Ballistic perforation dynamics. Appl. Mech., 1963, 30, 384-390.

96. Ben-Dor G., Dubinsky A., Elperin T., On the Lambert-Jonas approximation for ballistic impact. Mech. Research Communications, 2002, 29, 137-139.

97. Hoo Fatt M.S., Sirivolu D., A wave propagation model for the high velocity impact response of a composite sandwich panel. Impact Eng., 2010, 37, 117-130.

98. LS-DYNA Keyword User's Manual. Livermore Software Technology Corporation (LSTC). Volume 1, version 971, 2007.

99. Chang F.K., Chang K.Y., Post-failure analysis of bolted composite joints in tension or shear-out mode failure. Compos. Mater., 1987, 21(9), 809-833.

100. Chang F.K., Chang K.Y., A progressive damage model for laminated composites containing stress concentrations. Compos. Mater., 1987, 21(9), 834-855.

101. LS-DYNA Theory Manual. Livermore Software Technology Corporation (LSTC). March 2006.

102. Kay G., Goto D., Couch R., Statistical testing of aluminum, titanium, lexan and composites for transport airplane rotor burst fragment shielding. FAA Rep. No. DOT/FAA/AR-07/26, Federal Aviation Administration, Washington, D.C., 2007.

103. http://www.varmintal.com/aengr.htm.

104. Peters S.T., Handbook of Composites. 2nd ed. London: Chapman and Hall, 1988.

105. Vlot A., Krull M., Impact damage resistance of various fibre metal laminates. Phys IV, 1997, 7(C3), 1045–1050.

106. Armenakas A.E., Sciammarella C.A., Response of glass–fiber-reinforced epoxy specimens to high rates of tensile loading. Exp. Mech., 1973, 13, 433–440.

PUBLICATIONS RELEVANT TO THE DISSERTATION

Journal Articles:

1. A. Seyed Yaghoubi, Y. Liu, B. Liaw, Stacking Sequence and Geometrical Effects on Low-Velocity Impact Behaviors of GLARE 5 (3/2) Fiber–Metal Laminates. Journal of Thermoplastic Composite Materials, 25(2), 223-247, 2012.

2. A. Seyed Yaghoubi, Y. Liu, B. Liaw, Low Velocity Impact on GLARE 5 Fiber-Metal Laminates: Influences of Specimen Thickness and Impactor Mass. ASCE, Journal of Aerospace Engineering, 25(3), 409-420, 2012.

3. A. Seyed Yaghoubi, B. Liaw, Thickness influence on ballistic impact behaviors of GLARE 5 fiber-metal laminated beams: experimental and numerical studies. Composite Structures, 94(8), 2585-2598, 2012.

4. A. Seyed Yaghoubi, B. Liaw, Variation of lay-up orientation on ballistic impact behaviors of GLARE 5 fiber-metal laminated beams: experimental and numerical studies. International Journal of Impact Engineering (under review).

5. A. Seyed Yaghoubi, B. Liaw, Influences of thickness and stacking sequence on ballistic impact behaviors of GLARE 5 FML plates: Part I-Experimental Observations. Composites Science and Technology (under review).

6. A. Seyed Yaghoubi, B. Liaw, Influences of thickness and stacking sequence on ballistic impact behaviors of GLARE 5 FML plates: Part II-Numerical Analysis. Composites Science and Technology (under review).

Conference Papers:

1. A. Seyed Yaghoubi, M.F. Chow and B.M. Liaw, Velocity Measuring Approaches for the Determination of Ballistic Limits of GLARE 5 Fiber-Metal Laminate Plates. Experimental and Applied Mechanics, Volume 6. Conference Proceedings of the Society for Experimental Mechanics Series, 2011, Volume 9999, 129-138, DOI: 10.1007/978-1-4614-0222-0_18. June 13-15, 2011, Mohegan Sun, Uncasville, Connecticut, USA.

2. A. Seyed Yaghoubi, Y.X. Liu and B.M. Liaw, Drop-Weight Impact Studies of GLARE 5 Fiber-Metal Laminates. Experimental and Applied Mechanics, Volume 6. Conference Proceedings of the Society for Experimental Mechanics Series, 2011, Volume 9999, 267-279, DOI: 10.1007/978-1-4614-0222-0_33. June 13-15, 2011, Mohegan Sun, Uncasville, Connecticut, USA.

3. A. Seyed Yaghoubi, B. Liaw, Specimen Thickness and Impactor Mass Effects on Drop-Weight Impact Studies of GLARE 5 Fiber-Metal Laminates. Proceedings of the ASME 2011 International Mechanical Engineering Congress & Exposition. November 11-17, 2011, Denver, Colorado, USA**.**

4. A. Seyed Yaghoubi, B. Liaw, Determination of Ballistic Limits of GLARE 5 Fiber-Metal Laminates: the Influences of Geometry, Thickness and Stacking Sequence. Proceedings of the ASME 2011 International Mechanical Engineering Congress & Exposition. November 11-17, 2011, Denver, Colorado, USA**.**

5. A. Seyed Yaghoubi, B. Liaw, Experimental and Numerical Approaches on Behavior of GLARE 5 Beams: Influences of Thickness and Stacking Sequence. IMAC XXX A Conference and Exposition on Structural Dynamics. January 30 – February 2, 2012, Hyatt Regency Jacksonville Riverfront Jacksonville, Florida, USA.

6. A. Seyed Yaghoubi, B. Liaw, Thickness Effect on Cross-ply GLARE 5 FML Beams Subjected to Ballistic Impact. SEM XII International Congress & Exposition on Experimental and Applied Mechanics, Measurement Challenges for New Structures and Materials. June 11-14, 2012, Hilton Orange County/Costa Mesa, Costa Mesa, California, USA.

7. A. Seyed Yaghoubi, B. Liaw, Damage Assessments of Ballistic Impact Behaviors of GLARE 5 (3/2) Beams with Various Stacking Sequences. SEM XII International Congress & Exposition on Experimental and Applied Mechanics, Measurement Challenges for New Structures and Materials. June 11-14, 2012, Hilton Orange County/Costa Mesa, Costa Mesa, California, USA.

8. A. Seyed Yaghoubi, B. Liaw, Ballistic Impact Behaviors of GLARE 5 Fiber-Metal Laminated Plates. SEM XII International Congress & Exposition on Experimental and Applied Mechanics, Measurement Challenges for New Structures and Materials. June 11-14, 2012, Hilton Orange County/Costa Mesa, Costa Mesa, California, USA.

9. A. Seyed Yaghoubi, B. Liaw, An Experimental and Numerical Investigation of Thickness Effect on Cross-ply GLARE 5 FML Plates Subjected to Ballistic Impact. ASME 2012 International Mechanical Engineering Congress & Exposition. November 9-15, 2012, Houston, Texas, USA.

10. A. Seyed Yaghoubi, B. Liaw, Experimental and Numerical Investigations of Stacking Sequence Effect on GLARE 5 FML Plates Subjected to Ballistic Impact. ASME 2012 International Mechanical Engineering Congress & Exposition. November 9-15, 2012, Houston, Texas, USA.

OTHER PUBLICATIONS

Journal Articles:

1. J.J. Harrigan, S.R. Reid, A. Seyed Yaghoubi, The correct analysis of shocks in a cellular material. International Journal of Impact Engineering, 37, 918-927, 2010.

2. Y. Liu, A. Seyed Yaghoubi, B. Liaw, Low-velocity Impact Study on Fiber-metal Laminates Using Various Indenters. ASCE, Journal of Aerospace Engineering (under review).

3. M.F. Chow, B. Weeks, A. Seyed Yaghoubi, B. Liaw, Acoustic emission characteristics of fiber-metal laminates under monotonic tensile loading: effect of stacking sequence. Journal of Nondestructive Testing and Evaluation (in preparation).